Modelling and Analysis of Ophthalmic Fluid Dynamics

Gareth Alan Douglas Hurst

Submitted in accordance with the requirements for the degree of

Doctor of Philosophy

THE UNIVERSITY OF LEEDS

School of Mathematics

and

School of Mechanical Engineering

March 2014

The candidate confirms that the work submitted is his own and that appropriate credit has been given where reference has been made to the work of others.

For my inspirational parents.

"*The hardest thing to see is what is in front of your eyes.*"

– Johann Wolfgang von Goethe (1749 - 1832)

Acknowledgements

I would like to express my sincere and heartfelt gratitude to my supervisors Professor Mark A Kelmanson and Dr Jon L Summers for their support, advice and encouragement throughout this project. It has been a privelege to work with two such inspirational mathematicians, and I have thoroughly enjoyed the discussions we have had during our meetings together; some academic, and others not-so-academic!

I would also like to thank the postgraduates and lecturers in Applied Mathematics for stimulating conversations and advice. Particular thanks go to the postgraduates who I have shared a communal office with over the four years of my PhD study.

Further thanks go to my family and friends who have made my life outside of academia so enjoyable: my parents Alan and Caroline for their unceasing support of my endeavours; my sisters Alison, Katrina and Frances for always being able to raise a smile on my face, and; the Weightman family who have welcomed me with open arms. I am also grateful to the Leeds Symphony Orchestra and the Leeds & Bradford Triathlon Club for providing me with extra-curricular outlets on which to focus.

Last, but not least, I will never be able to thank my wonderful wife Jess enough. Her never-ending patience, love and encouragement have been invaluable to me throughout my research and especially during the writing-up period.

This research would not have been possible without the financial support of the University of Leeds through a “School of Mathematics Full-time Doctoral Training Grant” and the EPSRC through a “Targeted Enhanced Stipend”.

Abstract

Mathematical models and numerical methods are developed for analysing and simulating the spatio-temporal evolution of the tear film coating the anterior surface of the human eye during an interblink period. The novelty of the work is on two distinct fronts.

- First, a systematic approach is taken to ensure that the (coupled) model evolution equations — one each for film thickness and lipid-surfactant concentration — arising from asymptotic thin-film approximations of the Navier-Stokes equations, are uniformly valid when realistic ophthalmic data are used in the parameterisation. In this way, the present model does not — as occurs in related literature — yield results that are in conflict with *a priori* approximation hypotheses. More specifically, novel results are obtained on the effects of substrate curvature by proposing a specific coordinate system in which: the influence of curvilinearity on the evolution of the tear film can be parameterised, and; the limiting case recovers the Cartesian models of related literature. Additionally, the evolution equations are developed using sophisticated bespoke computer-algebra (MAPLE) techniques that permit the correct *a priori* scalings — of the competing effects of gravity, inertia, evaporation and surface tension — that guarantee the above-mentioned uniform validity. A novel consideration of the physical viability of boundary conditions at three-phase contact line on the eyelid in the existing mathematical literature leads to the proposal, implementation and investigation of novel Neumann boundary conditions that are supported by the results of recent *in vitro* experimental work.

- Second, bespoke spectral numerical methods are developed for solving the thin-film approximations, yielding hitherto-unseen explicit formulæ for high-order Chebyshev differentiation matrices. Inherent errors are quantified, thereby yielding an explicit understanding of both the modelling limitations and the plausibility of results. A suite of post-processing tools is developed to negotiate the complexities of implementing the novel boundary conditions in a spectral environment. All

numerical techniques are validated on test problems; a high degree of both accuracy and efficiency is demonstrated. An analysis is presented of the errors incurred in the numerical approximation of the (steep) film-profile gradients near the eyelids; the results of this error analysis prompt questions on the accuracy of many of the results of previously published models.

Through the combination of new, uniformly valid, thin-film approximations and bespoke, fully validated numerical methods, the coupled evolution equations for the thin-film thickness and lipid surfactant concentration are solved with confidence that the results obtained are credible. The novel boundary conditions lead to results that predict behaviours of the tear film that, whilst unseen in all prior related *mathematical* literature, encouragingly align with *in vivo* experimental observations in the *ophthalmic* literature. As a result, a novel hypothesis is presented for the behaviour of the tear-film contact line, through which predictions are made regarding the development and treatment of dry-eye pathologies. Suggestions for future work conclude the thesis.

Contents

List of figures

List of tables

Chapter 1

Introduction and Background

The work contained in this thesis studies the movement of a body of fluid that is, quite literally, right before your eyes! The tear film located on the anterior surface of the eye is an example of the diverse range of macroscopic thin films of fluid that can be found in both nature and engineering, and it provides the primary focus of the present research. The fluid dynamics of the tear film are studied through a mathematical model that is generated from basic physical principles, which model incorporates the interaction of the fluid with a layer of lipid surfactant found at the free surface of the tear film. Throughout the modelling process, meticulous care is taken to ensure that any assumptions made in the derivation are not invalidated by subsequent choices of parameter values: this philosophy is motivated by the frequent violation of this apparently obvious principle in much existing related literature.

In addition to novel developments made within the derivation of the mathematical model for the tear film, a significant proportion of this thesis is dedicated to the numerical methods employed in finding approximate solutions of the model. The resultant pair of coupled initial-boundary-value problems (IBVPs)—for the film thickness and surfactant concentration—is, in itself, difficult to tackle due to the non-periodic domain in which the tear film is located; this difficulty is exacerbated by the absence of any critically-important

minutiæ in the description of numerical methods used in existing published models of the tear film (*cf.* §1.2). Hence the explicit description and derivation of methods in this thesis is motivated by the aim that all results are readily replicable by the reader.

This introductory chapter is divided into three sections. In the first, the composition and certain physical properties of the human tear film are discussed, followed by the physiology of the secretory and drainage systems; these details are pertinent to the subsequent modelling of the fluid mechanics of the tear film. The second section comprises a review of published mathematical literature modelling the dynamics of the tear film. The third section comprises an outline of the structure of the remainder of the thesis.

1.1 Ophthalmic physiology

The pre-corneal tear film is an essential part of the ocular system: it acts as a barrier to debris, maintains the outermost cells of the eye, and acts as a lubricating layer for the rapidly-moving upper eyelid during a blink. The cells of the *cornea* (the transparent cap of fibrous material located anterior to the iris and pupil) do not receive a blood supply, making them reliant on a fresh tear film for their supply of nutrients. Continual replacement of the tear film allows dead cells and any debris that is not deflected by the eyelashes to be washed away from the ocular surface. In addition to these functions, the tear film is the first and major refractive interface of the eye (Bron *et al.*, 1997; Németh *et al.*, 2002) and so must remain as uniform as possible over the central region of the cornea in order that its shape does not deleteriously diffract the incident light, thereby affecting the visual acuity of the eye. In subsequent sections of this thesis, reference is made to the *palpebral* region of the eye. This term refers to the areas containing the eyelids and their associated structures, which structures are the location of the secretory and drainage systems for the tear film. The elliptic opening between the upper and lower eyelids is

known anatomically as the *palpebral fissure*.

1.1.1 Tear-film structure

The ocular surface exposed within the palpebral fissure is covered by the tear film and its menisci, which form where the fluid abuts the eyelid margins. The tear film is widely accepted to be formed as a tri-laminar structure (Holly & Lemp, 1973; Bron *et al.*, 1997); however, recent advances have suggested that the boundaries between the individual layers are not distinct, leading to blending of the layers (Rolando & Zierhut, 2001; Gipson, 2004; Szczęsna *et al.*, 2006). Periodic blinking refreshes and replenishes the tear film (Snell & Lemp, 1998). A variety of techniques have been devised to measure the thickness of the tear film, with published measurements ranging from as low as $2.7\,\mu$m (King-Smith *et al.*, 2000) to as high as $46\,\mu$m (Prydal *et al.*, 1992). The general consensus within the published data suggests that the true thickness is under $10\,\mu$m; such data can readily be found in the review articles of Bron *et al.* (2004) and King-Smith *et al.* (2004).

The layers of the tri-laminar model of the tear film, from posterior to anterior, are as follows.

A mucus layer lining the epithelial cells of the cornea. The long-standing model of Holly (1973) suggests that a deep mucus layer forms a hydrophilic surface to aid the wetting of the cornea. However, more recent studies (Sharma, 1998, for example) have shown the epithelial surface to be hydrophilic and as wettable as the mucus layer. Furthermore, there is evidence that the mucus layer is not distinct, and is intermixed with the overlying aqueous layer (Rolando & Zierhut, 2001). Measurements of the thickness of the mucus layer vary widely; Prydal *et al.* (1992) suggest that the tear film (of depth $\sim 40\,\mu$m) is largely composed of mucus, whilst values of roughly $1\,\mu$m are given by Rolando & Refojo (1983) and Nichols *et al.* (1985). The modelling of the dynamics of the viscous mucus layer falls outside the

scope of this thesis due to its interaction with membrane-associated glycoproteins at the highly-folded surface of the corneal epithelia (Sharma *et al.*, 1999; Gipson, 2004).

An aqueous layer consisting principally of water with dissolved salts, enzymes and proteins (Bron *et al.*, 1997). A diverse range of depths for the aqueous layer have been reported in the ophthalmic literature; however, the majority fall within the range of 3 - $10\,\mu$m (Holly & Lemp, 1977; Rolando & Refojo, 1983; Sharma, 1998; King-Smith *et al.*, 2004). Little dissolved mucin was found in the aqueous layer by Nagyová & Tiffany (1999), casting into dispute the aforementioned intermixed mucus-aqueous model of Rolando & Zierhut (2001) and others.

A lipid layer at the free surface of the tear film. This layer is composed chiefly of wax esters, cholesterol esters and phospholipids, and is 75 - 100 nm thick (McDonald, 1969; Holly & Lemp, 1977; Norn, 1979; Bron *et al.*, 1997; Goto & Tseng, 2003). The presence of the lipid layer reduces evaporative losses from the aqueous layer (Mishima & Maurice, 1961; Mathers, 1993; Craig & Tomlinson, 1997), and decreases the surface tension of the film, increasing its stability (Holly, 1973; Bron *et al.*, 2004). Furthermore, inhomogeneous distributions of superficial lipid have been suggested to drive flows within the underlying aqueous layer through the induced gradients in surface tension (Brown & Dervichian, 1969; Berger & Corrsin, 1974; Holly & Lemp, 1977; King-Smith *et al.*, 2009).

A schematic diagram of the tear film is shown in Figure 1.1. The mathematical analysis presented in Chapters 2 *et seq.* employs the tri-laminar model of the tear film in order to develop equations describing the interaction between a deep aqueous fluid covered with a superficial surfactant layer. As noted above, the movement of the mucus layer is not studied.

The rate of evaporation from the aqueous fluid reservoir of the tear film is a major

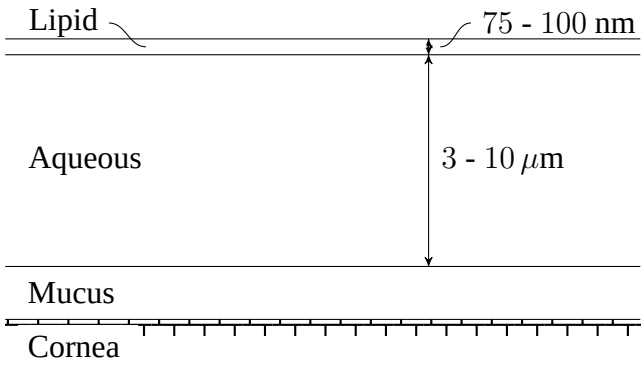

Figure 1.1: A cross-sectional schematic view of the tear film showing the tri-laminar model. Layer thicknesses are not represented to scale, and the depth of the pre-corneal mucus layer is omitted as its dynamics are not within the scope of this work.

factor in so-called 'dry eye' disorders (Holly & Lemp, 1977; Craig & Tomlinson, 1997; Tomlinson *et al.*, 2011), symptoms of which are reported by "*nearly half of women between the ages of 35 and 60*" and are prevalent in "*10 – 15% of the older adult population*" (Mathers, 2004). These disorders are divided into two major classes: *aqueous* or *tear-deficient* dry eye, in which there is a reduction in the volume of the aqueous layer of the tear film, and; *evaporative* dry eye, which is caused by excessive evaporation and is associated with deficiencies of the lipid layer (Baudouin, 2001; Bron, 2001; Tomlinson & Khanal, 2005). Ophthalmologists have derived a variety of techniques to quantify the rates of evaporation from normal and dry eyes in an effort to find a treatment for the disorder. Average rates of evaporation from normal eyes of 4×10^{-6}, 15×10^{-6} and 4×10^{-7} kg m^{-2} s^{-1} were respectively obtained by Rolando & Refojo (1983), Mathers (1993) and Craig & Tomlinson (1997); further collated results may be found in the review articles of Mathers (2004) and Tomlinson & Khanal (2005). In all cases, the rates of evaporation from the eyes of subjects with lipid-layer deficiencies were higher than those from eyes with normal lipid layers. King-Smith *et al.* (2008) argue that high humidities induced in the experimental apparatus of the studies above (and others) have caused the results published in the literature to be lower than the true rate of evaporation from normal

eyes; they suggest the rate of 39×10^{-6} kg m^{-2} s^{-1} obtained by Liu *et al.* (2005) as an accurate representative value.

Studies of the surface tension of tears have shown that, by comparison with a value of 7.3×10^{-2} N m^{-1} for a pure air-water interface, the presence of the superficial lipid layer markedly reduces the surface free energy of the tear film. Millar (1969) obtained a measurement of 4.6×10^{-2} N m^{-1} for normal tears, which is similar to the value of 4.36×10^{-2} N m^{-1} found by Tiffany *et al.* (1989). Further corroboration is provided by the results of Nagyová & Tiffany (1999), in which intact and lipid-depleted tears were tested to isolate the components responsible for the surface tension: a range of 4.2 – 4.6×10^{-2} N m^{-1} was stated for intact tears.

Observations of the lipid layer during a blink have shown that it is extremely resilient to the actions of compression and expansion enforced upon it by respectively the descent and ascent of the upper eyelid (McDonald, 1968, 1969; Mishima & Maurice, 1969; Bron *et al.*, 2004). Through such observations, McDonald (1968, 1969) suggests that the lipid layer moves in a manner similar to a 'pleated drape', folding and unfolding in reaction to the movement of the upper eyelid during a blink. After the upper lid has ceased moving, an upward drift of the lipid layer is observed for roughly one second (Brown & Dervichian, 1969; Berger & Corrsin, 1974; Owens & Phillips, 2001; King-Smith *et al.*, 2009). To explain this phenomenon, Brown & Dervichian (1969), Berger & Corrsin (1974) and Holly & Lemp (1977) propose that the deposition of the tear film is a two-phase process in which the upper lid first deposits a thin layer of aqueous fluid without a lipid covering; the lipid layer then lags behind slightly, and is drawn from a reservoir near the lower lid (Bron *et al.*, 2004) by the induced surface-tension gradient. Through movement of the lipid layer, viscous drag of aqueous fluid completes the second phase of deposition, thickening the film to its full depth across the eye. Observations of thickening of the tear film over the superior cornea after a blink (Benedetto *et al.*, 1984; Zhu *et al.*, 2007) appear to support this two-phase hypothesis. Contradicting this model, Wong *et al.*

(1996) hypothesize that the film "*is directly deposited at close to its final thickness by the rising upper lid*", and hence that the subsequent spreading of the lipid is not essential for the creation of a stable tear film. Eyelid kinetics observed by Doane (1980) show that, regardless of the hypothesis used, there is a significant lag between the completion of the upstroke of the upper eyelid and the establishment of a stable tear film, and Németh *et al.* (2002) suggest that it can take up to ten seconds for the tear film to stabilize after a blink. Corroborating these observations, King-Smith *et al.* (2009) observe a slow upward drift of the lipid layer persisting after the initially fast dynamics of the first second have subsided. The modelling of the post-blink distribution of the lipid surfactant is discussed in §2.4.1.

1.1.2 Palpebral physiology

The components of the tear film are secreted by organs within the palpebral region. The mucus that forms the posterior layer of the tear film is secreted by the *goblet cells* of the *conjunctiva*, which itself is a thin mucous membrane that lines the inner eyelids and the anterior surface of the eyeball.

Secretion and drainage of the aqueous layer is controlled by the *lacrimal*[1] apparatus, which consists of the *lacrimal gland*, *lacrimal lake*, *lacrimal canaliculi*, *lacrimal sac*, *puncta*, and *nasolacrimal duct*. The *lacrimal gland* is the source of the aqueous fluid, and is situated above the eye towards the lateral side, opening onto the ocular surface at the junction of the upper eyelid with the eyeball (known as the *superior conjunctival fornix*). In addition to the main lacrimal gland, a number of small accessory lacrimal glands are scattered around the upper eyelid. Aqueous fluid accumulates within the area below the eyelid (the *conjunctival sac*) and is distributed across the surface of the eye by the periodic action of blinking.

[1] '*lacrima*' is the latin word for tear.

Drainage of aqueous fluid occurs through the *puncta*, which are two small orifices found at the medial end of the lid margins, and are the openings of the *lacrimal canaliculi*, the small tubes that connect the puncta to the *lacrimal sac*. The muscular action of blinking opens the puncta onto the ocular surface whilst also pumping the canaliculi, creating a pressure gradient that draws fluid away from the eyeball (Maurice, 1973; Zhu & Chauhan, 2005). The lacrimal sac opens into the *nasolacrimal duct*, which itself drains into the nasal cavity.

The superficial lipid layer of the tear film is secreted by the *tarsal (Meibomian) glands*. These glands are located within the upper and lower eyelids, lying anterior to the conjunctiva, and opening onto the eye at the lid margins. There are around 20 – 25 glands in each lid (Snell & Lemp, 1998). The secretion of the Meibomian lipid onto the eyelid margins alters the wettability of the eyelid margin in a transition zone called the *mucocutaneous junction* that is located immediately posterior to the orifices of the Meibomian glands. The abrupt change in wettability prescribes the anterior limit of the tear-film meniscus that forms at the eyelid (Bron *et al.*, 1997). The tear film is stated by Bron *et al.* (2011) to always reach the mucocutaneous junction. However, this is contradicted by the repeatability results of Golding *et al.* (1997), which show that the reach of the tear meniscus up the eyelid margin[2] is variable in the same subject. The pinning of the meniscus at the mucocutaneous junction is an important topic in this thesis, and is discussed further in §2.4.1.

For more detailed information on the anatomy and physiology of the eye and palpebral region, the reader is referred to the text-books by Bron *et al.* (1997) and Snell & Lemp (1998), among others.

[2] called the ‘tear-meniscus width’ (TMW) in the ophthalmic literature.

1.2 Tear-flow models

A plethora of literature has been published containing mathematical models for thin-film flows, of which a small subset (cited below) is focussed on the modelling of the human tear film. Many papers have been published within the last fifteen years, as mathematicians and ophthalmologists have started to forge strong links. The majority of published work focusses on the movement of the aqueous layer, and its interaction with the lipid surfactant at the free surface. However, papers have also been published on the mucus layer, as well as on convection of the humours inside the eyeball itself. In all literature cited in the following paragraphs, the models are derived using a two-dimensional Cartesian coordinate system unless explicitly stated otherwise.

Motivated by the results of Brown & Dervichian (1969), a Lagrangian model for the post-blink drift of the lipid and aqueous layers is presented by Berger (1973) and Berger & Corrsin (1974), which respectively comprise a PhD thesis and summary article. In these works, a comparison of simulated results with *in vivo* data leads to a conclusion that surface-tension gradients are a suitable mechanism for driving the tear film up the cornea after a blink. As mentioned in §1.1.1, an alternative theory for the post-blink drift of the tear film is presented in Wong *et al.* (1996), which models the deposition of the tear film as a coating process with fluid drawn from the meniscus of the moving upper lid. This model predicts the thickness of the deposited profile to be proportional to the speed of the advancing lid. Interblink simulations in Wong *et al.* (1996) show significant thinning of the film at the join of the meniscus to the main tear film, a phenomenon that is also studied by Miller *et al.* (2002), who conclude that the menisci and the interior film are hydrodynamically isolated by the thinned region. This region of meniscus-induced thinning is called the ‘black line’ by ophthalmologists (McDonald & Brubaker, 1971; Holly & Lemp, 1977; Bron *et al.*, 2011), in reference to the reduced fluorescence of the thinned region when visualized using flourescein dye.

A significant body of work on the tear film has been published by Braun and co-authors. Braun & Fitt (2003) model the draining of the tear film under the effects of gravity and evaporation, concluding that, whilst the two effects are not dominant in the flow, they can influence the drainage process and so must be included within models. The full blink cycle is modelled in Braun & King-Smith (2007), using a domain length and flux boundary conditions that vary sinusoidally in time to simulate periodic movement of the upper eyelid. A simplified model for the concentration of lipid surfactant is included, and computed film profiles are matched to *in vivo* data. Heryudono *et al.* (2007) extend this work by incorporating realistic lid motions and fluid fluxes into the temporal variation used to simulate the blink cycle. Results are again compared with ophthalmic data.

Maki *et al.* (2008) use an overset-grid method for their spatial discretization, and extend the model of Heryudono *et al.* (2007) to simulate the opening of the eye followed by reflex tearing from the lacrimal gland; specifically, this is modelled via an alteration to the fluid influx boundary condition specified at the upper eyelid. The same numerical method is employed in Maki *et al.* (2010a) and Maki *et al.* (2010b), which are sister papers modelling the tear film using three-dimensional Cartesian coordinates on an eye-shaped domain. The two parts study the influence of different boundary conditions, respectively variable pressures and variable fluxes for papers (a) and (b). Three-dimensional modelling is retained in Braun *et al.* (2012) by employing prolate spheroidal coordinates to incorporate the curvature of the ocular substrate. Newtonian and shear-thinning fluids are modelled, drawing a conclusion that corneal shape does not have a significant effect on the thinning of the tear film. To the author's knowledge, this is the only existing model outside of the present work that includes the influence of the curved corneal substrate on tear-film dynamics.

The work of Braun & Fitt (2003) is extended in Winter *et al.* (2010) through the use of a more-realistic model for the evaporation from the tear film, and a conjoining pressure to model a simulate corneal surface. Qualitative agreement between model results and

in vivo data is obtained for the speed at which ruptures in the tear film expand. The temperature distribution within the tear film is studied in Li & Braun (2012) by modelling the diffusion of heat through the tear film and from the underlying cornea. A parameter set is found that captures the temperature decreases observed *in vivo*. A review article on the mathematical modelling of the tear film is presented in Braun (2012).

A model for the deposition of the tear film is presented in Jones *et al.* (2005), which extends the model of Braun & Fitt (2003) by studying the opening phase of the eye and including a simplistic model for the effects of the superficial lipid layer. Boundary conditions specifying the influx of fluid from below the opening upper lid are enforced, and it is found that the deposition of a viable tear film requires an influx of fluid from under the lid. Jones *et al.* (2006) extend the work by improving the modelling of the surfactant layer to study the post-blink movement of lipid. By altering the initial surfactant distribution, the results of the model are found to support the hypothesis of Brown & Dervichian (1969), Berger & Corrsin (1974) and Holly & Lemp (1977). A model for the elastohydrodynamics of the eyelid as a 'wiper' mechanism is presented in Jones *et al.* (2008).

Further insight on the deposition of the tear film is given in Please *et al.* (2011), which studies the influence of meniscus shape and storage on the film profile deposited by the upper eyelid, modelled in three-dimensional Cartesian coordinates with an elliptic domain acting as a simplified palpebral fissure. The shape of the deposited tear film is found to be strongly affected by the geometry of the menisci at the eyelids. Aydemir *et al.* (2011) studies the effect of the lipid layer on the deposition and subsequent thinning of the tear film in the absence of evaporation, and includes an asymptotic study of the early stages of deposition. Again, the conclusions drawn support the two-stage deposition model of Brown & Dervichian (1969), Berger & Corrsin (1974) and Holly & Lemp (1977).

A model for the solute concentration within the aqueous layer of the tear film is coupled to the dynamics of the film thickness and surfactant concentration in Zubkov

et al. (2012), and used to study hyperosmolarity in the black-line regions caused by meniscus-induced thinning. Further meniscus dynamics are examined in Zubkov *et al.* (2013), which compares the tear-film behaviour predicted by a lubrication-approximation model with the behaviour modelled through solution of the Navier-Stokes equations in the menisci. Lubrication theory is found to be qualitatively accurate *except* in the menisci, wherein the Navier-Stokes model predicts a convective mixing region that is absent from the lubrication model.

With the exception of Please *et al.* (2011), which models the radius of curvature of the menisci, a common thread running through the models cited above is the prescription of the tear-film thickness at the eyelid, to emulate the position of the mucocutaneous junction introduced in §1.1.2. This so-called 'pinning' of the film thickness yields a Dirichlet boundary condition for the resulting partial differential equation for the evolution of the tear-film thickness. Further, more detailed, comment on the validity of pinning the film thickness is made in §2.4.1.

In addition to modelling the dynamics of the tear film's aqueous layer and its interaction with the superficial lipid layer, a variety of fluid mechanical models have been inspired by the eye, including: studies of the mucus layer and its interactions with the cornea and the overlying aqueous fluid (Sharma, 1998; Sharma *et al.*, 1999); flow of the aqueous humour in the anterior chamber of the eye (Fitt & Gonzalez, 2006; Avtar & Srivastarva, 2006); movement-induced dynamics of the vitreous humour (Repetto, 2006); models of shear-thinning tear substitutes (Jossic *et al.*, 2009); the dynamics of the tear film in the presence of a contact lens (Trinh *et al.*, 2014), and; the aforementioned studies of Zhu & Chauhan (2005) and Jones *et al.* (2008).

1.3 Outline of the thesis

Having described the palpebral physiology and the existing models of the tear film, the objective of this thesis is to develop a spatio-temporal model for the lacrimal dynamics of the open eye during the interblink period, which constitutes at least 95% of the total blink-cycle duration (calculated using data from Berger & Corrsin, 1974, and Doane, 1980), and to employ accurate numerical methods to solve this model. With this motivation in mind, the structure of this thesis is as follows.

Chapter 2 presents an asymptotic derivation of the thin-film evolution equations for the thickness of the tear film and the concentration of lipid surfactant that incorporates the effects of gravity, hydrostatic pressure, evaporation, and a spatially-varying surface tension that is dependent on the local concentration of adsorbed surfactant. Despite the existence of many models for the tear film as outlined above, the present approach is distinguished from prior work through its meticulous treatment of the asymptotic ordering of terms within the governing equations, which ordering is achieved through an *a priori* rescaling of all variables and physical quantities in the model. Through such scalings, the leading-order evolution equations are, by construction, uniformly valid in the considered parameter régime. The modelling of the tear film includes two novel developments that are hitherto unseen in all other models. The first is the use of a novel curvilinear coordinate system that allows the curvature of the underlying substrate to be controlled through variation of a single parameter, allowing the influence of the curved corneal substrate on the flow dynamics to be quantified. The second is the specification of the contact angle, formed between the eyelid margin and the free surface of the tear film, as a boundary condition for the spatio-temporal evolution equation for the film thickness. Such a boundary condition represents a significant departure from the modelling in *all* prior models for the tear film, as it replaces the Dirichlet 'pinning' mentioned above, enabling the tear film to evolve under the influence of only Neumann boundary conditions. This

change to the modelling is motivated because, as indicated previously, pinning of the film does not appear to have a firm physical justification. The specification of the boundary conditions is addressed fully in §2.4.1.

Following the derivation of the coupled thin-film evolution equations for the film thickness and surfactant concentration, Chapters 3 and 4 are respectively devoted to a detailed description of the numerical methods used in solving the tear-flow model, and to the validation of the numerical techniques employed. Chapter 3 describes the spatial discretization process using Chebyshev spectral methods, which are chosen in order to improve (dramatically) upon the accuracy of the finite-difference methods used in the solution of the majority of prior tear-flow models (see, for example, Braun & Fitt, 2003; Jones *et al.*, 2006; Aydemir *et al.*, 2011). To further improve the accuracy of the numerical scheme, novel explicit forms of the third- and fourth-order Chebyshev differentiation matrices are derived. The spatial discretization is augmented by post-processing tools that allow the boundary conditions to be enforced with spectral accuracy, and allow the mass within the system to be calculated, which mass provides a validation of the accuracy of the numerical scheme in the absence of evaporation. To remain consistent in the present transparent approach to numerical modelling, the temporal discretization is carried out using a coupled fourth-order Runge-Kutta scheme that is briefly outlined. Such an approach is in contrast to a number of tear-film models, which use undiscussed proprietary software packages to carry out temporal integration (see, for example, Braun & Fitt, 2003; Heryudono *et al.*, 2007; Maki *et al.* 2010a; Maki *et al.*, 2010b; Zubkov *et al.*, 2012, 2013). The presentation of the numerical scheme is made as general as possible in order that the techniques may be employed, with suitable modifications, to other spatio-temporal problems on a finite domain. All the methods of Chapter 3 are meticulously tested in Chapter 4 using model problems with known analytic solutions, giving confidence that the results obtained through numerical solution of the tear-flow model are accurate representations of the physical processes included within the derivation. Motivated by the steep menisci in tear-film profiles occurring in the existing ophthalmic and mathematical

literature, Chapter 4 concludes with an analysis of the absolute errors encountered in the numerical approximation of derivatives of "steep-sided" functions using Chebyshev spectral methods.

With the numerical methods thus outlined and tested, they are employed in the solution of the new coupled evolution equations in Chapters 5 and 6. More specifically, Chapter 5 contains results from simulations of the film-thickness evolution equation in the absence of a motile surfactant layer, allowing the effects of the novel coordinate system and boundary condition to be observed in isolation. The fully coupled system of evolution equations is solved in Chapter 6, demonstrating the non-trivial influence of the surfactant layer on the dynamics of the tear film. In both chapters, the results of the model are compared and contrasted with both the ophthalmic observations described in §1.1 and the data from the existing mathematical models for the tear film outlined in §1.2. Through such comparisons, novel conclusions are drawn regarding the onset of dry-eye phenomena within the human tear film, which conclusions motivate the formulation of a new hypothesis for the movement of the tear-film contact line during the interblink period. This hypothesis enables alternative methods for the treatment of dry-eye diseases to be suggested.

Finally, a summary of the major emphases of the thesis is given in Chapter 7, in which possible future developments for the model are also discussed.

Chapter 2

Governing Equations

This chapter contains the derivation of a mathematical model for describing the ophthalmic flow introduced in Chapter 1; specifically, the equations describing the motion of a two-dimensional incompressible, viscous, evaporating fluid coating a curved substrate enclosed by solid boundaries, with a non-uniform distribution of adsorbed lipid surfactant at its free surface are derived. A definition sketch for the flow is given in Figure 2.1.

A pair of coupled spatio-temporal evolution equations, for the film thickness and the concentration of surfactant, is derived from first principles under the assumptions that the characteristic depth of the film is small by comparison with the arc length along the substrate, and that the concentration of adsorbed surfactant is low enough that the molecules are not densely packed, and hence can be treated as being in an expanded state (Adam, 1941). The competing effects of gravity, evaporation and capillarity are included within the modelling. To observe the effect of substrate curvature on the behaviour of the system, the equations are derived in cylindrical polar coordinates, with a change of coordinate system to so-called 'marginal-surface' coordinates (see §2.2 for details) that are introduced to admit a simple transition to a Cartesian coordinate system in the fluid as the radius of curvature of the substrate is increased to infinity. This is done because, with

the exception of Braun *et al.* (2012), the literature in this area focusses exclusively on a Cartesian model, hence this development provides a novel quantification of the effects of *controllable* curvilinearity.

2.1 Derivation of governing equations

The thin-film thickness evolution equation has been derived to study a diverse range of applications[1]. In the majority of formulations, the combination of physical parameters within the modelled fluid flow yield a Reynolds number that is negligible by comparison with the dominant terms of the governing equations, and the resulting Stokes-flow approximation is studied under the assumptions detailed above.

The notation convention used below is as follows: subscripts appended to dependent variables denote differentiation with respect to the subscript; subscripts in Roman font are an exception to this rule, and the purpose of such terms will be made clear by the surrounding text; superscripts are employed to identify terms pertaining to the vapour and free-surface phases of the system. In equations where such superscripts are present, terms without superscripts pertain to the fluid phase.

[1]These include: coating and rimming flows (Moffat, 1977; Pukhnachev, 1977; Hinch & Kelmanson, 2003; Hinch *et al.*, 2004; Benilov & O'Brien, 2005; Noakes *et al.*, 2006, and 2011; King *et al.*, 2007; Kelmanson, 2009a,b; Groh, 2010); biophysical fluid dynamics (Berger & Corrsin, 1977; Borgas & Grotberg, 1988; Gaver & Grotberg, 1990, and 1992; Halpern & Grotberg, 1992; Wong *et al.*, 1996; Braun & Fitt, 2003; Jones *et al.*, 2005; Braun & King-Smith, 2007; Aydemir *et al.*, 2011; Zubkov *et al.*, 2012); flow of surfactant-laden drops and films (Afsar-Siddiqui *et al.*, 2003a,b,c; Warner *et al.*, 2004a,b; Edmonstone *et al.*, 2004, and 2005; Jensen & Naire, 2006); stability analyses of evaporating films (Burelbach *et al.*, 1988; Joo *et al.*, 1991); geophysical flows (Griffiths, 2000; Hindmarsh, 2004; Huppert, 2006), and; fluid flow over curved substrates (Roy *et al.*, 2002; Myers *et al.*, 2002; Howell, 2003), to name a few. Review articles on thin-film dynamics can be found within Oron *et al.* (1997), Myers (1998), and Craster & Matar (2009).

2.1.1 Equations of fluid motion

The Navier-Stokes equations describing the motion of an incompressible Newtonian fluid are (Acheson, 1990)

$$\rho\Big(\mathbf{U}_t \,+\, \mathbf{U}\cdot\nabla\mathbf{U}\Big) \;=\; -\nabla P \,+\, \mu\nabla^2\mathbf{U} \,+\, \rho\mathbf{G}\,, \tag{2.1}$$

where $\mathbf{U}$ (m s^{-1}), P (kg m^{-1} s^{-2}) and $\mathbf{G}$ (m s^{-2}) respectively denote the fluid velocity field, pressure and gravitational acceleration, with parameters ρ (kg m^{-3}) and μ (kg m^{-1} s^{-1}) respectively corresponding to the fluid density and dynamic viscosity. In an incompressible flow the fluid density remains constant, and the continuity equation is

$$\nabla\cdot\mathbf{U} \;=\; 0\,. \tag{2.2}$$

Transport of heat energy within the tear film is modelled using an advection-diffusion equation (see, for example, Burelbach *et al.*, 1988)

$$T_t \,+\, \mathbf{U}\cdot\nabla T \;=\; \kappa\nabla^2 T\,, \tag{2.3}$$

where T (K) and κ (m^2 s^{-1}) are respectively the temperature and fluid thermal diffusivity.

To incorporate the effects of a curved substrate, the tear film is modelled as a layer of fluid coating the exterior of a cylinder of radius a (m). In keeping with prior models of the tear film, the model considers a longitudinal cut through the anterior-posterior axis of the eye (see, for example, Berger & Corrsin, 1973; Wong *et al.*, 1996; Braun & Fitt, 2003; Jones *et al.*, 2005; Braun & King-Smith, 2007; Aydemir *et al.*, 2011; Zubkob *et al.*, 2012), whence all derivatives and equations pertaining to variations parallel with the axis of the cylinder are henceforth neglected. Thus, the flow can be treated as two-dimensional, and the cylindrical geometry can be simplified to plane-polar coordinates, (R, θ), as depicted in Figure 2.1, with orthonormal unit vectors perpendicular and parallel to the ocular substrate defined by

$$\begin{aligned} \mathbf{e}_R \;&=\; \big(\cos(\theta),\,\sin(\theta)\big)^T \qquad \text{and} \\ \mathbf{e}_\theta \;&=\; \big(-\sin(\theta),\,\cos(\theta)\big)^T\,. \end{aligned} \tag{2.4}$$

For ease of comparison with Cartesian coordinates in the limit of infinite cylinder radius, the velocity vector is defined non-conventionally, with U and V "reversed" to represent respectively the radial and azimuthal components of velocity, so that

$$\mathbf{U} \;=\; V\mathbf{e}_R \,+\, U\mathbf{e}_\theta \,. \tag{2.5}$$

Equations (2.1), (2.2) and (2.3) require augmentation with boundary conditions in order to close the system. The fluid is permitted to slip along the corneal mucus, but not to penetrate into the rigid substrate, and the temperature is equal to that of the eye; these give the respective conditions

$$\mathbf{U}\cdot\hat{\mathbf{t}}_{\text{EYE}} \;=\; \frac{Z}{\mu}\hat{\mathbf{n}}_{\text{EYE}}\cdot\mathbf{T}\cdot\hat{\mathbf{t}}_{\text{EYE}}\,, \quad \mathbf{U}\cdot\hat{\mathbf{n}}_{\text{EYE}} \;=\; 0\,, \;\text{ and }\; T = T_{\text{EYE}} \quad \text{at} \quad R = a\,. \tag{2.6}$$

The first of these relationships is the Navier slip condition, which relates the tangential

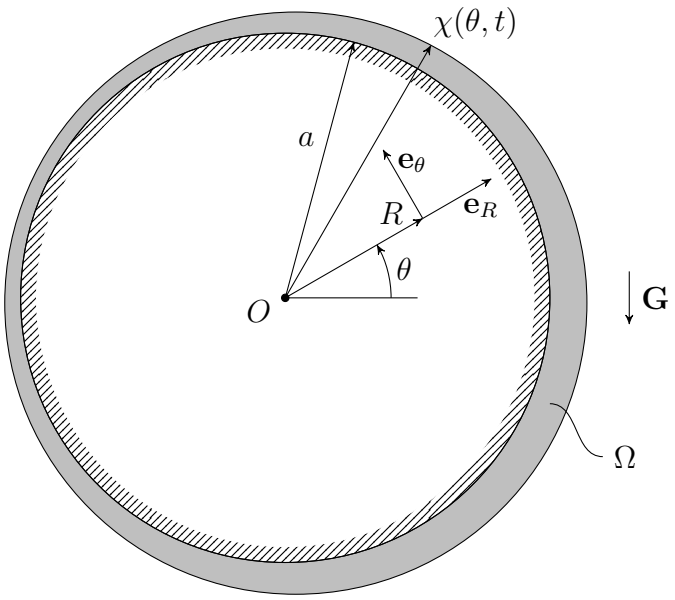

Figure 2.1: Geometry (in standard plane-polar coordinates) for the incompressible coating-flow problem on the exterior of an impermeable cylinder of radius a. The coordinate origin is marked O, and the locus of the free surface of the fluid is given by $\chi(\theta,t)$ (see §2.1.2 for further details). The fluid-filled area is denoted by Ω. Gravity, $\mathbf{G}$, acts in the $\theta = 3\pi/2$ direction.

velocity to the shear rate at the substrate (Navier, 1823; Huh & Scriven, 1971). In this condition $\hat{\mathbf{n}}_{\text{EYE}}$ and $\hat{\mathbf{t}}_{\text{EYE}}$ respectively denote the unit vectors normal and tangential to the ocular substrate (identified with $\mathbf{e}_R$ and $\mathbf{e}_\theta$ in this coordinate system), Z (m) represents the slip length along the eye, and $\mathbf{T}$ (kg m^{-1} s^{-2}) is the fluid stress tensor, defined in (2.10). In §2.2.1 the scaling of Z will mean the effect of slip is found to be negligible in the model; nevertheless, the Navier slip condition is included in (2.6) for completeness. At the free surface, boundary conditions are provided by considering the balances of mass, momentum and energy (Delhaye, 1974; Shikhmurzaev, 2008). The permeable fluid-vapour interface is modelled as a mathematical dividing surface of infinitesimal thickness and density of the same order as the bulk fluid, hence its role as a sink or source of mass is assumed negligible by comparison with the evaporative mass flux passing through the boundary (Shikhmurzaev, 2008). The effects of the variable surfactant layer are modelled purely within the interface, causing variation in the local surface tension. The mass balance at the fluid-vapour interface is thus (Delhaye, 1974, equation 12; Shikhmurzaev, 2008, equation 2.134)

$$\rho\Big(\mathbf{U}-\mathbf{U}^S\Big)\cdot\hat{\mathbf{n}} \;=\; \rho^V\Big(\mathbf{U}^V-\mathbf{U}^S\Big)\cdot\hat{\mathbf{n}} \;=\; J\,, \tag{2.7}$$

wherein superscripts ^{S} and ^{V} respectively denote the surface and vapour[2], and $\hat{\mathbf{n}}$ is a unit normal vector pointing from the fluid into the vapour. J (kg m^{-2} s^{-1}) is an evaporative mass flux, and equation (2.7) states that all mass leaving the tear film is transported into the vapour, with no change of mass in the interface. Through the scalings and asymptotic expansion respectively made in §2.2 and §2.3 to solve (2.1) and (2.2) for the fluid velocities, equation (2.7) yields an evolution equation for the height of the tear film above the ocular surface. The vector momentum balance is

$$J\Big(\mathbf{U}-\mathbf{U}^V\Big) \;-\; \hat{\mathbf{n}}\cdot\Big(\mathbf{T}-\mathbf{T}^V\Big) \;=\; -\nabla_s\cdot\mathbf{T}^S\,, \tag{2.8}$$

in which $\mathbf{T}$ is the stress tensor corresponding to each phase and ∇_s represents the surface

[2] as mentioned on page 18, quantities without a superscript pertain to the fluid

gradient operator,

$$\nabla_s \;\equiv\; \nabla - \hat{\mathbf{n}}\,\frac{\partial}{\partial n} \;=\; (\mathbf{I} - \hat{\mathbf{n}}\hat{\mathbf{n}}) \cdot \nabla\,. \tag{2.9}$$

The stress tensors in the bulk phases and the interface are respectively defined as

$$\mathbf{T} \;=\; -P\mathbf{I} + 2\mu\boldsymbol{\tau}\,, \quad \mathbf{T}^V \;=\; -P^V\mathbf{I} + 2\mu^V\boldsymbol{\tau}^V\,, \quad \text{and} \quad \mathbf{T}^S \;=\; \sigma\,(\mathbf{I} - \hat{\mathbf{n}}\hat{\mathbf{n}})\;, \tag{2.10}$$

where $\mathbf{I}$ is the identity matrix, $\boldsymbol{\tau}$ (s^{-1}) is the rate-of-strain tensor in each bulk phase, and σ ($\mathrm{N\ m}^{-1}$) is the surface tension. The bracketed term $(\mathbf{I} - \hat{\mathbf{n}}\hat{\mathbf{n}})$ found in both (2.9) and $\mathbf{T}^S$ signifies that the action of each quantity lies solely within the interface. Note that through (2.10), the surface stress tensor $\mathbf{T}^S$ is expressed in units of force-per-unit-*length* rather than force-per-unit-*area*, as used for the bulk stress tensors $\mathbf{T}$ and $\mathbf{T}^V$. Equation (2.7) has been used to simplify the equations of Delhaye (1974, equation 15) and Shikhmurzaev (2008, equation 4.12) to yield (2.8).

It should be noted here that the divergence term on the right-hand side of Shikhmurzaev's momentum balance (4.12) utilises the full, three-dimensional gradient operator ∇ in conjunction with the *constraint* that the normal to the interface satisfies

$$\hat{\mathbf{n}} \cdot \nabla\hat{\mathbf{n}} \;=\; \mathbf{0}\,. \tag{2.11}$$

If this constraint were to be relaxed, the terms arising from the (non-vanishing) left-hand side of (2.11) are found to lie within the plane of the free surface. That $\hat{\mathbf{n}} \cdot \nabla\hat{\mathbf{n}}$ is parallel to $\hat{\mathbf{t}}$ follows from a standard vector calculus identity (Spiegel, 1959), which gives

$$\hat{\mathbf{n}} \cdot \nabla\hat{\mathbf{n}} \;=\; \frac{1}{2}\nabla(\hat{\mathbf{n}} \cdot \hat{\mathbf{n}}) \;+\; (\nabla \times \hat{\mathbf{n}}) \times \hat{\mathbf{n}}\,. \tag{2.12}$$

Since $\hat{\mathbf{n}}$ is a unit normal, the first term on the right-hand side of (2.12) vanishes, but the second term clearly lies within the plane of the free surface. Then (2.11) and (2.12) are compatible only if $\nabla \times \hat{\mathbf{n}}$ either vanishes or is parallel to $\hat{\mathbf{n}}$, the latter of which is impossible: the former requires $\hat{\mathbf{n}}$ to be irrotational and conservative.

With the fluid interface defined by a function $f(\mathbf{r}, t) = 0$, the unit normal is $\hat{\mathbf{n}} = \nabla f/|\nabla f|$, hence one only obtains a conservative field if $|\nabla f| = 1$ at all points and times,

which is not true for general functions f. That is, the constraint (2.11) is not realisable as presented. However, it *is* realisable provided that (2.11) is amended to

$$\hat{\mathbf{n}} \cdot \nabla_s \hat{\mathbf{n}} \;=\; \mathbf{0}\,, \tag{2.13}$$

in which ∇_s is the surface divergence operator, (2.9). This can be explicitly proven using standard Einstein suffix notation as follows:

$$\begin{aligned}
\hat{\mathbf{n}} \cdot \nabla_s \hat{\mathbf{n}} \;&=\; \hat{\mathbf{n}} \cdot \Big\{ \big[(\mathbf{I} - \hat{\mathbf{n}}\hat{\mathbf{n}}) \cdot \nabla \big] \hat{\mathbf{n}} \Big\}, \\
&=\; n_i\, \mathbf{e}_i \cdot \Big\{ \big(\mathbf{I} - n_j\, n_k\, \mathbf{e}_j\, \mathbf{e}_k \big) \cdot \big(n_{m,l}\, \mathbf{e}_l\, \mathbf{e}_m + n_m\, \mathbf{e}_l\, \mathbf{e}_{m,l} \big) \Big\}, \\
&=\; n_i\, \mathbf{e}_i \cdot \Big\{ n_{m,l}\, \mathbf{e}_l\, \mathbf{e}_m + n_m\, \mathbf{e}_l\, \mathbf{e}_{m,l} - n_j\, n_k\, n_{m,k}\, \mathbf{e}_j\, \mathbf{e}_m - n_j\, n_k\, n_m\, \mathbf{e}_j\, \mathbf{e}_{m,k} \Big\}, \\
&=\; n_i\, n_{m,i}\, \mathbf{e}_m + n_i\, n_m\, \mathbf{e}_{m,i} - \underbrace{(n_i\, n_i)}_{=1}\, n_k\, n_{m,k}\, \mathbf{e}_m - \underbrace{(n_i\, n_i)}_{=1}\, n_k\, n_m\, \mathbf{e}_{m,k}, \\
&=\; \mathbf{0}\,.
\end{aligned} \tag{2.14}$$

The balance of energy at the fluid-vapour interface is given by (Delhaye, 1974, equation 18; Shikhmurzaev, 2008, equation 4.17)

$$\begin{aligned}
&T^S \left(\left(\rho^S S^S \right)_t + \nabla \cdot \left[\rho^S \mathbf{U}^S S^S + \frac{\mathbf{q}^S}{T^S} \right] \right) + \frac{1}{T^S}\, \mathbf{q}^S \cdot \nabla T^S \\
&\quad + J \left[L_v + \frac{1}{2} \left(\mathbf{U}^V - \mathbf{U}^S \right)^2 - \frac{1}{2} \left(\mathbf{U} - \mathbf{U}^S \right)^2 \right] + k\, \nabla T \cdot \hat{\mathbf{n}} - k^V\, \nabla T^V \cdot \hat{\mathbf{n}} \\
&\quad + 2\mu\, (\boldsymbol{\tau} \cdot \hat{\mathbf{n}}) \cdot \left(\mathbf{U} - \mathbf{U}^S \right) - 2\mu^V \left(\boldsymbol{\tau}^V \cdot \hat{\mathbf{n}} \right) \cdot \left(\mathbf{U}^V - \mathbf{U}^S \right) \;=\; 0\,.
\end{aligned} \tag{2.15}$$

Here, ρ^S (kg m^{-2}), S^S (J kg^{-1} K^{-1}), $\mathbf{q}^S$ (W m^{-1}), L_v (J kg^{-1}) and k (W m^{-1} K^{-1}) respectively represent the interfacial density, specific entropy of the interface, heat flux within the interface, latent heat of vaporisation and thermal conductivity. By treating the interface as a dividing surface, the changes in interfacial density and interfacial specific entropy, and the interior heat flux are taken to be negligible in the model, whence all terms in the first line of (2.15) vanish: this is equivalent to modelling the transport of heat energy through the interface as a reversible thermodynamic process, the first line being a statement of the second law of thermodynamics within the interface. Equation (2.15),

with its first line removed through the argument above, is employed in the later workings of this model. In its reduced form (2.15) balances: the energy required to vaporize the bulk fluid and the jump in kinetic energy of particles incident on each side of the free surface (contained in the remaining square bracket); heat fluxes within the bulk phases, which fluxes are modelled using Fourier's Law of heat conduction (Fourier, 1822; Kundu & Cohen, 2002), and; viscous dissipation of heat energy in the bulk phases (contained in the final line of (2.15)). Furthermore, it should be noted that with the interface modelled as a dividing surface, any viscous heating that occurs at the interface will be manifest in the bulk fluids only, and so will in fact be governed by (2.3) and its analogue in the vapour (which is not treated herein); such bulk terms would then affect (2.15) through the heat flux terms. Despite this, the final line is retained in this form for completeness and to allow comparison to the existing literature. The same (reduced) equation is presented in Burelbach *et al.* (1988, equation 2.9); however, the explanation and assumptions leading to the removal of the first line of (2.15) are not presented therein.

To close the system, a conservation equation is required for the concentration, Ψ (molecules m^{-2}), of adsorbed lipid surfactant along the fluid-vapour interface. The equation for surfactant motion is taken from Berger & Corrsin (1974), which uses the surface analogue of Reynolds' transport theorem (Aris, 1962) for the material derivative of the surfactant concentration in the surface; this yields the evolution equation

$$\Psi_t \,+\, \nabla_s \cdot \left(\Psi \mathbf{U}^S\right) \,-\, \Psi \left(\mathbf{U}^S \cdot \hat{\mathbf{n}}\right) \left(\nabla \cdot \hat{\mathbf{n}}\right) \,=\, D^S \nabla_s^2 \Psi \,, \tag{2.16}$$

where D^S ($\mathrm{m}^2\ \mathrm{s}^{-1}$) is the surface diffusivity of surfactant molecules. In addition to the time derivative and advective terms, the third term on the left-hand side of (2.16) expresses the change in concentration caused through dilatation: the process by which the local area of the free surface is distorted due to the underlying fluid movement (Aris, 1962; Slattery, 1972; Stone, 1990). Lipid sorption kinetics between the interface and bulk fluid are not modelled.

Alternative form of the surfactant-transport equation

An alternative form of equation (2.16) can be found in the brief analysis of Stone (1990), and it is important to stress here that $\mathbf{U}^S$ is the full surface velocity at the interface, and has not been decomposed into components normal and tangential to the interface. In Stone (1990), the full surface velocity is decomposed into the coordinate system of the interface and, through manipulations, a dilatation term is obtained through expansion of the advective term. Note that, in a potentially confusing clash of notation, Stone's $\mathbf{u}_s$ is the tangential component of the surface velocity, rather than the full surface velocity, here represented by $\mathbf{U}^S$; that is,

$$(\mathbf{u}_s)_{\text{STONE}} \;=\; (\mathbf{I} - \hat{\mathbf{n}}\hat{\mathbf{n}}) \cdot \mathbf{U}^S \;\equiv\; \mathbf{U}_{\text{TANGENTIAL}} \;,$$

say. The left-hand side of the evolution equation for the conserved surfactant at the interface presented in Stone (1990, equation 5) contains only terms concerning the time derivative of Ψ and advection using the full surface velocity, expressed in the current notation as

$$\Psi_t \;+\; \nabla_s \cdot \left(\Psi \mathbf{U}^S\right) \;.$$

By setting $\mathbf{U}^S \;=\; \mathbf{U}_{\text{TANGENTIAL}} \;+\; (\mathbf{U}^S \cdot \hat{\mathbf{n}})\hat{\mathbf{n}}$, expanding using standard vector calculus identities (Spiegel, 1959), and noting that the surface gradient operator admits vectors with no normal component, the advective term above can be manipulated into a form which contains a dilatation-type term. Through these manipulations, the surfactant-evolution equation of Stone (1990, equation 7) is

$$\Psi_t \;+\; \nabla_s \cdot (\Psi \mathbf{U}_{\text{TANGENTIAL}}) \;+\; \Psi \left(\mathbf{U}^S \cdot \hat{\mathbf{n}}\right) (\nabla_s \cdot \hat{\mathbf{n}}) \;=\; D^S \nabla_s^2 \Psi \;. \qquad (2.17)$$

Comparison of the formulation of equations (2.16) and (2.17) shows that the former contains a dilatation term *ab initio*, modelled through the time-dependence of the surface metric (see Aris, 1962, for further details), whereas the latter derives a dilatation term (of different sign) through advection of the surface. This derived dilatation term is simply an

artefact of the form of decomposition of the surface velocity, thus, whilst (2.17) appears to contain dilatative effects, tests using trial geometries confirm that the term is removed through interaction with the surface divergence of the tangential velocity, yielding the pure-advective left-hand side of Stone (1990, equation 5). Equation (2.16) is employed in this thesis as it is in the form of a so-called surface advection-dilatation-diffusion equation.

Calculation of curvature

A further difference between equations (2.16) and (2.17) is in the calculation of the curvature term within the dilatation; (2.16) uses the full divergence operator acting on $\hat{\mathbf{n}}$, whereas (2.17) employs the surface divergence. For a *unit* normal vector, both methods yield the same result;

$$\nabla \cdot \hat{\mathbf{n}} \;=\; \nabla_s \cdot \hat{\mathbf{n}}\,, \tag{2.18}$$

in which the left-hand term is less computationally expensive to evaluate. The surface gradient operator is defined in (2.9) as $(\mathbf{I} - \hat{\mathbf{n}}\hat{\mathbf{n}}) \cdot \nabla$, hence the proof of (2.18) lies in showing that the term $(\hat{\mathbf{n}}\hat{\mathbf{n}} \cdot \nabla) \cdot \hat{\mathbf{n}}$ is equal to zero, which follows from

$$\begin{aligned}
(\hat{\mathbf{n}}\hat{\mathbf{n}} \cdot \nabla) \cdot \hat{\mathbf{n}} &= [\hat{\mathbf{n}}\,(\hat{\mathbf{n}} \cdot \nabla)] \cdot \hat{\mathbf{n}}\,, \\
&= \hat{\mathbf{n}} \cdot (\hat{\mathbf{n}} \cdot \nabla)\,\hat{\mathbf{n}}\,, \\
&= \hat{\mathbf{n}} \cdot (\hat{\mathbf{n}} \cdot \nabla\hat{\mathbf{n}})\;, \qquad \textit{cf.}\ \text{equation (2.12)}, \\
&= \hat{\mathbf{n}} \cdot \left[\frac{1}{2}\nabla\,(\hat{\mathbf{n}} \cdot \hat{\mathbf{n}}) \;+\; (\nabla \times \hat{\mathbf{n}}) \times \hat{\mathbf{n}}\right]\;, \\
&= 0\,,
\end{aligned} \tag{2.19}$$

because $\hat{\mathbf{n}} \cdot \hat{\mathbf{n}} = 1$ and $(\nabla \times \hat{\mathbf{n}}) \times \hat{\mathbf{n}}$ is perpendicular to $\hat{\mathbf{n}}$.

2.1.2 Plane-polar equations and free surface geometry

The equations of motion (2.1), (2.2), (2.3), (2.6), (2.7), (2.8), (2.15), and (2.16) are expanded in plane-polar coordinates, with the free surface of the fluid defined in terms

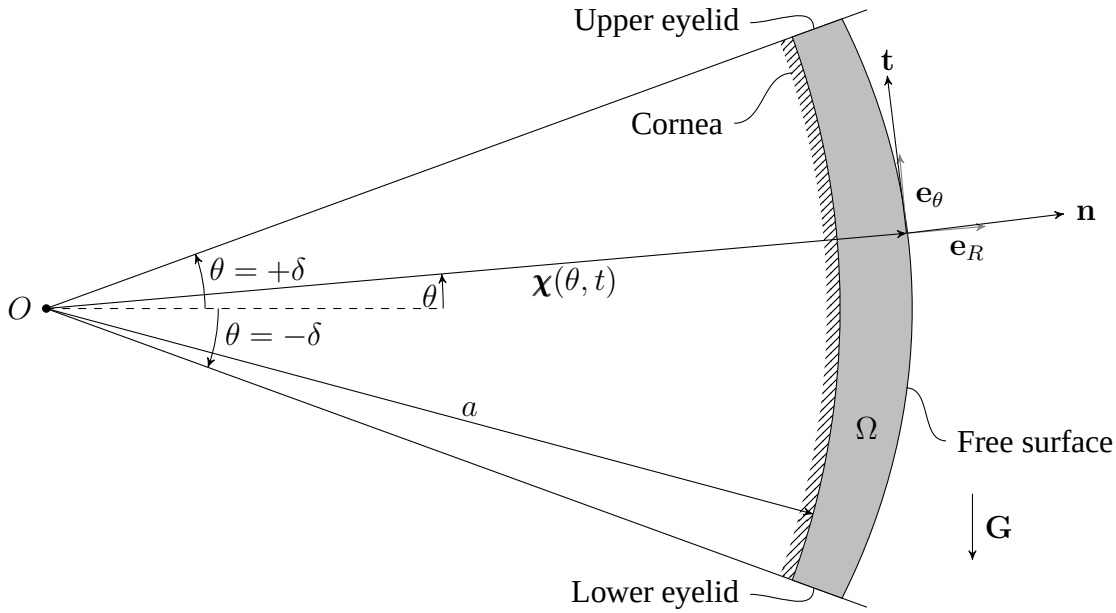

Figure 2.2: The locus of the free surface $\boldsymbol{\chi}$ at a fixed station θ, together with the normal, $\mathbf{n}$, and tangential vector, $\mathbf{t}$, defined at that point. The set of orthonormal basis vectors $\mathbf{e}_R$ and $\mathbf{e}_\theta$ (2.4) are also displayed and, for the sake of clarity, the normal and tangential vectors have been expanded from their unit length. The eyelids are located at polar angles $\theta = \pm\delta$, whence θ is confined to the interval $[-\delta, \delta]$. As previously, the fluid-filled region is labelled Ω.

of the height from the ocular (cylinder) surface using standard differential geometry techniques (Struik, 1961). In this coordinate system, the Navier-Stokes equations (2.1) become

$$\rho\left(U_t + VU_R + \frac{UU_\theta}{R} + \frac{UV}{R}\right) = -\frac{P_\theta}{R} + \rho G_{(\theta)} + \mu\left(U_{RR} + \frac{U_R}{R} + \frac{U_{\theta\theta}}{R^2} - \frac{U}{R^2} + \frac{2V_\theta}{R^2}\right), \tag{2.20a}$$

$$\rho\left(V_t + VV_R + \frac{UV_\theta}{R} + \frac{U^2}{R}\right) = -P_R + \rho G_{(R)} + \mu\left(V_{RR} + \frac{V_R}{R} + \frac{V_{\theta\theta}}{R^2} - \frac{V}{R^2} - \frac{2U_\theta}{R^2}\right), \tag{2.20b}$$

in the azimuthal and radial directions, respectively. The bracketed subscripts on the

gravitational terms represent the components of the gravity vector, rather than partial differentiation. Note that these equations differ from the standard form (see, for example, Acheson, 1990, §A.2; Kundu & Cohen, 2002, §B2) due to the non-conventional velocity definition (2.5), where V and U respectively represent the radial and azimuthal velocity components. The continuity equation (2.2) becomes

$$V_R + \frac{V}{R} + \frac{U_\theta}{R} = 0\,, \tag{2.21}$$

and the heat equation (2.3) yields

$$T_t + VT_R + \frac{UT_\theta}{R} = \kappa\left(T_{RR} + \frac{T_R}{R} + \frac{T_{\theta\theta}}{R^2}\right). \tag{2.22}$$

Associating the normal and tangent vectors to the ocular substrate with $\mathbf{e}_R$ and $\mathbf{e}_\theta$, respectively, the boundary conditions at the eye (2.6) become

$$U = Z\left(U_R - \frac{U}{R}\right), \qquad V = 0\,, \quad \text{and} \qquad T = T_{\text{EYE}}\,, \tag{2.23}$$

at $R = a$, wherein the boundary condition on V has been used to simplify the slip condition through removal of the V_θ term, and Z is the slip length along the cornea.

The locus of the free surface is defined by

$$\boldsymbol{\chi} \equiv \chi(\theta,\, t)\mathbf{e}_R\,. \tag{2.24}$$

At time t, the curve $\boldsymbol{\chi}$ is a regular curve in $\mathbb{R}^2$, confined by eyelids (see Figure 2.2); $\chi(\theta,\, t) > 0$, $t \geq 0$, $\theta \in [-\delta,\, \delta]$. A unit tangent vector to the free surface is defined by

$$\hat{\mathbf{t}} \equiv \|\boldsymbol{\chi}_\theta\|^{-1}\boldsymbol{\chi}_\theta = \left[\chi^2 + \chi_\theta^2\right]^{-1/2}\left(\chi_\theta\,\mathbf{e}_R + \chi\mathbf{e}_\theta\right), \tag{2.25}$$

wherein the prefactor normalises the vector's magnitude, reflecting the fact that $\boldsymbol{\chi}$ is not a unit-speed curve. The unit outward-facing normal $\hat{\mathbf{n}}$ (satisfying $\hat{\mathbf{n}} \cdot \hat{\mathbf{t}} = 0$) is therefore

$$\hat{\mathbf{n}} = \left[\chi^2 + \chi_\theta^2\right]^{-1/2}\left(\chi\mathbf{e}_R - \chi_\theta\,\mathbf{e}_\theta\right). \tag{2.26}$$

The velocity at the free surface is defined as

$$\mathbf{U}^S \;\equiv\; \frac{D\boldsymbol{\chi}}{Dt} \;=\; \left(\chi_t + \frac{U\chi_\theta}{\chi}\right)\mathbf{e}_R \;+\; U\mathbf{e}_\theta\,, \tag{2.27}$$

wherein the azimuthal velocity U is evaluated at $R = \chi$.

With the geometry of the free surface thus defined, the balances of mass, momentum and energy, and the surfactant transport equation may now be expanded to yield the boundary conditions at the interface. The vapour phase is modelled as an inviscid gas at atmospheric pressure, P_{ATM}, with a homogeneous temperature distribution. Furthermore, at the interface, the tangential components of velocity of each phase are taken to be continuous;

$$\mathbf{U}\cdot\hat{\mathbf{t}} \;=\; \mathbf{U}^V\cdot\hat{\mathbf{t}} \;=\; \mathbf{U}^S\cdot\hat{\mathbf{t}}\,.$$

Two boundary conditions are derived from the vectorial momentum balance (2.8), whose scalar product with $\hat{\mathbf{n}}$ yields the balance of stresses normal to the interface

$$\begin{aligned} -P \;+\; P_{\text{ATM}} + \frac{2\mu\left(\chi^3 V_R - \chi^2\chi_\theta U_R - \chi\chi_\theta V_\theta \;+\chi\chi_\theta U + \chi_\theta^2 V + \chi_\theta^2 U_\theta\right)}{\chi\left(\chi^2+\chi_\theta^2\right)} \\ -\; J^2\left(\frac{1}{\rho} - \frac{1}{\rho^V}\right) \;=\; -\frac{\sigma\left(\chi^2 + 2\chi_\theta^2 - \chi\chi_{\theta\theta}\right)}{\left(\chi^2+\chi_\theta^2\right)^{3/2}}\,, \end{aligned} \tag{2.28}$$

in which both formulations of equation (2.7) have been used to obtain the evaporative term, which term can be attributed to the recoil of the surface as fluid particles evaporate. Similarly, the scalar product of (2.8) with $\hat{\mathbf{t}}$ gives the balance of tangential stresses as

$$\frac{\mu\Big[\left(\chi^2-\chi_\theta^2\right)\left(\chi U_R + V_\theta - U\right) + 2\chi\chi_\theta\left(\chi V_R - V - U_\theta\right)\Big]}{\chi\left(\chi^2+\chi_\theta^2\right)^{1/2}} \;=\; \sigma_\theta\,. \tag{2.29}$$

The energy balance (2.15) at the free surface becomes

$$\begin{aligned} J\left[L_v + \frac{1}{2}J^2\left(\frac{1}{(\rho^V)^2} - \frac{1}{\rho^2}\right)\right] \;+\; \frac{k\left(\chi^2 T_R - \chi_\theta T_\theta\right)}{\chi\left(\chi^2+\chi_\theta^2\right)^{1/2}} \\ +\; \frac{\mu}{\left(\chi^2+\chi_\theta^2\right)^{1/2}}\left[2\chi V_R - \chi_\theta\left(U_R + \frac{V_\theta}{\chi} - \frac{U}{\chi}\right)\right]\left(V - \chi_t - \frac{U\chi_\theta}{\chi}\right) \;=\; 0\,, \end{aligned} \tag{2.30}$$

wherein the continuous tangential velocities at the interface have been combined with both forms of (2.7) to obtain the term inside the first square bracket; as in (2.28), this term can be attributed to the transfer of kinetic energy across the interface as molecules evaporate from the tear film.

The mass balance (2.7) and surfactant transport equation (2.16), which will yield the governing pair of coupled spatio-temporal evolution equations for the tear-film flow, are respectively

$$\frac{\rho\left(\chi V-\chi\chi_t-\chi_\theta U\right)}{\left(\chi^2+\chi_\theta^2\right)^{1/2}} \;=\; J\,, \tag{2.31}$$

and

$$\begin{aligned}\Psi_t+\frac{\Psi\chi_t\left(\chi^2+2\chi_\theta^2-\chi\chi_{\theta\theta}\right)}{\left(\chi^2+\chi_\theta^2\right)^2}+\frac{1}{\chi^2\left(\chi^2+\chi_\theta^2\right)}\Bigg\{\chi\Psi_\theta\Big[U\left(\chi^2+\chi_\theta^2\right)+\chi\chi_t\chi_\theta\Big]\\ +\Psi\Big[\chi\left(\chi_\theta U_R+U_\theta\right)\left(\chi^2+\chi_\theta^2\right)+\chi_\theta U\left(\chi\chi_{\theta\theta}-\chi_\theta^2\right)+\chi^2\left(\chi\chi_t+\chi_\theta\chi_{\theta t}\right)\Big]\Bigg\}\\ =\;D^S\frac{\Psi_{\theta\theta}\left(\chi^2+\chi_\theta^2\right)-\chi_\theta\Psi_\theta\left(\chi+\chi_{\theta\theta}\right)}{\left(\chi^2+\chi_\theta^2\right)^2}\,.\end{aligned} \tag{2.32}$$

The final diffusive term (containing Ψ_θ) on the right-hand side of (2.32) is omitted in many works that model the evolution of the surfactant concentration on the tear film (Jones *et al.*, 2006; Braun & King-Smith, 2007; Heryudono *et al.*, 2007; Aydemir *et al.*, 2011). This term arises through the decomposition of the surface Laplacian operator into the surface divergence operator acting upon the surface gradient of Ψ, and (to the author's knowledge) is presented in the tear flow models of only Berger (1973), Berger & Corrsin (1974), and Zubkov *et al.* (2012), the first of which contains a meticulous treatment of the differential geometry at the free surface. The inclusion of this term is shown to be academic in subsequent sections of this chapter, as an order-of-magnitude analysis identifies that its impact on the surfactant concentration is minor by comparison with other terms in (2.32). However, the significance of this term would be greatly increased in a physical system with a large surfactant diffusivity or with a free surface that has steep gradients and/or large curvatures, thus this term should not be omitted from the general form of the surfactant-transport equation.

Whilst the coupling of equations (2.31) and (2.32) is clear in the latter through the advection, dilatation and diffusion terms, it is not currently obvious that surfactant concentration has any impact on the former. Variations in local surfactant concentration affect the strength of the surface tension acting along the interface, hence the normal- and tangential-stress conditions will provide feedback to (2.31) via the boundary conditions enforced on the bulk pressure and velocity fields. A constitutive relationship is thus required to link the surface tension to the concentration of surfactant at the free surface. The final term to be considered is the evaporative mass flux, J, which is itself dependent on the pressure and temperature of the vapour phase, and the local concentration of surfactant. These additional relationships are discussed in the following section.

2.1.3 Constitutive relationships

A discussion of the colloid chemistry that occurs at a free surface with adsorbed surfactant molecules falls outside of the scope of this thesis. However, a wealth of literature exists modelling the influence of adsorbed surfactant on the underlying fluid (see, for example: Borgas & Grotberg, 1988; Gaver & Grotberg, 1990 and 1992; Warner *et al.*, 2004a and 2004b; Edmonstone *et al.*, 2004 and 2005). In the present model, the surfactant concentration is taken to be dilute at the free surface (known as a 'liquid-expanded film': Adam & Jessop, 1926; Langmuir, 1934; Adam, 1941; Sakata & Berg, 1969). Dilute concentrations are characterized by the density of molecules in the film being significantly below the level at which they become tightly packed, which limit is referred to as the *critical micelle limit*. For such a regime, the constitutive relationship between the surface tension and surfactant concentration is taken from Gaver & Grotberg (1992);

$$\sigma \;=\; \frac{\sigma_0}{\left\{1+\left[\left(\dfrac{\sigma_0}{\sigma_m}\right)^{1/3}-1\right]\dfrac{\Psi}{\Psi_m}\right\}^3}\,, \tag{2.33}$$

where Ψ_m represents the critical micelle concentration, σ_0 is the surface tension of the

uncontaminated film, and σ_m is the surface tension of the film when $\Psi = \Psi_m$. The presence of meibomian lipid lowers the surface tension of tears, so that $\sigma_m < \sigma_0$.

A large quantity of literature is dedicated to the study of fluid evaporating into a surrounding vapour (Alty, 1931; Wyllie, 1949; Maa, 1967; Palmer, 1976; Higuera, 1987; Burelbach *et al.*, 1988). The equations presented in such papers require accurate modelling of the changes in temperature and pressure of the vapour phase, as well as knowledge of the experimentally-obtained evaporation coefficient, a dimensionless constant that parameterises the likelihood that molecules from one phase that are incident on the interface are transported through to the other bulk phase, rather than being reflected back. Within this model, the equations derived in §2.1.2 can be viewed as 'one-sided' as they are concerned only with the fluid phase of the system, and so changes in the vapour phase remain unknown but negligible. Additionally, the data for the evaporation coefficient of the human eye has not been experimentally obtained.

In the absence of such data, and with the model so defined, a constitutive relationship for the evaporative mass flux will not be given. The evaporation rate from human eyes has been measured by the ophthalmic community using a variety of techniques to discern if there is a notable difference in the rate of evaporation between patients with normal eyes, and those who suffer from lipid-deficient dry-eye pathologies (see, for example, Bron *et al.*, 2004; Mathers, 2004; Tomlinson & Khanal, 2005). An evaporation rate of roughly 1.5×10^{-5} kg m^{-2} s^{-1} is reported for normal eyes in Mathers (1993), and values of the same magnitude can be found within reviews in the papers mentioned above. This value is used in the mathematical model of Braun & Fitt (2003). To incorporate the resistive effects of greater concentrations of surfactant to evaporation from the tear film, an heuristic model is used for the evaporation mass flux, using the measured value from above;

$$J \;=\; \frac{J_0}{1 \;+\; A\left(\dfrac{\Psi}{\Psi_m}\right)^B}\,, \text{ where } \; J_0 \;=\; 1.5 \times 10^{-5} \text{ kg m}^{-2} \text{ s}^{-1}. \tag{2.34}$$

The positive parameters A and B allow the heuristic model to be altered, controlling the rate at which evaporation drops as the concentration decreases, and the evaporation rate at critical micelle concentration, respectively. With the surfactant modelled in dilute concentrations, it will be found (*cf.* §2.2.2) that these parameters do not play a role in the leading-order behaviour of the system.

2.2 Marginal-surface coordinates

To model the effect of substrate curvature, a change of coordinate system is defined within a marginal surface which, in cylindrical geometry, sits a small distance below the ocular surface. In the limit that the radius of the cylinder tends to infinity, the distance between the marginal surface and ocular surface decreases to zero, and the marginal-surface coordinates coincide with Cartesian coordinates defined on the flat plane, in which coordinates comparison can be made with all of the existing literature (with the exception of Braun *et al.*, 2012).

The marginal-surface coordinates are defined as

$$\xi \equiv -a\theta\cos\delta\,, \qquad \text{and} \qquad \eta \equiv R - a\cos\delta\,, \tag{2.35}$$

where δ is the half-angle of the palpebral fissure, as shown in Figure 2.3. The half-length, L, along the ocular surface remains fixed for all simulations, thereby imposing a constraint on δ through

$$a\delta = L \quad \rightarrow \quad \lim_{a\to\infty}\delta = \lim_{a\to\infty}\frac{L}{a} = 0\,. \tag{2.36}$$

Hence the geometry of the substrate is controlled solely by δ, with $\delta = 0$ corresponding to a Cartesian plane. Thus defined, coordinates (ξ, η) are configured so that the $\mathbf{e}_\eta$-direction is the same as that of $\mathbf{e}_R$, whilst $\mathbf{e}_\xi$ is opposite to $\mathbf{e}_\theta$ in order that the prevailing direction of gravity is aligned with increasing ξ. Note that the minus sign in the definition of ξ in (2.35) accounts for the sign change associated with changing from a left-handed set

of orthonormal vectors in Figure 2.2 to a right-handed set in Figure 2.3. To simplify calculations, the azimuthal velocity is re-defined in the marginal-surface coordinates and the gravity vector can now be defined:

$$U_{(\xi,\eta)} \;=\; -U_{(R,\theta)}\,, \text{ and } \mathbf{G} \;=\; G\cos\left(\frac{\xi}{a\cos\delta}\right)\mathbf{e}_\xi \;+\; G\sin\left(\frac{\xi}{a\cos\delta}\right)\mathbf{e}_\eta\,,$$

where G is the gravitational field strength, and the coordinate subscripts on U will be dropped in subsequent calculations. The locus of the free surface is re-defined according to (2.35) as

$$\boldsymbol{\phi} \;=\; \phi(\xi,\,t)\,\mathbf{e}_\eta\,, \qquad \text{with} \qquad \phi(\xi,\,t) \;=\; \chi(\xi,\,t) - a\cos\delta\,. \tag{2.37}$$

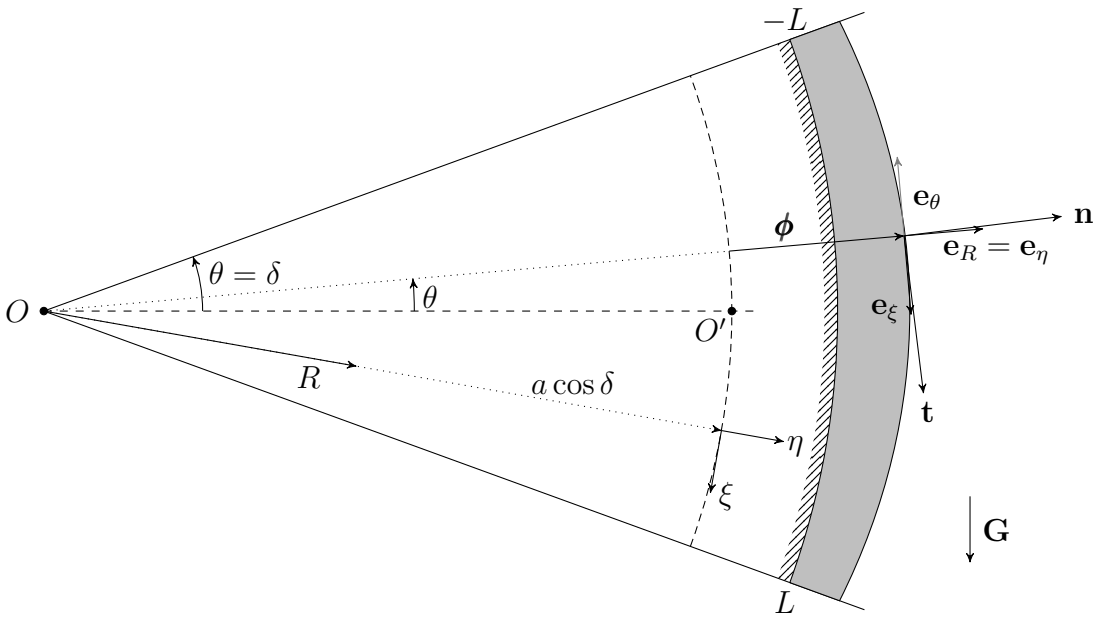

Figure 2.3: Defining sketch for the marginal-surface coordinates (ξ, η) of (2.35). The surface $\eta = 0$ is defined a distance $a\cos\delta$ from the polar coordinate origin, O, with the origin of the marginal-surface coordinates, O', falling on the intersection of this surface and the line $\theta = 0$. Orthonormal basis vectors $\mathbf{e}_\xi$ and $\mathbf{e}_\eta$ are shown, as well as the transformed normal, $\mathbf{n}$, and tangent, $\mathbf{t}$. In the marginal-surface coordinates, the locus of the free surface is given by $\boldsymbol{\phi}$.

2.2.1 Non-dimensional, scaled equations of motion

To make progress with the system of equations (2.20) - (2.22) subject to boundary conditions (2.23) and (2.28) - (2.30), the thin-film lubrication approximation is employed with the aim of reducing the equations to a coupled pair of approximate evolution equations for the film thickness and surfactant concentration. The central principle underlying the lubrication approximation is an assumption that the ratio of fluid activity in one coordinate direction to that in the other coordinate direction(s) can be characterized by a small parameter, ϵ, with $0 < \epsilon \ll 1$, the ultimate goal being to expand each dependent variable as a power series in ϵ to generate an asymptotic hierarchy of terms within each equation. In making such expansions, the standard theory assumes that all coefficients multiplying powers of ϵ within the governing equations are of order $\mathcal{O}(1)$; however, it will be shown in §2.2.2 that this is not the case. A review of the magnitude of terms is thus required before an expansion can be made.

The lengthscales of the eye yield a convenient small parameter defined as the aspect ratio between the half-length of the palpebral fissure, $L = 5 \times 10^{-3}$ m, and the characteristic film height away from the eyelids, $d = 5 \times 10^{-6}$ m (Braun & King-Smith, 2007);

$$\epsilon \equiv \frac{d}{L} = 10^{-3}\,. \tag{2.38}$$

The perpendicular height of the tear fluid above the ocular substrate, $H(\xi, t)$, is used to redefine the locus of the free surface

$$\phi(\xi, t) = a(1 - \cos\delta) + H(\xi, t)\,. \tag{2.39}$$

The lengthscales mentioned above, together with equation (2.39), motivate the definition of the following non-dimensional marginal-surface coordinates and tear-film depth

$$\xi = \frac{L\cos\delta}{C}\tilde{\xi}\,, \quad \eta = a(1-\cos\delta) + d\tilde{\omega} = \frac{L}{\delta}\Big(1 - \cos\delta + \epsilon\delta\tilde{\omega}\Big)\,, \quad H = d\tilde{h}\,, \tag{2.40}$$

where $0 \leq \tilde{\omega} \leq \tilde{h}$, and C is a yet-unspecified, order $\mathcal{O}(1)$ constant that scales the azimuthal direction and is central to the enforcement of the boundary conditions for the

pair of coupled evolution equations when they are solved using the numerical scheme that is introduced in Chapter 3. C is introduced here as it permeates through the equations of motion; however, its definition is deferred to equation (3.16) in §3.2. Note that equations (2.36) and (2.38) have been used in the definition of η. Here, and in subsequent definitions, tildes will be used to denote scaled non-dimensional variables, i.e. variables that are strictly of order $\mathcal{O}(1)$. With the non-dimensional coordinates so defined, derivatives with respect to the original, dimensional plane-polar coordinates $(R,\, \theta)$ are transformed via (2.35) and (2.40) into

$$\frac{1}{R}\frac{\partial}{\partial\theta} = \frac{-C}{L(1+\epsilon\delta\tilde{\omega})}\frac{\partial}{\partial\tilde{\xi}} \qquad \text{and} \qquad \frac{\partial}{\partial R} = \frac{1}{d}\frac{\partial}{\partial\tilde{\omega}}\,.$$

The dependent variables in the bulk flow are non-dimensionalised using a typical draining velocity, $U_0 = 1 \times 10^{-3}$ m s^{-1} (Braun & Fitt, 2003). This velocity is used to adopt a viscous pressure scale and an advective timescale. Temperature is non-dimensionalised using the difference in temperature between the eye and the ambient environment. The non-dimensional *ansatz* employed within the model to define the order $\mathcal{O}(1)$ 'tilded' variables is

$$\begin{gathered}(U,\, V) = U_0(\tilde{u}, \epsilon\tilde{v})\,, \quad P = \frac{\mu U_0}{\epsilon^2 L}\tilde{p}\,, \quad P_{\text{ATM}} = \frac{\mu U_0}{\epsilon^2 L}\tilde{p}_{\text{ATM}}\,, \\ T = \left(T_{\text{EYE}} - T^V_{\text{SAT}}\right)\tilde{\Theta} + T^V_{\text{SAT}}\,, \qquad t = \frac{L}{U_0}\tilde{t}\,, \qquad Z = \epsilon d\,\tilde{\zeta}\,,\end{gathered} \tag{2.41}$$

in which $\mu = 1.002 \times 10^{-3}$ kg m^{-1} s^{-2} is the kinematic viscosity and T^V_{SAT} is the vapour saturation temperature, taken to be $T^V_{\text{SAT}} = 293$ K. The *ansatz* (2.41) contains scalings for both the velocity normal to the ocular surface and the pressure. The fluid is not allowed to penetrate the ocular surface, forcing the velocity normal to the surface to be zero at that point. Furthermore, the fluid is presumed to be extremely thin compared with its length along the ocular surface, leading to the assumption that radial velocity, V, is an order of ϵ smaller than the transverse velocity, U, which itself requires no scaling as the draining velocity U_0 is taken along the ocular surface. The pressure terms are scaled in order that the asymptotic hierarchy obtained from expansion of the normal-stress condition (2.28)

Table 2.1: Physical parameters for the tear-flow problem. Values of fluid properties are taken for water, whilst vapour properties are for air at atmospheric pressure at 20°C. The critical surfactant concentration is a representative value for condensed films (Adam, 1941; Burdon, 1949), and the surfactant diffusivity is taken from Sakata & Berg (1969). The critical micelle value for the surface tension is taken from Tiffany *et al.* (1989).

Parameter	Value	Unit	Description
L	5×10^{-3}	m	Half-length of palpebral fissure
d	5×10^{-6}	m	Typical film depth
U_0	10^{-3}	m s^{-1}	Typical velocity
ρ	998.2	kg m^{-3}	Fluid density
ρ^V	1.2	kg m^{-3}	Vapour density
μ	1.002×10^{-3}	kg m^{-1} s^{-1}	Fluid kinematic viscosity
g	9.81	m s^{-2}	Gravitational acceleration
P_{ATM}	1.01×10^5	kg m^{-1} s^{-2}	Atmospheric pressure
T^V_{SAT}	293	K	Vapour saturation temperature
T_{EYE}	310	K	Eye temperature
k	0.68	W m^{-1} K^{-1}	Fluid thermal conductivity
κ	1.7×10^{-7}	m^2 s^{-1}	Fluid thermal diffusivity
L_v	2.3×10^6	J kg^{-1}	Latent heat of vaporization
J_0	1.5×10^{-5}	kg m^{-2} s^{-1}	Evaporative mass flux
Ψ_m	10^{18}	molecules m^{-2}	Critical surfactant concentration
D^S	3×10^{-8}	m^2 s^{-1}	Surfactant diffusivity
σ_0	0.073	N m^{-1}	Surfactant-free surface tension
σ_m	0.045	N m^{-1}	Surface tension when $\Psi = \Psi_m$

yields a well-posed system of equations. Additionally, the ϵ scaling of the slip length means Z falls within the lower limit of the range of values presented in Braun & King-

Smith (2007). Similar scalings can be found in other mathematical literature on the tear film (Braun & Fitt, 2003; Aydemir *et al.*, 2011).

Finally, surfactant-based quantities within the free surface are non-dimensionalised using their critical micelle values;

$$\Psi = \epsilon^2 \Psi_m \tilde{\psi}\,, \qquad \sigma = \sigma_m \tilde{\sigma}\,, \tag{2.42}$$

where the scaling of the surfactant concentration reflects that the lipid molecules are not densely packed. It should be noted that the value of Ψ_m is taken for a tightly-packed, condensed film, but that the term itself will be found to drop out of the non-dimensional equations; the important factor is the ϵ^2 scaling, which will affect the constitutive relationship for the surface tension (2.33). The physical parameters for the tear-flow model are summarised in Table 2.1.

Upon changing variables, non-dimensionalising, and dropping tildes on all subsequently presented variables, the differential equations governing the fluid flow are transformed thus: the transverse Navier-Stokes equation (2.20a) becomes

$$\begin{aligned} Re\left(u_t + v u_\omega + \frac{C u u_\xi}{1+\epsilon\delta\omega} + \frac{\epsilon\delta u v}{1+\epsilon\delta\omega}\right) \;=\; & -\frac{C\,p_\xi}{\epsilon^2(1+\epsilon\delta\omega)} + \frac{u_{\omega\omega}}{\epsilon^2} + \frac{\delta\, u_\omega}{\epsilon(1+\epsilon\delta\omega)} \\ & + \frac{C^2\, u_{\xi\xi}}{(1+\epsilon\delta\omega)^2} - \frac{\delta^2 u}{(1+\epsilon\delta\omega)^2} + \frac{2\epsilon\delta C\, v_\xi}{(1+\epsilon\delta\omega)^2} + St\cos\left(\frac{\delta\xi}{C}\right), \end{aligned} \tag{2.43a}$$

and the radial Navier-Stokes equation (2.20b) becomes

$$\begin{aligned} \epsilon^2 Re\left(v_t + v v_\omega + \frac{C\,u v_\xi}{1+\epsilon\delta\omega} - \frac{\delta^2 u}{1+\epsilon\delta\omega}\right) = & -\frac{p_\omega}{\epsilon^2} + v_{\omega\omega} + \frac{\epsilon\delta\, v_\omega}{1+\epsilon\delta\omega} \\ & + \frac{\epsilon^2 C^2\, v_{\xi\xi}}{(1+\epsilon\delta\omega)^2} - \frac{\epsilon^2\delta\, v}{(1+\epsilon\delta\omega)^2} - \frac{2\epsilon\delta C\, u_\xi}{(1+\epsilon\delta\omega)^2} + St\sin\left(\frac{\delta\xi}{C}\right). \end{aligned} \tag{2.43b}$$

The continuity equation (2.21) yields

$$C\,u_\xi + (1+\epsilon\delta\omega)v_\omega + \epsilon\delta v = 0\,, \tag{2.44}$$

and the heat equation (2.22) becomes

$$Re\,Pr\left(\Theta_t + v\Theta_\omega + \frac{C\,u\Theta_\xi}{1+\epsilon\delta\omega}\right) = \frac{\Theta_{\omega\omega}}{\epsilon^2} + \frac{\delta\,\Theta_\omega}{\epsilon(1+\epsilon\delta\omega)} + \frac{C^2\,\Theta_{\xi\xi}}{(1+\epsilon\delta\omega)^2}\,. \tag{2.45}$$

The non-dimensional constants introduced in the above equations are formed from groupings of the physical parameters for the flow;

$$Re = \frac{\rho U_0 L}{\mu}\,, \qquad St = \frac{\rho g L^2}{\mu U_0}\,, \qquad \text{and} \qquad Pr = \frac{\mu}{\rho \kappa} \tag{2.46}$$

are respectively the Reynolds number (quantifying the relative importance of inertial forces to viscous forces), the Stokes number (the ratio of gravitational forces to viscous forces) and the Prandtl number (the ratio of the rates of viscous diffusion to thermal diffusion).

At the ocular surface, the boundary conditions (2.6) become

$$u \,=\, \epsilon\zeta\Big(u_\omega \,-\, \epsilon\delta u\Big)\,, \qquad v \,=\, 0\,, \qquad \text{and} \qquad \Theta \,=\, 1\,, \tag{2.47}$$

at $\omega = 0$ (this value has already been substituted into the slip boundary condition). It is important to note here that the scaling of the slip length, Z, in the *ansatz* (2.41) means that slip effects are observed at order $\mathcal{O}(\epsilon)$ in the boundary condition for u; a 'no-slip' boundary condition is obtained at leading order in (2.47). At the free surface $\omega = h$, the normal- and tangential-stress conditions, (2.28) and (2.29), respectively become

$$\begin{aligned}
&-\frac{p}{\epsilon^2} \,+\, \frac{p_{\text{ATM}}}{\epsilon^2} \,+\, \frac{J_0^2 L}{\mu U_0 \left(1 + A(\epsilon^2\psi)^B\right)^2}\left(\frac{1}{\rho^V} - \frac{1}{\rho}\right) \\
&+\, \frac{2}{(1+\epsilon\delta h)^2 + \epsilon^2 C^2\, h_\xi^2}\Bigg[(1+\epsilon\delta h)^2\, v_\omega \,-\, \epsilon^2 C^2\, v_\xi h_\xi \,+\, \frac{\epsilon^3\delta C^2\, v h_\xi^2}{1+\epsilon\delta h} \\
&\qquad\qquad + \epsilon\delta C\, u h_\xi \,-\, (1+\epsilon\delta h)\, C\, h_\xi u_\omega \,+\, \frac{\epsilon^2 C^3\, u_\xi h_\xi^2}{1+\epsilon\delta h}\Bigg] \\
&\qquad = \frac{\alpha\mathcal{A}\Big((1+\epsilon\delta h)\,\epsilon C^2\, h_{\xi\xi} \,-\, 2\epsilon^2\delta C^2\, h_\xi^2 \,-\, \delta(1+\epsilon\delta h)^2\Big)}{\Big((1+\epsilon\delta h)^2 + \epsilon^2 C^2\, h_\xi^2\Big)^{3/2}\Big(1 - \epsilon^2\mathcal{B}\psi/\mathcal{A}\Big)^3}\,,
\end{aligned} \tag{2.48}$$

and

$$\frac{1}{\epsilon\left((1+\epsilon\delta h)^2+\epsilon^2C^2\,h_\xi^2\right)^{1/2}}\Bigg[u_\omega\Big(\epsilon C^2\,h_\xi^2\;-\;(1+\epsilon\delta h)^2\Big)\;+\;2\epsilon^2\delta C\,h_\xi v$$
$$+\left(\epsilon\delta u-\epsilon^2C\,v_\xi\right)\left(1+\epsilon\delta h-\frac{\epsilon^2C^2\,h_\xi^2}{1+\epsilon\delta h}\right)\;+\;2\epsilon^2C^2\,h_\xi u_\xi\;-\;2\epsilon^2(1+\epsilon\delta h)\,C\,h_\xi v_\omega\Bigg]$$
$$=\;-\frac{3\epsilon^2\alpha\mathcal{B}C\,\psi_\xi}{\left(1-\epsilon^2\mathcal{B}\psi/\mathcal{A}\right)^4}\,. \tag{2.49}$$

The constitutive equations (2.33) and (2.34) have been substituted into the stress conditions and, furthermore, the non-dimensional form of (2.33) has been simplified by making the substitutions (see Table 2.1)

$$\mathcal{A}\;\equiv\;\frac{\sigma_0}{\sigma_m}\;=\;\frac{73}{45}\,,\qquad\text{and}\qquad\mathcal{B}\;\equiv\;\mathcal{A}(1-\mathcal{A}^{1/3})\,. \tag{2.50}$$

The balance of energy (2.30) is transformed to

$$\begin{aligned}&\frac{J_0L}{\mu U_0^2\,(1\;+\;A(\epsilon^2\psi)^B)}\left[L_v\;+\;\frac{J_0^2}{2}\left(\frac{1}{(\rho^V)^2}\;-\;\frac{1}{\rho^2}\right)\right]\\&\qquad+\;\frac{\Theta_\omega(1+\epsilon\delta h)^2\;-\;\epsilon^2C^2\,h_\xi\Theta_\xi}{\epsilon Br\,(1+\epsilon\delta h)\left((1+\epsilon\delta h)^2\;+\;\epsilon^2C^2\,h_\xi^2\right)^{1/2}}\\&\qquad+\;\frac{\epsilon\Big((v-h_t)\,(1+\epsilon\delta h)\;-\;C\,uh_\xi\Big)}{(1+\epsilon\delta h)^2\left((1+\epsilon\delta h)^2\;+\;\epsilon^2C^2\,h_\xi^2\right)^{1/2}}\Big\{2(1+\epsilon\delta h)^2v_\omega\\&\qquad\qquad+C\,h_\xi\Big[\epsilon\delta u\;-\;(1+\epsilon\delta h)u_\omega\;-\;\epsilon^2C\,v_\xi\Big]\Big\}\;=\;0\,.\end{aligned} \tag{2.51}$$

By aggregating the physical parameters within the boundary conditions at the free surface, two further non-dimensional numbers that characterize the flow can be obtained in (2.48) and (2.51), these are

$$\alpha\;=\;\frac{\sigma_m}{\mu U_0}\,,\qquad\text{and}\qquad Br\;=\;\frac{\mu U_0^2}{k\,(T_{\text{EYE}}-T_{\text{SAT}}^V)}\,. \tag{2.52}$$

α is the inverse Capillary number, which measures the relative influence of surface-tension forces to viscous forces, and Br is the Brinkman number, the ratio of heat

produced through viscous friction to heat transported by conduction within the fluid. It should be noted that the first lines of (2.48) and (2.51) contain non-dimensional groupings of the evaporative mass flux and other physical parameters; these groupings are not assigned specific names, but their magnitudes will be calculated in §2.2.2, along with those of all non-dimensional numbers defined above.

Finally, with the redefinition (2.39) of the locus of the free surface, the pair of coupled evolution equations (2.31) and (2.32) yield PDEs for the non-dimensional height above the ocular surface and surfactant concentration, respectively;

$$\frac{\epsilon\left((v-h_t)\,(1+\epsilon\delta h)\;-\;C\,uh_\xi\right)}{\left((1+\epsilon\delta h)^2+\epsilon^2C^2\,h_\xi^2\right)^{1/2}}\;=\;\frac{J_0}{\rho U_0\,(1+A(\epsilon^2\psi)^B)}\,, \tag{2.53}$$

and

$$\begin{aligned}\psi_t\;-\;&\frac{\epsilon\,\psi h_t\,(1+\epsilon\delta h)\left(\epsilon C^2\,h_{\xi\xi}(1+\epsilon\delta h)-2\epsilon^2\delta C^2\,h_\xi^2-\delta(1+\epsilon\delta h)^2\right)}{\left((1+\epsilon\delta h)^2\;+\;\epsilon^2C^2\,h_\xi^2\right)^2}\\
&+\;\psi\left[\frac{C(u_\xi\;+\;h_\xi u_\omega)}{(1+\epsilon\delta h)}\;+\;\frac{\epsilon\left(\delta h_t\,(1+\epsilon\delta h)\;+\;\epsilon C^2\,h_\xi h_{\xi t}\right)}{\left((1+\epsilon\delta h)^2\;+\;\epsilon^2C^2\,h_\xi^2\right)}\right.\\
&\qquad\left.+\;\frac{\epsilon^2\,C^3\,h_\xi u\left(h_{\xi\xi}(1+\epsilon\delta h)\;-\;\epsilon\delta h_\xi^2\right)}{(1+\epsilon\delta h)^2\left((1+\epsilon\delta h)^2\;+\;\epsilon^2C^2\,h_\xi^2\right)}\right]\\
&+\;C\,\psi_\xi\left(\frac{u}{(1+\epsilon\delta h)}\;+\;\frac{\epsilon^2C\,h_\xi h_t}{\left((1+\epsilon\delta h)^2\;+\;\epsilon^2C^2\,h_\xi^2\right)}\right)\\
=\;&\frac{C^2}{Pe\left((1+\epsilon\delta h)^2\;+\;\epsilon^2C^2\,h_\xi^2\right)}\left(\psi_{\xi\xi}-\frac{\epsilon h_\xi\psi_\xi\left(\delta(1+\epsilon\delta h)+\epsilon C^2\,h_{\xi\xi}\right)}{\left((1+\epsilon\delta h)^2\;+\;\epsilon^2C^2\,h_\xi^2\right)}\right).\end{aligned} \tag{2.54}$$

Here, the Péclet number on the right-hand side of (2.54) is defined to be the ratio of advective movement of surfactant molecules to diffusive movement,

$$Pe\;\equiv\;\frac{LU_0}{D^S}\,. \tag{2.55}$$

The grouping of physical parameters on the right-hand side of (2.53) also yields a non-dimensional quantity, the magnitude of which is discussed in the following subsection.

2.2.2 Scaling of non-dimensional terms

Through the scaled non-dimensional *ansatz*, (2.40) and (2.41), the equations governing the tear-flow problem (2.43) - (2.45), (2.47) - (2.49), (2.51), and (2.53) - (2.54) have been transformed to contain non-dimensional variables with magnitude of order $\mathcal{O}(1)$. However, the non-dimensional numbers defined in §2.2.1 are formed from un-scaled groupings of the physical parameters in Table 2.1. Before simply expanding all equations as power series in the small parameter to form a thin-film approximation, the magnitudes of the non-dimensional groups are first investigated in the spirit of representing, as accurately as possible, physically-realistic scalings of their magnitudes in terms of ϵ. Using real ophthalmic data for the tear film, the non-dimensional numbers are scaled in terms of ϵ to obtain a physically-consistent form of the equations of motion. Under such scalings, the aforementioned governing equations are transformed from generic equations of lubrication approximation modelling to equations that are claimed to represent *no more than* the flow of tears upon the human eye; this ensures that results generated by the model will genuinely merit interpretation.

Using the parameter values collated in Table 2.1, the non-dimensional numbers defined in (2.46), (2.52) and (2.55) are found to have the following values

$$\begin{aligned} Re &= 4.98 && \approx \epsilon^{-0.232}, \\ St &= 2.44 \times 10^{5} && \approx \epsilon^{-1.796}, \\ Pr &= 5.90 && \approx \epsilon^{-0.257}, \\ \alpha &= 4.49 \times 10^{4} && \approx \epsilon^{-1.551}, \\ Br &= 8.67 \times 10^{-11} && \approx \epsilon^{3.354}, \\ Pe &= 167 && \approx \epsilon^{-0.740}. \end{aligned} \tag{2.56}$$

The realistic scalings suggested by (2.56) are built into the modelling via a rescaling of the non-dimensional parameters using

$$\begin{aligned} Re &= \epsilon^0\, re\,, \\ St &= \epsilon^{-2}\, st\,, \\ Pr &= \epsilon^0\, pr\,, \\ \alpha &= \epsilon^{-3}\, \alpha_0\,, \\ Br &= \epsilon^3\, br\,, \\ Pe &= \epsilon^{-1}\, pe\,, \end{aligned} \tag{2.57}$$

wherein all lower-case parameters and α_0 are *by genuine physical considerations* constants of order $\mathcal{O}(1)$. It should be noted here that the scaling of the inverse capillary number, α, has been altered to increase the importance of terms relating to surface tension and surface-tension gradients, respectively arising in the normal- and tangential-stress conditions at the free surface. One of the primary aims of this work is to study the effects of variable surface tension on the tear film, hence this rescaling is necessary to promote such effects in the model. Furthermore, in order that the effects of evaporation from the bulk fluid occur at leading-order in the balance of mass, the non-dimensional grouping in (2.53) is rescaled using an order $\mathcal{O}(1)$ parameter E via

$$\frac{J_0}{\rho U_0} \;=\; 1.50\times 10^{-5} \;\approx\; \epsilon^{1.608} \;\longrightarrow\; \frac{J_0}{\rho U_0} \;=\; \epsilon\, E\,. \tag{2.58}$$

Within the normal-stress condition (2.48) the two non-dimensional groupings model the transfer of momentum through the interface as fluid molecules evaporate into the vapour phase. The scaled terms become

$$\begin{aligned} \frac{J_0^2 L}{\rho\,\mu U_0} &= 1.12\times 10^{-9} \;\approx\; \epsilon^{2.983} \;\longrightarrow\; \frac{J_0^2 L}{\rho\,\mu U_0} \;=\; \epsilon^3\, m\,, \\ \frac{J_0^2 L}{\rho^V \mu U_0} &= 9.36\times 10^{-7} \;\approx\; \epsilon^{2.010} \;\longrightarrow\; \frac{J_0^2 L}{\rho^V \mu U_0} \;=\; \epsilon^2\, m^V\,, \end{aligned} \tag{2.59}$$

with m and m^V defined as $\mathcal{O}(1)$ factors. Finally, the three non-dimensional quantities in

the energy balance at the interface (2.51) are rescaled using

$$\begin{aligned}
\frac{J_0 L L_v}{\mu U_0^2} &= 1.72 \times 10^8 \approx \epsilon^{-2.745} \longrightarrow \frac{J_0 L L_v}{\mu U_0^2} = \epsilon^{-3}\,\lambda\,, \\
\frac{J_0^3 L}{2\rho^2 \mu U_0^2} &= 8.45 \times 10^{-15} \approx \epsilon^{4.961} \longrightarrow \frac{J_0^3 L}{2\rho^2 \mu U_0^2} = \epsilon^{5}\,K\,, \\
\frac{J_0^3 L}{2(\rho^V)^2 \mu U_0^2} &= 5.85 \times 10^{-9} \approx \epsilon^{2.744} \longrightarrow \frac{J_0^3 L}{2(\rho^V)^2 \mu U_0^2} = \epsilon^{3}\,K^V\,,
\end{aligned} \tag{2.60}$$

where λ, K and K^V are defined to be $\mathcal{O}(1)$. These groupings of parameters multiply terms that respectively model the heat energy released from the bulk fluid phase as molecules evaporate into the vapour phase, and the kinetic energies of the fluid and vapour molecules themselves.

Upon replacing the non-dimensional numbers and groupings of physical parameters in the governing equations with their scaled equivalents (2.57) - (2.60), the tear-flow model now contains factors that are all of order $\mathcal{O}(1)$, with the exception of the small parameter ϵ that governs the relative size of all terms in the equations. Through the use of real physical data, the equations of motion have been consistently represented, allowing expansions of the dependent variables as power series in ϵ to be made in with confidence that the asymptotic equations obtained will be uniformly valid and physically viable.

2.3 Asymptotic expansion and leading-order solution

To make progress with the non-dimensional, scaled (subject to the rescalings detailed in §2.2.2) set of differential equations (2.43) - (2.45) and associated boundary conditions (2.47) - (2.49) and (2.51), the field variables u, v, p, and Θ are expanded as power series in the small parameter ϵ

$$\begin{Bmatrix} u(\xi,\,\omega,\,t) \\ v(\xi,\,\omega,\,t) \\ p(\xi,\,\omega) \\ \Theta(\xi,\,\omega,\,t) \end{Bmatrix} = \sum_{j=0}^{N} \epsilon^j \begin{Bmatrix} u_j(\xi,\,\omega,\,t) \\ v_j(\xi,\,\omega,\,t) \\ p_j(\xi,\,\omega) \\ \Theta_j(\xi,\,\omega,\,t) \end{Bmatrix} + o(\epsilon^N)\,, \tag{2.61}$$

with the aim of transforming the original nonlinear problem into a hierarchy of linearised differential equations at each order of ϵ. Through substitution of (2.61) into the aforementioned governing equations and expanding everything in ϵ, a hierarchy of fully closed boundary value problems is created at different orders of ϵ, solution of which yields the coefficient functions of (2.61) that yield uniformly-valid asymptotic expansions for the field variables. Substitution of the expanded field variables into (2.53) and (2.54) converts the pair of coupled evolution equations to an asymptotic form.

In keeping with the existing literature on the tear-flow problem, the leading-order solution to the system of differential equations listed above is sought, and substituted into the pair of coupled evolution equations to study the dominant behaviours within the tear film. Making the expansion of the field variables, the leading-order components of all relevant partial differential equations are

$$\begin{aligned}
&\text{(2.43a):} \qquad u_{0,\,\omega\omega} \;=\; C\,p_{0,\,\xi} \;-\; st\cos\left(\frac{\delta\xi}{C}\right)\,, \\
&\text{(2.43b):} \qquad p_{0,\,\omega} \;=\; 0\,, \\
&\text{(2.44):} \qquad C\,u_{0,\,\xi} \;+\; v_{0,\,\omega} \;=\; 0\,, \qquad \text{and} \\
&\text{(2.45):} \qquad \Theta_{0,\,\omega\omega} \;=\; 0\,,
\end{aligned} \tag{2.62}$$

wherein $j = 0$ in (2.61) and differentiation with respect to a variable is denoted after a subscript comma. These equations reveal that the leading-order temperature distribution is at most a linear function of depth through the tear film. The radial component of the momentum equation shows that the pressure gradient through the film is zero, thus the leading-order pressure field represents a depth-averaged value that is dependent only upon the azimuthal coordinate ξ; this is a typical feature of thin-film lubrication models. Finally, the azimuthal component of the momentum equation shows $u_0(\xi, \omega, t)$ to be a quadratic function of depth, ω, with all ξ- and t-dependence arising through p_0 and the boundary conditions.

The differential equations (2.62) must be supplemented by the order $\mathcal{O}(1)$ components

of the expansions of the slip, no-penetration and continuity of temperature boundary conditions (2.47) at the ocular surface, which are respectively

$$u_0\Big|_{\omega=0} = 0\,, \qquad v_0\Big|_{\omega=0} = 0\,, \quad \text{and} \quad \Theta_0\Big|_{\omega=0} = 1\,, \tag{2.63}$$

and the normal- and tangential-stress conditions, (2.48) and (2.49), and energy balance (2.51) boundary conditions at the free surface

$$\begin{aligned} p_0\Big|_{\omega=h} &= p_{\text{ATM}} - \alpha_0 \mathcal{A}\, C^2\, h_{\xi\xi} - \alpha_0 \mathcal{A}\, \delta^2 h\,, \\ u_{0,\omega}\Big|_{\omega=h} &= 3\,\alpha_0 \mathcal{B}\, C\, \psi_\xi\,, \quad \text{and} \\ \Theta_{0,\omega}\Big|_{\omega=h} &= 0. \end{aligned} \tag{2.64}$$

The solution of equations (2.62), satisfying the boundary conditions (2.63) and (2.64), is

$$\begin{aligned} u_0 &= \left(h\omega - \frac{\omega^2}{2}\right)\left\{\alpha_0 \mathcal{A}\, C\Big[C^2\, h_{\xi\xi\xi} + \delta^2 h_\xi\Big] + st\cos\left(\frac{\delta\xi}{C}\right)\right\} + 3\omega\,\alpha_0 \mathcal{B}\, C\, \psi_\xi\,, \\ v_0 &= -\frac{\omega^2}{6}\Bigg[(3h-\omega)\left\{\alpha_0 \mathcal{A}\, C^2\Big[C^2\, h_{\xi\xi\xi\xi} + \delta^2 h_{\xi\xi}\Big] - \delta st \sin\left(\frac{\delta\xi}{C}\right)\right\} \\ &\qquad + 3C\, h_\xi\left\{\alpha_0 \mathcal{A}\, C\Big[C^2\, h_{\xi\xi\xi} + \delta^2 h_\xi\Big] + st\cos\left(\frac{\delta\xi}{C}\right)\right\} + 9\,\alpha_0 \mathcal{B}\, C^2\, \psi_{\xi\xi}\Bigg]\,, \\ p_0 &= p_{\text{ATM}} - \alpha_0 \mathcal{A}\, C^2\, h_{\xi\xi} - \alpha_0 \mathcal{A}\, \delta^2 h\,, \\ \Theta_0 &= 1\,. \end{aligned} \tag{2.65}$$

The velocity and pressure fields in (2.65) demonstrate that the curvature of the substrate has a non-trivial influence on the leading-order solution to the tear-flow problem, which influence is unseen in all prior models of the tear film (with the exception of Braun *et al.*, 2012). In the Cartesian limit ($\delta = 0$), the leading-order velocity and pressure fields agree with the solutions of other formulations that employ the tangential stress condition (2.49) at $\omega = h$ (Jones *et al.*, 2005, in their "zero-stress limit"; Jones *et al.*, 2006; Aydemir *et al.*, 2011; Zubkov *et al.*, 2012, 2013). However, the fluid velocities of (2.65) differ both from those of formulations that model the free surface to be tangentially immobile, and from the velocities of Braun & King-Smith (2007) and Heryudono *et al.* (2007), in which

slip at the cornea is modelled as a leading-order effect. Under the scalings of §2.2.2, the uniform leading-order temperature field of (2.65) differs from the spatially-variable distributions derived in Braun & Fitt (2003), Winter *et al.* (2010) and Li & Braun (2012).

Through the form of u_0 in (2.65), two simplifying substitutions can be made that partition the behaviours influencing the movement of the tear film into the combined effects of capillarity and gravity, and the effect of surfactant concentration gradients. Two functions are defined as

$$M(\xi) \;\equiv\; \alpha_0 \mathcal{A}\, C\Big[C^2\, h_{\xi\xi\xi} \;+\; \delta^2 h_\xi\Big] \;+\; st\cos\left(\frac{\delta\xi}{C}\right)\,, \tag{2.66a}$$

$$\Omega(\xi) \;\equiv\; 3\,\alpha_0 \mathcal{B}\, C\,\psi_\xi\,, \tag{2.66b}$$

using which, the leading-order velocity field in (2.65) is simplified to

$$\begin{aligned} u_0 \;&=\; \left(h\omega \;-\; \frac{\omega^2}{2}\right) M \;+\; \omega\Omega\,, \\ v_0 \;&=\; -C\,\frac{\omega^2}{6}\Big[(3h-\omega)M_\xi \;+\; 3h_\xi M \;+\; 3\Omega_\xi\Big]\,. \end{aligned}$$

To identify the limits of validity of the leading-order solution (2.65) to the tear-flow problem, the order $\mathcal{O}(\epsilon)$ components of the governing equations and boundary conditions are considered as these are the terms of largest magnitude that are neglected through truncation at $\mathcal{O}(1)$. The linearised differential equations for the component terms at $\mathcal{O}(\epsilon)$ in (2.43) - (2.45) are

$$\begin{aligned} &u_{1,\,\omega\omega} \;=\; C\,p_{1,\,\xi} \;-\; \delta\,(u_{0,\,\omega} + C\omega p_{0,\,\xi})\;, \\ &p_{1,\,\omega} \;=\; st\sin\left(\frac{\delta\xi}{C}\right)\,, \\ &C\,u_{1,\,\xi} \;+\; v_{1,\,\omega} \;=\; -\delta\,(\omega v_{0,\,\omega} + v_0)\;, \qquad \text{and} \\ &\Theta_{1,\,\omega\omega} \;=\; -\delta\Theta_{0,\,\omega}\,, \end{aligned} \tag{2.67}$$

in which all terms on the right-hand side are explicitly known through (2.65). These are augmented by the $\mathcal{O}(\epsilon)$ components of the boundary conditions; at the ocular surface

$$u_1\Big|_{\omega=0} \;=\; \zeta u_{0,\,\omega}\,, \qquad v_1\Big|_{\omega=0} \;=\; 0\,, \quad \text{and} \quad \Theta_1\Big|_{\omega=0} \;=\; 0\,, \tag{2.68}$$

and at the free-surface, the stress conditions and energy balance yield

$$\begin{aligned} p_1\Big|_{\omega=h} &= \alpha_0 \mathcal{A}\delta\left(2\,C^2\,hh_{\xi\xi} + \delta^2 h + \frac{1}{2}C^2\,h_\xi^2\right) + 3\,\alpha_0\mathcal{B}\delta\,\psi, \\ u_{1,\omega}\Big|_{\omega=h} &= \delta\left(u_0 - h\,u_{0,\omega}\right), \quad \text{and} \\ \Theta_{1,\omega}\Big|_{\omega=h} &= -\lambda br\,. \end{aligned} \tag{2.69}$$

At this point it is instructive to re-iterate that all linearised differential equations, boundary conditions and solutions presented within this section are obtained under the inherent assumptions of the long-wavelength, thin-film lubrication approximation, specifically: that the ratio of the fluid activity in the coordinate direction through the film to the fluid activity in the direction along the film is characterized by the small parameter, ϵ. Through the scalings made in §2.2.1 and §2.2.2, *all* variables and derivatives in the leading-order set of differential equations and boundary conditions used to obtain (2.65), and in (2.67) - (2.69) are assumed to be strictly of order $\mathcal{O}(1)$. When this is not the case (for example near a steepening front in the free surface, $|h_\xi| \gg 1$; or where the free surface has a large curvature, $|h_{\xi\xi}| \gg 1$) the asymptotic hierarchy formed to enable solution of the governing equations ceases to be uniformly valid. Scaled into the notation of the present work, steep gradients and large curvatures are indeed found throughout the models of the tear film in the published literature. Despite this, a study of the terms neglected in the order $\mathcal{O}(1)$ differential equations is never undertaken. Hence near the pinned menisci, where the first and second derivatives of the free-surface height may be of order $\mathcal{O}(\epsilon^{-1})$ or larger, terms that were originally omitted through scaling arguments may need to be promoted in the asymptotic hierarchy, into the leading-order equations. The invalidation of the assumptions of the lubrication approximation is illustrated in Zubkov *et al.* (2013), wherein a comparison of fluid velocities from a lubrication model and from solution of the full Navier-Stokes equations in a meniscus pinned at a height of order $\mathcal{O}(100)$ shows the lubrication model to omit a convective mixing region that is observed in the Navier-Stokes model and, moreover, to predict movement of the *fixed* contact line. Notably, qualitative agreement between predicted tear-film thickness profiles from both

models is demonstrated. However, this similarity of results may be born of the constraints of the modelled scenario, specifically: a thin film coupled to a large, pinned meniscus, hence there is very little movement the film could exhibit that would lead to significantly different results between the two models.

Herein the assumptions employed to obtain the leading-order flow variables (2.65) are used to inform the choice of boundary and initial conditions in §2.4.1, enforcing that all expansions used to derive the model evolution equations remain uniformly valid. With the ordering of the terms in the governing equations (2.43) - (2.45), (2.47) - (2.49), and (2.51) remaining intact, the leading-order solution (2.65) is henceforth adopted as an accurate approximation to the tear-flow problem. Through this truncation of the power-series expansion, it is noted that each field variable in (2.61) is effectively expanded with only one component term on the right-hand side ($u = \epsilon^0 u_0$, etc.). This notation is relaxed in the following sections, and so the subscript zeros appended to each field variable in (2.65) are subsequently removed, the implication being that it is the $\mathcal{O}(1)$ system under consideration. As the leading-order temperature distribution (2.65) is shown to be spatio-temporally constant, its evolution is not considered in the remainder of this work.

2.4 Coupled evolution equations

The pair of coupled evolution equations for the leading-order tear-flow problem is obtained through the substitution of the leading-order flow dynamics (2.65) into (2.53) and (2.54), which are respectively subjected to the rescalings of (2.58) and (2.57). To simplify the expressions, the functions defined in (2.66) are utilised.

Evaluating the fluid velocity components, u and v (2.65), at the free surface, $\omega = h$, and substituting into (2.53) allows all spatial derivatives of h to be identified with the gradient of a mass flux, Q, of fluid along the ocular surface. This flux is defined as

$$Q(\xi) \;\equiv\; \int_0^h u\, d\omega \;=\; \frac{h^3}{3} M \,+\, \frac{h^2}{2}\Omega\,, \tag{2.70}$$

and is used to cast the leading-order thin-film evolution equation for the film thickness into a conservative form given by

$$h_t \,+\, C Q_\xi \,+\, E \;=\; 0\,. \tag{2.71}$$

Upon substitution of u (2.65) and its derivatives at $\omega = h$ into (2.54), the leading-order thin-film evolution equation for the concentration of surfactant at the fluid-air interface may be expressed as

$$\psi_t \,+\, C R_\xi \;=\; 0\,, \tag{2.72}$$

in which

$$R(\xi) \;\equiv\; \psi\, u\Big|_{\omega=h} \;=\; \frac{\psi h^2}{2} M \,+\, \psi h\, \Omega \tag{2.73}$$

plays a role that is here called a 'concentration flux' for the surfactant. It should be noted that the scaling (2.57) of the Péclet number naturally telescopes diffusive terms in the asymptotic hierarchy of (2.54) to lower than order $\mathcal{O}(1)$, so that the leading-order evolution equation contains only advective terms in addition to the time derivative.

Equations (2.71) and (2.72) form the pair of coupled evolution equations to be solved in Chapters 5 and 6. These must be augmented by initial profiles for each distribution, together with physically-motivated boundary conditions for both the height and surfactant profiles at the eyelids.

2.4.1 Boundary and initial conditions for h and ψ

Evolution equations (2.71) and (2.72) are first-order in time and respectively fourth- and second-order in the spatial coordinate ξ. Thus, in order that the system of equations is well-posed, (2.71) requires a single initial condition to be enforced on the film thickness, h, as well as four boundary conditions at the eyelids; similarly, (2.72) requires one initial

condition, and two boundary conditions to be imposed upon the surfactant concentration, ψ. Due to the requirement that the initial conditions satisfy the appropriate boundary conditions, a discussion of the initial conditions is deferred until after the boundary conditions at the eyelids have been defined.

Contact-angle boundary condition

The first boundary condition for h is specified by the contact angle, θ_{OPHTH}, subtended between the eyelid margin and the free surface of the tear film. The contact angle arises through the physical interaction of the surface tensions at the three-phase contact line, at which point the balance of forces acting along the interfaces between each phase is given by Young's law (Young, 1805; Adam, 1941; Snoeijer & Andreotti, 2013)

$$\sigma_{\text{SV}} \;=\; \sigma_{\text{SF}} \;+\; \sigma_0 \cos\theta_{\text{OPHTH}} \,, \tag{2.74}$$

wherein subscripts SV and SF respectively denote the surface tensions along the solid-vapour and solid-fluid interfaces, and σ_0 is the surface tension of the clean fluid-vapour interface (*cf.* Table 2.1). In dimensional coordinates, the contact angle satisfies

$$\cot\theta_{\text{OPHTH}} \;=\; \mp\frac{1}{\chi}\frac{\partial\chi}{\partial\theta}\bigg|_{\theta=\pm\delta} \,.$$

Converting to scaled, non-dimensional, marginal-surface coordinates (2.40), the gradient of the film thickness at the contact line is related to the contact angle through

$$h_\xi\Big|_{\xi=\pm C} \;=\; \pm\frac{1+\epsilon\delta h}{\epsilon C}\cot\theta_{\text{OPHTH}} \,. \tag{2.75}$$

However, using the *in vivo* measurements of Johnson & Murphy (2006, page 522) the contact angle can readily be estimated as $\theta_{\text{OPHTH}} \approx \pi/6$, from which (2.75) yields gradients of the scaled film thickness of magnitude

$$|\, h_\xi \,| = \mathcal{O}(\epsilon^{-1}) \;\gg\; 1 \,.$$

As such, boundary condition (2.75) is not feasible for the present model as it is currently presented, because it invalidates the constraint that all terms and their derivatives are strictly of order $\mathcal{O}(1)$ (as mentioned on page 48). To ensure that the 'long-wavelength' assumptions (relative to h) of the lubrication approximation remain valid, (2.75) must be recast in an analogous form, modelling $|h_\xi|$ as an order $\mathcal{O}(1)$ quantity through the use of a *scaled* contact angle, $\hat{\theta}$, yielding

$$h_\xi\Big|_{\xi=\pm C} = \pm\frac{1+\epsilon\delta h}{C}\cot\hat{\theta}\,, \tag{2.76}$$

with $\hat{\theta} \gtrsim \pi/4$. Importantly, the constraint placed on $\hat{\theta}$ by the lubrication approximation effectively models an unscaled contact angle that is unphysically large, $\theta_{\text{OPHTH}} \approx \pi/2$, yielding a tear film that is nearly flat. Nevertheless, the use of (2.76) enables novel behaviours of the tear film to be observed in Chapters 5 and 6.

The use of boundary condition (2.76) is, to the author's knowledge, wholly new to the field of mathematically modelling the tear film. In all previous literature (eg. Braun & Fitt, 2003; Jones *et al.*, 2005; Aydemir *et al.*, 2011) a pair of Dirichlet boundary conditions are chosen at the contact line, effectively *pinning* the height of the fluid and allowing the film profile to assume any contact angle. Such an approach is justified through a discussion of the change in the hydrophilicity of the eyelid margin at the mucocutaneous junction; the presence of the lipid-secreting Meibomian glands forming an anterior limit for the tear film on the eyelid. It is accepted that the mucocutaneous junction provides a barrier to the tear film as it advances, anteriorly, along the eyelid margin. However, nowhere in the literature is there either given or discussed a physical reason for the tear film not to recede over the already-wetted and hydrophilic epithelia of the eyelid, which are not covered by lipid. Hence, in the following sections and chapters, what is believed to be a pioneering investigation is undertaken that uses the (considerably more difficult to implement) condition (2.76) as a physically more-justifiable replacement of the 'Dirichlet pinning' used in all prior studies. Through employing boundary condition (2.76), the tear film is allowed to slip to a level that is naturally defined by the surface energies

at the three-phase contact line. Thus, by replacing θ_{OPHTH} with $\hat{\theta}$ in Young's law (2.74), boundary condition (2.76) effectively models a contact line located at a point below the mucocutaneous junction, where the epithelia both anterior and posterior to the point of contact on the eyelid margin are similarly wettable, $\sigma_{\text{SV}} \approx \sigma_{\text{SF}}$. This variation of the contact-line position complements the *in vivo* observations of Golding *et al.* (1997).

Furthermore, pinning of the tear film at the eyelids appears to be contradictory in models which include evaporative losses from the bulk fluid, particularly as the eyelid margins have been shown to maintain a higher temperature than the cornea (Tomlinson *et al.*, 2011), and hence should enhance evaporation in the meniscus regions. In pinned models, the thickness of the tear film is reduced in all areas *except* at the eyelids, inducing increasingly steep gradients in the film profile that themselves will influence the flow field. By contrast, through allowing the tear film to slip at the eyelid margin in the present model, the full film profile may be steadily diminished through evaporation without the creation of artificial flow dynamics.

Velocity-motivated boundary conditions

The remaining boundary conditions for the film thickness, h, and the boundary conditions for the concentration of surfactant, ψ, are motivated by modelling the eyelids as solid boundaries in the tear film flow. These cause the azimuthal velocity to vanish at all heights along the eyelid

$$u(\pm C,\, \omega,\, t) \;=\; \left[\left(h\omega \;-\; \frac{\omega^2}{2}\right) M \;+\; \omega\Omega\right]_{\xi=\pm C} \;=\; 0\,, \text{ for } \; 0 < \omega \leq h\,,$$

thereby automatically being consistent with zero flux at the eyelids (in the absence of lacrimal influx or punctal efflux in the derivation of the model). This equation is satisfied when both $M(\xi)$ and $\Omega(\xi)$ vanish at $\xi \;=\; \pm C$ whence, from (2.66a) and boundary condition (2.76), a boundary condition can also be derived on third derivative of h as

$$h_{\xi\xi\xi}\Big|_{\xi=\pm C} \;=\; \frac{-st\cos\delta}{\alpha_0 \mathcal{A}\, C^3} \;\mp\; \frac{\delta^2(1+\epsilon\delta h)}{C^3}\cot\hat{\theta}\,, \tag{2.77}$$

which, under the assumptions of the lubrication approximation, effectively specifies the rate of change of interfacial curvature at the contact line; and from (2.66b), the first derivative of ψ satisfies

$$\psi_\xi\Big|_{\xi=\pm C} \;=\; 0\,, \tag{2.78}$$

giving a concentration of surfactant that is spatially constant in the vicinity of the contact line. Although boundary condition (2.77) was formulated using similar arguments to those in the published literature, it may be argued that enforcing a boundary condition on any derivative higher than h_ξ is tantamount to enforcing a boundary condition on the pressure field through the expression for p_0 in (2.65). This is an artefact of the modelling, in which the elimination of the pressure in the velocity field introduces $h_{\xi\xi}$, $h_{\xi\xi\xi}$ and $h_{\xi\xi\xi\xi}$ to the evolution equation, about which the original system (2.1) – (2.3) cannot possibly 'know'. As such, instead of evolving under the fourth-order partial differential equation (2.71) for the film thickness, which is a mathematical construction, the real-life tear film would evolve according to the Navier-Stokes equations and boundary conditions as presented in §2.1.

As introduced above, the eschewal of a Dirichlet boundary condition within this model allows slippage of the contact line along the surface of the eyelid as the height of the tear film evolves. This suggests that a *dynamic* contact angle, $\hat{\theta}_D$, should be used to model the motion-dependent changes to the advancing and receding contact angle. However, in the absence of any data for the behaviour of the contact angle during dynamic wetting of the epithelia of the eyelid margin, $\hat{\theta}$ is modelled as a *static* parameter. Furthermore, the scaling of the fluid velocity perpendicular to the ocular surface (2.41) and the value of U_0 (*cf.* Table 2.1) mean that any dynamic model for the contact angle (for example Voinov, 1976) yields perturbations to the specified static angle that are of order $o(1)$, thus for the purposes of this thesis a static contact angle is employed,

$$\hat{\theta}_D \simeq \hat{\theta}\,.$$

Initial conditions

To close the system, a pair of initial conditions, $h_0(\xi)$ and $\psi_0(\xi)$, must be specified that respectively define the shape of the tear film and distribution of lipid molecules at the end of a blink. The initial conditions must be chosen from the set of profiles that satisfy the boundary conditions (2.76) - (2.78); if this is not the case, the imposition of the boundary conditions on the system would cause an un-natural forcing on the initial dynamics of the tear film and the surfactant concentration.

In the published literature many of the initial conditions for the height of the thin film contain similar characteristics; a wide, flat central region with steep menisci at the eyelids. In many cases (Braun & Fitt, 2003; Jones *et al*., 2005; Braun & King-Smith, 2007) the initial condition consists of a flat-centred, steep-sided, 'U-shaped' initial condition obtained using a high even power of the azimuthal coordinate. Importantly, in all cases it should be noted that such initial conditions contain very steep gradients near the interval end points; features that invite the condition $|h_\xi| \gg 1$, which is incompatible with the assumptions of the lubrication approximation employed in the modelling.

To preclude the artificial introduction of discontinuous derivatives[3], a splined initial condition is used to blend a steep-sided, U-shaped profile with one that has shallower menisci and satisfies the boundary conditions. The U-shaped profile is defined as

$$\mathcal{U}(\xi) \;=\; h_{\text{MID}} \left(1 \;+\; (r-1)\frac{\xi^8}{C^8} \right) , \tag{2.79}$$

where h_{MID} is the height of the flat central region at $\xi = 0$, and $r > 0$ is the ratio of the meniscus height at $\xi = \pm C$ to the height at $\xi = 0$. A blend point $\xi = b$ is specified, at

[3]The model of Braun & Fitt (2003) uses a piecewise-continuous initial condition h_0, which matches quadratic boundary menisci to a flat central profile. Thus defined, the initial profile has a discontinuous second derivative of h_0 at the matching points. Furthermore, with gravity included, this initial condition will fail to satisfy the boundary conditions that are imposed on the third spatial derivative of h. Not only have these aspects not been critically questioned, but also they have been adopted verbatim by the subsequent study of Winter *et al.* (2010).

which the function, h_0, and its derivatives up to fourth-order match those of $\mathcal{U}$, forming five constraints on h_0.

The forms of function $\mathcal{U}(\xi)$ and boundary condition (2.76) suggest defining h_0 as an even function of ξ. However, boundary condition (2.77) enforces a break in the symmetry of h_0 when gravity is included in the model, whence h_0 is constructed as the combination of a symmetry-breaking function $\mathcal{G}(\xi)$ and a polynomial formed of nine even powers of ξ

$$h_0(\xi) \;\equiv\; \mathcal{G}(\xi) \;+\; \sum_{j=0}^{8} a_j\, \xi^{2j}\,, \tag{2.80}$$

from which the nine constants a_j are fixed using the constraints described above and four further requirements that are subsequently outlined.

The symmetry-breaking function $\mathcal{G}(\xi)$ must be determined first and is required to satisfy six constraints. As such, it is defined as a fifth-order polynomial in single powers of ξ

$$\mathcal{G}(\xi) \;=\; \sum_{j=0}^{5} A_j\, \xi^{j}\,, \tag{2.81}$$

where the six coefficients, A_j, are fixed through enforcing that $\mathcal{G}(\xi)$ satisfies boundary condition (2.77) and

$$\mathcal{G}\Big|_{\xi=\pm C} \;=\; 0\,, \qquad \text{and} \qquad \mathcal{G}_\xi\Big|_{\xi=\pm C} \;=\; 0\,.$$

The latter two pairs of conditions ensure that $\mathcal{G}(\xi)$ and its first derivative vanish at the eyelids, allowing all 'even-power behaviour' to be enforced by the polynomial in h_0.

Equation (2.80) contains nine free parameters, a_j, of which five are fixed through asserting that the value of h_0 and its first four derivatives match those of $\mathcal{U}$ at the blend point. The remaining four conditions are

$$h_0\Big|_{\xi=0} \;=\; h_{\text{MID}}\,, \qquad h_0\Big|_{\xi=C} \;=\; r\,h_{\text{MID}}\,, \qquad \frac{dh_0}{d\xi}\Big|_{\xi=C} \;=\; \frac{1+\epsilon\delta r h_{\text{MID}}}{C}\cot\hat{\theta}\,, \quad \text{and}$$
$$\frac{d^3h_0}{d\xi^3}\Big|_{\xi=C} \;=\; \frac{-st\cos\delta}{\alpha_0\mathcal{A}\,C^3} \;-\; \frac{\delta^2(1+\epsilon\delta r h_{\text{MID}})}{C^3}\cot\hat{\theta}\,,$$

in which the restrictions on $\mathcal{G}(\xi)$ and the even powers of ξ in (2.80) ensure that all four boundary conditions are satisfied, and that the meniscus height is identical at both eyelids. The functions $\mathcal{U}$, $\mathcal{G}$ and h_0 may be readily programmed using an algebraic manipulator such as MAPLE, which can be used to solve for the unknown coefficients in terms of the order $\mathcal{O}(1)$ parameters in the model. The general form of these coefficients is extremely cumbersome, and is not presented in this thesis.

To study the effects of surfactant on the thickness of the tear film, three initial conditions are defined for $\psi_0(\xi)$. The first models a clean surface with no surfactant, allowing the bulk fluid to move under the effects of gravity and constant surface tension. The second models a uniform concentration of surfactant after the eye has opened, which would create no surface tension gradients to drive the initial flow characteristics. Instead, any movement of the fluid would be created from the relaxation of the initial height profile, which itself would advect the surfactant, causing interaction and feedback between the coupled equations. Enforcing a uniform initial distribution of surfactant is akin to modelling the 'pleated-drape' effect observed by McDonald (1968, 1969), in which the movement of the lipid layer during a blink resembles that of a curtain gathering in front of the advancing lid as the eye closes, and subsequently unfolding as the eyelid opens. These two options are given by

$$\psi_0(\xi) \;=\; 0\,, \qquad \text{for a surfactant-free interface, and} \tag{2.82a}$$

$$\psi_0(\xi) \;=\; 1\,, \qquad \text{for a uniform surfactant distribution,} \tag{2.82b}$$

both of which initial conditions also satisfy boundary condition (2.78).

The third initial condition models a variable distribution of surfactant, in which the concentration of lipid is higher in the inferior half of the free surface ($\xi > 0$) than in the superior half ($\xi < 0$). This models the delivery of Meibomian lipid of Brown & Dervichian (1969), Holly & Lemp (1977), and Bron *et al.* (2004) in which, during the upstroke of a blink, lipid is drawn from a reservoir located at the lower lid, lagging

slightly behind the advancing upper eyelid. Despite the rapid spreading of the lipid during the opening phase, the location of the reservoir leads to a non-uniform distribution of lipid, with greater concentrations over the inferior cornea, $\xi > 0$. The initial condition is constructed as a polynomial consisting of a constant term and odd powers of ξ,

$$\psi_0(\xi) \;=\; b_0 \;+\; \sum_{j=1}^{3} b_j\, \xi^{2j-1}\,, \tag{2.83}$$

in which three of the four coefficients, b_j, are fixed by asserting that

$$\psi_0\Big|_{\xi=-C} \;=\; \psi_{\text{MIN}}\,, \qquad \psi_0\Big|_{\xi=0} \;=\; \bar{\psi}\,, \;\; \text{and} \;\; \left.\frac{d\psi_0}{d\xi}\right|_{\xi=C} \;=\; 0\,,$$

where ψ_{MIN} is the minimum concentration of surfactant (found at the upper lid), and $\bar{\psi}$ is the mean concentration of lipid, taken to be $\bar{\psi} = 1$ in scaled, non-dimensional variables. The third condition is a statement of boundary condition (2.78). The remaining coefficient is fixed using an additional, fictitious boundary condition that is required by the numerical scheme (see §3.2.2 for details). MAPLE may, again, be used to solve for the coefficients, b_j, in terms of the parameters of the model.

2.4.2 Viability of pinned boundary conditions

Central to the derivation of the initial condition (2.80) is the enforcement of the physically-motivated boundary conditions, (2.76) and (2.77), for the evolution equation (2.71). This enforcement averts an artificial forcing of the system when the boundary conditions are abruptly applied at the initiation of temporal integrations. As previously mentioned, the specification of only Neumann boundary conditions allows slip of the three-phase contact line, with the rate of slippage defined by the free-surface velocity at the eyelid. Boundary condition (2.77) enforces no penetration of the fluid into the eyelid margin, whence the velocity field at the contact line is purely radial, i.e. tangential to the eyelid. The initial speed of advancement or recession is specified by the initial conditions enforced on both the film and the surfactant concentration, *cf.* (2.65). Thus, by studying

the initial conditions used within the published literature, the conflict arising between pinned boundary conditions and the initial speeds and stresses induced at the contact line is now discussed for two papers that model drainage of the tear film in an open eye.

The initial condition of Braun & Fitt (2003) is formed from quadratic menisci matched to a flat central profile, as mentioned in a prior footnote[3] on page 55. For such an initial condition, the vertical velocity (Braun & Fitt, 2003, equation 38) is simplified through the removal of the third and fourth derivatives of h to

$$v_{\text{BF}} = -\frac{y^2}{4} h_x \,,$$

where y measures non-dimensional distance from the ocular surface. Using parameter values taken from Table 1 and Figure 2 of Braun & Fitt (2003), the dimensional velocity and normal component of the stress tensor acting along the eyelid margin (in Braun & Fitt's Cartesian geometry) induced at the three-phase contact line are

$$\begin{aligned} v_{\text{BF}} &= -3.4 \times 10^{-3} \text{ m s}^{-1}, \quad \mathbf{T}_{\text{BF},yy} = 13.6 \text{ Pa}, \quad \text{at } x = L_{\text{BF}} \,, \\ v_{\text{BF}} &= 3.4 \times 10^{-3} \text{ m s}^{-1}, \quad \mathbf{T}_{\text{BF},yy} = 14.0 \text{ Pa}, \quad \text{at } x = -L_{\text{BF}} \,, \end{aligned} \tag{2.84}$$

where $x = L_{\text{BF}}$ denotes the lower eyelid, and $x = -L_{\text{BF}}$ the upper eyelid; note that the height profile induces an advancing (anterior) velocity at the upper eyelid. These velocities, on the order of millimetres per second, are induced within a meniscus that is modelled to be dimensionally $90\,\mu$m thick, hence they are significant to the tear-film dynamics in the meniscus regions. These speeds clearly contradict the Dirichlet boundary conditions enforced in the model of Braun & Fitt (2003), causing the menisci to be unnaturally held at a fixed height throughout simulations. The stresses induced at each contact line are positive, hence the initial condition yields a stress field that acts to push the contact lines in an anterior direction. Notably, this agrees with the predicted contact-line motion at the upper lid, but is at odds with the predicted motion at the lower lid. In each case the magnitude of the induced normal stress component is four orders of magnitude smaller than that of standard atmospheric pressure, thus its effect on the fluid flow would not be expected to be significant.

A similar contradiction is seen in the model of Maki *et al.* (2010a) and Maki *et al.* (2010b), which may be simplified by taking a cut through the sagittal plane of their three-dimensional eye to yield a two-dimensional profile. Approximations to the dimensional contact-line speeds and stresses can then be obtained for the two-dimensional analogue of the exponentially-decaying initial condition used within the model. Temporarily adopting Maki *et al.*'s coordinate system, the two-dimensional film profile is studied along the plane $x = 0$, with the y-axis (which runs between the eyelids along the ocular surface) shifted in order that $y = 0$ represents the centre of the plane (Maki *et al.*, 2010a, Figure 2). The z-axis is identified with the direction normal to the cornea. In the shifted y-coordinate, the initial condition (Maki *et al.*, 2010a, equation 9) is approximated by

$$h_{\text{MBHK}}(y) \;=\; (h_0 - 1)\exp\left[-\frac{0.775 - |y|}{x_0}\right] + 1\,, \qquad y \in [-0.755, 0.755]\,,$$

in which $h_0 = 13$ is the meniscus height, and $x_0 = 0.1$ is a parameter. The upper and lower eyelids are respectively positioned at $y = 0.755$ and $y = -0.755$. Parameter values from Maki *et al.* (2010a, Table 1) are used to calculate the dimensional contact-line velocities and stresses along the eyelid induced through this initial condition, giving

$$\begin{aligned} v_{\text{MBHK}} \;&=\; -5.4 \times 10^{-3}\ \text{m s}^{-1}, \quad \mathbf{T}_{\text{MBHK},\,zz} \;=\; 11.7\ \text{Pa}, \quad \text{at}\ \ y \;=\; -0.775\,, \\ v_{\text{MBHK}} \;&=\; -2.9 \times 10^{-3}\ \text{m s}^{-1}, \quad \mathbf{T}_{\text{MBHK},\,zz} \;=\; 11.9\ \text{Pa}, \quad \text{at}\ \ y \;=\; 0.775\,. \end{aligned} \tag{2.85}$$

Thus relatively large initial speeds of recession are induced in a meniscus of depth $65\,\mu$m. These speeds are, again, in conflict with the Dirichlet boundary condition enforced upon the system. Normal stresses of the same magnitude as those in (2.84) are predicted, and represent a force pushing the contact line in the anterior direction, in opposition to the initial velocity of the contact line.

The conflict between pinned contact lines and induced velocities arises through the scalings, (2.40) and (2.41), and the inherent assumptions made in the lubrication approximation. These cause the leading-order equations and boundary conditions (2.62) - (2.64) to yield a first-order differential equation for v, with a boundary condition enforced

at the ocular surface. Hence, there is no mechanism by which to specify the radial velocity at the contact lines, as this would require boundary conditions to be specified at $(\pm C, h)$. Results presented in Chapters 5 and 6 show that recessional contact-line velocities are observed in the initial dynamics of simulations of (2.71). However, the lack of pinning at the eyelid enables a swift relaxation of the menisci that dissipates the contact-line stresses manifest by the initial condition, before a slower, draining flow towards a steady state.

2.4.3 Mass conservation and steady states

The pair of coupled evolution equations (2.71) and (2.72) are obtained through substitution of the leading-order asymptotic solutions (2.65) to the equations of motion into equations derived from concepts of mass and surfactant conservation, respectively (2.7) and (2.16). In the absence of evaporation from the tear film, the mass of fluid in the system must remain constant as the tear-film dynamics act solely to redistribute the tears around the ocular surface under the influence of gravity and surface tension. Similarly, with no influx or efflux of surfactant defined, the total amount of lipid must be conserved. An estimate of the accuracy of the leading-order solutions to the equations of motion is therefore given by the calculation of the fluid mass and total amount of surfactant in the system at a given time.

The dimensional mass, m, of the tear film is obtained in cylindrical polar coordinates through the integral

$$m \;=\; \int_{\theta=-\delta}^{\delta} \int_{R=a}^{\chi} \hat{\rho}\, R\, dR\, d\theta\,,$$

in which $\hat{\rho}$ (kg m^{-2}) is an areal density[4]. Changing to non-dimensional, scaled marginal-surface coordinates via (2.35) and (2.40), and scaling the non-dimensional mass of fluid as $m = \hat{\rho} L d\, \tilde{m}$, the conservation of fluid mass is observed by calculating (with the tilde

[4]In a three-dimensional model, an additional integral of the volumetric density, ρ, along the lateral-medial axis of the eye would be required; $\hat{\rho}$ may be thought of as the simplified outcome of such an integral.

notation immediately dropped)

$$m \;=\; \frac{1}{C}\int_{\xi=-C}^{C} h + \frac{1}{2}\epsilon\delta h^2 \, d\xi \,, \tag{2.86}$$

at time $t > 0$, and comparing the computed value with the mass obtained from the initial condition (2.80). For simulations in which evaporation is not modelled, the change in mass is expected to be negligible.

The quantity of surfactant, m_Ψ, is calculated through an integral of the surfactant concentration along the free surface

$$m_\Psi \;=\; \int_{\theta=-\delta}^{\delta} \Psi(s)\, ds \,,$$

in which s is the dimensional length along the free surface of the tear film. In cylindrical polar coordinates the metric form for the length along the free surface is

$$ds^2 \;=\; dR^2 \,+\, R^2\, d\theta^2 \,, \qquad \text{at} \qquad R \,=\, \chi \,.$$

Asserting, through the thin-film lubrication approximation, that s acts primarily in the azimuthal direction, the length along the surface and the total amount of surfactant are respectively non-dimensionalised via $s = L\tilde{s}$, and $m_\Psi = \epsilon^2 \Psi_m \tilde{m}_\psi$. Changing to non-dimensional, scaled marginal-surface coordinates and dropping the tilde notation, the integral for the non-dimensional total amount of surfactant is

$$m_\psi \;=\; \frac{1}{C}\int_{\xi=-C}^{C} (1+\epsilon\delta h)\left(1 + \frac{\epsilon^2 C^2 h_\xi^2}{(1+\epsilon\delta h)^2}\right)^{1/2} \psi \, d\xi \,. \tag{2.87}$$

In addition to checking the accuracy of the evolution equations and their numerical discretization through the calculation of the integrals above, the large-time behaviour of the system may also be checked by obtaining the steady-state solutions to the differential equations, which the film-thickness and surfactant-concentration distributions will migrate towards as time increases. In the steady state, the time derivatives in (2.71) and (2.72) are set to zero, leaving a pair of coupled ordinary differential equations for

the steady-state distributions $h_\infty(\xi)$ and $\psi_\infty(\xi)$. Integrating these ordinary differential equations once with respect to ξ, the steady state solutions satisfy

$$\begin{aligned} h_\infty^2\left(\frac{h_\infty}{3}M\,+\,\frac{\Omega}{2}\right) \;&=\; \frac{k_1}{C} \quad \text{and} \\ \psi_\infty h_\infty\left(\frac{h_\infty}{2}M\,+\,\Omega\right) \;&=\; \frac{k_2}{C}\,, \end{aligned} \tag{2.88}$$

where k_1 and k_2 are constants of integration. These equations are valid throughout the region for which the partial differential equations are applicable, thus they apply at the eyelids, $\xi = \pm C$, where M and Ω are forced to vanish through the boundary conditions, (2.77) and (2.78). k_1 and k_2 are accordingly set to zero, and by asserting that both $h_\infty,\, \psi_\infty \neq 0$ at the eyelids, the steady states enforce that

$$M(\xi) \;=\; \Omega(\xi) \;=\; 0\,, \qquad \forall \xi \in [-C,\, C]\,,$$

which decouples the ordinary differential equations: $M = 0$ and boundary condition (2.76) yield a third-order differential equation for h_∞ that is strongly dependent upon the parameter δ that specifies the coordinate system, and; $\Omega = 0$ gives a homogeneous first-order differential equation for ψ_∞. The remaining boundary condition required to solve each differential equation is obtained through the appropriate mass integral, evaluated using the initial conditions. This is used to fix the arbitrary constant of integration in each case.

Equation (2.66a) shows that the differential equation governing the steady film profile is greatly simplified when the ocular surface is modelled as a Cartesian plane, $\delta = 0$. In this case, the differential equation is readily solved as a polynomial in ξ;

$$h_\infty(\xi) \;=\; \frac{-st}{6\alpha_0 \mathcal{A} C^3}\xi^3 + \frac{\cot\hat{\theta}}{2C^2}\xi^2 + \frac{st}{2\alpha_0\mathcal{A}C}\xi + \frac{1}{2}\left(m_0 - \frac{\cot\hat{\theta}}{3}\right)\,, \quad \delta = 0\,, \tag{2.89}$$

where m_0 is the mass integral (2.86) evaluated using the initial film profile, $h_0(\xi)$. In curvilinear coordinates, $\delta \neq 0$, the equation $M = 0$ is integrated once with respect to ξ to yield an inhomogeneous, linear, constant-coefficient, second-order ordinary differential

equation for h_∞ with boundary conditions given by (2.76), in which the first integration adds a constant that is fixed using the mass integral (2.86) of the initial condition. The steady-state height profile for a curved ocular substrate is

$$h_\infty(\xi) \;=\; c_1 \cos\left(\frac{\delta\xi}{C}\right) + c_2 \sin\left(\frac{\delta\xi}{C}\right) + \frac{st}{2\alpha_0 \mathcal{A}\delta^2 C}\,\xi\cos\left(\frac{\delta\xi}{C}\right) + c_3\,, \tag{2.90}$$

where

$$\begin{aligned} c_1 \;&=\; \frac{-(1+\epsilon\delta\, c_3)\cot\hat{\theta}}{\delta(\sin\delta + \epsilon\cos\delta\cot\hat{\theta})}\,, \quad \text{and} \\ c_2 \;&=\; \frac{st}{2\alpha_0\mathcal{A}\delta^2}\,\frac{\sin\delta - \delta^{-1}\cos\delta + \epsilon\cos\delta\cot\hat{\theta}}{\cos\delta - \epsilon\sin\delta\cot\hat{\theta}}\,. \end{aligned}$$

The constant c_3 is found by the solving the quadratic equation

$$f(c_3) \;=\; \left(\frac{1}{C}\int_{-C}^{C} h_\infty + \frac{1}{2}\epsilon\delta h_\infty^2\, d\xi\right) \;-\; m_0 \;=\; 0\,,$$

from which selecting the positive square root in the standard quadratic formula yields a physically-realistic steady-state film profile.

The steady-state surfactant concentration distribution is found through setting $\Omega = 0$ in (2.66b), yielding a constant value. With the total amount of surfactant conserved, the steady-state concentration is the total amount of surfactant calculated from the initial condition (2.83) divided by the length along the steady-state film profile, giving

$$\psi_\infty(\xi) \;\equiv\; \psi_\infty \;=\; \frac{\displaystyle\int_{\xi=-C}^{C}(1+\epsilon\delta h_0)\left(1+\frac{\epsilon^2C^2(dh_0/d\xi)^2}{(1+\epsilon\delta h_0)^2}\right)^{1/2}\psi_0\, d\xi}{\displaystyle\int_{\xi=-C}^{C}(1+\epsilon\delta h_\infty)\left(1+\frac{\epsilon^2C^2(dh_\infty/d\xi)^2}{(1+\epsilon\delta h_\infty)^2}\right)^{1/2} d\xi}\,. \tag{2.91}$$

With the initial conditions (2.80), and (2.82) or (2.83) known, and the geometry and boundary conditions defining the steady-state film profile (2.89) or (2.90), the uniform steady state ψ_∞ can be obtained from the initial set-up of the tear-flow problem.

2.5 Summary and discussion

The leading-order thin-film approximations to the tear-flow problem derived within this chapter form the basis for the studies in subsequent chapters. Meticulous care has been taken to employ an accurate *a priori* scaling when performing asymptotic expansions of the governing flow equations, ensuring that the expanded equations yield a uniformly-valid hierarchy of terms when realistic ophthalmic data are used in the IBVP.

Evolution equations (2.71) and (2.72) form a highly-nonlinear pair of coupled evolution equations respectively describing the changes to the non-dimensional thickness of the tear film and non-dimensional surfactant concentration. They are both derived from conservation equations (in the absence of evaporation from the bulk fluid; $E = 0$), whence any numerical scheme used to model these equations may be validated through monitoring the mass lost or gained by the system over time. The equations are augmented by naturally-motivated boundary conditions, derived through a consideration of the physical conditions in which the tear-flow problem finds itself. Boundary condition (2.76) is novel to the field of tear-flow modelling, and allows the fluid to slip along the eyelid margin where previous studies have pinned the menisci at the mucocutaneous junction; this pinning condition appears unphysical when modelling evaporative losses from the bulk fluid and, moreover, has been found to be in contradiction with the contact line velocities induced by the initial conditions of existing studies (*cf.* §2.4.2). Boundary conditions (2.77) and (2.78) are derived through the modelling of the static eyelids as impermeable barriers to the tear film. The system of equations is closed through the specification of initial conditions for the film height (2.80), and surfactant concentration (2.82) - (2.83), with various surfactant initial conditions allowing the study of different models arising from the ophthalmic literature.

A further novel development in the derivation of equations (2.71) and (2.72) and their associated boundary and initial conditions is the use of marginal-surface coordinates

(2.35) that allow the tear film to be modelled on a substrate of variable curvature, which curvature is controlled through the parameter δ. To the author's knowledge, all existing models for the tear film are derived using a Cartesian coordinate system, with the exception of Braun *et al.* (2012) in which the tear film is modelled using prolate spheroidal geometry. δ is treated as an order $\mathcal{O}(1)$ parameter throughout the asymptotic derivation of the coupled evolution equations, and the influence of the curved substrate is clearly observable in the leading-order expressions for the velocity and pressure fields (2.65). By allowing δ to tend to zero, the substrate is flattened to a Cartesian plane, whereas, with a realistic ocular radius of approximately 0.012 m (Singh *et al.*, 2006), an upper limit of $\delta = 5/12$ can be obtained from the constraint (2.36) to model the true curvature of the cornea.

The numerical methods that will be employed to solve the pair of coupled evolution equations (2.71) and (2.72) are respectively outlined and validated in Chapters 3 and 4. To study the 'isolated' tear flow (i.e. in the absence of a variable surfactant concentration), (2.71) is solved in Chapter 5 and subjected to a variety of boundary and initial conditions in order to demonstrate their influence on the dynamics of the tear film. The effects of substrate curvature and evaporation are also investigated using the isolated system of Chapter 5. Finally, the effects of the overlying surfactant layer are observed in Chapter 6 by solving the full coupled system with different initial conditions for the surfactant concentration (2.82) and (2.83) employed to emulate behaviour observed in the ophthalmic literature. A comparison of the results from Chapters 5 and 6 will allow the non-trivial effects of the lipid surfactant on the dynamics of the tear film to be observed.

Chapter 3

Numerical Methods

Numerical methods are discussed for the simulation of the nonlinear pair of coupled evolution equations (2.71) and (2.72). The equations are solved in a non-periodic, bounded spatial domain that is discretized using Chebyshev spectral methods to convert the partial differential equations into a system of first-order ordinary differential equations in time. A fourth-order, explicit Runge-Kutta time-stepping algorithm for coupled systems of equations is employed to advance the simulations in time. It is noteworthy that information on the specific details of implementation of numerical schemes employed in the published mathematical literature on the tear film is scant, even non-existent. This is not only unhelpful because of the well-known difficulties associated with solving *non*-periodic IBVPs, but also it moreover precludes completely any possibility of comparison with the results presently obtained and, indeed, the absence of implementational detail potentially undermines confidence in the published results. Thus motivated, it is an aim of this thesis that the numerical algorithms used herein are manifestly clear to the reader, in order that they may be readily reproduced for the purposes of comparison and verification.

The structure of this chapter is as follows. A summary of the theory of approximating aperiodic functions using Chebyshev spectral methods is presented, and differentiation matrices for the numerical approximation of second, third, and fourth derivatives are

derived using novel computer-algebra techniques. Implementation of the boundary conditions (2.76), (2.77) and (2.78) is discussed, requiring the as-yet-undefined constant C to be prescribed, and the development of an appropriate (novel) boundary condition for the surfactant concentration, ψ. To evaluate test quantities obtained using laws of conservation in §2.4.3, a process of integration using spectral methods is prescribed in §3.3. Finally, the time-stepping algorithm is briefly outlined.

The notation utilised in this chapter is as follows: approximations of the function $u(x,t)$ are augmented with a tilde; vectors or matrices that have had entries removed are augmented with a hat; upper-case subscripts are used to denote functions that depend upon the number of nodes employed in the spatial discretization; lower-case subscripts are used as indices that label components of a particular vector or matrix; complete vectors and matrices are respectively represented by emboldened lower- and upper-case letters; square-bracketed superscripts augmenting vectors and matrices denote their dimensions; differentiation with respect to spatial coordinate x is represented by superscript parentheses containing a number denoting the order of the derivative; differentiation with respect to time, t, is represented by a superscript dot, and; the bounds of incremented indices are annotated as $i = X(Y)Z$ where X is the lowest value, Y the increment, and Z the highest value.

3.1 Chebyshev spectral methods

Spectral methods are used in a diverse range of mathematical, engineering and physical applications (Boyd, 2001; Canuto *et al.*, 2006, and references therein). The popularity of spectral methods is derived from their high-order convergence properties when modelling infinitely-differentiable functions. Furthermore, spectral methods are global in nature: that is, they use the *full* spatial domain to compute an approximation to the *local* solution using a globally-defined orthonormal basis, and hence they are seen as memory-

minimizing (Boyd, 2001, page 8) when compared with other methods such as finite differences or finite elements.

3.1.1 Cardinal function and differentiation matrix

The bounded spatial domain is scaled onto the finite interval $x \in [-1, 1]$, which itself is discretized with a set of as-yet-undefined nodes $\{x_j\}$ for $j = 0(1)N$, with $N \in \mathbb{N}$. The values of the function $u(x)$[1] are known at the nodes, yielding a data set $\{u_j\} = \{u(x_j)\}$ from which the approximation may be obtained. To interpolate the nodal data set, a cardinal function, $C_j(x)$, is constructed using a basis of polynomial functions, which, in this case, are chosen to be Chebyshev polynomials due to their role in near-minimax interpolation (Atkinson, 1989); the N^{th} Chebyshev polynomial of the first kind is given by

$$T_N(x) \;=\; \cos N\theta\,, \qquad \theta \;=\; \cos^{-1} x\,, \qquad N \geq 0\,. \tag{3.1}$$

The Chebyshev polynomials are bounded: $|T_N(x)| \leq 1$, from which the nodes are defined at the $N + 1$ extrema of the Chebyshev polynomials located at

$$x_j \;=\; \cos\frac{j\pi}{N}\,, \qquad j = 0(1)N\,. \tag{3.2}$$

This set of nodes $\{x_j\}$, more commonly known as a Gauss-Lobatto grid, may be visualized as the projection of points located at equidistant angles around a semi-circular arc onto the straight line joining the two ends of the arc. This means the nodes are non-uniformly distributed along the line, their density increasing towards the boundaries, $x = \pm 1$.

For a given N, the cardinal-function interpolation of the function $u(x)$ is defined to be

[1] For simplicity, u is defined as a function of x only during the derivation of the spatial discretization. The spatial and temporal discretization processes are fully independent of each other, thus the function $u(x)$ defined here may be thought of as $u(x, t)$ at a fixed time t.

$$\tilde{u}_N(x) \;=\; \sum_{j=0}^{N} C_j(x)\, u(x_j)\,, \tag{3.3}$$

with (Boyd, 2001)

$$C_j(x) \;=\; \frac{(-1)^{j+1}\,(1-x^2)\,T'_N(x)}{(1+\delta_{j0}+\delta_{jN})N^2\,(x-x_j)}\,, \qquad j = 0(1)N\,, \tag{3.4}$$

wherein δ_{ik} is the Kronecker symbol, defined as

$$\delta_{ik} \;=\; \begin{cases} 1 & \text{if } i = k\,, \\ 0 & \text{otherwise}\,. \end{cases}$$

The cardinal function (3.4) requires some explanation: the product $(1-x^2)T'_N(x)$ vanishes at *all* nodes because $T'_N(x_j) = 0$ for $j = 1(1)N-1$, and $(1-x^2)$ vanishes at the external points $x = \pm 1$, which are extrema but not turning points of $T_N(x)$; the remaining terms ensure that the cardinal function has the filtering property

$$C_j(x_i) \;=\; \delta_{ij}\,, \tag{3.5}$$

whence the interpolant $\tilde{u}_N$ in (3.3) is exact at all nodes. Derivatives of the function $u(x)$ are approximated by differentiating (3.3), thus the first derivative is approximated by

$$\frac{d}{dx}\Big(u(x)\Big) \;\approx\; \tilde{u}_N^{(1)}(x) \;=\; \sum_{j=0}^{N} C_j^{(1)}(x) u(x_j)\,, \tag{3.6}$$

with higher derivatives of u approximated by the corresponding derivative of C_j (3.4).

The discrete nature of the numerical scheme enforces the differential equations (2.71) and (2.72) to be evaluated and incremented forward in time at only the nodes $\{x_i\}$. By representing the set of interpolation data points $\{u(x_i)\}$ as a vector, the vector of approximate derivative values at each of the nodes, $\tilde{u}_i^{(1)}$, may be obtained from (3.6) as a matrix-vector product through substituting $x = x_i$ into the derivative of the cardinal function, yielding

$$\tilde{u}_i^{(1)} \;=\; D_{ij}^{(1)} u_j\,, \qquad \text{where} \qquad D_{ij}^{(1)} \;\equiv\; C_j^{(1)}(x_i)\,, \tag{3.7}$$

in which repeated suffices imply summation from $j = 0(1)N$. $\mathbf{D}^{(1)}$ is called the first-order Chebyshev differentiation matrix and its entries can be found in texts on spectral methods (see, for example, Trefethen, 2000). As shown in (3.7), the entries of $\mathbf{D}^{(1)}$ are obtained through making the substitution $x = x_i$ in the derivative of (3.4). Taylor series expansions are required to calculate the leading-order terms of $C_j^{(1)}(x_i)$ in the diagonal cases when $i = j$, and when populating the top-left and bottom-right entries, $i = j \in \{0, N\}$. The entries of the first-order Chebyshev differentiation matrix are readily determined to be

$$D_{ij}^{(1)} = \begin{cases} \dfrac{1+2N^2}{6}, & i = j = 0, \\ -\dfrac{1+2N^2}{6}, & i = j = N, \\ \dfrac{-x_j}{2\left(1-x_j^2\right)}, & i = j,\ i = 1(1)N-1, \\ \dfrac{(1+\delta_{i0}+\delta_{iN})}{(1+\delta_{j0}+\delta_{jN})}\dfrac{(-1)^{i+j}}{x_i - x_j}, & i \neq j. \end{cases} \tag{3.8}$$

By discretizing the process of differentiation into a matrix-vector multiplication, higher derivatives of the function $u(x)$ may be approximated through repeatedly multiplying the vector of function values, $\mathbf{u}$, by the differentiation matrix

$$\tilde{\mathbf{u}}^{(m)} = \left(\mathbf{D}^{(1)}\right)^m \mathbf{u},$$

hence higher-order differentiation matrices can be constructed by using powers of (3.7):

$$D_{ij}^{(m)} = \left[\left(\mathbf{D}^{(1)}\right)^m\right]_{ij}. \tag{3.9}$$

Alternatively, explicit forms of the entries of higher-order differentiation matrices may be obtained through the repeated differentiation and expansion of (3.4) around $x = x_i$. With a view to minimizing the errors associated with the repeated matrix multiplication implicit in (3.9), these explicit forms are now investigated.

3.1.2 Higher-order differentiation matrices

Motivated by the aim of obtaining the most accurate possible fourth-order numerical differentiation in the modelling of the film-thickness evolution equation (2.71), the explicit forms of the Chebyshev differentiation matrices up to fourth order are now derived. The explicit form of the second-order differentiation matrix is well-known, and can be found in Canuto *et al.* (2006); however, no formulæ for the elements of the third- and fourth-order differentiation matrices appear to exist in the prior literature.

Differentiating the cardinal function (3.4) twice with respect to x and setting $x = x_i$, the entries of the second-order differentiation matrix can be obtained. In a similar procedure to that used to derive the entries of the first-order Chebyshev differentiation matrix, Taylor series expansions are required to calculate the entries on the main diagonal, and the first and last rows of the matrix. The explicit forms of the entries are

$$D_{ij}^{(2)} = \begin{cases} \dfrac{N^4-1}{15}\,, & i=j=0 \text{ and } i=j=N\,, \\ \dfrac{x_j^2\left(N^2-1\right)-N^2-2}{3\left(1-x_j^2\right)^2}\,, & i=j\,,\ i=1(1)N-1\,, \\ \dfrac{2(-1)^j}{1+\delta_{jN}}\left(\dfrac{2N^2+1}{3\left(1-x_j\right)}-\dfrac{2}{\left(1-x_j\right)^2}\right), & i\neq j\,,\ i=0\,, \\ \dfrac{2(-1)^{j+N}}{1+\delta_{j0}}\left(\dfrac{2N^2+1}{3\left(1+x_j\right)}-\dfrac{2}{\left(1+x_j\right)^2}\right), & i\neq j\,,\ i=N\,, \\ \dfrac{(-1)^{i+j+1}}{1+\delta_{j0}+\delta_{jN}}\left(\dfrac{x_i}{\left(1-x_i^2\right)\left(x_i-x_j\right)}+\dfrac{2}{\left(x_i-x_j\right)^2}\right), & \\ & i\neq j\,,\ i=1(1)N-1\,. \end{cases} \tag{3.10}$$

Again differentiating the cardinal function and expanding using Taylor series, the third-order differentiation matrix is populated with entries, hitherto unpresented, given by

$$
D_{ij}^{(3)} = \begin{cases}
\dfrac{2N^6 - 7N^4 - 7N^2 + 12}{210}, & i = j = 0, \\
-\dfrac{2N^6 - 7N^4 - 7N^2 + 12}{210}, & i = j = N, \\
\dfrac{x_j\left(2x_j^2\left(N^2-1\right) - 2N^2 - 13\right)}{4\left(1-x_j^2\right)^3}, & i = j,\ i = 1(1)N-1, \\
\dfrac{2(-1)^j}{1+\delta_{jN}}\left(\dfrac{N^4-1}{5\left(1-x_j\right)} - \dfrac{2N^2+1}{\left(1-x_j\right)^2} + \dfrac{6}{\left(1-x_j\right)^3}\right), & i \neq j,\ i = 0, \\
\dfrac{2(-1)^{N+j+1}}{1+\delta_{j0}}\left(\dfrac{N^4-1}{5\left(1+x_j\right)} - \dfrac{2N^2+1}{\left(1+x_j\right)^2} + \dfrac{6}{\left(1+x_j\right)^3}\right), & i \neq j,\ i = N, \\
\dfrac{(-1)^{i+j}}{1+\delta_{j0}+\delta_{jN}}\left(\dfrac{x_i^2\left(N^2-1\right) - N^2 - 2}{\left(1-x_i^2\right)^2\left(x_i - x_j\right)}\right. & \\
\qquad \left. + \dfrac{3\,x_i}{\left(1-x_i^2\right)\left(x_i-x_j\right)^2} + \dfrac{6}{\left(x_i-x_j\right)^3}\right), & i \neq j,\ j = 1(1)N-1.
\end{cases}
\tag{3.11}
$$

Finally, taking the fourth derivative of (3.4), the entries in the fourth-order Chebyshev differentiation matrix are the newly determined

$$
D_{ij}^{(4)} = \begin{cases}
\dfrac{N^8 - 12N^6 + 21N^4 + 62N^2 - 72}{945}, & i = j = 0 \text{ and } i = j = N, \\
\dfrac{N^4\left(1-x_j^2\right)^2 - 5N^2\,x_j^2\left(1-x_j^2\right) - \left(6x_j^4 + 83x_j^2 + 16\right)}{5\left(1-x_j^2\right)^4}, & \\
\qquad\qquad i = j,\ i = 1(1)N-1, & \\
\dfrac{4(-1)^j}{1+\delta_{jN}}\left(\dfrac{\left(N^4-5N^2+4\right)\left(2N^2+3\right)}{105\left(1-x_j\right)} - \dfrac{2\left(N^4-1\right)}{5\left(1-x_j\right)^2}\right. & \\
\qquad \left. + \dfrac{2\left(2N^2+1\right)}{\left(1-x_j\right)^3} - \dfrac{12}{\left(1-x_j\right)^4}\right), & i \neq j,\ i = 0, \\
\dfrac{4(-1)^{j+N}}{1+\delta_{j0}}\left(\dfrac{\left(N^4-5N^2+4\right)\left(2N^2+3\right)}{105\left(1+x_j\right)} - \dfrac{2\left(N^4-1\right)}{5\left(1+x_j\right)^2}\right. & \\
\qquad \left. + \dfrac{2\left(2N^2+1\right)}{\left(1+x_j\right)^3} - \dfrac{12}{\left(1+x_j\right)^4}\right), & i \neq j,\ i = N, \\
\qquad \vdots &
\end{cases}
$$

$$D_{ij}^{(4)} \;=\; \begin{cases} \dfrac{(-1)^{i+j+1}}{1+\delta_{j0}+\delta_{jN}} \left(\dfrac{-x_i\Big(2x_i^2\,(N^2-1)-2N^2-13\Big)}{\left(1-x_i^2\right)^3\,(x_i-x_j)} + \dfrac{12\,x_i}{\left(1-x_i^2\right)\,(x_i-x_j)^3} \right. \\ \qquad \left. + \dfrac{4\Big(x_i^2\,(N^2-1)-N^2-2\Big)}{\left(1-x_i^2\right)^2\,(x_i-x_j)^2} + \dfrac{24}{(x_i-x_j)^4} \right), \; i \neq j, \; i = 1(1)N-1. \end{cases} \tag{3.12}$$

The process of differentiating (3.4) and expanding may be continued *ad infinitum* to derive differentiation matrices of all orders. However, as the highest order derivative in (2.71) and (2.72) is of fourth-order, matrices up to only this order have been derived. The workings required to obtain the entries of the differentiation matrices are readily carried out using the algebraic manipulator MAPLE.

The accuracy of the derived matrices (3.10) - (3.12) is tested against repeated action of the first-order Chebyshev differentiation matrix (3.8) in §4.1.1. Before such tests are carried out, the accuracy of the differentiation matrices may first be improved by making use of trigonometric identities.

3.1.3 Alternative formulations

In addition to the derivation of explicit forms of the Chebyshev differentiation matrices, the accuracy of the numerical scheme may be improved by taking steps to reduce the round-off error introduced through the explicit definition of the Chebyshev nodes and differentiation matrices. Following Weidemann & Reddy (2000), the set of Chebyshev nodes (3.2) are redefined using the trigonometric identity

$$\cos\theta \;=\; \sin\left(\frac{\pi}{2}-\theta\right)$$

to

$$x_j \;=\; \sin\left[\frac{\pi}{2N}(N-2j)\right], \qquad j = 0(1)N\,. \tag{3.13}$$

The significance of this substitution is not immediately obvious; however, in floating-point arithmetic it yields a set of collocation nodes $\{x_j\}$ that are perfectly symmetrically

spaced about the origin, which is not the case when employing (3.2). The round-off error in the entries of the Chebyshev differentiation matrices can be further reduced by noting that the denominators in the third and fourth lines of, for example, (3.8), contain differences of quantities that are nearly equal for certain values of i and j. To improve accuracy, the following identities are used to replace differences of trigonometric terms with multiplications (see Canuto *et al.*, 2006):

$$\begin{aligned} x_i - x_j &= \cos\frac{i\pi}{N} - \cos\frac{j\pi}{N} &&= 2\sin\left[\frac{(i+j)\pi}{2N}\right]\sin\left[\frac{(j-i)\pi}{2N}\right], \\ 1 - x_j &= 1 - \cos\frac{j\pi}{N} &&= 2\sin^2\frac{j\pi}{2N}, \\ 1 + x_j &= 1 + \cos\frac{j\pi}{N} &&= 2\cos^2\frac{j\pi}{2N}. \end{aligned} \tag{3.14}$$

The resulting form of the first-order Chebyshev differentiation matrix (3.8) is

$$D^{(1)}_{i,j} = \begin{cases} \dfrac{1+2N^2}{6}, & i = j = 0, \\ -\dfrac{1+2N^2}{6}, & i = j = N, \\ \dfrac{-x_j}{2\sin^2(j\pi/N)}, & i = j,\ i = 1(1)N-1, \\ \dfrac{(1+\delta_{i0}+\delta_{iN})}{(1+\delta_{j0}+\delta_{jN})}\dfrac{(-1)^{i+j}}{2\,\sin[(i+j)\pi/2N]\,\sin[(j-i)\pi/2N]}, & i \neq j. \end{cases} \tag{3.15}$$

The identities (3.14) are similarly substituted into the higher-order Chebyshev differentiation matrices (3.10) - (3.12) to obtain the alternative form of these matrices. Due to their cumbersome nature, presentation of these is deferred to Appendix A.

3.2 Implementation of boundary conditions

The enforcement of the boundary conditions is a subtle and crucial aspect of the numerical scheme that is barely mentioned in any of the previous related ophthalmic literature[2].

[2]Maki *et al.* (2010b, Appendix 3) is a notable exception.

The boundary conditions (2.76) - (2.78) must be converted into their discrete forms, and through manipulation of the entries of the relevant differentiation matrices, the conditions are applied with spectral accuracy to the profiles obtained numerically at each time-step. Because this model employs only Neumann boundary conditions, the values of the film-thickness and surfactant-concentration distributions at *all* nodes between *and including* the simulated eyelid positions must be found using the evolution equations (2.71) and (2.72). In the absence of Dirichlet boundary conditions, the fourth-order spatial derivatives in (2.71) therefore warrant the addition of four fictitious 'ghost' nodes outside the solution domain of the evolution equations (Smith, 1985). The values of h and ψ at these ghost nodes may then be extrapolated from the interior (i.e. physical) data as shown below.

3.2.1 Ghost-node scalings and methods

Because all physical and ghost nodes are restricted to the Chebyshev interval, $x \in [-1, 1]$, the eyelid locations are symmetrically positioned at $x_2 = C$ and $x_{N-2} = -x_2$. This yields the definition

$$C \equiv \cos\frac{2\pi}{N}, \tag{3.16}$$

which specifies the constant that appears in (2.40) and reoccurs through each subsequent differentiation with respect to ξ. The ghost nodes are located outside $x \in [-C, C]$, occupying positions x_0, x_1, x_{N-1} and x_N.

At each time-step, the evolution equations must be temporally integrated at the Chebyshev nodes using the complete film-thickness and surfactant-concentration distributions at the start of the time-step. The boundary conditions are then enforced at $x = \pm C$, and spectral extrapolation determines h and ψ at the ghost nodes using the newly-obtained interior profiles for h and ψ. To demonstrate the method, the boundary-condition procedure for h is outlined briefly below for the unknown function $u(x)$. A

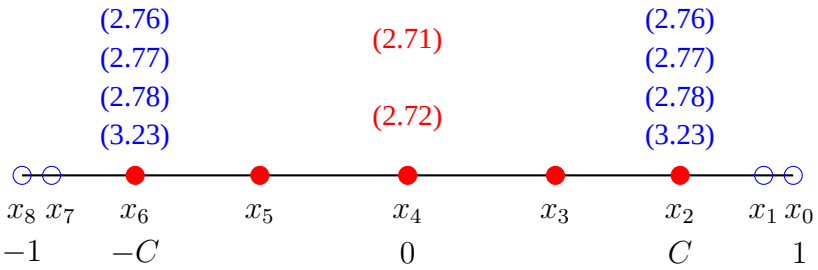

Figure 3.1: The spatial distribution of the Gauss-Lobatto grid (3.2) when $N = 8$. Filled circles denote physical data points, and empty circles represent ghost nodes. Within a time-step, the evolution equations are solved at each of the colour-coded nodes to determine h and ψ. The boundary conditions are then applied at points $x_2 = C$ and $x_6 = -C$, and spectral extrapolation from the newly-obtained physical data yields the ghost-node values. The additional boundary condition (3.23) is discussed in §3.2.2.

sketch of the computational domain is given in Figure 3.1.

The calculation of all nodal derivatives occurs via a matrix-vector multiplication. Since the boundary conditions (2.76) and (2.77) respectively specify the first and third derivatives, and are enforced at nodes x_2 and x_{N-2}, the entries in the second and $(N-2)^{\text{th}}$ rows of both the first- and third-order Chebyshev differentiation matrices are isolated. These entries are subdivided into those that multiply the known interior values (columns 2 to $N-2$) and those that multiply the ghost-node data (columns 0, 1, $N-1$, and N). The data set $\{u_j\}$ is also split into its interior and ghost values, and the partitioned entries assembled into the following matrix-vector system, in which each of the four rows represents one of the four boundary conditions in (2.76) and (2.77)

$$\widehat{\mathbf{D}}_{\text{GHOST}}^{[4\times 4]}\,\hat{\mathbf{u}}_{\text{GHOST}}^{[4\times 1]} + \widehat{\mathbf{D}}_{\text{INNER}}^{[4\times(N-3)]}\,\hat{\mathbf{u}}_{\text{INNER}}^{[(N-3)\times 1]} = \mathbf{b}^{[4\times 1]}\,, \tag{3.17}$$

wherein the vectors are defined as

$$\hat{\mathbf{u}}_{\text{GHOST}}^{[4\times 1]} = (\tilde{u}_0,\, \tilde{u}_1,\, \tilde{u}_{N-1},\, \tilde{u}_N)^T\,, \tag{3.18a}$$

$$\hat{\mathbf{u}}_{\text{INNER}}^{[(N-3)\times 1]} = (\tilde{u}_2,\, \cdots,\, \tilde{u}_{N-2})^T\,, \tag{3.18b}$$

and the entries of $\mathbf{b}$ are obtained from the boundary conditions (2.76) and (2.77) as

$$\mathbf{b}^{[4\times1]} = \begin{pmatrix} (1+\epsilon\delta\tilde{u}_2)\cot(\theta)/C & ((2.76) \text{ at } x=C) \\ -(1+\epsilon\delta\tilde{u}_{N-2})\cot(\theta)/C & ((2.76) \text{ at } x=-C) \\ -st\cos(\delta)/(\alpha\mathcal{A}C^3) - (1+\epsilon\delta\tilde{u}_2)\cot(\theta)/C^3 & ((2.77) \text{ at } x=C) \\ -st\cos(\delta)/(\alpha\mathcal{A}C^3) + (1+\epsilon\delta\tilde{u}_{N-2})\cot(\theta)/C^3 & ((2.77) \text{ at } x=-C) \end{pmatrix}. \tag{3.18c}$$

The entries of the boundary condition matrices are

$$\widehat{\mathbf{D}}^{[4\times4]}_{\text{GHOST}} = \begin{bmatrix} D^{(1)}_{2,0} & D^{(1)}_{2,1} & D^{(1)}_{2,N-1} & D^{(1)}_{2,N} \\ D^{(1)}_{N-2,0} & D^{(1)}_{N-2,1} & D^{(1)}_{N-2,N-1} & D^{(1)}_{N-2,N} \\ D^{(3)}_{2,0} & D^{(3)}_{2,1} & D^{(3)}_{2,N-1} & D^{(3)}_{2,N} \\ D^{(3)}_{N-2,0} & D^{(3)}_{N-2,1} & D^{(3)}_{N-2,N-1} & D^{(3)}_{N-2,N} \end{bmatrix} \tag{3.19a}$$

and

$$\widehat{\mathbf{D}}^{[4\times(N-3)]}_{\text{INNER}} = \begin{bmatrix} D^{(1)}_{2,2} & D^{(1)}_{2,3} & \cdots & D^{(1)}_{2,N-3} & D^{(1)}_{2,N-2} \\ D^{(1)}_{N-2,2} & D^{(1)}_{N-2,3} & \cdots & D^{(1)}_{N-2,N-3} & D^{(1)}_{N-2,N-2} \\ D^{(3)}_{2,2} & D^{(3)}_{2,3} & \cdots & D^{(3)}_{2,N-3} & D^{(3)}_{2,N-2} \\ D^{(3)}_{N-2,2} & D^{(3)}_{N-2,3} & \cdots & D^{(3)}_{N-2,N-3} & D^{(3)}_{N-2,N-2} \end{bmatrix}. \tag{3.19b}$$

With (3.17) thus configured, the first and second rows enforce boundary condition (2.76) and the third and fourth rows enforce boundary condition (2.77); odd and even rows respectively represent boundary conditions at $x = C$ and $x = -C$. The unknown data values at the ghost nodes are obtained by inverting (3.17); with matrix dimensions omitted, this gives

$$\hat{\mathbf{u}}_{\text{GHOST}} = \widehat{\mathbf{D}}^{-1}_{\text{GHOST}}\,\mathbf{b} - \widehat{\mathbf{D}}^{-1}_{\text{GHOST}}\,\widehat{\mathbf{D}}_{\text{INNER}}\,\hat{\mathbf{u}}_{\text{INNER}}\,, \tag{3.20}$$

upon which all nodal data in $[-1, 1]$ has been updated, and Chebyshev differentiation can be performed at the next time-step, the process being repeated as required.

The process outlined above yields data at the four ghost nodes that accommodate the four boundary conditions for the fourth-order evolution equation (2.71). A slight

complication arises because the *same* node set has to be employed to integrate the second-order evolution equation (2.72), which therefore only requires two ghost nodes to accommodate its Neumann boundary condition (2.78). Thus to avoid an under-determined system, the values of ψ at the remaining ghost nodes must be specified via additional 'ghost boundary conditions'.

3.2.2 Ghost boundary condition for ψ

The required ghost boundary condition for ψ must be compatible with the natural boundary condition (2.78), which specifies a vanishing surfactant-concentration gradient at the eyelids, $x = \pm C$. The specification of a fictitious Dirichlet condition is unfeasible as the fixed ghost value may vary significantly from the physical value at the eyelid, creating a large gradient within the ghost region. As the evolution equation (2.72) is second-order in space, the additional boundary condition is enforced on the gradient of ψ at the nodes located immediately outside the simulated eyelid positions by proposing that

$$\tilde{\psi}_1^{(1)} \propto -\tilde{\psi}_3^{(1)} \qquad \text{and} \qquad \tilde{\psi}_{N-1}^{(1)} \propto -\tilde{\psi}_{N-3}^{(1)}\,, \tag{3.21}$$

which is compatible with the natural boundary condition (2.78), and is tantamount to modelling a local maximum or minimum in ψ at the eyelids through the changing sign of the concentration gradient on either side of each boundary.

The surfactant concentration is approximated over each of the three-node intervals that straddle the eyelids, $[x_3,\, x_2,\, x_1]$ and $[x_{N-1},\, x_{N-2},\, x_{N-3}]$, using a quadratic polynomial interpolant

$$\tilde{\psi}(x) = a_0 + a_1 x + a_2 x^2\,.$$

The ghost boundary condition is obtained using the same method at each eyelid, which method is illustrated for the subinterval over $x = x_2$. First, boundary condition (2.78) is employed to solve for a_1 in terms of a_2, yielding

$$a_1 = -2a_2 x_2\,.$$

Then by evaluating $\tilde{\psi}^{(1)}$ at nodes x_1 and x_3, an expression for a_2 may be obtained from each location. Equating these expressions, and defining the constant

$$c \equiv \frac{x_1 - x_2}{x_3 - x_2} = \frac{x_{N-1} - x_{N-2}}{x_{N-3} - x_{N-2}}, \tag{3.22}$$

the additional boundary conditions are found to be

$$\tilde{\psi}_1^{(1)} = c\,\tilde{\psi}_3^{(1)}, \qquad \text{and} \qquad \tilde{\psi}_{N-1}^{(1)} = c\,\tilde{\psi}_{N-3}^{(1)}, \tag{3.23}$$

in which the fractional constant c is negative, satisfying the original proposal for the ghost boundary condition (3.21).

With the additional boundary condition thus obtained, a matrix-vector system akin to (3.17) is created for (2.78) and (3.23) as

$$\widehat{\mathbf{D}}_{\psi,\text{GHOST}}^{[4\times4]}\,\hat{\boldsymbol{\psi}}_{\text{GHOST}}^{[4\times1]} + \widehat{\mathbf{D}}_{\psi,\text{INNER}}^{[4\times(N-3)]}\,\hat{\boldsymbol{\psi}}_{\text{INNER}}^{[(N-3)\times1]} = \mathbf{b}_{\psi}^{[4\times1]}, \tag{3.24}$$

in which $\hat{\boldsymbol{\psi}}_{\text{GHOST}}$ and $\hat{\boldsymbol{\psi}}_{\text{INNER}}$ are respectively analogous to (3.18a) and (3.18b), and $\mathbf{b}_{\psi} = \mathbf{0}$ because (2.78) yields a vanishing gradient at the eyelids and (3.23) is expressed using only differentiation matrix entries. The entries of the boundary condition matrices are

$$\widehat{\mathbf{D}}_{\psi,\text{GHOST}}^{[4\times4]} = \begin{bmatrix} D_{2,0}^{(1)} & D_{2,1}^{(1)} & D_{2,N-1}^{(1)} & D_{2,N}^{(1)} \\ D_{N-2,0}^{(1)} & D_{N-2,1}^{(1)} & D_{N-2,N-1}^{(1)} & D_{N-2,N}^{(1)} \\ D_{1,0}^{(1)} - cD_{3,0}^{(1)} & D_{1,1}^{(1)} - cD_{3,1}^{(1)} & D_{1,N-1}^{(1)} - cD_{3,N-1}^{(1)} & D_{1,N}^{(1)} - cD_{3,N}^{(1)} \\ D_{N-1,0}^{(1)} - cD_{N-3,0}^{(1)} & D_{N-1,1}^{(1)} - cD_{N-3,1}^{(1)} & D_{N-1,N-1}^{(1)} - cD_{N-3,N-1}^{(1)} & D_{N-1,N}^{(1)} - cD_{N-3,N}^{(1)} \end{bmatrix} \tag{3.25a}$$

and

$$\widehat{\mathbf{D}}_{\psi,\text{INNER}}^{[4\times(N-3)]} = \begin{bmatrix} D_{2,2}^{(1)} & \cdots & D_{2,N-2}^{(1)} \\ D_{N-2,2}^{(1)} & \cdots & D_{N-2,N-2}^{(1)} \\ D_{1,2}^{(1)} - cD_{3,2}^{(1)} & \cdots & D_{1,N-2}^{(1)} - cD_{3,N-2}^{(1)} \\ D_{N-1,2}^{(1)} - cD_{N-3,2}^{(1)} & \cdots & D_{N-1,N-2}^{(1)} - cD_{N-3,N-2}^{(1)} \end{bmatrix}. \tag{3.25b}$$

3.3 Spectral integration

The spectral differentiation methods described in §3.1 for the solution of (2.71) and (2.72) can be adapted to provide relatively cost-free numerical integration of the free-surface profile and the surfactant-concentration distribution. Hence an efficient and accurate computation of the bulk fluid mass (2.86) and the total amount of lipid surfactant (2.87) can be made as the partial differential equations are integrated. This data gives an insight into the accuracy of (2.71) and (2.72), which are leading-order approximations to the governing equations in §2.2.1. Each of the integrals is of the form

$$I \;=\; \int_{x=-C}^{C} f(x)\,dx\,, \tag{3.26}$$

allowing the method of spectral integration outlined in Trefethen (2000) to be amended to approximate such an integral. Differentiating both sides of (3.26), the integral may be restated as an ordinary differential equation for an unknown function $u(x)$

$$u'(x) \;=\; f(x)\,, \qquad u(-C) \;=\; 0\,, \tag{3.27}$$

from which the value of the integral (3.26) is given by $I \;=\; u(C)$. The differential equation is discretized on the Chebyshev collocation nodes (3.13) as

$$\mathbf{D}^{(1)}\,\tilde{\mathbf{u}} \;=\; \mathbf{f}\,, \tag{3.28}$$

wherein $\tilde{u}_2(\equiv \tilde{u}(C))$ is the spectral approximation $\tilde{I}$ of the integral I sought in (3.26).

The boundary condition of (3.27) enforces that $\tilde{u}_{N-2} = 0$. This means that the $(N-2)^{\text{th}}$ column of $\mathbf{D}^{(1)}$ has no effect on (3.28) as its entries are all multiplied by zero, and the $(N-2)^{\text{th}}$ row of $\mathbf{D}^{(1)}$ represents an equation that does not require solution, the unknown $\tilde{u}_{N-2}$ having been specified by (3.27) with a *homogeneous* Dirichlet boundary condition. To impose the boundary condition, the $(N-2)^{\text{th}}$ column and row of $\mathbf{D}^{(1)}$ are removed to create an $N \times N$ matrix

$$\widehat{\mathbf{D}}^{(1)} \;=\; \begin{bmatrix} D^{(1)}_{0,0} & \cdots & D^{(1)}_{0,N-3} & D^{(1)}_{0,N-1} & D^{(1)}_{0,N} \\ \vdots & \ddots & \vdots & \vdots & \vdots \\ D^{(1)}_{N-3,0} & \cdots & D^{(1)}_{N-3,N-3} & D^{(1)}_{N-3,N-1} & D^{(1)}_{N-3,N} \\ D^{(1)}_{N-1,0} & \cdots & D^{(1)}_{N-1,N-3} & D^{(1)}_{N-1,N-1} & D^{(1)}_{N-1,N} \\ D^{(1)}_{N,0} & \cdots & D^{(1)}_{N,N-3} & D^{(1)}_{N,N-1} & D^{(1)}_{N,N} \end{bmatrix}, \tag{3.29}$$

and similarly the $(N-2)^{\text{th}}$ entries of $\tilde{\mathbf{u}}$ and $\mathbf{f}$ are removed, yielding the system

$$\widehat{\mathbf{D}}^{(1)}\,\hat{\mathbf{u}} \;=\; \hat{\mathbf{f}}\,.$$

Obtaining the inverse of the matrix $\widehat{\mathbf{D}}^{(1)}$ and noting that $\tilde{u}_2$ is the only data point required as it approximates $u(C)$ in (3.27), the spectral approximation $\tilde{I}$ to the integral (3.26) is found by calculating the scalar product of the third row of $(\widehat{\mathbf{D}}^{(1)})^{-1}$ with $\hat{\mathbf{f}}$

$$\tilde{I} \;=\; \sum_{j=0}^{N} \left[\left(\widehat{\mathbf{D}}^{(1)} \right)^{-1} \right]_{2,j} \hat{f}_j\,. \tag{3.30}$$

The accuracy of the spectral integration procedure (3.30) is tested in §4.1.2.

3.4 Time-stepping method

To close the numerical discretization of the system (2.71) and (2.72), a method must be employed to advance the solutions through time. Within the existing literature on the tear film, little to no detail is given on the temporal integration scheme used to simulate the models. For example, Jones *et al.* (2005) and Jones *et al.* (2006) simply state that their solutions are "*advanced in time using a semi-implicit method [in which] the non-linear terms are evaluated at the current time level, [and] the linear terms are treated at the future time level*"; thus the order of the error is not discussed. This is a critical issue as inferences are drawn relating to the issue of so-called 'black lines' (see, for example, Miller *et al.*, 2002), defined by the location of the domain at which $h \to 0^+$, i.e. where $|h|$ may be comparable to the order of the unknown error. The present

concerns are augmented further by observations regarding the approximation of fourth derivatives of steep-sided functions near the boundary (*cf.* §4.3). In many cases, the first-order ordinary differential equations resulting from the spatial discretization are integrated using proprietary software packages such as DASPK[3] (Braun & Fitt, 2003; Braun & King-Smith, 2007), DASSL[3] (Maki *et al.*, 2010a; Maki *et al.*, 2010b), MATLAB's `ode15s`[3] (Heryudono *et al.*, 2007; Li & Braun, 2012) and `ode23s`[3] (Winter *et al.*, 2010), and modules within COMSOL[3] (Zubkov *et al.*, 2012; 2013). Aydemir *et al.* (2011) use an implicit backward Euler discretization with a Newton-Raphson method. Despite the obvious benefits to be gained from using such software packages, it is felt that the use of so-called 'black-box' time integrators masks the level of error in the approximate solutions, and hence violates the explicitly-stated aim of this chapter: that the algorithms used in the numerical scheme are manifestly transparent to the reader. Thus motivated, the time-stepping method is briefly outlined here.

To remain consistent with the approach of §3.1, in which Chebyshev spectral methods are employed to achieve a high accuracy in the spatial discretization, high-order Runge-Kutta methods are used to discretize the first-order temporal derivative in each of the evolution equations. Runge-Kutta methods are used to approximate the solution to the differential equation

$$\dot{u} = \frac{du}{dt} = f(t, u)\,, \tag{3.31}$$

[3] Both DASSL and DASPK use variable-order, variable-stepsize backward difference formulæ within a 'predictor' step, followed by an iterative 'corrector' step (Brenan *et al.*, 1989; Li & Petzold, 1999). Information on MATLAB packages can be found in Shampine & Reichelt (1997), revealing that `ode15s` uses quasi-constant stepsize backward differences, and `ode23s` uses a linearly implicit scheme. COMSOL (2012a; 2012b, pages 348 - 352) identify that the software's time-dependent solver uses backward differences or a generalised-alpha method. Importantly, each software package allows an error tolerance to be set for the solution calculated at every time-step, through which the package varies its time discretization parameters. Hence, whilst the documents listed herein give some information on the discretization errors, it is not possible to know the errors implicit in the results of published ophthalmic models without knowing the minutiæ of the software-package configuration.

in which $u = u(t)$. The time is discretized using a time-step h from initial time t_0 to time $t = t_n = t_0 + nh$, with $n \in \mathbb{N}$. Approximations to $u(t_n)$ are notated as $\tilde{u}_n$. The well-known, fourth-order, explicit Runge-Kutta method (see, for example, Atkinson, 1989; Iserles, 1996) used to integrate (3.31) is extended to model the coupled system of equations in two dependent variables

$$\begin{aligned} \dot{u} &= f(t,\, u,\, v)\,, \\ \dot{v} &= g(t,\, u,\, v)\,, \end{aligned}$$

which represents the (h, ψ) system of (2.71) and (2.72). The time-step integration is given by the algorithm

$$\begin{aligned} k_1 &= h\, f(t_n,\, \tilde{u}_n,\, \tilde{v}_n)\,, & l_1 &= h\, g(t_n,\, \tilde{u}_n,\, \tilde{v}_n)\,, \\ k_2 &= h\, f\left(t_n + \frac{h}{2},\, \tilde{u}_n + \frac{k_1}{2},\, \tilde{v}_n + \frac{l_1}{2}\right), & l_2 &= h\, g\left(t_n + \frac{h}{2},\, \tilde{u}_n + \frac{k_1}{2},\, \tilde{v}_n + \frac{l_1}{2}\right), \\ k_3 &= h\, f\left(t_n + \frac{h}{2},\, \tilde{u}_n + \frac{k_2}{2},\, \tilde{v}_n + \frac{l_2}{2}\right), & l_3 &= h\, g\left(t_n + \frac{h}{2},\, \tilde{u}_n + \frac{k_2}{2},\, \tilde{v}_n + \frac{l_2}{2}\right), \\ k_4 &= h\, f(t_n + h,\, \tilde{u}_n + k_3,\, \tilde{v}_n + l_3)\,, & l_4 &= h\, g(t_n + h,\, \tilde{u}_n + k_3,\, \tilde{v}_n + l_3)\,, \\ \tilde{u}_{n+1} &= \tilde{u}_n + \frac{1}{6}\Big(k_1 + 2k_2 + 2k_3 + k_4\Big), & \tilde{v}_{n+1} &= \tilde{v}_n + \frac{1}{6}\Big(l_1 + 2l_2 + 2l_3 + l_4\Big). \end{aligned} \tag{3.32}$$

Through this algorithm, the solution is iterated forwards in time using a weighted average of four estimates of the solution in the interval $t \in [t_n, t_{n+1}]$.

3.5 Summary and discussion

The goals motivating this chapter were to outline the numerical methods and post-processing techniques to be used in the solution of the pair of coupled evolution equations (2.71) and (2.72) on a non-periodic spatial domain. Due to the scant level of detail in the descriptions of numerical algorithms used in the existing mathematical literature on the tear film, an explicit aim of this chapter has been that all methods employed can be readily

reproduced by the reader. As such, it is hoped that the presented techniques are adopted for the modelling of further related evolution equations on bounded spatial domains.

Chebyshev spectral methods have been used to discretize all spatial derivatives in the system of evolution equations. In an effort to improve the accuracy in the calculation of derivatives up to fourth-order, explicit formulæ for the entries of higher-order Chebyshev differentiation matrices have been derived. Of these formulæ, the author believes the third- and fourth-order differentiation matrices to be hitherto-unpublished in mathematical literature, despite the method for their derivation being readily available. Further improvements to the accuracy of the matrices have been made through the use of simple trigonometric identities. All testing and validating of Chebyshev differentiation matrices presented herein occurs in Chapter 4.

Motivated by the lack of information regarding the enforcement of boundary conditions in existing models on the tear film, a procedure has been outlined in which *spectral extrapolation* allows the boundary conditions to be enforced upon the discretized system. In the absence of Dirichlet conditions that pin the menisci at the eyelids, the boundary-condition procedure for the fourth-order evolution equation (2.71) warrants the addition of four ghost nodes within the Chebyshev domain $x \in [-1, 1]$, as depicted in Figure 3.1. The specification of the boundary-condition procedure for the second-order (2.72) on the *same* set of collocation nodes reveals the need for an additional "ghost" boundary condition (3.23) for ψ, which condition is informed by the natural boundary condition (2.78). The hybrid matrices and vectors required by the boundary-condition procedures are presented in §3.2.1 and §3.2.2.

A method for the spectral integration of functions across the physical domain $x \in [-C, C]$ is outlined in §3.3, which allows the integrals (2.86) and (2.87) to be computed as (2.71) and (2.72) are solved. These integrals respectively represent the total fluid mass and the total amount of surfactant within the coupled system, hence tracking the value of such conservation integrals allows the accuracy of the evolution equations to be tested:

specifically, (2.71) represents the conservation of mass (in the absence of evaporation, $E = 0$), and (2.72) represents the concentration distribution of adsorbed surfactant.

To integrate the solutions in time, a coupled formulation of the fourth-order, explicit Runge-Kutta scheme has been outlined. This method is preferred over the use of proprietary software packages as it ensures that the time-step size remains fixed and known to the user, and therefore the error associated with the method can be estimated.

Chapter 4

Validation of Numerical Tools

Rigorous testing of the numerical methods and boundary condition procedure described in Chapter 3 is required to validate the techniques to be used in the integration of the pair of coupled spatio-temporal evolution equations (2.71) and (2.72). Tests using Chebyshev methods are carried out in §4.1 to illustrate the spectral accuracy of the differentiation matrices and spatial-integration procedure, respectively outlined in §3.1 and §3.3. To test the accuracy of the full numerical scheme, comprising spatial and temporal discretization, §4.2 contains simulated solutions to both a linear partial differential equation with a known analytic solution, and the nonlinear film-thickness evolution equation (2.71). These tests demonstrate the accuracy of the boundary-condition procedure outlined in §3.2, and the fourth-order, explicit Runge-Kutta time-stepping algorithm of §3.4. Novel insights on the applicability of Chebyshev spectral methods in the approximation of derivatives of functions containing steep gradients (which model the menisci at the eyelids) *near boundaries* are presented in §4.3.

The notation of Chapter 3 is retained herein, with tildes augmenting numerical approximations to functions and their derivatives. Functions that have been differentiated are represented by superscript parentheses denoting the order of differentiation. Quantities that depend upon the number N of spatial discretization nodes are identified

with a subscript.

4.1 Testing Chebyshev differentiation and integration

The spectral convergence of numerically-approximated derivatives and integrals to their analytical values as the spatial discretization parameter N is increased is illustrated in this section. Calibrations are performed using a variety of test functions defined using both polynomial and transcendental terms. The improved performance of the alternative differentiation matrices (those which employ the identities in (3.14) to replace differences of trigonometric terms with products) over their original forms is demonstrated. Furthermore, the errors arising through use of the explicit higher-order matrices, of which the third- and fourth-order matrices represent novel developments within this thesis, are compared to the errors arising through repeated action of the first-order differentiation matrix, identifying the optimum method for generating higher-order spatial derivatives, which method introduces the minimum error from the discretization process.

4.1.1 Differentiation-matrix accuracy

The accuracy of the Chebyshev differentiation matrices in their original form, (3.8) - (3.12), and their alternative form, (3.15) and (A.1) - (A.3), is tested in this section. Three test functions are defined using a combination of purely-transcendental terms, purely-polynomial terms, and a mixture of polynomial and transcendental terms. These are

$$\begin{aligned} u(x) &= \exp(\sin(3x))\,, \\ v(x) &= x^5 + x^4 + x^3 + x^2 + x + 1\,, \quad \text{and} \\ w(x) &= 1 - x + 4x^2 + x\,\exp(-3x)\,\cos(2x) + 3x^3\,\sin(3x)\,. \end{aligned} \tag{4.1}$$

Each function is differentiated four times both analytically and numerically, and the analytically calculated derivatives are evaluated at the Chebyshev nodes $\{x_j\}$. Higher derivatives are obtained using both the original and alternative forms of the explicit differentiation matrix of relevant order, and also using repeated action of both forms, (3.8) and (3.15), of the first-order matrix. At the nodes, the infinity norm of the percentage absolute error in the approximation

$$\left\| \% \text{ error in } \tilde{f}_N^{(k)} \right\|_\infty = \max_{x\in[-1,1]} \left[100 \left| \frac{\tilde{f}_N^{(k)}}{f^{(k)}} - 1 \right| \right] , \tag{4.2}$$

is obtained. This is shown to converge to zero rapidly with increasing N and, for $N \gtrsim 40$, the limiting factor in the accuracy of the calculation of the derivative is shown to be the precision of the machine itself. In each test case, the symmetrically-distributed form of the Gauss-Lobatto grid (3.13) is used in favour of the original definition (3.2).

Results from tests of the accuracy of both forms, (3.8) and (3.15), of the first-order differentiation matrix are presented in Figure 4.1, which show that, for values of $N \geq 20$, the maximum absolute error in the first derivative of each function in (4.1) is less than 0.01%. As N is increased, both test functions containing transcendental functions display rapid convergence to zero of the maximum absolute error, which error reaches the numerical round-off plateau located between $10^{-10} - 10^{-8}\%$. For all values of N shown in Figure 4.1, the accuracy of the approximate gradient of the polynomial function $v(x)$ is such that the round-off error of the finite-precision machine swamps the differentiation error. This occurs because, for $N \geq 5$, the fifth-order polynomial can be represented accurately by the linear combination of Chebyshev polynomials used in the cardinal function interpolant (3.3). A slight positive gradient with increasing N is observable in the data falling within the round-off plateau, reflecting the accumulation, with N, of rounding errors from the manipulation of matrices of size $(N+1)\times(N+1)$, which themselves are populated with entries of large magnitude.

Importantly, the coloured pairs of symbols in Figure 4.1 demonstrate the improved performance of the alternative first-order Chebyshev differentiation matrix (3.15) over

that of the original matrix (3.8). In the falling limbs of the transcendental test-function data, the accuracy of the interpolant (which is dependent upon N) dominates the error calculation, leading to data points that overlie each other. Within the round-off plateau, the vast majority of coloured symbol pairs appear with the blue data point *below* the red point, showing the improved accuracy in the calculation of the entries of the first-order differentiation matrix computed via (3.15).

For higher orders of differentation, the behaviour of the error for each function in

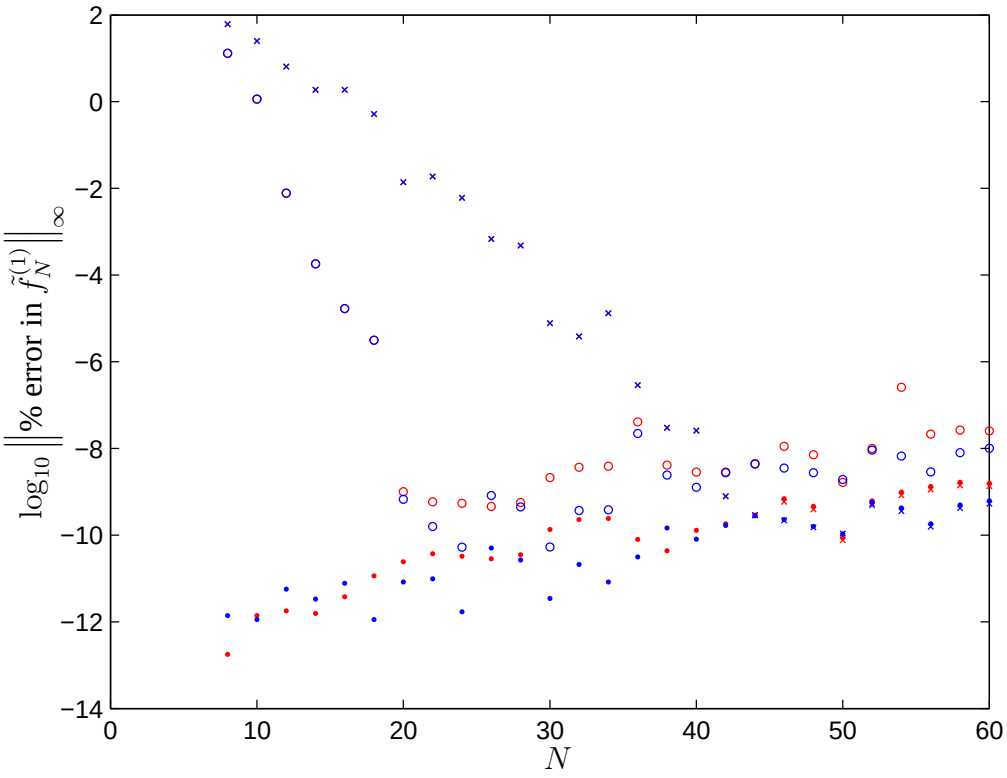

Figure 4.1: Logarithm of the maximum percentage absolute error in the numerical approximation of the first derivative obtained using the Chebyshev differentiation matrix in its original form (3.8) and its alternative form (3.15) for $N = 8(2)60$. Test functions (4.1) are denoted by u (crosses), v (dots) and w (circles). Blue circles and crosses overlie their red counterparts in each of the descending limbs, giving the impression that only blue data exists for these values of N.

(4.1) is qualitatively the same as that displayed in Figure 4.1 for the first derivative, but the magnitude of the errors is greater. Four methods of calculation are available to approximate higher-order derivatives, these are: (i) repeated application of the first-order matrix (3.8); (ii) the appropriate explicitly-derived matrix (3.10) - (3.12), and; methods (i) and (ii) with the alternative formulations of the matrices, respectively (3.15) and (A.1) - (A.3). The accuracy of the hitherto-unseen explicit third- and fourth-order differentiation matrices (3.11) and (3.12) is evidenced in Figure 4.2, which figure contains

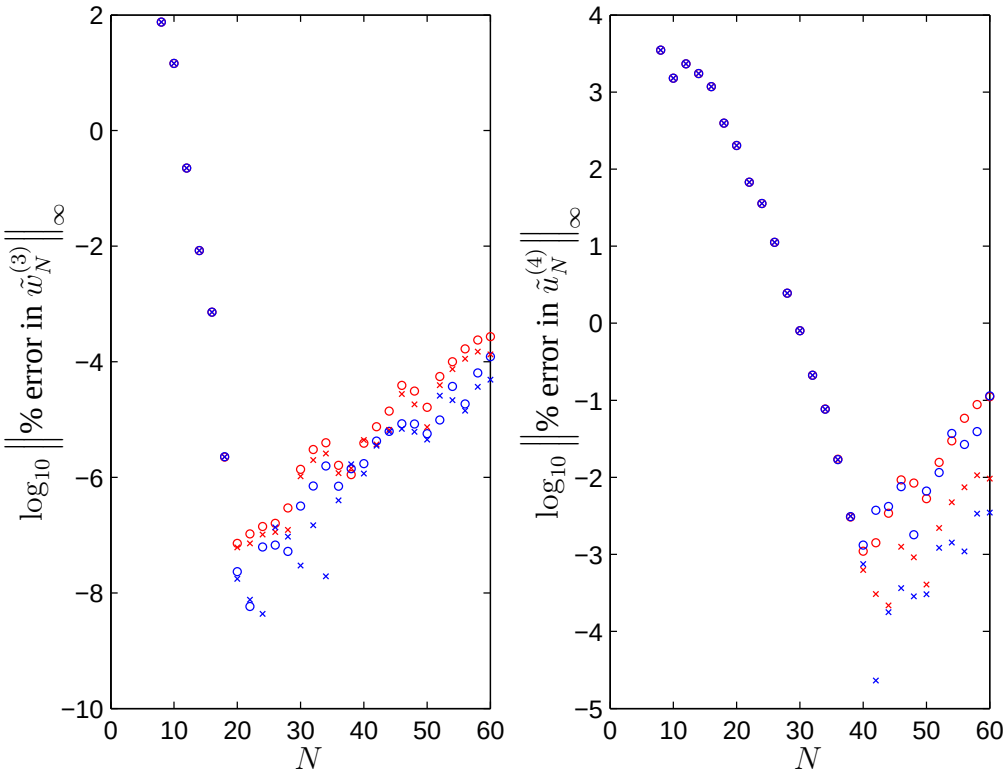

Figure 4.2: Logarithm of the maximum percentage absolute error in the numerical approximation of **(left)** $w^{(3)}(x)$, and **(right)** $u^{(4)}(x)$, for $N = 8(2)60$. In both plots, colours and symbols denote: matrices defined in their original form; matrices defined in their alternative forms using (3.14); $\circ$ the colour-specific explicitly-derived matrix, and; $\times$ multiple applications of the colour-specific first-order matrix.

the maximum percentage errors in the approximations of $w^{(3)}(x)$ and $u^{(4)}(x)$. These results are representative of the results from the second- to fourth-order derivatives of all three test functions in (4.1). These similar results are not presented, but they all support the conclusions that are drawn below.

The data located in the round-off plateaux of Figure 4.2 show that, in the majority of cases, the best-performing method for calculating a higher derivative is multiple application of the alternative first-order matrix (3.15), represented graphically by blue crosses. The overlaying data in the descending limbs both illustrates the accuracy of the explicit formulæ, and identifies that all four methods for calculating the derivative are primarily dependent on the accuracy of the interpolant, rather than the accuracy of the representation of matrix entries. As in Figure 4.1, it is only in the round-off plateaux that differences are observed between the performances of the different calculation methods, which differences identify that repeated matrix multiplication using the first-order matrices shows a marked improvement over that of the explicitly-derived formulæ of §3.1.2. An explanation for the large errors attributed to the explicit formulæ is that, for all values of N, the entries in the top-left and bottom-right corners of the differentiation matrices grow as N^{2k}, where k is the order of differentiation. Thus as N is increased, the accumulated errors are magnified through the use of steadily-growing $(N+1)\times(N+1)$ matrices containing entries of high magnitude, which entries can only be represented to a finite degree of accuracy by finite-precision arithmetic. Alternatively, through repeated action of the first-order matrix, the accumulation of errors is reduced because the magnitude of the entries within the matrix is significantly lower; for example when $N = 60$, $D^{(1)}_{0,0}$ is of order $\mathcal{O}(10^3)$, whereas $D^{(4)}_{0,0}$ is of order $\mathcal{O}(10^{11})$. Hence, the errors in the finite-precision representation of $\mathbf{D}^{(1)}$ are of a smaller magnitude the errors in the formulation of $\mathbf{D}^{(k)}$ for $k = 2, 3, 4$.

Despite the efforts made to generate the novel, explicit, higher-order Chebyshev differentiation matrices, the results presented in Figures 4.1 and 4.2 support the use

of repeated applications of the alternative form (3.15) of $\mathbf{D}^{(1)}$ to calculate *all* spatial derivatives required for the modelling of the pair of coupled evolution equations (2.71) and (2.72).

4.1.2 Testing spectral integration

The accuracy of the spectral integration procedure of §3.3 is now tested using five functions formed from a mixture of polynomial and transcendental terms

$$\begin{aligned} s_1(x) &= (1+x)^4\,, \\ s_2(x) &= \exp(x^2)\,\sin\frac{\pi x}{C}\,, \\ s_3(x) &= \exp\left(\sin\frac{\pi x}{C}\right)\,, \\ s_4(x) &= 1 - x + 2x^2 + x\cos\frac{\pi x}{C} + 3x^3\sin\frac{\pi x}{C}\,, \\ s_5(x) &= 4\cos\frac{5\pi x}{C}\,. \end{aligned} \tag{4.3}$$

These functions are chosen because, for $x \in [-C, C]$: s_1 and its gradient increase monotonically with x; s_2, s_3 and s_4 all contain multiple turning points and are formed from combinations of transcendental and polynomial functions, and; s_5 is a rapidly-oscillating function with steep gradients. For each test function in (4.3), the integral

$$I_i = \int_{-C}^{C} s_i(x)\,dx\,, \qquad (\textit{cf.}\ (3.26)) \tag{4.4}$$

is performed analytically in MAPLE using 20-digit precision arithmetic, and compared to the N-node spectral approximation $\tilde{I}_{i,N}$ of I_i calculated through the Chebyshev integration procedure (3.30) in MATLAB using standard IEEE 754 64-bit double-precision arithmetic, with a machine-ϵ of 2.22×10^{-16}: results are presented in Figure 4.3.

The improvement in the accuracy of the spectral approximation with increasing N is clearly demonstrated by the test functions $s_3(x)$, $s_4(x)$, and $s_5(x)$, which respectively reach the round-off plateau at roughly 10^{-14} when $N = 42$, 22 and 42. The spectral

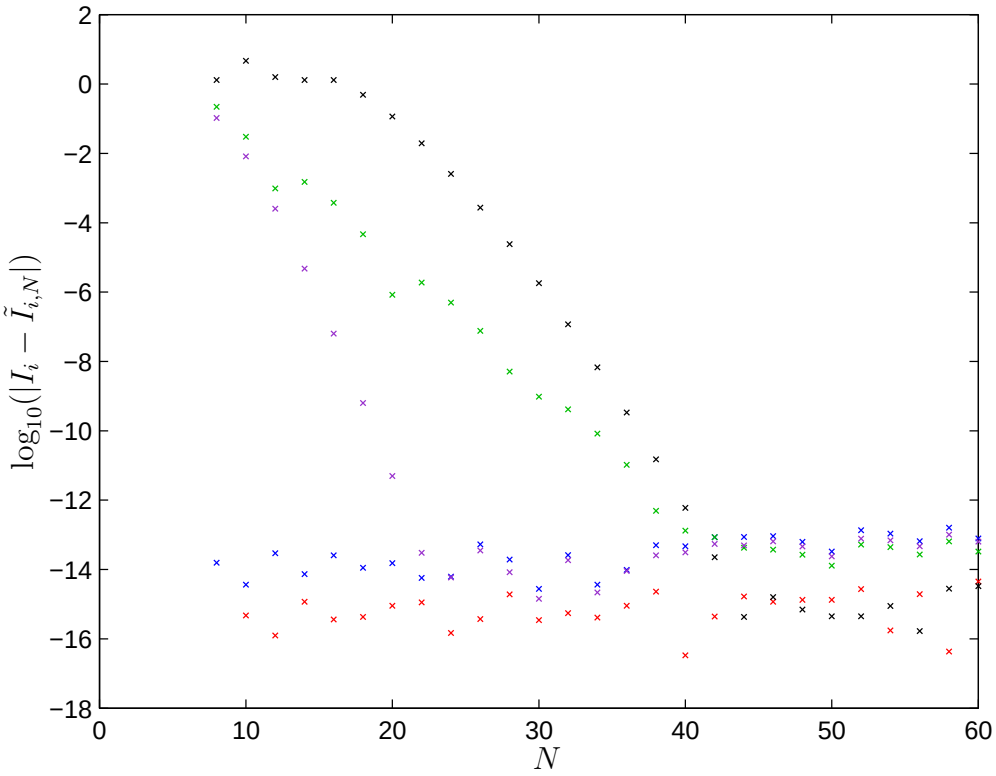

Figure 4.3: The convergence with N of the error $|I_i - \tilde{I}_{i,N}|$, for the various test functions of (4.3), calculated for $N = 8(2)60$. The test integrands $s_i(x)$ are represented by the colour scheme $i = 1, 2, 3, 4, 5$. For all functions tested, the round-off plateau, at $|I_i - \tilde{I}_{i,N}| \approx 10^{-14}$, is reached when $N = 42$. The omitted red data point when $N = 8$ is because the numerical integration is exact. *Absolute* rather than *relative* errors (*cf.* Figures 4.1 and 4.2) are shown as $I_i = 0$ for $i = 2, 5$, and all other integrals are of order $\mathcal{O}(1)$.

integration of $s_1(x)$ and $s_2(x)$ yields errors in the round-off plateau for all values of N tested. As in §4.1.1, an explanation for the rapid convergence of the error in these functions in comparison to, for example, the error convergence in the integral of $s_5(x)$ in Figure 4.3 may be obtained by considering the error in the interpolation of the functions using (3.3). For $s_1(x)$ and $s_2(x)$, the interpolant (3.3) yields a maximum error of order $\mathcal{O}(10^{-6})$ for the range of N displayed in Figure 4.3. The maximum errors in the

interpolation of $s_5(x)$ when $N = 10$, 20, and 30 are respectively $\mathcal{O}(10)$, $\mathcal{O}(10^{-1})$, and $\mathcal{O}(10^{-5})$; this marked improvement in the interpolation is reflected in the greater accuracy of the spectral approximation (3.30) of the integral. The errors in the interpolation of $s_5(x)$ with low N arise through interpolating a rapidly-oscillating function using a coarse discretization mesh.

4.2 Validation of the numerical scheme

To ensure that the dynamics observed in the subsequent chapters are due to the tear-flow model, and not spurious artefacts of the numerical scheme and associated parameter combinations used within simulations, two tests of the full numerical scheme are carried out in which the discretization parameters, N and dt, are varied to demonstrate the consistency of spatio-temporal integrations. Both tests compute the solutions to partial differential equations containing first-order temporal derivatives and fourth-order spatial derivatives, complemented with Neumann boundary conditions specified upon the first- and third derivatives at the ends of the computational domain: such boundary conditions are compatible with those of the full tear-flow model.

4.2.1 Linear test simulation

Preliminary tests of the numerical scheme are carried out using a linear partial differential equation containing an inhomogeneous forcing function, augmented by homogeneous Neumann boundary conditions. The IBVP is given by

$$u_t + C^4 u_{xxxx} = 24C^4 - 72C^2x^2\,, \quad u_x(\pm C, t) = 0\,, \quad u_{xxx}(\pm C, t) = 0\,. \tag{4.5}$$

Two initial conditions are specified to test different attributes of the numerical scheme,

$$u_1(x,0) = 1 - \frac{7C^2}{5}x^2 + x^4 - \frac{1}{5C^2}x^6 + \sin\left(\frac{\pi x}{2C}\right)\,, \tag{4.6a}$$

and

$$u_2(x,0) \;=\; 0\,. \tag{4.6b}$$

Initial condition u_1 in (4.6a) satisfies the evolution equation and boundary conditions (4.5) exactly, and demonstrates the accuracy of the numerical scheme as it approximates the temporal evolution of the explicitly-known analytic solution

$$u(x,t) \;=\; 1 - \frac{7C^2}{5}x^2 + x^4 - \frac{1}{5C^2}x^6 + \exp\left(-\frac{\pi^4 t}{16}\right)\sin\left(\frac{\pi x}{2C}\right)\,. \tag{4.7}$$

Initial condition u_2 in (4.6b) fails to satisfy the evolution equation, and enables the convergence of the scheme towards a steady-state solution to be tested. The steady solution to (4.5) subject to initial condition (4.6b) is

$$u_\infty(x) \;\equiv\; \lim_{t\to\infty} u(x,t) \;=\; \frac{31C^4}{105} - \frac{7C^2}{5}x^2 + x^4 - \frac{1}{5C^2}x^6\,, \tag{4.8}$$

wherein the constant has been determined from the integral condition

$$\int_{-C}^{C} u_\infty(x)\,dx \;=\; 0\,,$$

which follows from (4.6b). This second test replicates the behaviour expected of solutions to (2.71) because the initial condition (2.80) does not conform to the steady-state shape, and so will induce movement of the bulk fluid through which the free surface will relax towards its coordinate-system-dependent quiescent profile, (2.89) or (2.90). The consistency of the numerical scheme is illustrated through such a test by varying the discretization parameters and tracking the behaviour as the solution converges from (4.6b) towards (4.8).

Evolution equation (4.5) is simulated using parameter sets $\mathcal{P}_1 = \{N = 20, dt = 10^{-7}\}$, $\mathcal{P}_2 = \{N = 26, dt = 5\times10^{-8}\}$ and $\mathcal{P}_3 = \{N = 32, dt = 10^{-8}\}$. The behaviour of the system is displayed using results obtained with parameter set $\mathcal{P}_2$ in Figure 4.4. These results are representative of results obtained with parameter sets $\mathcal{P}_1$ and $\mathcal{P}_3$, which are not presented in the interest of clarity as the value of N is used in the definition (3.16)

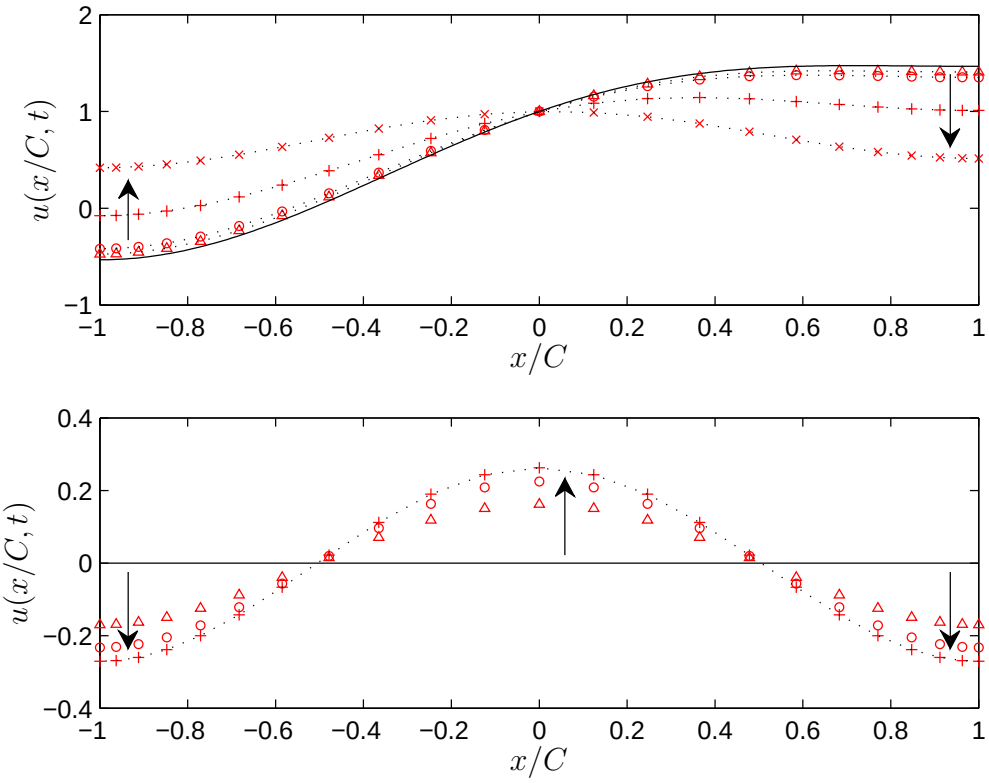

Figure 4.4: Snapshots of solutions to (4.5) with initial conditions given by **(top)** $u_1(x,0)$ of (4.6a), and **(bottom)** $u_2(x,0)$ of (4.6b). $N = 26$ and $dt = 5 \times 10^{-8}$. Red symbols represent snapshots taken at $t = 0.01$ ($\triangle$), $t = 0.02$ ($\circ$), $t = 0.1$ ($+$) and $t = 0.5$ ($\times$). Solid black lines denote the initial conditions, and dotted lines represent: **(top)** analytic solutions (4.7) at the relevant point in time, and **(bottom)** the steady state (4.8). Arrows show the direction of increasing time.

of C, whence (4.5) - (4.8) are all altered by the spatial discretization. Figure 4.5 plots the time-evolution of the maximum error in the simulations using initial condition u_1 (4.6a) that approximate (4.7), and the convergence towards the steady state (4.8) of simulations using initial condition u_2 (4.6b).

The upper plot of Figure 4.4 shows the numerical solutions closely approximate the exact solution (4.7): the level of accuracy is quantified in the upper plot of Figure 4.5, which shows the logarithm of the maximum absolute error between the exact solution

and its numerical approximation, obtained using each set of discretization parameters. The rapid convergence from initial condition u_2 of (4.6b) to the steady state is shown in the lower plot of Figure 4.4; by $t = 0.1$, the difference between the numerical simulation and the steady state has a maximum relative error of $6.2 \times 10^{-3}\%$. Furthermore, the lower plot of Figure 4.5 shows that, after $t \approx 0.25$, the discrepancy between the steady state and the numerical solution is small enough that it is dominated by errors introduced through the numerical scheme itself. The relative magnitude of the numerical error is found to be

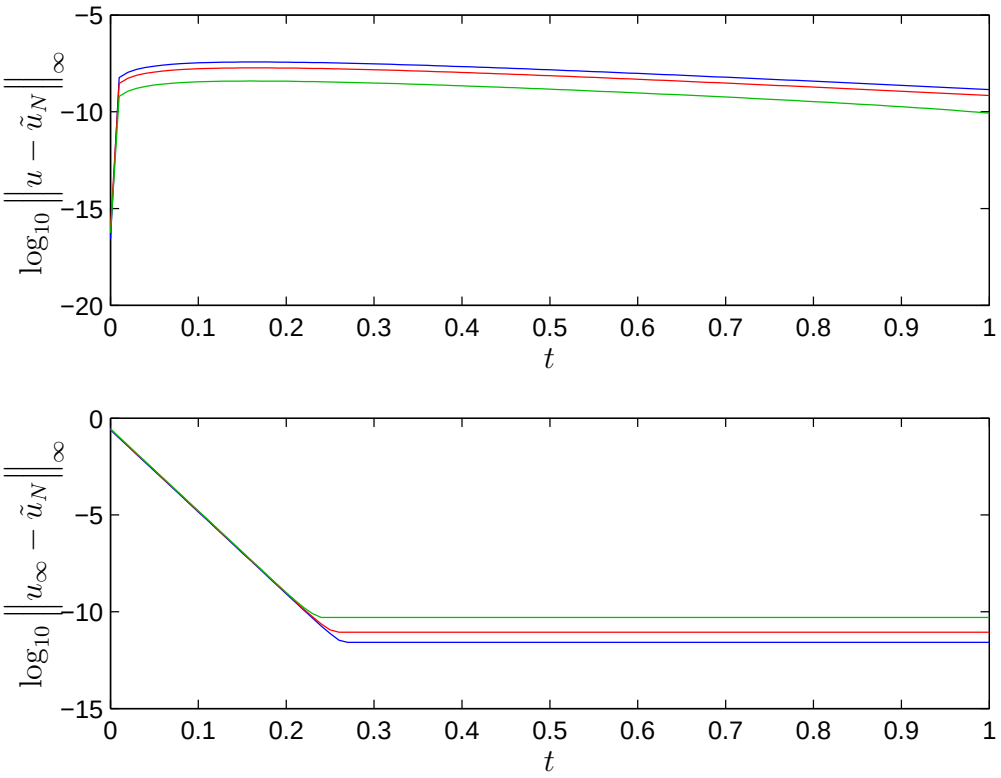

Figure 4.5: Logarithm of the maximum absolute difference between: **(top)** the numerical- and analytical (4.7) solutions in simulations using initial condition (4.6a), and **(bottom)** simulations using the homogeneous initial condition (4.6b) and the steady state (4.8), displaying rapid convergence. Colours represent numerical discretization parameter sets $\mathcal{P}_1 = \{N = 20, dt = 10^{-7}\}$, $\mathcal{P}_2 = \{N = 26, dt = 5 \times 10^{-8}\}$ and $\mathcal{P}_3 = \{N = 32, dt = 10^{-8}\}$.

negligible: the largest steady error in the lower plot of Figure 4.5 occurs in the parameter-set-$\mathcal{P}_3$ simulations, and is of order $\mathcal{O}(10^{-10})$ in the approximation of a function of order $\mathcal{O}(10^{-1})$.

These results show the numerical scheme to be accurate and consistent in the solution of the linear partial differential equation (4.5) with initial conditions (4.6).

4.2.2 Test of nonlinear evolution equation (2.71)

Further tests of the consistency of the numerical scheme are now carried out on the nonlinear evolution equation for the film thickness (2.71) in the absence of a dynamic surfactant layer. Simulations are computed using different sets of numerical parameters, N and dt, with two different choices for the contact angle, $\hat{\theta} \in \{\pi/4, \pi/2\}$. Physical parameters of $\delta = 5/12$ and $E = 0.1$ are chosen in order that all terms are included in the differential equation and its boundary and initial conditions, and that presented snapshots of the film profile are easily displayed without overlaying closely. A value of $E = 0.1$ represents a significantly higher evaporative flux than the value reported in Mathers (1993), and is not used in subsequent chapters. An initial condition with small menisci is formed by setting $h_{\text{MID}} = 3/4$ and $r = 4/3$ in (2.79), and specifying a blend-point of $b = 0.4$. Simulations are integrated to a non-dimensional time of $t = 1$, which corresponds to five dimensional seconds.

Snapshots of the film profiles from simulations with $\hat{\theta} = \pi/2$ and $\hat{\theta} = \pi/4$ are respectively presented in Figures 4.6 and 4.7, which display rapid migration towards the steady-state profile, similar to that shown in the lower plot of Figure 4.4. This rapid convergence towards the quiescent state is shown in Figure 4.8 for $t < 0.2$, as the early phase of motion generates a near-steady-state profile in each simulation, regardless of the discretization parameters used. As the simulation progresses, the blue $\{N = 20, dt = 10^{-7}\}$ data are seen to diverge slightly from the red and green curves; however, the

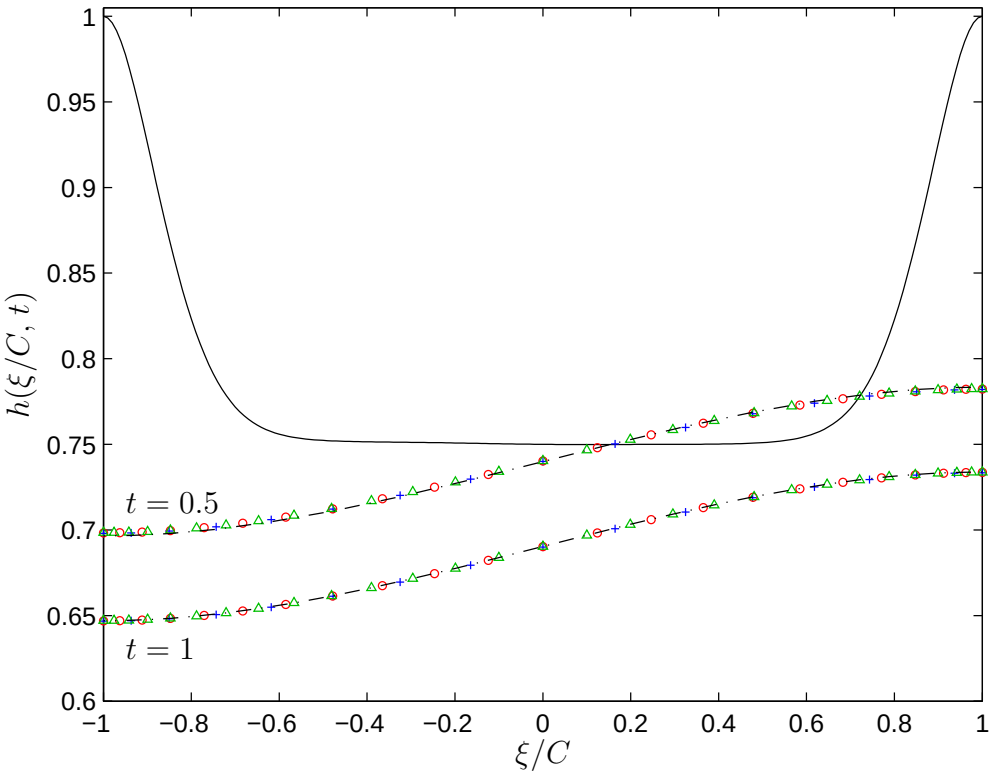

Figure 4.6: Film profiles generated by the film thickness evolution equation (2.71) with $E = 0.1$, $\delta = 5/12$, $st = 1$, $\alpha_0 = 5$ and $\hat{\theta} = \pi/2$, taken at $t = 0.5$ and $t = 1$, respectively the higher and lower datasets. Discretization parameter values for the numerical scheme are represented by: $\{N = 20, dt = 10^{-7}\}$ (+); $\{N = 26, dt = 10^{-8}\}$ (○), and; $\{N = 32, dt = 5 \times 10^{-9}\}$ (△). The initial condition is denoted by a solid black profile, created using 201-knot cubic interpolation splines of the initial data from the $N = 32$ simulation. Dot-dashed lines denote translations of the steady state (2.90), and display the quick relaxation of the film towards the steady-state profile.

logarithmic vertical scale belies the size of the divergence. At $t = 1$, the maximum differences between the film profile and the steady state in the $\{N = 20, dt = 10^{-7}\}$ simulations yield a percentage difference of order $\mathcal{O}(10^{-2}\%)$ when $\hat{\theta} = \pi/2$, and of order $\mathcal{O}(10^{-1}\%)$ when $\hat{\theta} = \pi/4$. This consistency in the behaviour of simulations allows a significant saving to be made in the real-time duration of simulations, enabling the

coarsest set of discretization parameters to be employed with confidence that the data computed by the numerical scheme will be accurate. For the simulations presented in Figures 4.6 and 4.7, the time taken to reach a non-dimensional time of $t = 1$ took approximately 2 hours for parameter set $\{N = 20,\ dt = 10^{-7}\}$, 23 hours for $\{N = 26,\ dt = 10^{-8}\}$, and 51.5 hours for $\{N = 32,\ dt = 5 \times 10^{-9}\}$ on a 2.66 GHz core with 4 GB RAM. Thus the coarsest set of discretization parameters represents a roughly 25-fold computational acceleration over the finest set.

The tests presented herein provide a validation of the accuracy and consistency of the numerical scheme outlined in Chapter 3, and enable investigations of the behavioural changes caused through altering the parameter values within the tear-flow model to be

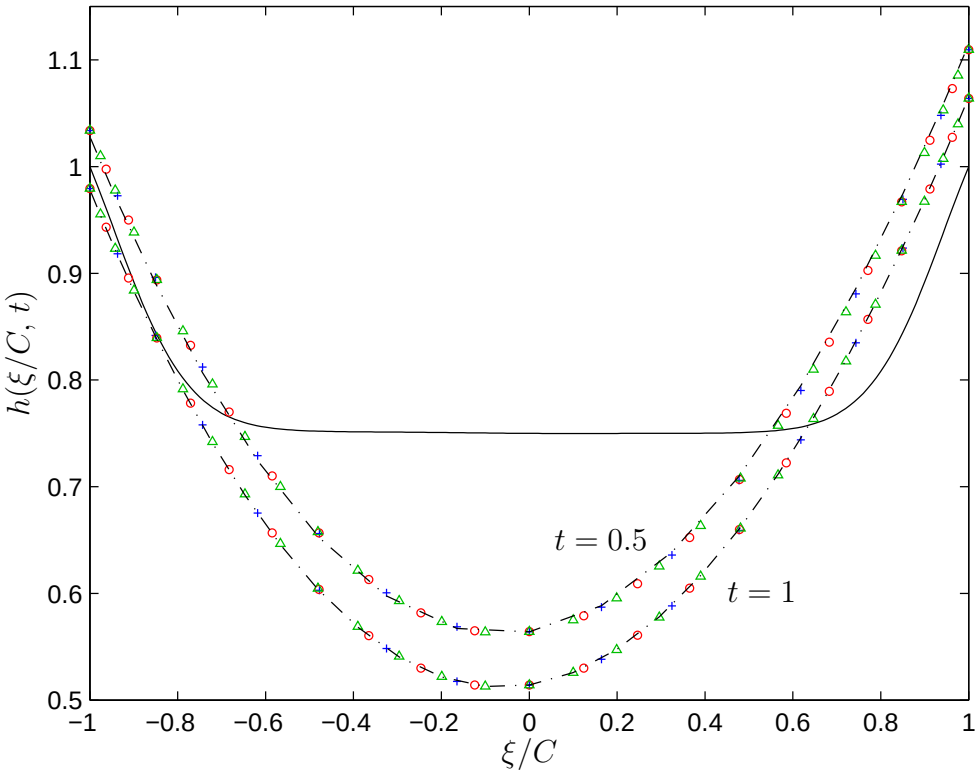

Figure 4.7: Snapshots of film profiles at $t = 0.5$ and $t = 1$ from simulations with $\hat{\theta} = \pi/4$. All other physical and discretization parameters are as given in Figure 4.6.

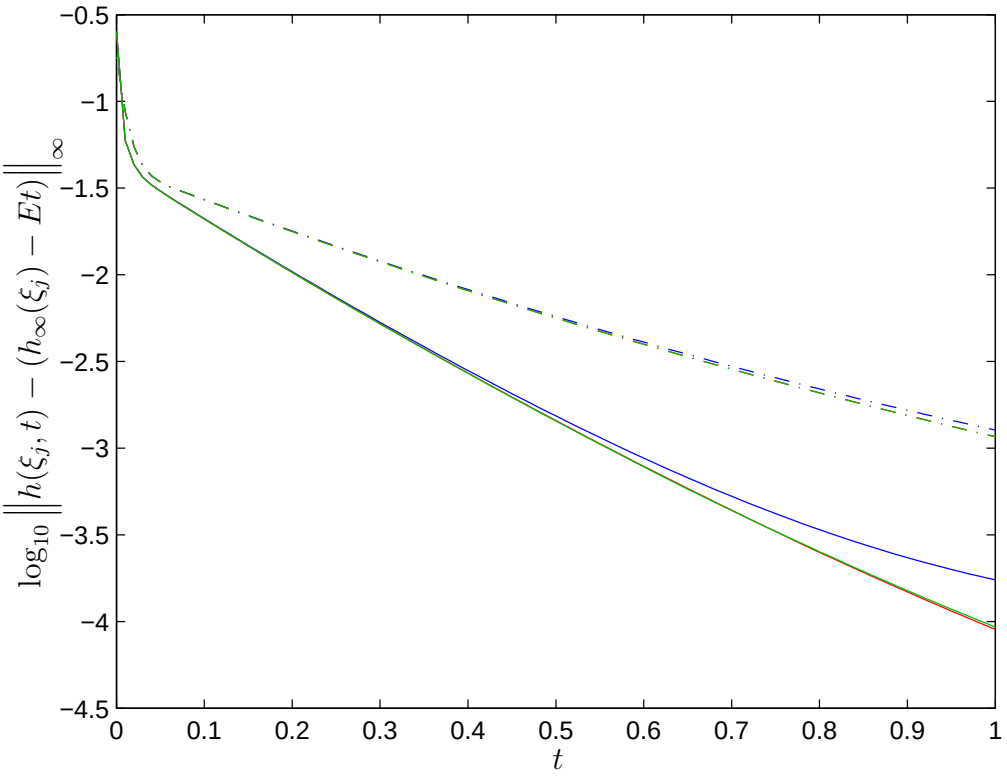

Figure 4.8: The maximum absolute difference between the tear-film profile and the evaporatively-displaced steady states in Figures 4.6 and 4.7, illustrating that the rapid early dynamics of the film are not influenced by the choice of discretization parameters. Colour coding is as per Figure 4.6, and solid and dashed lines respectively denote data from simulations with $\hat{\theta} = \pi/2$ and $\hat{\theta} = \pi/4$.

carried out with confidence that the results obtained will reflect the physical effects incorporated in the model.

4.3 Investigation of the effect of steepness induced by pinning

As mentioned in Chapter 3, the detailed derivation of numerical tools therein was driven by the scarcity of information on the numerical schemes employed in all related mathematical literature, with the aim that the results presented here may be easily reproduced by others. Furthermore, it is noted that, within *all* of the published models of the tear film, the pinning of the tear film at the mucocutaneous junction significantly influences the flow dynamics, leading to menisci that either retain their original steepness, or become progressively steeper as time increases[1]. In the interest of investigating the errors that accrue when using Chebyshev spectral methods in the models of the published literature, the numerical apparatus of Chapter 3 is applied to a test function that emulates the steep-sided initial conditions employed by the existing models.

Following the initial condition of Li & Braun (2012), a test function with steep gradients at the ends of the computational domain is defined as

$$u(x) \;=\; 1 + k\, x^m\,, \tag{4.9}$$

with $m = 2, 4, 8$ and 16, and $k = 10$ and 100. This function is also used to approximate the non-symmetric film profiles deposited during the 'eye opening' phase of models that simulate the blink cycle. In the absence of explicit forms for these profiles, (4.9) yields a good approximation to the shape of the deposited film (*cf.* the central ($t = \pi$) plot of Braun & King-Smith, 2007, Figure 4; and the top-right plot of Aydemir *et al.*, 2011, Figure 5). Variation of m when k is of order $\mathcal{O}(10)$ allows the derivatives of the initial condition of Li & Braun (2012), and of the deposited films in Braun & King-Smith (2007) and Heryudono *et al.* (2007), to be approximated using the spectral machinery. By setting $k = \mathcal{O}(10^2)$ and varying m, the derivatives of profiles in the open-eye phase of Aydemir *et al.*

[1] Discussions of the physical viability of a pinned boundary condition can be found in §2.4.1 and §2.4.2.

(2011) may be approximated. The absolute error in the approximation of the derivatives of (4.9) at all nodal locations is calculated using repeated action of the first-order Chebyshev differentiation matrix (3.15) for various values of the spatial discretization parameter N, and the results for each derivative when $k = 10$ are presented in Figures 4.9 - 4.12.

In Figure 4.9, the sequential increase in N from plot (a) to plot (d) shows an increasing magnitude of the error in the approximation of the gradient near the endpoints, $x \approx \pm 1$, by an amount of order $\mathcal{O}(10^2)$. This increase in magnitude with N is not observed in the central regions near $x = 0$, where the gradient of the function is not as severe. Thus the

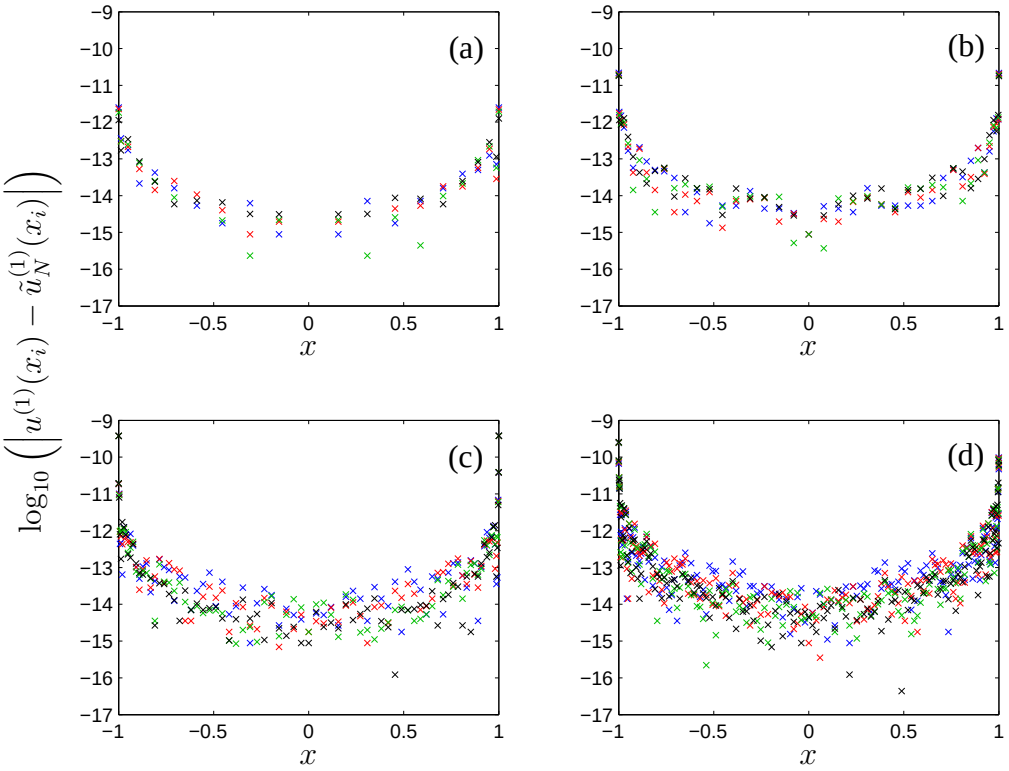

Figure 4.9: Logarithm of the absolute error in the calculation of the first derivative of (4.9) when $k = 10$, and **(a)** $N = 20$, **(b)** $N = 40$, **(c)** $N = 80$ and **(d)** $N = 160$. Data points are coloured to denote $m = 2$, 4, 8 and 16.

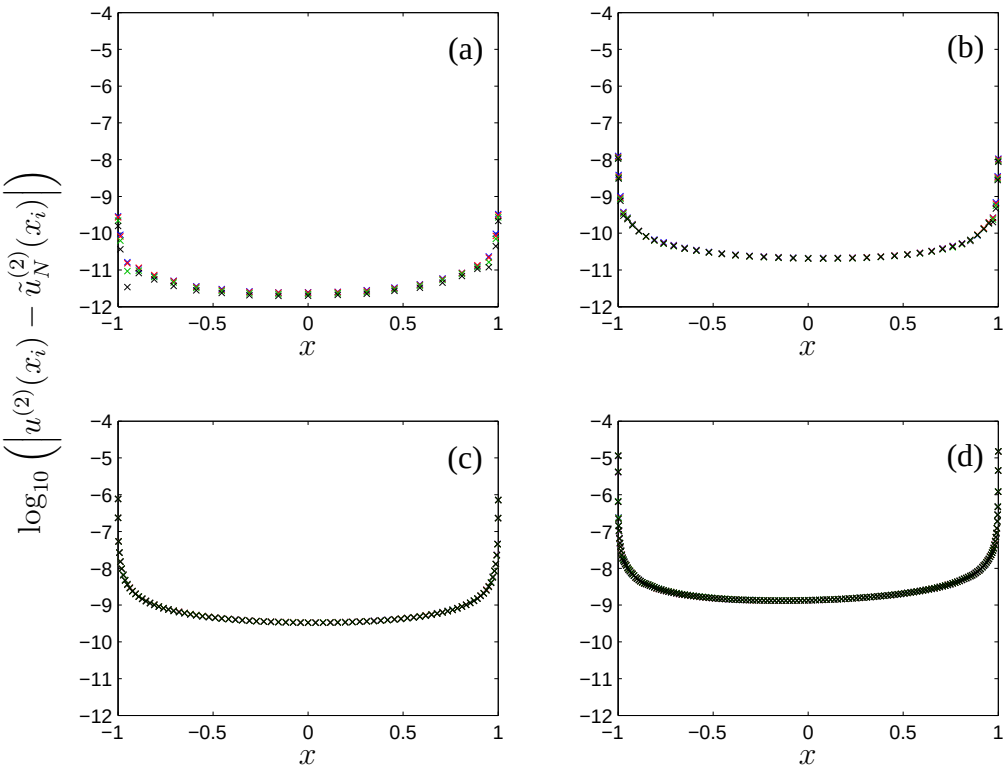

Figure 4.10: Logarithm of the absolute error in the calculation of the second derivative of (4.9) when $k = 10$. All colours and discretization parameters are as per Figure 4.9.

approximation with $N = 20$ yields derivative values in the centre of the computational domain that are *as accurate* as those from the approximation with $N = 160$, and values that are *more accurate* than the $N = 160$ approximation near the interval end points.

The data presented in Figures 4.10 - 4.12 demonstrate that the magnitude of the error in the numerical calculation of higher derivatives grows with both the order of differentiation and the number of spatial discretization nodes used in the approximation. For each derivative, the errors of largest magnitude are found in approximations with $N = 160$, and the $N = 160$ results also show the largest range of magnitudes in the numerical error. Importantly, the results of Figures 4.9 - 4.12 identify the errors of largest

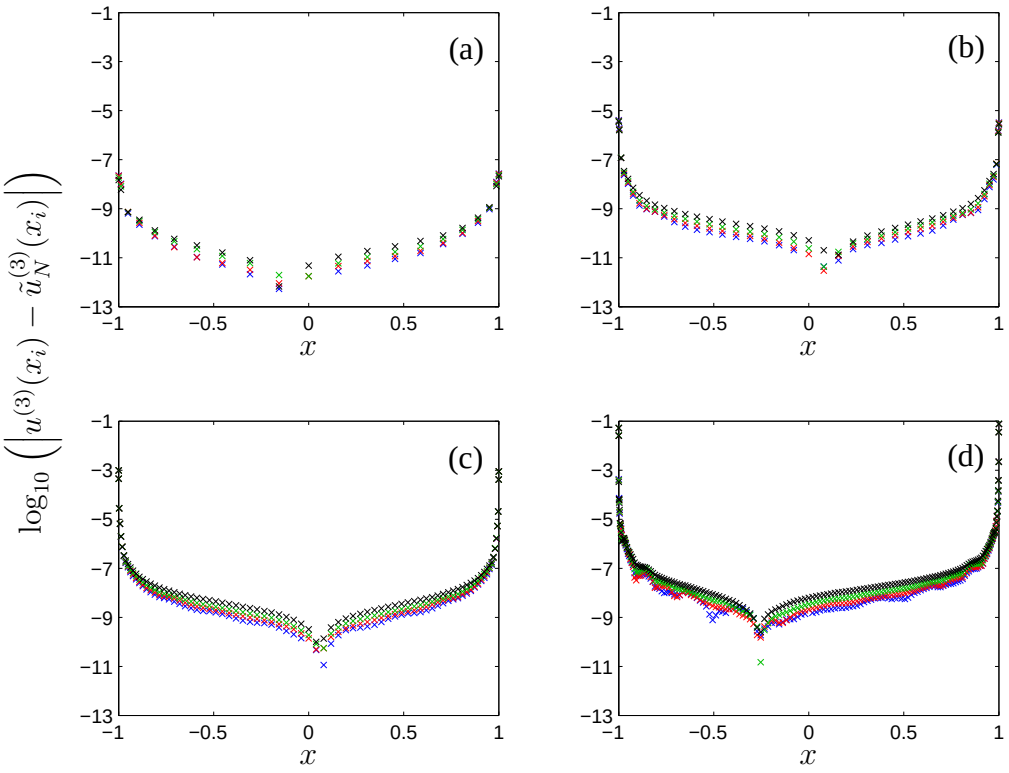

Figure 4.11: Logarithm of the absolute error in the calculation of the third derivative of (4.9) when $k = 10$. All colours and discretization parameters are as per Figure 4.9.

magnitude in the calculation of derivatives as those found at the ends of the computational domain. This means that tear-flow models that use both pinned menisci and Chebyshev discretization[2] will exhibit dynamics that are driven by regions of the computational

[2]Braun *et al.* (2012), and Li & Braun (2012). Heryudono *et al.* (2007) use a mapped Chebyshev spectral method that reduces the clustering of nodes near $x = \pm 1$, which method is applicable when solutions have high gradients away from boundaries or are smooth throughout the interval (Heryudono *et al.*, 2007, Appendix B). Notably, as pinned film profiles fail to satisfy the first option above, placing fewer nodes in the menisci will reduce the resolution in those regions, and, by transforming the Chebyshev collocation nodes (3.2), the near-minimax accuracy of the interpolant (3.3) (which motivated the choice of Chebyshev spectral methods in §3.1.1) will be reduced. Thus, a significant trade-off is made between numerical stability and the accuracy of simulations when employing such a transformation.

domain in which there is a high degree of numerical inaccuracy. Moreover, as the menisci steepen over time (particularly in the presence of *pinned* evaporative thinning), the underlying dynamics will become *more* inaccurate as the simulations progress.

The location of the largest errors in Figures 4.9 - 4.12 arises as the magnitude of each derivative of the function $u(x)$ of (4.9) attains its maximum at $x = \pm 1$. The derivatives in these positions are approximated using the first and last rows of the Chebyshev differentiation matrix, which itself contains the entries of largest magnitude. Hence, in the finite-precision arithmetic of the computer simulation, the sixteen-digit representation of a derivative of high magnitude is to be calculated using matrix entries which themselves

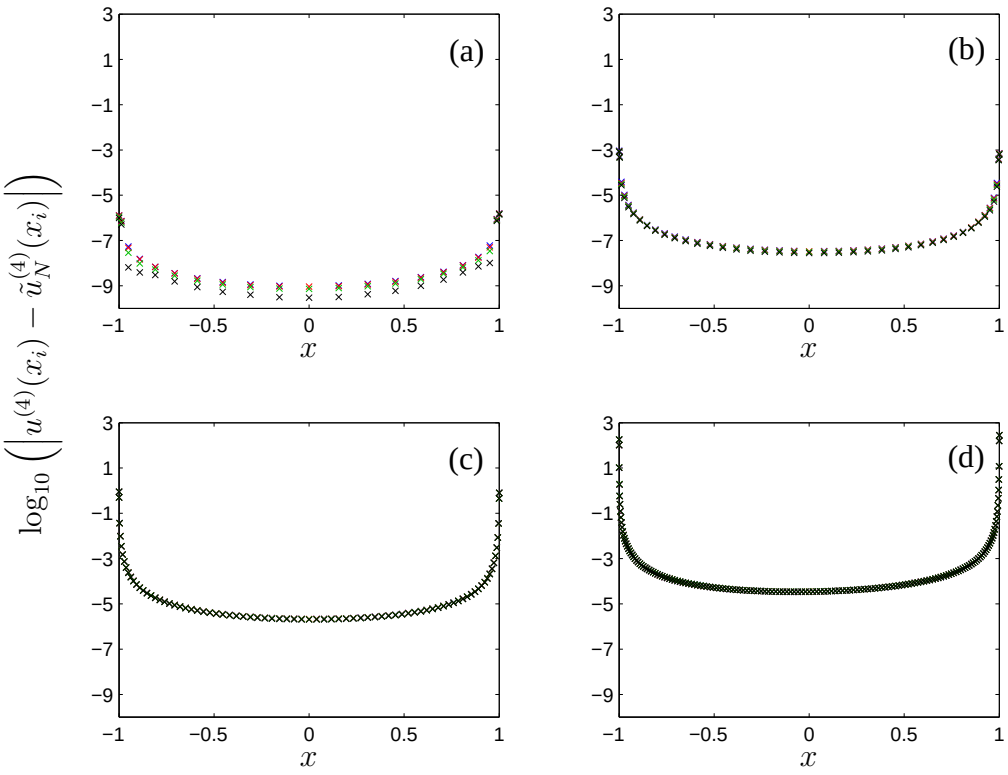

Figure 4.12: Logarithm of the absolute error in the calculation of the fourth derivative of (4.9) when $k = 10$. All colours and discretization parameters are as per Figure 4.9.

are large and evaluated only to sixteen-digit accuracy.

The predetermination of the location of the largest errors introduced by the numerical scheme gives justification for the use of initial conditions with shallower gradients than those used in the published literature. This justification is in addition to the requirement, imposed by the thin-film lubrication approximation, that all variation of quantities in the direction perpendicular to the ocular surface is of order $\mathcal{O}(\epsilon)$ relative to variation along the surface. This same approximation is employed in all the models of the published literature (with the exception of Zubkov *et al.*, 2013), yet the issue of pinning a film, which has been has been scaled to have a thickness of order $\mathcal{O}(1)$, with a meniscus height of order $\mathcal{O}(10)$ or $\mathcal{O}(100)$ is not addressed in these works.

4.4 Summary and discussion

The tests and results presented in this chapter were motivated by the need to validate the accuracy of Chebyshev differentiation, the boundary-condition and spectral-integration procedures, and the combined numerical scheme formed of the spectral spatial discretization and fourth-order, explicit Runge-Kutta time-stepping outlined in Chapter 3.

The accuracy of numerical approximations of derivatives obtained though the use of Chebyshev differentiation matrices has been demonstrated in Figures 4.1 and 4.2, wherein the maximum absolute error in the numerically-obtained derivatives converges spectrally to zero with increasing values of N, reaching the round-off plateau enforced by the finite-precision arithmetic for $N \geq 42$. Moreover, the results illustrate that first derivatives calculated using the alternative form (3.15) of $\mathbf{D}^{(1)}$, derived using the identities of (3.14), are more accurate than derivatives obtained using the original form (3.8) for the majority of values of N. This spectrally-accurate calculation of derivatives allows the spatial discretization to be carried out with significantly fewer nodes than required in the finite difference schemes of (for example) Braun & Fitt (2003), yielding a considerable

reduction in the amount of computational resource required to automate the simulations. Through a comparison of different methods for calculating higher derivatives, results show that repeated multiplication using $\mathbf{D}^{(1)}$ as defined in (3.15) yields the optimum error minimization, even when compared to the errors obtained through use of the newly-derived, explicit, higher-order differentiation matrices of §3.1.2. As a result of this evidence, (3.15) will be used in the calculation of all derivatives in the simulations presented in subsequent chapters.

The accuracy of the spectral integration method of §3.3 is demonstrated in Figure 4.3, which shows the absolute error in the calculation of the integral (3.26) for a variety of integrands (4.3). In all cases tested, the integral is obtained to machine precision for values of N as low as 42.

Calibration of the numerical scheme in §4.2 using both linear and nonlinear test evolution equations has shown the scheme to yield consistent results for a variety of combinations of spatial and temporal discretization parameters. These results give confidence that the results obtained using a coarse set of discretization parameters are both sufficiently accurate and computationally efficient.

An experimental study of the error in the numerical approximation of derivatives of a steep-sided function (4.9) in §4.3 has shown that the use of Chebyshev spectral methods to approximate the derivatives of such functions leads to localized boundary errors of large magnitude, which moreover increase with increasing N. This evidence casts doubt on the results of prior models that have used spectral methods (listed in the footnote[2] on page 106) in the simulation of film profiles with steep, pinned menisci. This doubt occurs as, in addition to the universal absence of a physical argument to support pinning[3], *and* the invalidation of assumptions made through employing the thin-film lubrication approximation in the derivation of such models, the resulting fluid dynamics are driven

[3] i.e. an argument suggesting why the contact line shouldn't slip posteriorly along the pre-wetted margin of the eyelid.

by those regions of the computational domain that contain the largest numerical errors. As such, the results of §4.3 complement the modelling constraints enforced on the present model through use of the lubrication approximation, justifying the shallow menisci employed in the simulations of subsequent chapters. Strikingly, the results presented herein appear to contradict the conclusions made in Appendix 2 of Li & Braun (2012), wherein data from a test problem (but little detail on the implementation) suggests that spectral methods are well-suited to the approximation of steep-sided functions, and that the accuracy of such approximations improves with increasing N. However, it is noted that the tests in Li & Braun (2012) include both spatial and temporal discretization, with the time-stepping carried out using MATLAB's `ode15s` solver, hence these results may not be comparable to the purely-spatial data of §4.3. Finally, it is important to note that the results in Figures 4.9 - 4.12 were obtained through use of a *spectrally-accurate* method for the approximation of derivatives, hence they pose further questions about the numerical errors encountered by models that use lower-order methods (such as finite differences) in their spatial discretization.

With the numerical scheme now outlined and tested, it is applied with confidence in Chapter 5 to model the effect of physical parameters on simulations of the isolated film-thickness evolution equation (2.71), and in Chapter 6 to model the coupled behaviour of the full tear-flow model, (2.71) and (2.72).

Chapter 5

Dynamics of a Lipid-free Tear Film

The dynamics of the tear film and its adsorbed lipid surfactant are uncoupled in this chapter to allow the modelling of a (hypothetical) 'clean' tear film in which the surfactant concentration, ψ, is set to zero. The evolution equation (2.71) for the thickness of the tear film, h, is solved subject to the boundary and initial conditions discussed in Chapter 2, allowing the dynamics of the Newtonian fluid with a stress-free interface of (dimensional) surface tension σ_0 to be studied. This simplified model allows the effects of substrate curvature, evaporation and the contact angle enforced through the eyelid boundary conditions to be isolated, and their effects observed without the additional advective influence of the lipid surfactant.

The results obtained are compared and contrasted with other surfactant-free, draining models for the tear film in the published literature (Wong *et al.*, 1996; Miller *et al.*, 2002; Braun & Fitt, 2003; Jones *et al.*, 2005; Winter *et al.*, 2010; Maki *et al.*, 2010a; Maki *et al.*, 2010b; Braun *et al.*, 2012; Li & Braun, 2012; Zubkov *et al.*, 2013). Before proceeding, it is important to note the significant differences between the derivation presented in Chapter 2 and the modelling used to develop the published models. With the exception of Jones *et al.* (2005) and Zubkov *et al.* (2013), all assert that the free surface is tangentially immobile, replacing the tangential momentum balance (2.29) with

$\mathbf{U}\cdot\hat{\mathbf{t}} = 0$[1]. Furthermore, the menisci are pinned with boundary values of order $\mathcal{O}(10)$ (and order $\mathcal{O}(100)$ in the case of Zubkov *et al.*, 2013), with central plateau thicknesses scaled to be of order $\mathcal{O}(1)$. Such menisci are not feasible in this model, as §4.3 identifies the errors inherent with the spectral approximation of such profiles, and, moreover, their presence introduces steep gradients that invalidate the assumptions of the lubrication approximation upon which this model is derived. This invalidation is observed in Zubkov *et al.* (2013), wherein a comparison of a lubrication model with full Navier-Stokes simulations in the meniscus regions identifies significant differences in the velocity profiles inside the menisci, with the lubrication model predicting contact-line velocities that conflict with the pinned Dirichlet boundary conditions (*cf.* §2.4.2). The tear-flow dynamics within all prior models is dominated by the Dirichlet pinning, which leads to meniscus-induced thinning that creates the so-called 'black lines' (McDonald & Brubaker, 1971; Miller *et al.*, 2002); these lines are impossible to replicate using the model presented herein, which allows movement of the contact line along the eyelid margin. Finally, Winter *et al.* (2010), Maki *et al.* (2010a), and sections of Braun & Fitt (2003) enforce boundary conditions on $h_{\xi\xi}$ at each eyelid, which effectively specifies the pressure at these points. Such a boundary condition is not used in this model as it cannot be motivated by appealing to the physical environment in which a real tear film exists (*cf.* §2.4.1).

Unless otherwise stated, all simulations presented within this chapter have an initial condition (2.80) formed using $h_{\text{MID}} = 1$, $r = 2$ and a blend point $b = 0.4$; numerical simulations are discretized using parameters $\{N = 20, dt = 2 \times 10^{-8}\}$.

[1]This condition is used within the lubrication approximation to yield a vanishing azimuthal velocity, $u = 0$, at the free surface. Such an approximation is valid in the flat central plateau region of the tear film but, in the steep menisci, the tangent vector aligns more closely with the direction perpendicular to the ocular surface; hence in these regions, this boundary condition for the governing equations should change to $f_1 u + f_2 v = 0$, where f_1 and f_2 are functions of h_ξ. No such amendment is made in the models that employ this boundary condition.

5.1 The effect of environmental parameters, δ and E

To demonstrate the influence of environmental factors on the dynamics of the tear film, the curvature of the ocular substrate, δ, and the evaporative flux, E, are altered. Values of $\delta = 0$ and $\delta = 5/12$ are respectively chosen to model a flat cornea with a Cartesian coordinate system, and a substrate with a realistic corneal curvature. The evaporative flux $E = 1.503 \times 10^{-2}$ is used to approximate the experimentally-obtained result of Mathers (1993) after the rescaling (2.58), which scaling promotes evaporative effects to leading-order in the mass balance (2.53). Data from evaporative simulations are contrasted with non-evaporative results obtained with $E = 0$. To isolate these physical effects, all other parameters in the model are fixed with values of $st = 1$, $\alpha_0 = 5$, and $\hat{\theta} = \pi/2$ employed in the results presented in Figures 5.1 - 5.4. As mentioned on page 52, this value of $\hat{\theta}$ is uncharacteristically large for the tear film, and effectively models an unscaled film that is nearly flat in the menisci. However, $\hat{\theta}$ is chosen for numerical accuracy as §4.3 highlights the adverse affect of narrow contact angles on the approximation of derivatives near the boundaries. Discussions warranting the introduction of $\hat{\theta}$ are given in §2.4.1, and the effects of varying the contact angle are presented in §5.2.

The influences of evaporation and substrate curvature on the evolution of the tear-film flow are displayed in Figure 5.1, which shows the late-time ($t = 1$) film profiles, corresponding to a dimensional time of five seconds (a short, but realistic, human interblink duration – Berger & Corrsin, 1974). As in §4.2, migration towards the steady-state profile is observed in each case. This migration is starkly different from the movement of the tear film in the aforementioned published works, as the novel Neumann boundary condition (2.76) for the contact angle allows the contact line to slip to its natural level. Hence the profiles of Figure 5.1 do not display the characteristic meniscus-induced thinning that is observed in all prior models. The effect of substrate curvature is illustrated by the dotted lines representing the steady-state profiles, which

are evaporatively displaced when $E \neq 0$ and given by $h_\infty(\xi) - Et$. Blue and green dotted lines display the Cartesian form of the (displaced) steady state, and red and purple the curvilinear form with $\delta = 5/12$. By comparison with the Cartesian steady states, the curvature of the eye causes a marginal thickening of the steady-state profile near the

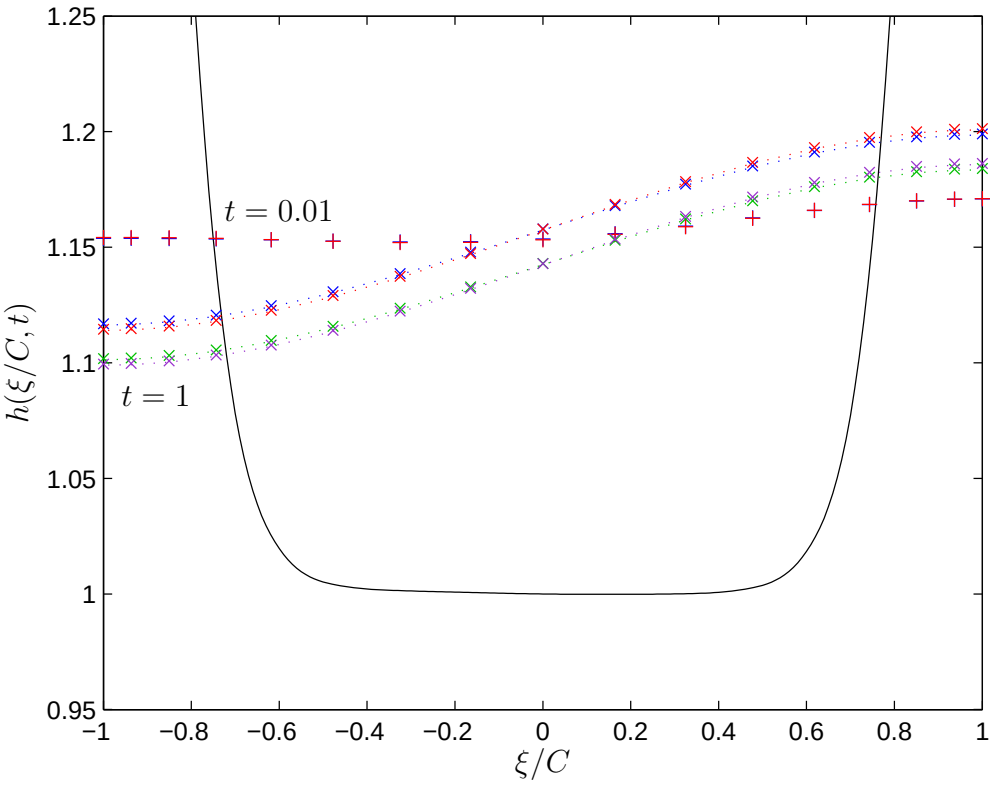

Figure 5.1: Snapshots of film profiles at $t = 0.01$ (+) and $t = 1$ (×) obtained with varying substrate-curvature and evaporative parameters, δ and E, and a scaled contact angle of $\hat{\theta} = \pi/2$. Colours represent: $\{\delta = 0,\ E = 0\}$; $\{\delta = 5/12,\ E = 0\}$; $\{\delta = 0,\ E = 1.503 \times 10^{-2}\}$, and; $\{\delta = 5/12,\ E = 1.503 \times 10^{-2}\}$. Note that at $t = 0.01$, red and blue profiles are plotted but overlay closely. Steady states and evaporatively displaced steady states (calculated as $h_\infty(\xi) - Et$) are denoted by colour-specific dotted lines. The solid black line displays a 201-knot cubic interpolation spline of the initial data when $\delta = 0$, and the apices of the menisci reach $h(\xi = \pm C, 0) = 2$.

lower eyelid ($\xi = C$) and a corresponding thinning near the upper eyelid ($\xi = -C$). This bulge over the inferior cornea when $\delta \neq 0$ reflects the changing orientation of the gravity vector relative to the ocular surface as ξ is varied in the curvilinear coordinate system; at the upper lid a component of the gravity vector pushes down upon the tear film, whilst at the lower lid the same component acts to pull the fluid away from the ocular surface (*cf.* Figure 2.2).

The effect of constant evaporation is shown to lead to a simple displacement of the film profiles in each coordinate system, supporting the conclusion of Braun & Fitt (2003) that evaporation causes thinning across the tear film (except at the pinned menisci in Braun & Fitt's model). The effect of evaporation is shown in the green and purple datasets of Figure 5.1. Comparisons between the displayed steady states and the numerically-simulated profiles show the constant loss of mass from the system to have a negligible effect on the evolution of the film towards its steady-state profile, as evidenced by the maximum difference between the $t = 1$ datasets and the appropriate steady-state profile. When $\delta = 0$, $\|h(\xi, 1) - (h_\infty(\xi) - E)\|_\infty = 5.2 \times 10^{-4}$ in both evaporative scenarios, the values agreeing to order $\mathcal{O}(10^{-8})$. Similarly, when $\delta = 5/12$ the maximum difference between numerically-simulated data and the evaporatively displaced steady state is 5.1×10^{-4} in both evaporative cases, with agreement to order $\mathcal{O}(10^{-9})$. That these maximum differences from different evaporative scenarios agree to such a high order suggests that the value of E has negligible effect on the transient film dynamics.

The non-evaporative profiles at $t = 0.01$ in both coordinate systems are represented in Figure 5.1 by the closely overlaying red and blue plus signs; they demonstrate the rapid relaxation of the tear film towards a near-steady-state shape. The subsequent motion of the film gives rise to a slower, gravity-driven transition towards the steady state (or displaced steady state when $E \neq 0$). The effect of gravitational drift on the tear film is also observed in the models mentioned on page 111, enhancing the meniscus-induced thinning near the upper eyelid. The close overlaying of the datasets at $t = 0.01$ shows substrate curvature to

have little influence on the initial relaxation phase of the tear-film evolution, the profiles displayed differing by a maximum amount of 3.9×10^{-4}.

Motivated by the (relatively) rapid early dynamics, the behaviour of the $\{\delta = 5/12, E = 0\}$ simulation (the red data of Figure 5.1) is displayed in Figure 5.2 for $t \in [0, 0.05]$, and shows the swift retraction of the menisci occurring for $t < 5 \times 10^{-3}$ (corresponding to the first 2.5×10^{-2} dimensional seconds). This dataset is representative of the early dynamics in all the simulations displayed in Figure 5.1. The initial retraction of the menisci, coupled with a more minor drop in the fluid depth in the region close to $\xi = 0$,

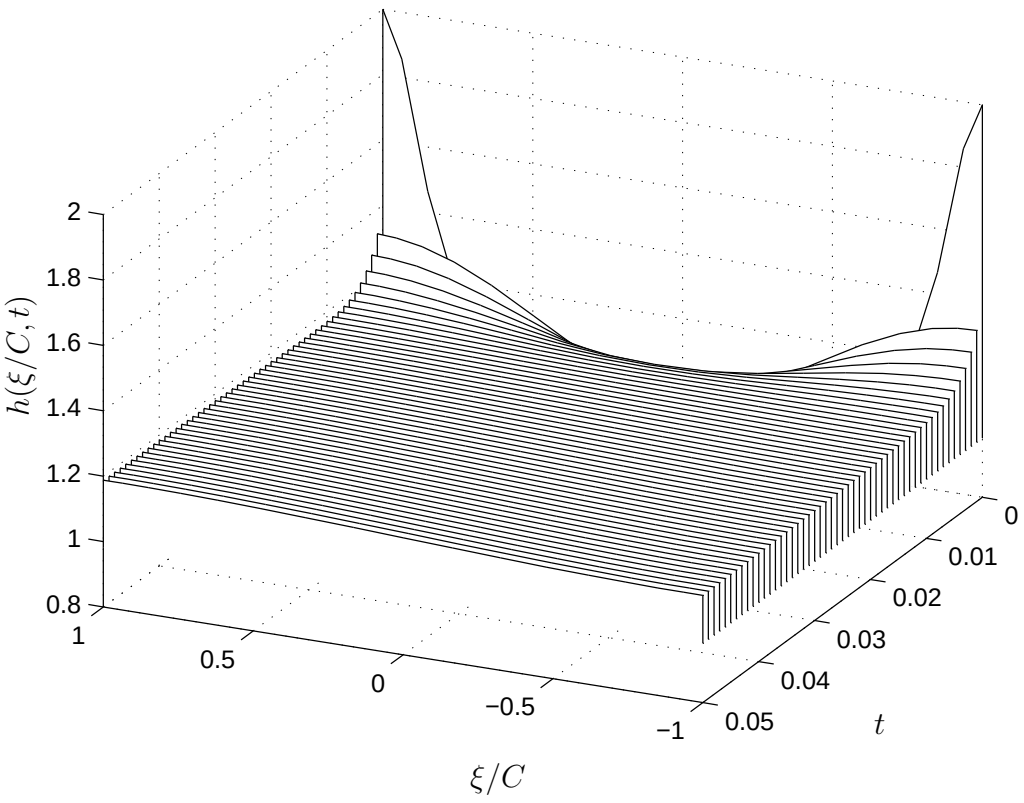

Figure 5.2: Initial dynamics of the simulation with $\delta = 5/12$ and $E = 0$ (*cf.* Figure 5.1), for $t \in [0, 0.05]$. Snapshots are spaced temporally by a step $\Delta t = 10^{-3}$. All discretization parameters are as before. The lower lid is positioned towards the left-hand side of the plot.

results in the film profile bulging upwards in regions around $\xi \approx \pm 0.7$ to conserve mass. Hence the initial movement of the tear film acts to thicken the regions associated with significant thinning in models that pin the meniscus, reinforcing that Dirichlet boundary conditions are required in order to generate black-line behaviour in simulations. At both eyelids, the rapid recession of the contact lines quickly subsides, giving way to a slower rate of recession at the upper lid ($\xi = -C$), whilst the lower-lid contact line recedes until $t \approx 1.2 \times 10^{-2}$, when its direction of motion changes and it begins advancing back up the eyelid.

The change in the direction of motion of the lower-lid contact line is shown more clearly in Figure 5.3, which tracks the position of the upper and lower contact lines over time in simulations that represent both $E = 0$ and $E \neq 0$ in the curvilinear coordinate system with $\delta = 5/12$. The effect of evaporation on the early dynamics of the flow is shown to be negligible as, at each eyelid, the positions of the contact lines in each evaporative scenario overlay closely, differing by an amount of order $\mathcal{O}(10^{-3})$ at each eyelid when $t = 0.1$. After the initial recession and subsequent change of direction of motion of the lower-lid contact line, the slow advancement up the eyelid marginally overshoots the steady-state position by an amount of order $\mathcal{O}(10^{-4})$ when $t > 0.19$ in the $E = 0$ simulation. In contrast, when $E \neq 0$, the long-term effect of evaporation is evident as the position of the lower-lid contact line undergoes a second change of direction of motion close to $t = 0.18$. At this time, constant evaporative losses diminish the film profile at a faster rate than the contact line's advancing velocity. The upper-lid contact line positions exhibit a monotonic convergence towards the steady-state profile in both evaporative scenarios. In the datasets at each eyelid, the effect of evaporation can be observed through the steady separation of the data at greater times in the lower plot of Figure 5.3, reinforcing the assertion that evaporation plays a minor role in the overall dynamics of the tear-film flow. This minor role is expected through the scalings (2.58) employed in the derivation of the model, which scalings promote evaporative effects to leading-order in the interfacial mass balance (2.53). To remain physically accurate, this

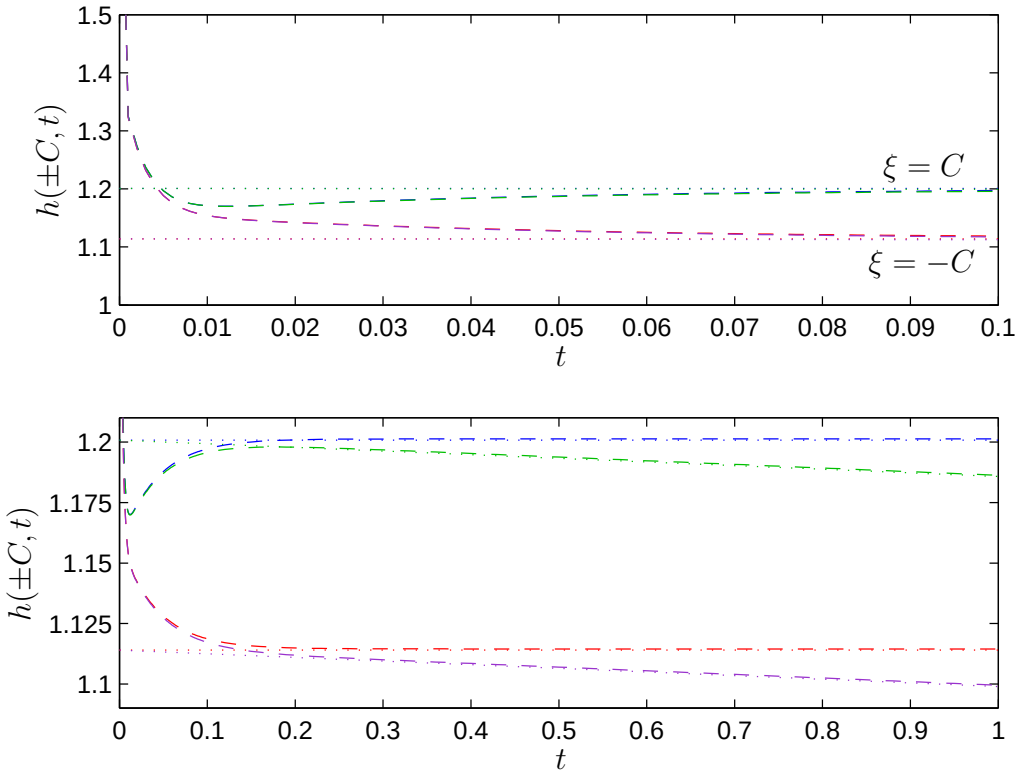

Figure 5.3: Temporal evolution of the contact-line positions with $\delta = 5/12$. **(Top)** $t \in [0, 0.1]$, and **(bottom)** $t \in [0, 1]$. Dashed coloured lines denote the following contact-line location and evaporative-parameter pairings: $\{\xi = C, E = 0\}$; $\{\xi = -C, E = 0\}$; $\{\xi = C, E = 1.503 \times 10^{-2}\}$, and; $\{\xi = -C, E = 1.503 \times 10^{-2}\}$. Colour-coordinated dotted lines represent the steady-state contact line positions $h_\infty(\pm C) - Et$. Note that the axis scalings are different in each plot.

promotion leads to the value of $E = 1.503 \times 10^{-2}$ used within simulations for which all terms are expected to be of order $\mathcal{O}(1)$, whence evaporation has only a large-time effect on the tear film dynamics.

Figure 5.4 displays the effect of the substrate curvature on the conservation of mass (in the absence of evaporation) and the $\omega\omega$-component of the stress tensor, $\mathbf{T}_{\omega\omega}$ (2.10), evaluated at the contact lines. This component represents the extra stress, above that of atmospheric pressure, exerted on the contact line by the shape of the tear-film profile, and

is not discussed in previous works on the tear film despite the large gradients induced in the film thickness through the pinning of the menisci. In scaled, marginal-surface coordinates the stress component's dimensional form is

$$\mathbf{T}_{\omega\omega}(\xi,\omega,t) \;=\; -\frac{\mu U_0}{\epsilon^2 L}\left(p - p_{\text{ATM}} - 2\epsilon^2 v_\omega\right) \,. \tag{5.1}$$

In the upper plot of Figure 5.4, the rapid initial dynamics cause a jump in the mass of the system; at $t = 10^{-4}$ the relative percentage increase in mass in both coordinate systems is

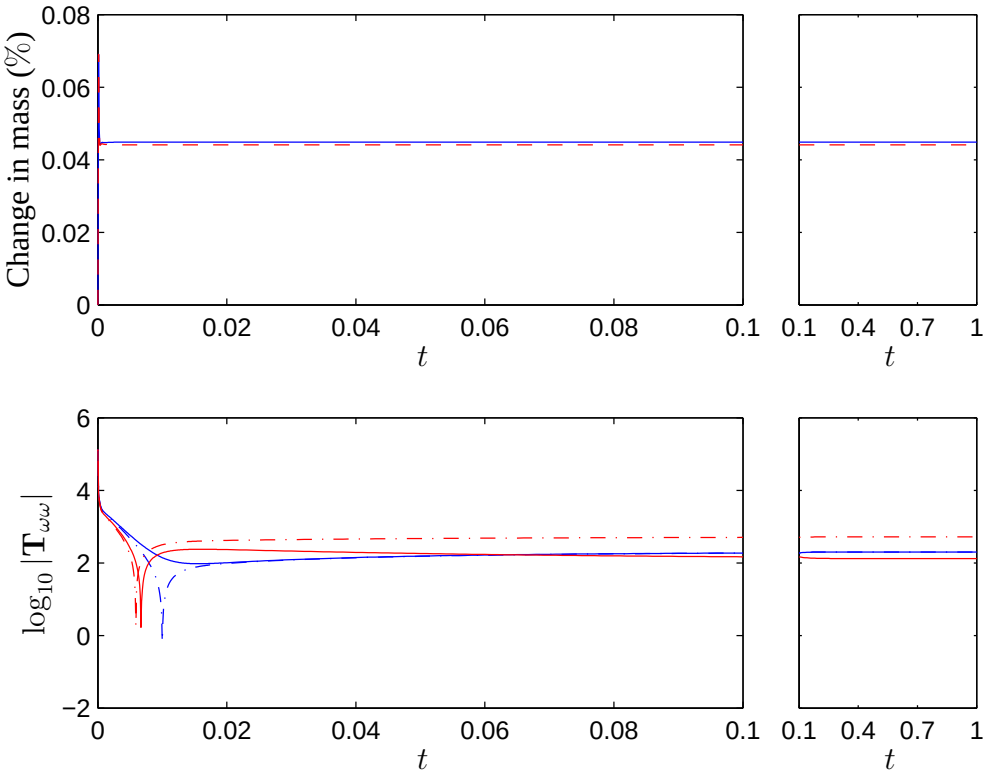

Figure 5.4: Temporal variation, in non-evaporative simulations ($E = 0$), of **(top)** the percentage change in mass with varied substrate curvature: $\delta = 0$, and $\delta = 5/12$; and **(bottom)** the logarithm of the modulus of $\mathbf{T}_{\omega\omega}$ (2.10) at the contact lines. Solid and dot-dashed lines respectively denote data at $\xi = C$, and $\xi = -C$, with colours as in the upper plot. In each row, the larger plot shows the early dynamics with $t \in [0, 0.1]$, whilst the smaller plot displays $t \in [0.1, 1]$. The use of dashed red lines in the upper plot is purely for clarity, allowing both traces to be seen.

$6.9\times10^{-2}\%$. In each simulation this value subsequently decreases, reaching $4.47\times10^{-2}\%$ when $t = 10^{-3}$ in the $\delta = 0$ simulation, and $4.42\times10^{-2}\%$ at the same time in the $\delta = 5/12$ simulation. After these initial jumps, the mass in the systems is quasi-constant throughout the remainder of the simulations, with the final ($t = 1$) percentage change (relative to the initial conditions) in mass found to be $4.48 \times 10^{-2}\%$ when $\delta = 0$, and $4.41 \times 10^{-2}\%$ when $\delta = 5/12$. To identify the mass-conserving properties of the evolution equation and numerical scheme during the slower phases of motion, the percentage changes are renormalized against the mass in the system at $t = 10^{-3}$. Relative to these masses, the percentage change in mass per time-step over the period $t \in [10^{-3}, 1]$ (corresponding to 4.995×10^7 steps) is found to be $2.37 \times 10^{-12}\%$ with $\delta = 0$, and $-2.64 \times 10^{-12}\%$ with $\delta = 5/12$. These figures pay testament to the accuracy of the integration scheme of Chebyshev spatial discretization coupled with fourth-order Runge-Kutta time-stepping described in Chapter 3, and also to the spectral integration procedure of §3.3.

In the lower plot of Figure 5.4, $\mathbf{T}_{\omega\omega}$ shows marked differences between the large-time behaviours in the Cartesian and curvilinear formulations. The initial contact-line stress at each eyelid in both datasets plotted is

$$\mathbf{T}_{\omega\omega}(\pm C, h, 0) \;=\; -1.3 \times 10^5 \text{ Pa} \;\approx\; -1.3 P_{\text{ATM}}\,,$$

where the minus sign denotes that this stress acts in the opposite direction to $\mathbf{e}_\omega$ (i.e. towards the ocular surface). In the absence of a Dirichlet boundary condition, this excess pressure causes the rapid retraction of the menisci described in the preceding paragraphs, which allows the stresses to dissipate. The sharp downward spikes exhibited at both eyelids when $t < 7 \times 10^{-3}$ in the $\delta = 5/12$ data, and at $t = 10^{-2}$ in the upper-lid data when $\delta = 0$ represent the change in the sign of (5.1) from negative to positive. The extra stress at the lower lid in the $\delta = 0$ simulation remains negative for all times tested.

The differences between the large-time stress behaviour in the Cartesian and curvilinear simulations (and the differences between stresses at $\xi = \pm C$ when $\delta = 5/12$) are caused by the position-dependent force of gravity in the curvilinear coordinate system.

When the contact angle is specified as $\hat{\theta} = \pi/2$, the contact-line stresses (5.1) in the Cartesian and curvilinear formulations may be simplified because $h_\xi(\pm C, t) = 0$. In this case, these stresses are given by

$$\begin{aligned}
\mathbf{T}^0 \equiv \mathbf{T}_{\omega\omega}\Big|_{\xi=\pm C,\,\hat{\theta}=\pi/2,\,\delta=0} &= -\frac{\mu U_0 \alpha_0 \mathcal{A}}{\epsilon^2 L}\Big(\epsilon^2 C^4 h^2 h_{\xi\xi\xi\xi} - C^2 h_{\xi\xi}\Big), \qquad \text{and} \\
\mathbf{T}^+ \equiv \mathbf{T}_{\omega\omega}\Big|_{\xi=\pm C\,,\hat{\theta}=\pi/2,\,\delta\neq 0} &= -\frac{\mu U_0}{\epsilon L}\left\{\frac{\alpha_0 \mathcal{A}}{\epsilon}\Big[\epsilon^2 C^4 h^2 h_{\xi\xi\xi\xi} - C^2\left(1-\epsilon^2\delta^2 h^2\right) h_{\xi\xi} \right.\right. \\
&\qquad \left.\left. - \delta^2 h\Big] - \epsilon\delta\, st\, h^2 \sin\left(\frac{\delta\xi}{C}\right)\right\},
\end{aligned} \tag{5.2}$$

wherein the pressure and radial velocity have been substituted using (2.65). After the rapid early dynamics the film profile has reached a near-steady-state shape, which profile then slowly evolves towards the true steady state. When $\delta = 0$, the overlaying blue data series in the lower plot of Figure 5.4 occur because the steady state (2.89) is a third-order polynomial in ξ with a second derivative that is an odd function. As such, the fourth derivative in $\mathbf{T}^0$ is removed and the remaining term has the same modulus at $\xi = \pm C$.

When $\delta \neq 0$, the steady state (2.90) is formed from a combination of transcendental functions, and has derivatives that are neither odd nor even. When these derivatives are substituted into $\mathbf{T}^+$ cancellations yield the difference between a position-dependent gravitational term, and a constant that is related to the initial mass in the system (*cf.* §2.4.3). This position dependence, which causes the gravitational term to have opposite signs at each lid, gives rise to the unequal contact-line stresses when $\delta \neq 0$. Note that, in all cases displayed in Figure 5.4, the magnitude of the stress for large times is less than 525 Pa. This value is three orders of magnitude smaller than standard atmospheric conditions, thus the stresses do not induce movement of the fluid during the latter stages of evolution.

5.2 The effect of boundary and initial conditions

In addition to the influence of environmental factors on the evolution of the tear film, the fluid dynamics are also found to be highly dependent on both the boundary conditions imposed at the eyelids and the initial configuration of the free surface. The contact angle $\hat{\theta}$ at the three-phase contact line specifies the value of h_ξ at the eyelids through boundary condition (2.76), which determines the shape of the apices of the menisci and further affects the boundary condition for $h_{\xi\xi\xi}$ (2.77). Alterations to the initial condition enable the effects of shallower menisci on the transient dynamics of the tear-film flow to be observed. In this subsection, results are presented from simulations with fixed parameter values of $st = 1$, $\alpha_0 = 5$, $\delta = 5/12$ and $E = 1.503 \times 10^{-2}$. It is important to reiterate here that $\hat{\theta}$ is a *scaled* contact angle, and as such is unphysically large for the tear film: this rescaling is required both to maintain validity of the assumptions of the thin-film lubrication approximation used in the derivation of the model, and to ensure accuracy in the numerical approximation of spatial derivatives (*cf.* §4.3). Nevertheless, in the absence of a boundary condition specifying the contact angle in prior models of the tear film, all results presented below are novel to the field of tear-film modelling.

Figure 5.5 displays the effect of the contact angle on the latter stages of the tear-film evolution. Each initial condition is obtained using the parameter values listed at the beginning of this chapter, hence the differences in the initial shape of the menisci are caused solely through the enforced contact angle. The effect of the contact angle is shown more notably in the profiles at $t = 1$ which, as in Figure 5.1, show near-steady-state behaviour. When $\hat{\theta} \neq \pi/2$, the non-zero value of h_ξ at the eyelids forces the film thickness to decrease with increasing distance from each boundary. This causes the central region of the tear film to form a shallow trough, and consequently, to conserve mass, the contact lines react by rising up the eyelids by comparison with the $\hat{\theta} = \pi/2$ profile. Hence, despite the boundary conditions being enforced at $\xi = \pm C$, their influence dramatically

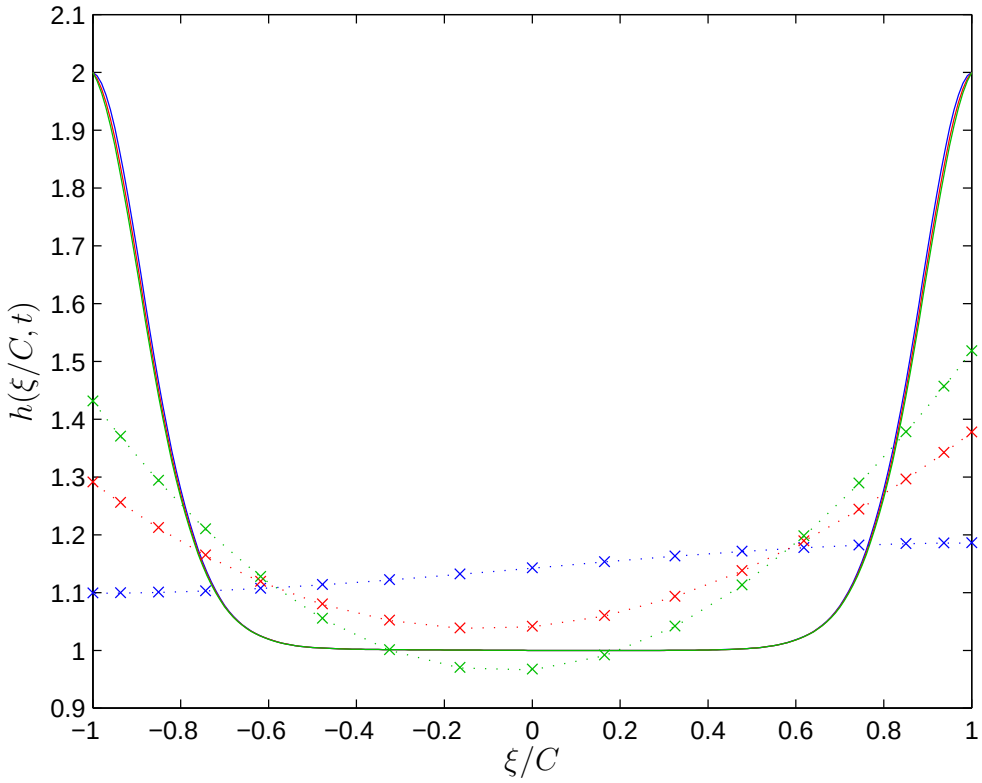

Figure 5.5: Film profiles at $t = 1$ ($\times$) with colours representing contact angles of $\hat{\theta} = \pi/2$, $\hat{\theta} = \pi/3$, and $\hat{\theta} = \pi/4$. For each contact angle, solid and dotted lines respectively plot the initial condition and evaporatively displaced steady-state profile. The blue dataset repeats the purple data presented in Figure 5.1.

affects the evolving global file profile. This is in contrast to the results of the published tear-film drainage models (listed on page 111), wherein the central plateau region of the flow is primarily influenced by gravity and evaporation, with the pinned menisci primarily affecting the level of thinning at the meniscus-plateau joins, which thinning results in the formation of 'black lines' (Miller *et al.*, 2002). The redistributive effect of gravity is illustrated in Figure 5.5 as, for all $\hat{\theta}$ values, the contact line at the lower lid $\xi = C$ is located higher on the eyelid than at the upper lid $\xi = -C$.

The dimensional contact-line velocities are obtained from the simulated film-thickness

profiles by calculating $v(\pm C, h, t)$ from (2.65), and re-dimensionalising using the *ansatz* (2.41). The evolution of the early ($t \leq 5 \times 10^{-2}$) contact-line velocities from the simulations presented in Figure 5.5 is displayed in the upper plot of Figure 5.6, showing that the initial dynamics quickly subside, giving way to slow movement towards the steady profile (*cf.* Figure 5.2). For each value of $\hat{\theta}$ displayed, the speeds of recession induced by the initial condition are given in the first line of Table 5.1. These speeds are extremely large when considered in the context of a meniscus of depth $2d = 10^{-5}$ m, and are several orders of magnitude greater than those predicted from the initial conditions in the models

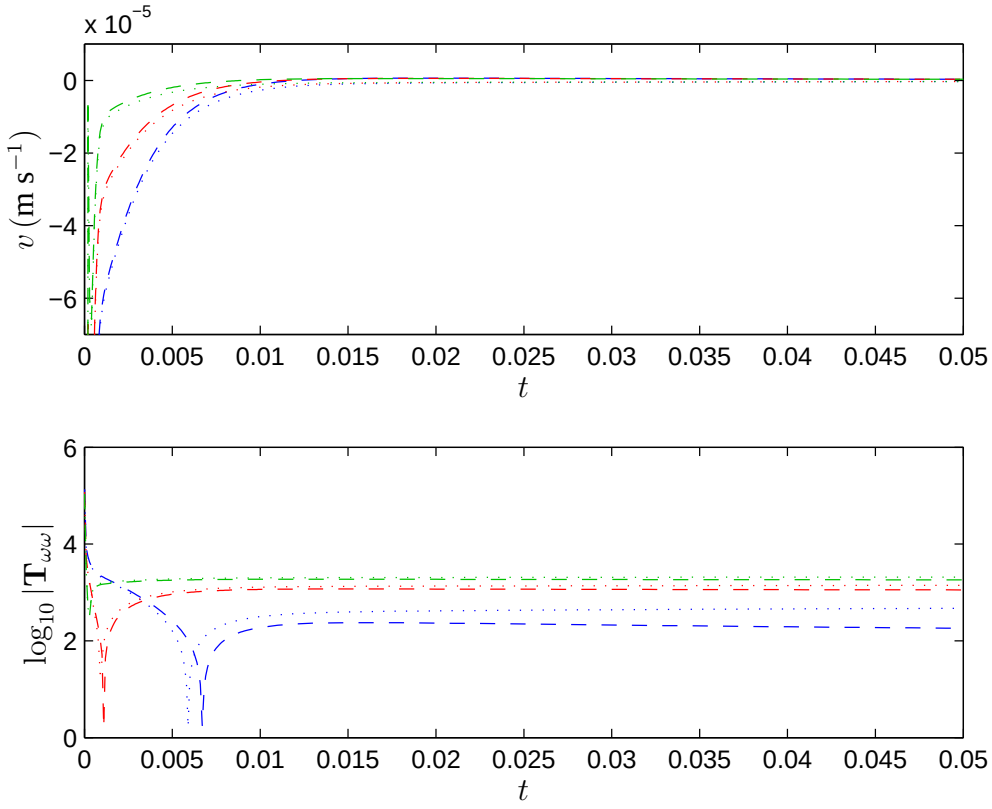

Figure 5.6: (Top) Dimensional contact-line velocities, and **(bottom)** logarithm of the magnitude of $\mathbf{T}_{\omega\omega}$ (2.10) at the contact lines for $t \in [0, 5 \times 10^{-2}]$, with parameter values and colour-coding as in Figure 5.5. Dashed and dotted datasets respectively represent quantities obtained at $\xi = C$ and $\xi = -C$. A discussion of the initial velocities is given in the text.

Table 5.1: The initial receding contact-line velocities, which are not displayed in the upper plot of Figure 5.6. All velocities are dimensional and expressed in units of m s^{-1}.

t	$\hat{\theta} = \pi/2$	$\hat{\theta} = \pi/3$	$\hat{\theta} = \pi/4$
0	1	0.91	0.85
10^{-4}	0.92×10^{-3}	1.1×10^{-3}	1.3×10^{-3}

of Braun & Fitt (2003) and Maki *et al.* (2010a), respectively (2.84) and (2.85). However, the movement of the contact lines leads to dissipation of the stresses, with the result that the contact-line speeds are rapidly diminished, reaching the values in the second line of Table 5.1 by $t = 10^{-4}$. These speeds are all of the same order as those in (2.84) and (2.85).

This deceleration continues: at $t = 10^{-3}$ the magnitude of the receding contact-line velocities in each simulation is of order $\mathcal{O}(10^{-5}$ m $s^{-1})$, and for each dataset the receding velocity at the lower lid is smaller than that at the upper lid. The direction of motion of the lower-lid contact line is reversed in all three datasets by a nondimensional time of $t = 1.3 \times 10^{-2}$, with the reversal in direction occurring first in the simulation with $\hat{\theta} = \pi/4$, and last when $\hat{\theta} = \pi/2$. This change in direction of motion reaffirms that the meniscus-driven dynamics rapidly diminish, being replaced by gravitational drift that pulls the tear fluid towards the impermeable lower lid. The accumulation of fluid causes the film profile to bulge outwards from the substrate, whence the contact line slowly advances along the lower lid to reach its steady-state position.

The rapid diminution of the contact-line velocities – in all cases, $v(\pm C, h, 0.1) = \mathcal{O}(10^{-7}$ m $s^{-1})$ – ensures that, for moderate and late times, the movement of the contact line (and the entire free surface) is increasingly influenced by a speed of recession that is attributed to the constant evaporative flux. The velocity component normal to the free

surface is readily obtained by rearranging the mass balance at the free surface (2.7)

$$\left(\mathbf{U} - \mathbf{U}^S\right) \cdot \hat{\mathbf{n}} \;=\; \frac{J}{\rho}\,.$$

As the simulations evolve towards the quiescent steady state, the late-time bulk fluid velocity, $\mathbf{U}$, is assumed to be negligible as all dynamic movement ceases. Using the unit normal (2.26) and the free-surface velocity (2.27), and changing to scaled, marginal-surface coordinates, the evaporative speed of recession of the quasi-steady profile is approximated by

$$\chi_t \;=\; -\frac{J}{\rho}\left(1 + \frac{\epsilon^2 C^2 \tilde{h}_{\tilde{\xi}}^2}{(1+\epsilon\delta\tilde{h})^2}\right)^{1/2} \approx -1.5 \times 10^{-8}\,\mathrm{m\,s^{-1}}\,, \tag{5.3}$$

wherein tildes have been re-appended to non-dimensional, scaled variables for clarity, and parameter values are taken from Table 2.1. Note that, by a non-dimensional time of $t = 0.26$, contact-line velocities in all simulations in Figure 5.6 are of order $\mathcal{O}(10^{-9}\ \mathrm{m\,s^{-1}})$, whence the dominant factor determining the location of the contact line is the constant rate of evaporation. The evaporative speed of recession (5.3) is attributed to *all* points across the tear film, thus, in collaboration with the lower plot of Figure 5.3, it highlights the contradiction inherent within all prior evaporative models of the tear film: that in the absence of a suction force drawing fluid up to the pinned height, the meniscus thickness *must* be diminished through the evaporative loss of fluid. Accordingly, such models could be trivially amended to contain a time-dependent Dirichlet boundary condition

$$h(\pm C, t) = h_{\text{PIN}} - Et\,, \tag{5.4}$$

where h_{PIN} is the non-evaporative pinning height. In addition to alleviating the contradiction described above, the use of such a boundary condition in pinned models would complement the observation that the eyelids maintain a higher temperature than the cornea (Tomlinson *et al.*, 2011), which observation identifies that evaporative loss should be enhanced in the menisci.

The lower plot of Figure 5.6 shows that a reduction in $\hat{\theta}$ increases the magnitude of the late-time stresses at the contact line. Moreover, reducing $\hat{\theta}$ also yields a reduction in the disparity between the late-time stresses at each eyelid, which reduction is enhanced in Figure 5.6 through the logarithmic scaling of the stress. When $\hat{\theta} \neq \pi/2$, the expression for the stress component (5.1) cannot be simplified through setting h_ξ equal to zero at the contact line, as substituted in (5.2). Instead, the expanded form of (5.1) is found to contain terms proportional to h_ξ^2 and $h_\xi h_{\xi\xi\xi}$ which, as $\hat{\theta}$ is reduced, become dominant in

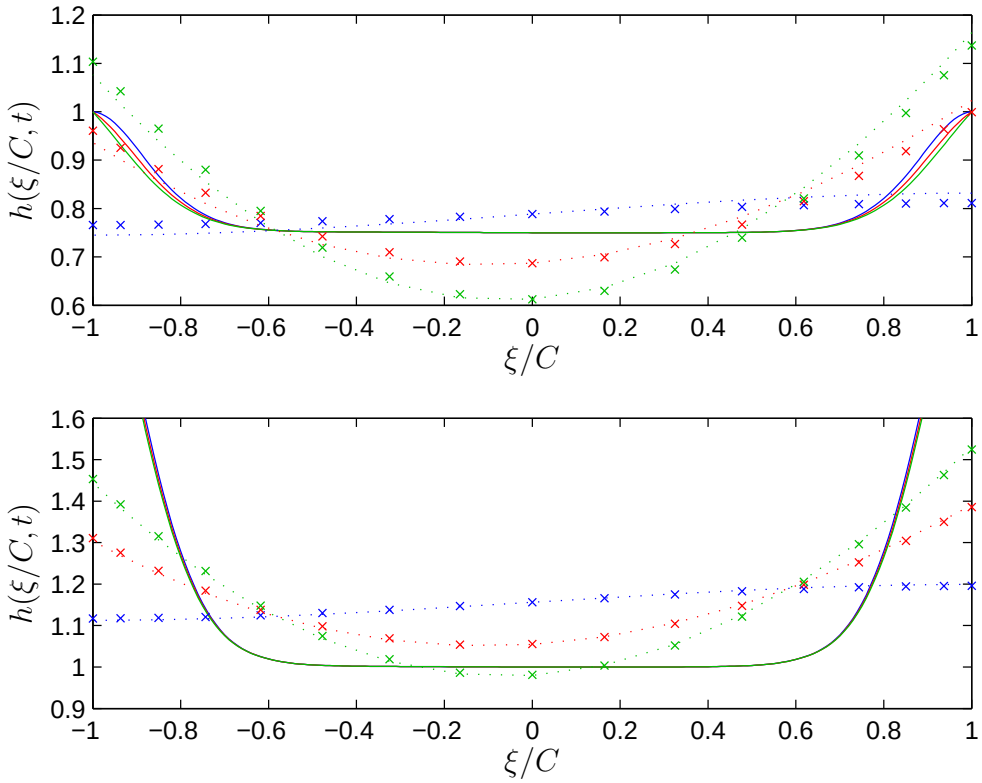

Figure 5.7: The effect of the initial condition upon the transient dynamics of the flow is illustrated using **(top)** an initial condition with $h_{\text{MID}} = 3/4$, $r = 4/3$, and $b = 0.4$ (*cf.* §4.2.2), and **(bottom)** the simulations of Figure 5.5. Crosses denote film profiles at $t = 0.1$, and colour coding and line styles are as per Figure 5.5. The upper dataset was simulated using discretization parameters of $N = 20$ and $dt = 10^{-7}$.

the calculation of the stress. Through the specification of the boundary conditions (2.76) and (2.77), the derivatives h_ξ and $h_{\xi\xi\xi}$ are individually found to have similar magnitudes at both contact lines

$$|h_\xi(C,t)| \approx |h_\xi(-C,t)| \qquad \text{and} \qquad |h_{\xi\xi\xi}(C,t)| \approx |h_{\xi\xi\xi}(-C,t)|\,;$$

hence, by reducing $\hat{\theta}$, the magnitudes of $\mathbf{T}_{\omega\omega}$ at each contact line are found to coincide at late times.

The influence of the initial condition on the subsequent film dynamics is illustrated by contrasting simulations that use the initial condition of §4.2.2 with results previously discussed in this section. The initial condition of §4.2.2 has shallower menisci, and a thinner central plateau region than the initial condition used throughout this chapter. By reducing the height of the initial condition, and hence the volume of fluid, the evolution of the tear film is slowed. This slowing is illustrated by comparing the differences between the numerically-simulated data at $t = 0.1$, and the evaporatively-translated steady states in the upper and lower plots of Figure 5.7, as shown in Table 5.2. This data demonstrates that the redistribution of fluid by gravity has occurred earlier in the simulations that use the taller initial condition, the maximum differences in this case being an order of magnitude smaller than those from simulations using the smaller initial condition. This slowing of the fluid dynamics in thinner films is expected, as the velocities (2.65) and evolution equation (2.71) are proportional to positive powers of h. Importantly, without

Table 5.2: The maximum difference, $\|h(\xi,0.1) - (h_\infty(\xi) - 0.1E)\|_\infty$, between the evaporatively displaced steady-state profiles, and the simulated data at $t = 0.1$ in the datasets shown in Figure 5.7.

Initial condition	$\hat{\theta} = \pi/2$	$\hat{\theta} = \pi/3$	$\hat{\theta} = \pi/4$
$h_0(\xi)$ from §4.2.2	2.1×10^{-2}	2.4×10^{-2}	2.7×10^{-2}
$h_0(\xi)$ from §5	4.7×10^{-3}	7.0×10^{-3}	9.1×10^{-3}

the inclusion of intermolecular forces in the bulk fluid stress tensor (2.10) in the derivation of the tear-film model, which forces affect the stability of especially thin regions of the tear film (see, for example, Ruckenstein & Jain, 1974; Jensen & Grotberg, 1992; Oron *et al.*, 1997), the positive powers of h in (2.71) preclude the film from rupturing through fluid advection alone; rupture is only achievable through evaporative loss when $E > 0$.

The size of the menisci, coupled with the contact angle at the eyelid, has a significant effect on the behaviour of the tear film. In the case of the initial condition of §4.2.2, the steady-state profile at $t = 0$ is predicted to be thicker than the initial condition at the lower meniscus when $\hat{\theta} = \pi/3$, and thicker at both menisci when $\hat{\theta} = \pi/4$. (This remains true of the evaporatively displaced steady states shown at $t = 0.1$ in the upper plot of Figure 5.6.) Hence, in the simulations with $\hat{\theta} = \pi/3$ and $\hat{\theta} = \pi/4$, the rapid initial retraction of the menisci is quickly reversed as the contact lines start to advance along the eyelid to reach their steady positions. These advancing contact-line speeds are found to be two orders of magnitude greater than those observed in Figure 5.6, reflecting that the advancement is not simply due to overshoot of the initial retraction of the menisci (which is seen at the lower lid in all simulations, see Figure 5.3), but that in these cases the initial retraction is contrary to the motion that is required for the film to reach its steady state, hence these contact lines advance at a faster rate than those for which the initial retraction aids the redistribution of the film under gravity.

The reduction in the height of the menisci affects the magnitude of the initial recessional velocities of the contact lines as, in each simulation using the initial condition of §4.2.2, the contact lines initially recede with dimensional velocities of order $\mathcal{O}(10^{-2}$ m s$^{-1})$, (*cf.* Table 5.1). This magnitude is reduced through the smaller disparity between the height of the central plateau and the contact lines, which induces smaller stresses acting along the line of the eyelid margin. The influence of taller menisci driving faster film dynamics is also observed in Braun & Fitt (2003), as steeper menisci are seen to yield faster rupture times. However, the increasingly-rapid thinning that leads

to the rupture observed in Braun & Fitt (2003) is driven by pinning the menisci at greater heights, whereas, through allowing contact-line movement, the present model predicts rupture times that are not dependent on the height of the menisci, with rupture being a large-time evaporative effect that occurs after the meniscus-driven dynamics have subsided. In the present model, the height of the menisci only affects the magnitude of the initial movement of the tear film.

5.3 Summary and discussion

The drainage of the tear film under the influence of gravity, substrate curvature, evaporation and the contact angle specified at the three-phase contact line has been studied in this chapter, allowing comparisons to be drawn with results from models within the published literature. In the absence of the interfacial stresses induced through the modelling of a heterogeneous adsorbed surfactant layer, this chapter allows the dynamic behaviour of the dissipative film-thickness evolution equation (2.71) to be studied in isolation.

The novel boundary condition (2.76) that specifies the contact angle between the eyelid and the free surface at the three-phase contact line is found to have a strong influence on the film profile, primarily as it allows the contact line to slip along the eyelid margin. This behaviour is unseen in all previously-published models for drainage of the tear film, wherein Dirichlet boundary conditions preclude contact-line movement, giving rise to flows that are driven by ever-steepening menisci with diminishing contact angles (see, for example, Braun & Fitt, 2003, Figure 2). Moreover, such Dirichlet pinning has been shown to be unphysical in the presence of evaporation from the tear film, and a pseudo-pinned boundary condition (5.4) suggested to ameliorate the issue. By tracking the temporal evolution of $\mathbf{T}_{\omega\omega}$ (5.1) at the contact lines, the present model shows the stresses induced by the menisci are dissipated as the fluid is redistributed to its equilibrium

position. A discussion of this stress is conspicuously absent in all of the existing tear-film models in the published literature, as the steepness of the menisci would generate large contact-line stresses that could well lead to de-pinning of the film. Furthermore, at the feet of the menisci (where they join the flat plateau region over the centre of the eye), the high curvatures in the free surface would induce large pressures. Thus in flows that pin the menisci, the spatial limits of the menisci are liable to be locations that experience large stresses, which stresses could damage the delicate ophthalmic tissues surrounding the tear film. In the absence of explicit forms for the late-time film profiles in these models, it has not been possible to calculate such stresses here.

In addition to allowing slip of the contact line, the contact angle $\hat{\theta}$ enforced through (2.76) affects the velocity of the contact line, and also acts jointly with gravity to specify the position and value of the thinnest part of the tear film. As such, when steady evaporation (which is found to have only large-time thinning effects) is included in the model, the site of rupture and the time taken for the film to reach zero depth are strongly dependent on $\hat{\theta}$ (for a given initial volume of tear fluid). For example, in the three simulations presented in Figure 5.5, the time to rupture and the position at which rupture occurs are displayed in Table 5.3. In all cases, the times taken to reach rupture are significantly longer than the duration of a normal human interblink of roughly five to eight seconds (Berger & Corrsin, 1974); via (2.41), the shortest nondimensional time presented here, $t_{h=0} = 65.2$, corresponds dimensionally to 5 minutes 26 seconds. The negligible effect of evaporation on transient film dynamics (*cf.* §5.1) coupled with the large dimensional times to rupture support the conclusion that it has only a minor effect on the dynamics of the tear film, and that evaporation must act in concert with another deficiency to develop the dry-eye phenomenon studied in, for example, Mathers (2004).

Importantly, through comparisons of the novel contact-line-slippage behaviour of the tear film enabled through boundary condition (2.76) with the behaviours demonstrated in existing models of the tear film, it is hypothesized here that the human tear film

exhibits both pinning and slip at the contact line, but that pinning is the cause of dry-eye phenomena such as the 'black lines' (McDonald & Brubaker, 1971; Miller *et al.*, 2002). Such contact-line behaviour is supported by the *in vitro* results of Leiske *et al.* (2011), in which dynamic wetting experiments using water droplets coated with insoluble Meibomian lipid show the contact line to exhibit both pinning and de-pinning. In this so-called 'bi-behavioural' model for the contact line, the stress-induced slip of 'normal' tear films towards their steady-state profiles allows fluid to leave the menisci, washing across the film to thicken the plateau regions as observed within, for example, Figure 5.2. Conversely, maladies of the eyelid margin may generate regions that resist the contact-line stresses causing the menisci to pin, which pinning is readily shown in the existing literature (listed on page 111) to create significantly-thinned regions at the feet of the menisci. Under this hypothesis, the treatment of aqueous-deficient dry-eye diseases would need to focus on possible issues at the eyelid margins, with the express aim of thinning the menisci, rather than thickening the central plateau through the use of tear substitutes (Holly & Lemp, 1977; Jossic *et al.*, 2009).

Variation of the parameter δ has shown the influence of the underlying corneal curvature on tear-film dynamics to be small but non-vanishing. In Figure 5.1, comparison of non-evaporative results obtained in Cartesian and curvilinear coordinate systems at $t = 1$ shows the latter system to yield a tear-film profile that is 0.21% thinner at the upper eyelid and 0.19% thicker at the lower lid than the former, which discrepancies

Table 5.3: Non-dimensional time to rupture and site of rupture in the three simulations shown in Figure 5.5.

$\hat{\theta}$	$t_{h=0}$	$\xi_{h=0}/C$
$\pi/2$	74.1	-1
$\pi/3$	70.0	-0.11
$\pi/4$	65.2	-0.06

are attributed to the position-dependent force of gravity relative to the substrate in the curvilinear formulation. Whilst this marginal dependence on δ appears to support the conclusions of Braun *et al.* (2012) – that the curvature of the cornea does not have a significant effect on the thinning of the tear film – the differing stresses at the two eyelids shown in Figures 5.4 and 5.6 indicate that the retention of a non-zero δ is important in the model, leading to a more accurate representation of the dynamics occurring in the tear film.

Finally, the thickness and shape of the initial profile has been seen to have a significant effect on the early dynamics of the tear flow, as thinner films act to inhibit movement, leading to slower bulk-fluid velocities acting under the redistributive influence of gravity. Furthermore, the combination of the contact angle and the height of the menisci compared to the central plateau can cause different behaviours in the contact-line velocities; for small menisci and contact angles, the position of the steady-state contact line can lie anterior to the initial condition. In such cases, the meniscus at the lower lid (and also at the upper lid for sufficiently small contact angles) advances along the eyelid after its initial stress-induced drop. The advancing contact-line speeds in simulations with such initial configurations are seen to be orders of magnitude greater than the advancing velocities exhibited by films with taller initial menisci.

Overall, the study of the isolated tear-film dynamics governed by the evolution equation (2.71), and subject to the boundary conditions (2.76) and (2.77), has shown that the flow can be broken down into three distinct phases: first, a rapid retraction of the menisci caused by relaxation of the capillary stresses induced by the initial condition; second, a period of slow movement as gravity and the contact-angle boundary conditions act to redistribute the tear film towards its steady-state profile; and third, a steady diminution of the late-time, near-steady-state profile under the action of constant evaporation, which leads to eventual tear-film rupture in the absence of the restorative action of a blink.

The influence of a non-uniform distribution of lipid surfactant on the underlying tear-film thickness is studied in the subsequent chapter, wherein results from simulations of the pair of coupled evolution equations (2.71) and (2.72) are presented. These results are compared to the ‘clean-surface’ results discussed in this chapter, and to those of models within the published mathematical literature on the tear film.

Chapter 6

Simulations of the Coupled System

The coupled dynamics of the tear film and the adsorbed lipid surfactant at its free surface are now studied through the numerical simulation of equations (2.71) and (2.72), respectively governing the time-evolution of the film thickness h and surfactant concentration ψ. Results from the coupled system are presented alongside the lipid-free results of Chapter 5, demonstrating the effect of the lipid layer upon the dynamics of the underlying tear film. Comparisons are also made with the results from other published models of the tear film that incorporate the dynamics of the lipid surfactant (Berger, 1973; Berger & Corrsin, 1974; Jones *et al.*, 2006; Braun & King-Smith, 2007; Heryudono *et al.*, 2007; Aydemir *et al.*, 2011; Zubkov *et al.*, 2012). In addition to the differences in the derivation of these models mentioned in Chapter 5 (page 111), many of these models include the opening phase of the blink cycle of dimensional duration 0.2 seconds (Doane, 1980), followed by a drainage flow during the interblink period (lasting at least five seconds: Berger & Corrsin, 1974; Heryudono *et al.*, 2007). Accordingly, the results from this model are compared only with the interblink dynamics reported in such papers, which interblink represents at least 95% of the blink-cycle duration. It is highlighted that, in respect to the differences in the mathematical derivations, the aim of this chapter is to illustrate how the redistributive effects of a motile surfactant layer can be observed in a

model that does not pin the menisci.

Throughout this chapter, the physical parameters within the model are fixed with values of $\alpha_0 = 5$, $st = 1$, $\delta = 5/12$ and $E = 1.503 \times 10^{-2}$ in order that the influence of ψ may be observed clearly. The initial condition for the film thickness (2.80) is formed using the same parameter values as in Chapter 5; specifically, $h_{\text{MID}} = 1$, $r = 2$ and $b = 0.4$. Numerical discretization parameters of $\{N = 20, dt = 2 \times 10^{-8}\}$ are employed in all simulations. Two initial conditions, $\psi_0(\xi)$, are used to model different post-blink surfactant configurations. The first is a uniform distribution given by (2.82b), which models a 'pleated-drape' distribution (McDonald, 1968; 1969) where the lipid layer has unfolded behind the upper lid to leave a homogeneous layer. Alternatively, a non-uniform initial condition is defined by (2.83) using a minimum concentration of $\psi_{\text{MIN}} = 3/4$. This distribution models a lipid layer that has lagged behind the upstroke of the upper lid (Berger & Corrsin, 1974; Owens & Phillips, 2001; Bron *et al.*, 2004), and is thus more highly-concentrated towards the lower lid, $\xi = C$.

6.1 Coupled film thickness and surfactant concentration results

To illustrate the effect of the lipid surfactant on the movement of the tear film, results from simulations that use each of the three[1] initial surfactant concentration distributions in (2.82) and (2.83) are presented. In addition, variation of the contact angle, $\hat{\theta}$, at the three-phase contact line allows the combined influence of ψ and the novel boundary condition (2.76) to be investigated.

Figures 6.1 and 6.2 respectively display coupled snapshots of $h(\xi, t)$ and $\psi(\xi, t)$ taken from simulations using the three initial conditions for the surfactant concentration and

[1] Including the $\psi \equiv 0$ simulations of Chapter 5.

a contact angle of $\hat{\theta} = \pi/2$.[2] The redistributive influence of surfactant on the tear-film dynamics is demonstrated in Figure 6.1 as, by comparison with the surfactant-free data, the red and blue datasets at each instant display a thickening of the tear film over the superior ocular surface ($\xi < 0$), and a corresponding thinning over the inferior surface. This superior thickening is shown more markedly in the red profiles, which

[2]Such an angle is unphysically large for the tear film, but is required through the constraints of the lubrication approximation used in the derivation of this model. See §2.4.1 for further discussion of $\hat{\theta}$.

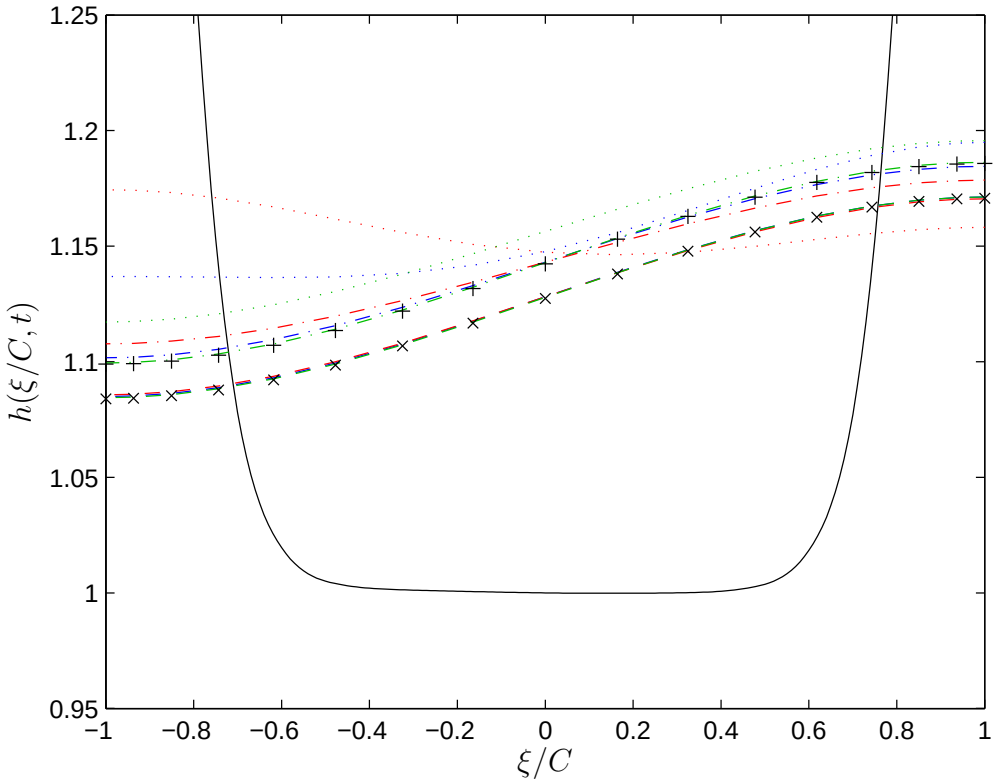

Figure 6.1: Snapshots of film profiles at $t = 0.1$ (dotted lines), $t = 1$ (dot-dashed lines) and $t = 2$ (dashed lines), with $\hat{\theta} = \pi/2$. Colours represent the initial condition for the coupled surfactant: uniform ψ_0; non-uniform ψ_0, and; $\psi \equiv 0$. The initial height profile is shown as a solid black line, and the evaporatively displaced steady state is displayed at $t = 1$ (+), and $t = 2$ (×). The green dataset repeats the purple data presented in Figure 5.1.

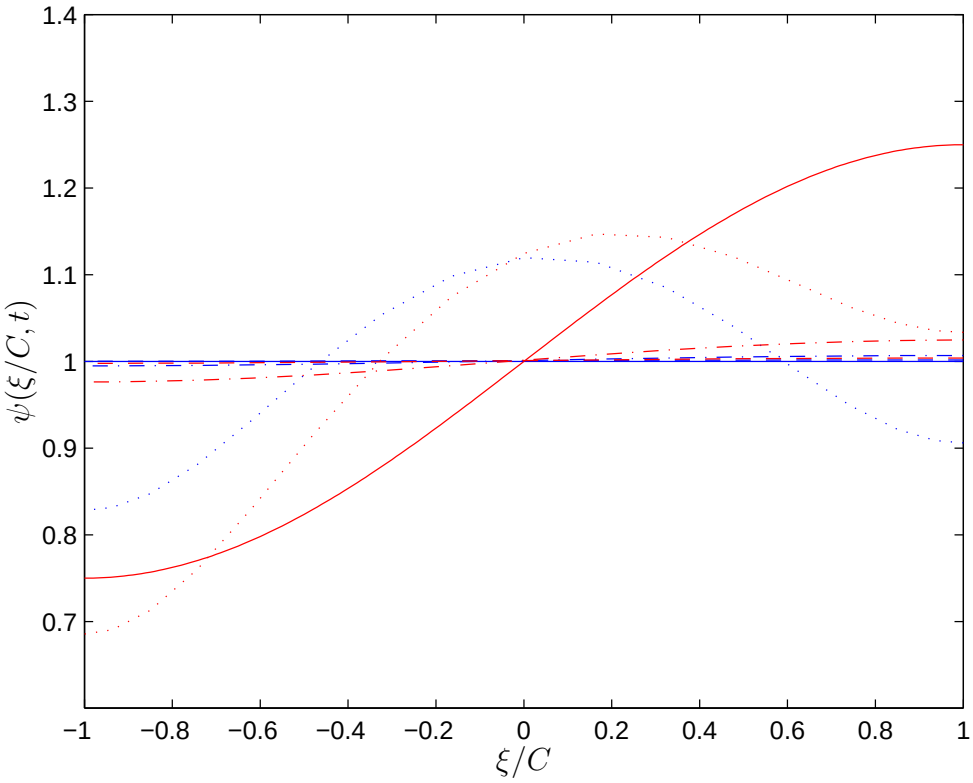

Figure 6.2: Snapshots of the surfactant concentrations coupled to the film profiles of Figure 6.1. Line styles and colours are as per Figure 6.1, with solid lines denoting the two different initial conditions. Steady-state profiles are not shown as they overlay the uniform initial condition.

correspond to a non-uniform ψ_0, indicating that a lipid layer that lags behind the opening eyelid can generate significant bulk flow. These results agree qualitatively with those of Jones *et al.* (2006, Figure 9), wherein superior drift of the central plateau region of the tear film is exhibited during the draining phase and, moreover, the non-uniform initial surfactant distribution rapidly migrates towards a uniform steady-state distribution, which agrees with the behaviour in Figure 6.2. The late-time data (at $t \geq 1$, corresponding to dimensional times greater than five seconds) of Figure 6.1 demonstrates that, after the initial ψ-induced drift, the tear film tends towards its steady-state profile (2.90) as described in §5.1. This persistence of movement in the coupled simulations agrees with

Table 6.1: The maximum difference between the simulated data shown in Figure 6.1 and the evaporatively displaced steady-state film profile (2.90).

	Non-uniform ψ_0	Uniform ψ_0	$\psi \equiv 0$
$\|h(\xi,1)-(h_\infty(\xi)-E)\|_\infty$	8.81×10^{-3}	2.75×10^{-3}	5.10×10^{-4}
$\|h(\xi,2)-(h_\infty(\xi)-2E)\|_\infty$	1.78×10^{-3}	1.01×10^{-3}	5.10×10^{-4}

the *in vivo* observations of Németh *et al.* (2002), which reports changes to the regularity of the tear film for up to 10 seconds after a blink, and Table 6.1 identifies that the early superior drift of fluid counteracts the effect of gravitational redistribution, delaying the onset of gravitational drift and yielding tear-film profiles that depart from the steady state by an amount greater than that seen in the $\psi \equiv 0$ simulation. This postponement of gravitational effects is discussed further in §6.2. Additionally, for $t > 1$, the relaxation of the surfactant concentration distributions in Figure 6.2 towards the uniform steady-state represents a slow upward drift of surfactant that is in agreement with the majority of observations in King-Smith *et al.* (2009).

The feedback between the temporal evolutions of h and ψ is well-illustrated by first considering the blue dataset in Figure 6.2, which corresponds to a uniform ψ_0. In the absence of any variation in ψ_0, the redistribution of ψ during the early stages of motion is caused solely through fluid advection. By $t = 0.1$, the rapid retraction of the tear menisci results in an increased lipid concentration over the centre of the eye, with a corresponding reduction near the eyelids. Reducing ψ causes a local increase in the surface tension, which manifests itself in the stress conditions, (2.48) and (2.49), at the free surface. This increased tension acts to flatten the free surface and 'pull' fluid in from the surrounding regions, whence the feedback loop is closed by noting that the aforementioned superior thickening of the tear film at $t = 0.1$ in Figure 6.1 occurs in the same position as the lowest surfactant concentrations in Figure 6.2. Importantly, the upper ($\xi < 0$) region of the uniform-ψ_0 dataset at $t = 0.1$ in Figure 6.2, which initial condition emulates McDonald's

(1968, 1969) 'pleated drape' distribution, displays behaviour that is contrary to the initial drift reported in Berger & Corrsin (1974), Owens & Phillips (2001) and King-Smith *et al.* (2009), as these *in vivo* observations identify only superiorly directed movement of the superficial lipid layer, whereas the blue $\psi(\xi, 0.1)$ data suggests an initial migration of surfactant *down* the eye into the central region from the rapidly-retracting upper meniscus. By comparison, the non-uniform-ψ_0 (red) trace at $t = 0.1$ in Figure 6.2 agrees with the observations, as the drop in concentration near the lower lid ($\xi = C$) drives surfactant molecules up the surface of the tear film, increasing the surfactant concentration over the

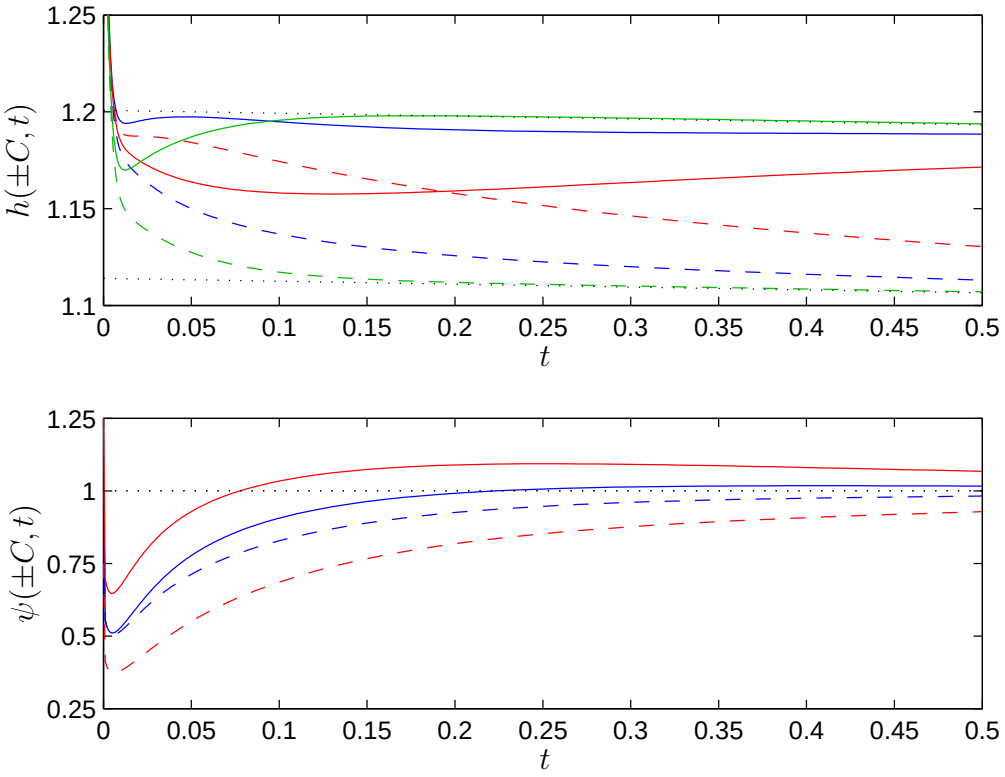

Figure 6.3: Collated **(top)** film thicknesses and **(bottom)** surfactant concentrations at the contact lines from the simulations in Figures 6.1 and 6.2. Solid and dashed lines respectively denote data at $\xi = C$ and $\xi = -C$. Colour-coding is as per Figure 6.1, with dotted black lines showing the steady-state values (which are evaporatively displaced in the upper plot).

central portions of the tear film. Downward movement of lipid molecules initially located close to the upper lid can again be inferred from the drop in concentration for $\xi < -0.7$ in the non-uniform-ψ_0 simulation; however, it is noted that *in vivo* data on the movement of the lipid layer close to the upper lid immediately after a blink is difficult to acquire due to the rapid nature of the eyelid motion, and the presence of eyelashes[3], hence the model predictions for the non-uniform ψ_0 are not necessarily at odds with observations.

To further illustrate the effect of the lipid surfactant on the tear-film dynamics, the contact-line data, $h(\pm C, t)$ and $\psi(\pm C, t)$, from the simulations in Figures 6.1 and 6.2 is collated in Figure 6.3, and the early-time behaviour of the same simulations across the full computational domain is displayed in Figure 6.4. After the initial drop of the menisci, Figure 6.3 demonstrates the significant redistributive effect of the non-uniform ψ_0, as for $t \in [5 \times 10^{-3}, 0.19]$, the film is thicker at $\xi = -C$ than at $\xi = C$. This inverted behaviour is not observed in either of the other two simulations. The ψ-induced redistribution is more clearly demonstrated via a comparison of Figures 6.4 (a), (b) and (d), in which the latter is greatly thickened over the superior regions, specifically: $h(-C, 0.2)$ from plot (d) is 4.1% thicker than its counterpart in plot (a), and 2.9% thicker than in plot (b). Furthermore, whilst the superior thickening is less obvious in Figure 6.4 (b) than in plot (a), the initial behaviour is significantly different from that in the $\psi \equiv 0$ simulation. The superior thickening and inferior thinning in Figure 6.4 (d) qualitatively replicates the early-time behaviour observed by Benedetto *et al.* (1984) and Zhu *et al.* (2007) and, moreover, the superiorly directed drift supports the hypothesis, of Brown & Dervichian (1969), Holly & Lemp (1977) and Bron *et al.* (2004), that the movement of the lipid layer after a blink can act to thicken the tear film to its full thickness after a blink (*cf.* §1.1.1). Notably, the $\psi(\xi, 0.2)$ datasets of Figures 6.4 (c) and (e), corresponding to one dimensional second, both show a near-uniform surfactant distribution that qualitatively agrees with the observations of Berger & Corrsin (1974), Owens & Phillips (2001) and

[3] *cf.* Braun & King-Smith (2007, Figure 18a), King-Smith *et al.* (2009, Figures 4b, 4c and 5b), and the lack of data points for $X/L > 0.8$ in Berger & Corrsin (1974, Figure 8).

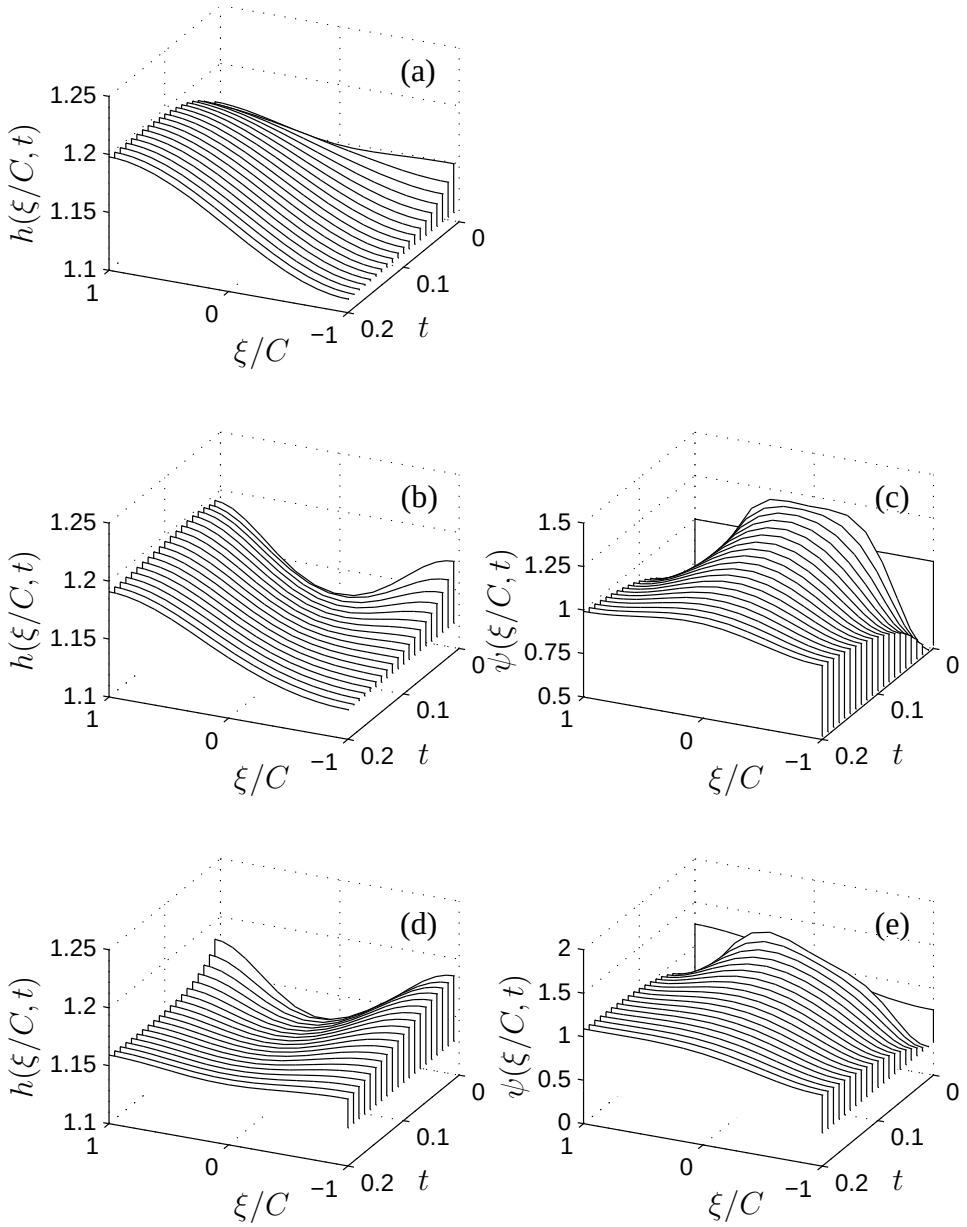

Figure 6.4: Numerical simulation of (2.71) and (2.72) showing **(left)** h, and **(right)** ψ for $t \in [0, 0.2]$, collating the results of Figures 6.1 and 6.2, in which the contact angle is $\hat{\theta} = \pi/2$. Snapshots are displaced temporally by a step $\Delta t = 10^{-2}$. The lower lid is positioned towards the left-hand side of each plot. **(a)** $\psi \equiv 0$; **(b, c)** uniform ψ_0; and **(d, e)** non-uniform ψ_0. $h(\xi, 0)$ is omitted due to the disparity in scales.

King-Smith *et al.* (2009), wherein the rapid initial movement of the lipid layer subsides after roughly one second.

Importantly, it should be noted that the upward drift of the tear film in both $\psi \neq 0$ simulations is predicted by a leading-order model from which the scalings of §2.2.2 have removed all inertial effects. Hence, the film is being advected purely through interaction with the heterogeneous surfactant distribution. As described above, this superior drift counteracts the effect of gravity leading to a tear film that is more-uniformly distributed across the corneal surface for a greater period of time, which is important for visual acuity as the tear film forms the first refractive interface encountered by light entering the eye (Bron *et al.*, 1997; Németh *et al.*, 2002). Notably, the use of the novel boundary condition (2.76) rather than Dirichlet pinning enables the ψ-induced redistribution to occur across the *whole* domain, rather than in the central plateau region perched between the two menisci as shown in Jones *et al.* (2006, Figure 9) and Aydemir *et al.* (2011, Figure 5). In addition to the contact-line movement engendered by boundary condition (2.76), this redistribution of the bulk fluid further alleviates the opportunity for 'black lines' (McDonald & Brubaker, 1971; Miller *et al.*, 2002) to be generated.

Under the action of the evolution equation (2.72), the total mass of surfactant (2.87) in the system shows the same qualitative behaviour as the non-evaporative, fluid mass data of Figure 5.4: specifically, for each of the initial conditions, ψ_0, the rapid initial dynamics cause an increase in the total mass of surfactant that reaches 0.114% by $t = 3\times10^{-3}$. After this increase the change in mass remains almost constant, with a mass loss of order $\mathcal{O}(10^{-2}\%)$ occurring over the period $t \in [3 \times 10^{-3}, 1]$ in both simulations. This quasi-steady period yields a percentage change in mass per time-step of approximately $-3 \times 10^{-10}\%$ for each of the 4.985×10^{7} time-steps required to integrate the solutions during $t \in [3 \times 10^{-3}, 1]$, demonstrating the accuracy of the numerical scheme applied to leading-order evolution equation (2.72).

The influence of ψ on tear films with a non-vanishing gradient of film thickness, h_ξ, at

the contact line is displayed in Figures 6.5 - 6.7, in which $\hat{\theta} = \pi/3$. (Results for $\hat{\theta} = \pi/4$ are qualitatively the same and are not presented.) In each figure, the non-zero gradient h_ξ reduces the severity of the initial retraction of the menisci (*cf.* Figure 5.6), which reduced advection yields a smaller disturbance to the early evolution of ψ. Nevertheless, Figure 6.5 shows the presence of surfactant to lead to an early thickening of the tear film over the superior cornea that persists throughout the period of gravitational redistribution of the fluid, repeating the qualitative behaviour of the $\hat{\theta} = \pi/2$ simulations. A comparison of the data at $t = 0.1$ in Figures 6.2 and 6.6 shows the displacement of the ψ distributions from their respective initial conditions to be greater in the $\hat{\theta} = \pi/2$ simulations.

The evolution of the coupled system for $t \in [0, 0.2]$ and $\hat{\theta} = \pi/3$ is displayed in

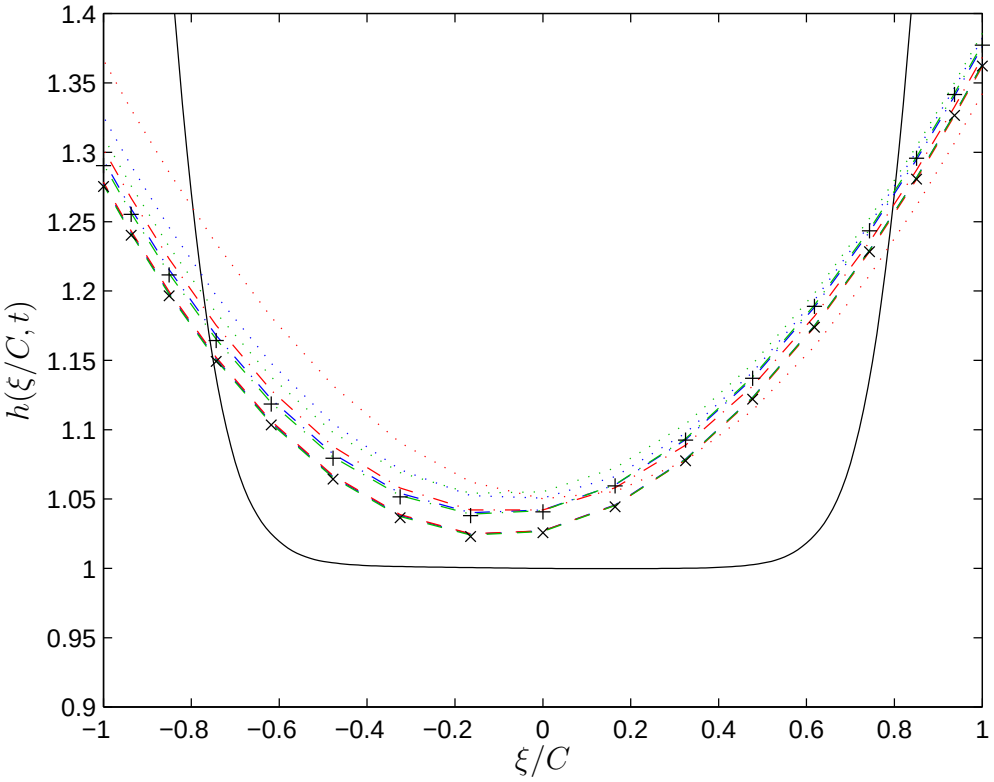

Figure 6.5: Snapshots of film profiles taken at the same times as those in Figure 6.1, with $\hat{\theta} = \pi/3$. All line styles are as per Figure 6.1.

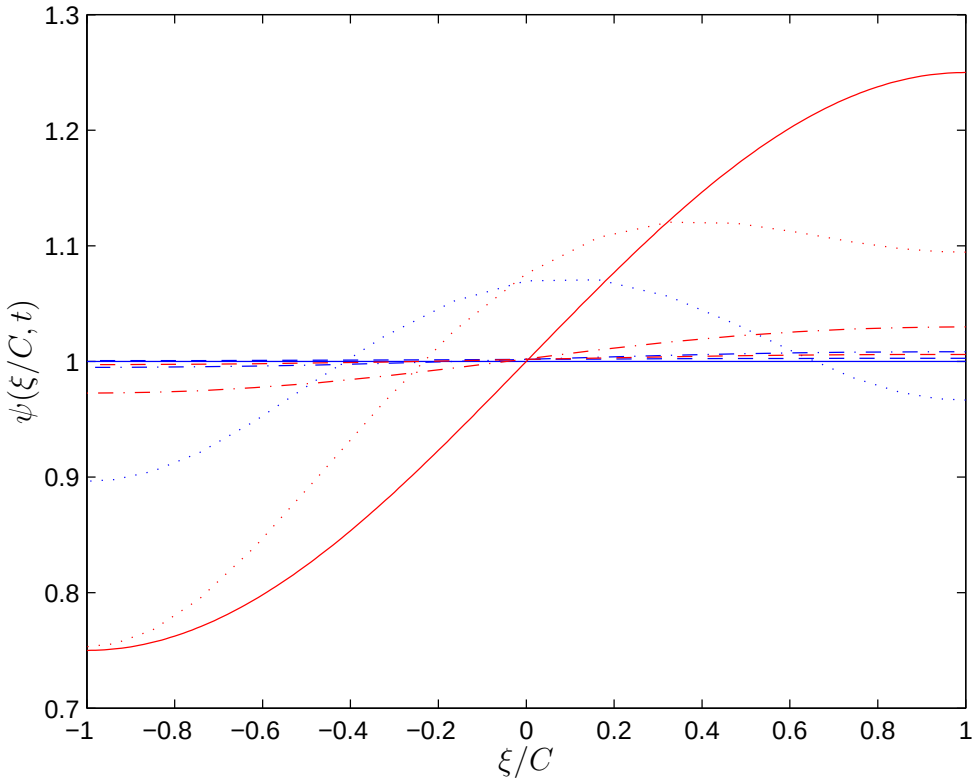

Figure 6.6: Snapshots of the surfactant concentrations coupled to the film profiles of Figure 6.5, with data displayed using the same line styles as in Figure 6.2.

Figure 6.7, wherein the ψ-induced superior drift of the tear film is discernable by noting the comparative reduction in the film thickness at the lower lid, $h(C,t)$, in plots (a), (b) and (d). A comparison of Figures 6.7 (c) and (e) with their counterparts in Figure 6.4 further corroborates the reduced magnitude of the initial dynamics when $\hat{\theta} = \pi/3$, as the ψ distributions show less distortion in this case, and, moreover, shows a similar near-uniform surfactant distribution to have been reached by $t = 0.2$, reaffirming the model prediction that the rapid initial movement of the lipid layer subsides during the first dimensional second (Berger & Corrsin, 1974; Owens & Phillips, 2001; King-Smith *et al.*, 2009). These results show that the novel boundary condition (2.76) has a greater effect on the overall dynamics of the tear-film flow than the initial distribution of surfactant $\psi_0(\xi)$,

despite the latter's redistributive influence during the early phases of the flow. This occurs because the value of $\hat{\theta}$ effectively specifies the magnitude of the initial flow characteristics, and also specifies the shape of the steady state to which the tear film migrates after the ψ-induced drift has subsided.

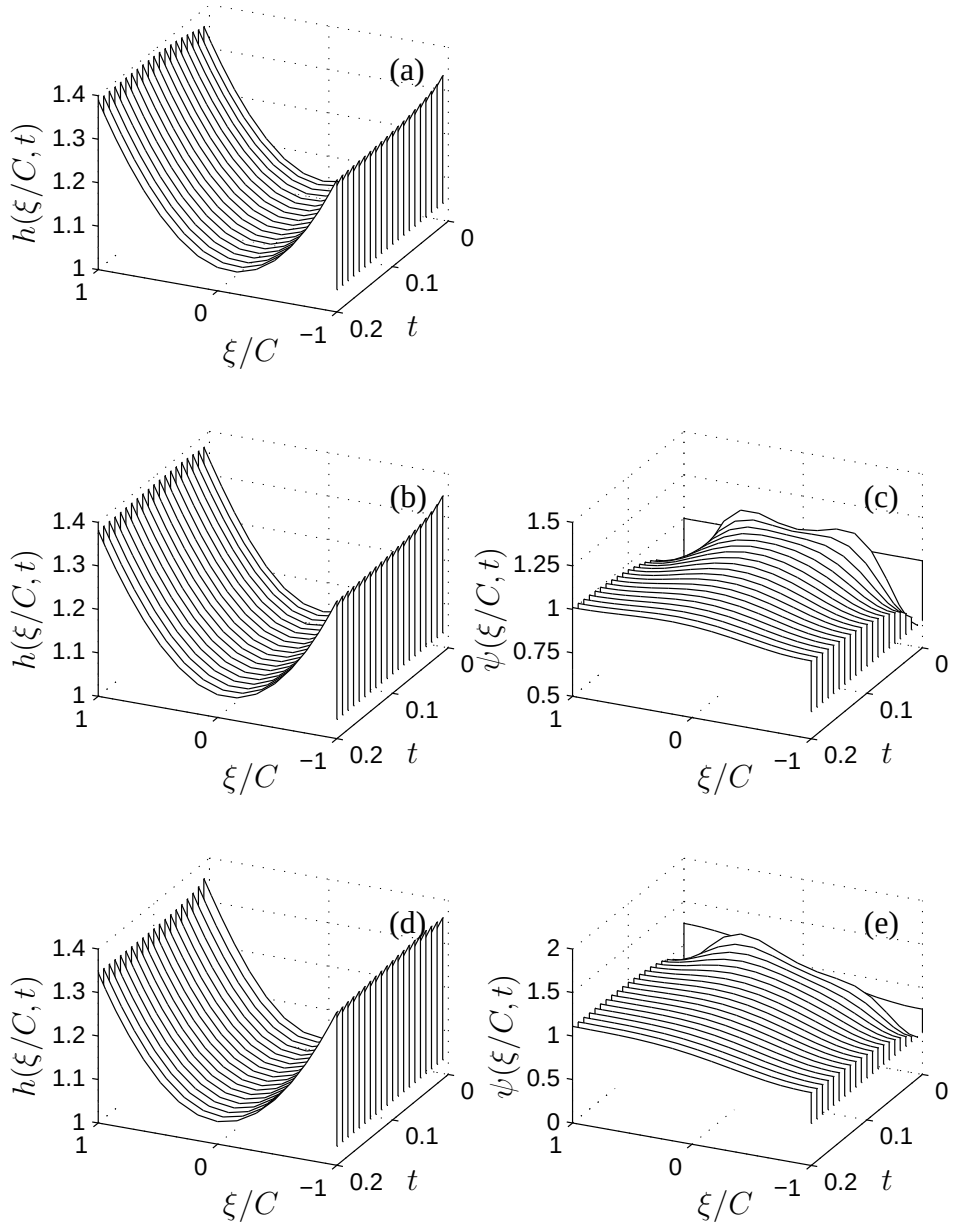

Figure 6.7: Early behaviour of the coupled system with a contact angle of $\hat{\theta} = \pi/3$, collating the results of Figures 6.5 and Figure 6.6. All other details are as per Figure 6.4.

6.2 The influence of surfactant on physiologically-significant quantities

In addition to studying the effect of ψ and its initial condition on the distribution of the tear film, and on the transient dynamics of the coupled system (2.71) and (2.72), the presence of lipid is shown to cause significant changes to the minimum film thickness, $h_{\text{MIN}} = \min_{\xi\in[-C,C]}[h(\xi/C,t)]$, and to the evolution of the contact-line stresses and velocities. These quantities are of physiological importance in the ocular system: an increase in h_{MIN} will yield a film that is less susceptible to evaporation-induced rupture, and (as mentioned in §5.3) the stresses at the contact line in simulations with pinned menisci may reach levels that are pathological to the epithelial cells of the eyelid margin. The dissipation of such stresses during simulations of this model is identified by tracking their temporal evolution. Despite their importance, the stresses at the contact line remain undiscussed in all prior works on the tear film, and movement of the contact line is precluded by the modelling in all such works.

In the absence of surfactant, h_{MIN} is located towards the upper lid due to the influence of gravity. In the presence of surfactant, the superiorly directed drift of the bulk fluid leads to an increase in h_{MIN} as shown in Figure 6.8, a result that is also observed in Aydemir *et al.* (2011). For each of the contact angles tested, the drift attributed to the non-uniform ψ_0 causes the greatest increase in h_{MIN} by comparison with the uniform-ψ_0 and $\psi \equiv 0$ simulations, this increase occurring earlier in the simulations for $\hat{\theta} = \pi/2$ than for $\hat{\theta} = \pi/3$. The influence of the superior drift on h_{MIN} is best-demonstrated by the $\{\text{non-uniform } \psi_0, \hat{\theta} = \pi/2\}$ dataset of Figure 6.8, in collaboration with Figure 6.4 (d). In this case, the location of h_{MIN} is shifted to the inferior half of the palpebral fissure for $t < 0.22$, and is also shown to increase during the same time period, after which the ψ-induced drift subsides and gravitational redistribution of the film leads to a reduction in h_{MIN}, the position of which rapidly moves through the computational domain to the upper

lid ($\xi = -C$) for all times $t \geq 0.26$. In each of the $\hat{\theta} = \pi/3$ simulations that include surfactant, h_{MIN} is marginally increased and displaced towards the upper lid in comparison with the $\psi \equiv 0$ simulation. This location converges towards the $\psi \equiv 0$ value with time. Importantly, the late-time behaviour in Figure 6.8 shows that the presence of surfactant leads to a thicker value of h_{MIN} for times up to $t = 2$ (corresponding to ten dimensional seconds, i.e. exceeding a normal interblink period), which behaviour suggests that the presence of the superficial lipid layer helps to prevent evaporation-induced rupture by

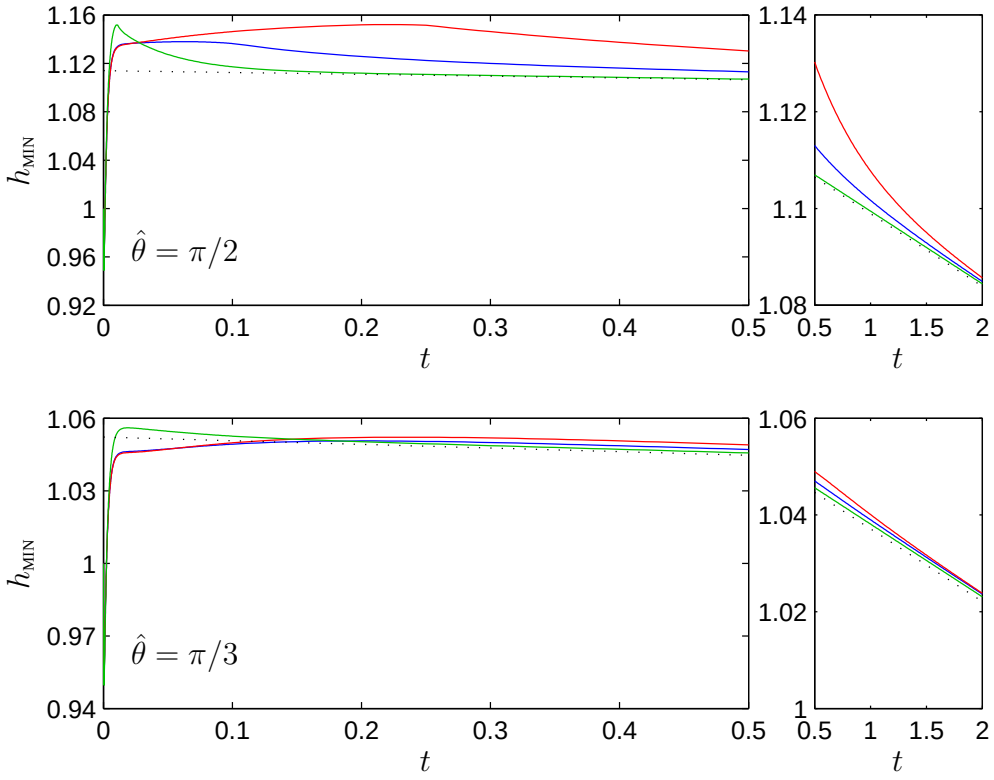

Figure 6.8: Minimum film thicknesses in simulations with different ψ_0 distributions, and contact angles of **(top)** $\hat{\theta} = \pi/2$, and **(bottom)** $\hat{\theta} = \pi/3$. Line colours denote the system with a uniform ψ_0, a non-uniform ψ_0 and $\psi \equiv 0$. Dotted black lines plot the evaporatively displaced minimum of the steady-state profile (2.90). In each row, the larger plot shows the early dynamics for $t \in [0, 0.5]$, whilst the smaller plot displays $t \in [0.5, 2]$. Note the different vertical scales in each plot.

causing large-time thickening of the film. As such, the film-thickening evidence augments the hypothesis (Mishima & Maurice, 1961; Mathers, 1993; Craig & Tomlinson, 1997) that the lipid layer plays an important role in preventing evaporation-induced rupture. However, this hypothesis is based on the lipid forming a barrier to evaporation, an effect not captured in the modelling of Chapter 2, thus it is only the film-thickening effects of the surfactant that are claimed by the present model. Notably the increase of h_{MIN} appears to require simply the *presence* of surfactant, rather than requiring the initial condition to be seeded with surface-tension gradients that promote upward drift of bulk fluid through the specification of a non-uniform ψ_0. Hence both the 'pleated-drape' (McDonald, 1968) and lagging-lipid-layer (Berger & Corrsin, 1974, for example) models for surfactant deposition are predicted to generate an increase in the minimum film thickness.

The evolution of the dimensional contact-line velocities for $t \in [4 \times 10^{-4}, 0.1]$ is displayed in Figure 6.9, wherein the initial velocities are omitted due to the disparity in scales. For each value of $\hat{\theta}$ tested, the presence of a non-uniform ψ_0 is found to alter the initial recessional velocities of the contact lines by an amount of order $\mathcal{O}(10^{-6}\ \text{m s}^{-1})$ by comparison with the $\psi \equiv 0$ velocities reported in Table 5.1. Hence the effect of surfactant on the initial recession of the menisci is found to be negligible[4]. Despite this, the behaviour of the contact-line velocities during the early dynamics of the flow is found to be markedly altered by the presence of surfactant. For each value of $\hat{\theta}$, the inclusion of surfactant is observed to cause a non-monotonic reduction in the magnitude of the contact-line velocity at each eyelid for $t < 0.005$, with the direction of motion briefly changing to advance up the eyelid in the simulations with $\hat{\theta} = \pi/3$ and $\pi/4$. No such fluctuation in this period is observed in the $\psi \equiv 0$ datasets, which progress rapidly towards their steady-state profiles (as evidenced by the green data at $t = 0.1$ in Figures 6.1 and 6.5). As such, the slowing of the fluid dynamics caused by the fluctuations in the $\psi \neq 0$ simulations both reduces the severity of the initial contact-line movement, and effectively marks the start of the process of upward drift of the tear film.

[4]The uniform ψ_0 generates no change to the initial velocities as $v(\xi, t)$ depends on $\psi_{\xi\xi}$.

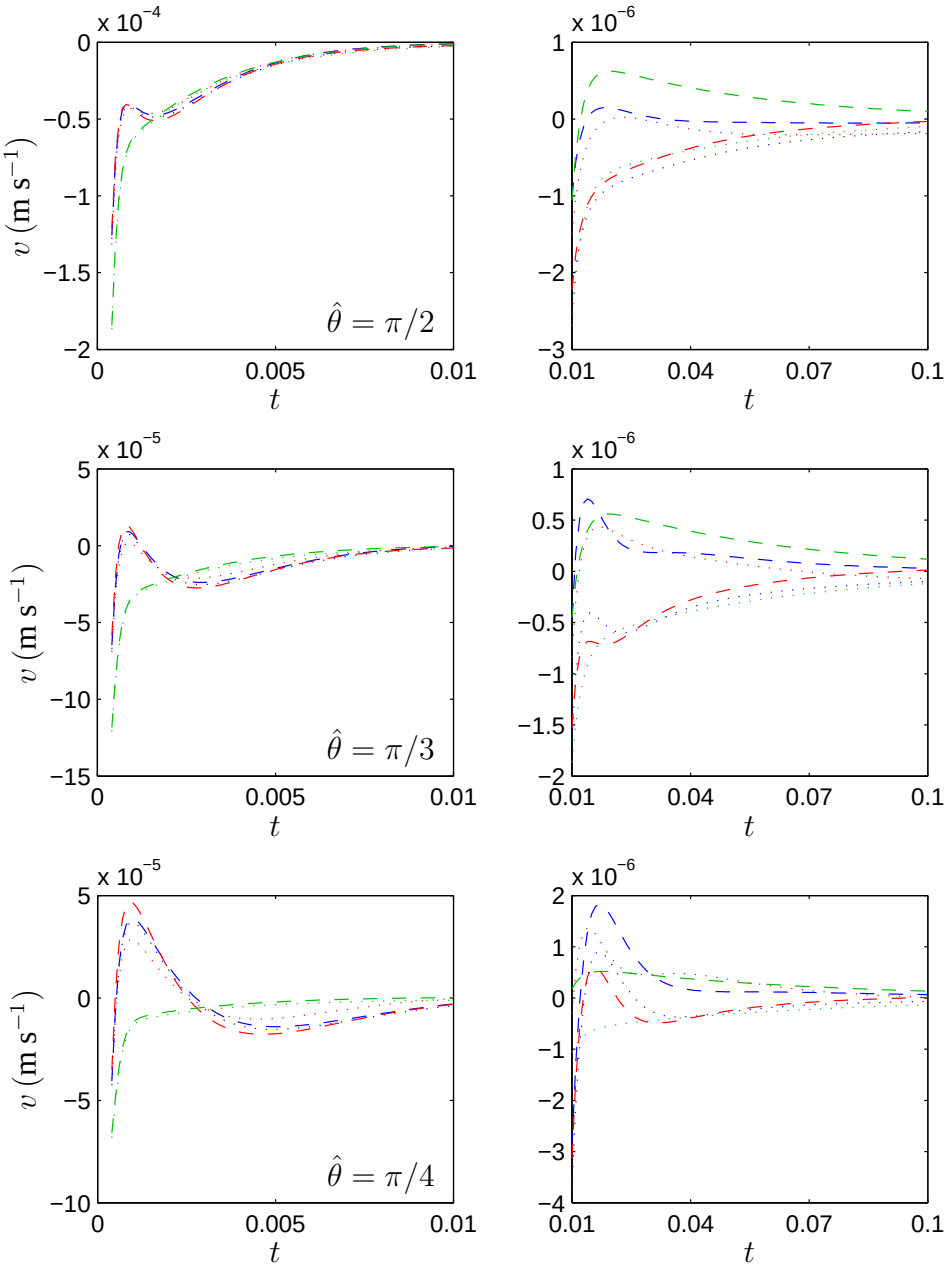

Figure 6.9: Dimensional contact-line velocities in simulations with contact angles of **(top)** $\hat{\theta} = \pi/2$, **(middle)** $\hat{\theta} = \pi/3$, and **(bottom)** $\hat{\theta} = \pi/4$, with **(left)** $t \in [0, 0.01]$, and **(right)** $t \in [0.01, 0.1]$. Velocities at the lower ($\xi = C$) and upper ($\xi = -C$) lids are respectively represented by dashed and dotted lines, and datasets are coloured as per Figure 6.8. Note the different vertical scales. This behaviour is precluded by the modelling in *all* related studies.

For each contact angle, the red, non-uniform-ψ_0 data at $t = 0.01$ in Figure 6.9 shows the advancing velocity of the lower-lid contact line ($\xi = C$) to be less (in some cases, *more negative*) than the advancing velocity of the upper-lid contact line ($\xi = -C$). This is a result of the ψ-induced drift of the bulk fluid towards the upper lid, which drift, as mentioned above, increases the global minimum film thickness h_{MIN}. This contact-line-velocity trend is reversed by $t = 0.1$ (i.e. the red datasets cross), demonstrating the influence of gravitational redistribution as the lower-lid contact line advances, and the upper-lid contact line recedes. A similar velocity inversion is not observed in the $\psi \equiv 0$ or uniform-ψ_0 simulations, yet it should be noted that, for $t > 0.04$, the dashed green traces show the largest advancing velocities at the lower lid, indicating that the presence of surfactant impedes the gravitational drift of the tear film, maintaining the thicker values of h_{MIN} exhibited for large times in Figure 6.8.

Figure 6.10 displays the effect of surfactant on $\mathbf{T}_{\omega\omega}$ (2.10) evaluated at the contact lines, a quantity that has, to the author's knowledge, not been reported in any of the previous literature on the tear film despite its physiological importance. For each simulation, the stress induced by the initial conditions is $\mathbf{T}_{\omega\omega}(\pm C, 0) = -1.33 \times 10^5$ Pa when $\hat{\theta} = \pi/2$, and $\mathbf{T}_{\omega\omega}(\pm C, 0) = -1.18 \times 10^5$ Pa when $\hat{\theta} = \pi/3$, where the negative sign denotes that this pressure pushes down on the contact lines, causing the initial retraction observed in Figures 6.4 and 6.7. In a similar analysis to that on the initial recessional velocities, the uniform-ψ_0 distribution is found to have no effect on the initial contact-line stresses. Furthermore, the non-uniform ψ_0 alters $\mathbf{T}_{\omega\omega}(\pm C, 0)$ by an amount of order $\mathcal{O}(10^{-3}\text{ Pa})$ by comparison with the $\psi \equiv 0$ value, reinforcing that ψ_0 has a negligible influence on the initial dynamics of the tear-film model. The presence of surfactant delays the onset of the change of sign of $\mathbf{T}_{\omega\omega}$ by comparison with the $\psi \equiv 0$ data, again demonstrating the slowing of the early dynamics in the coupled system. However, this delay has a lesser impact upon the temporal evolution of $\mathbf{T}_{\omega\omega}$ than the contact angle, which angle can be seen to strongly affect the time at which $\mathbf{T}_{\omega\omega}$ changes sign, regardless of the coupled-ψ distribution – the reader's attention is drawn to

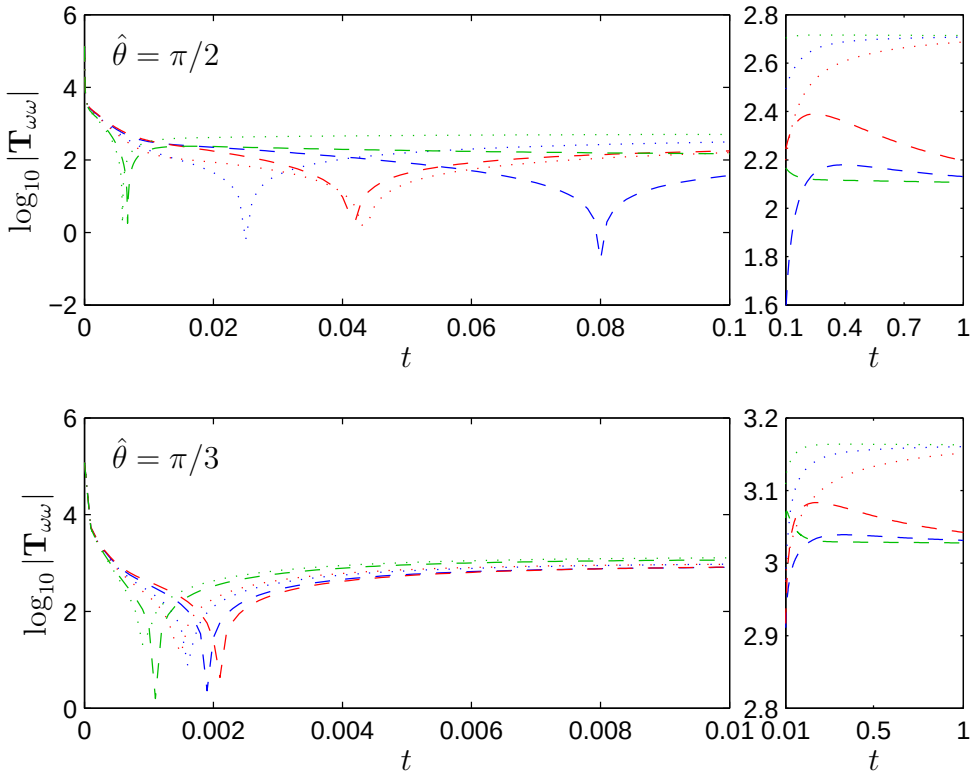

Figure 6.10: Logarithm of the modulus of $\mathbf{T}_{\omega\omega}$ (2.10), evaluated at the three-phase contact line for **(top)** $\hat{\theta} = \pi/2$, and **(bottom)** $\hat{\theta} = \pi/3$. Line styles are as per Figure 6.9. Note the differing horizontal and vertical scales in each plot.

the differing horizontal scales in Figure 6.10.

The large-time behaviour in Figure 6.10 shows the stresses at the lower lid to be increased by the presence of lipid, with the non-uniform-ψ_0 dataset yielding the largest lower-lid stresses for each value of $\hat{\theta}$. This trend is reversed at the upper lid, with the $\psi \equiv 0$ simulation showing the greatest upper-lid stress. These differences in the contact-line stresses reflect the level of impact that the surfactant has had on the transient dynamics of the flow, specifically: the (red) non-uniform-ψ_0 simulations experience the greatest level of ψ-induced drift, and thus depart from the $\psi \equiv 0$ dataset by the greatest amount. At each lid, the large-time evolution of the lipid distribution to its spatially-uniform steady

state (2.91) causes the contact-line stresses to monotonically converge towards the $\psi \equiv 0$ stress values, as all ξ-dependence in ψ vanishes, removing the $\psi_{\xi\xi}$ term from v (2.65), and hence from $\mathbf{T}_{\omega\omega}$ (5.1). Notably, in Figure 6.10, the convergence of the stresses towards the $\psi \equiv 0$ values has not occurred by $t = 1$, corresponding to five dimensional seconds, which agrees with the results of Németh *et al.* (2002) and King-Smith *et al.* (2009), both of which report slow movement of the tear film persisting after the initial rapid movements that take place in the first second after deposition (Berger & Corrsin, 1974; Owens & Phillips, 2001).

6.3 Summary and discussion

This chapter studies the results from simulations of the pair of coupled evolution equations (2.71) and (2.72) with the aim of showing that the model derived in Chapter 2 can capture the redistributive effects of the lipid surfactant that have been observed both *in vivo* by ophthalmologists, and in prior mathematical models in all of which, unlike here, the menisci are pinned.

The results of Figures 6.1 - 6.7 demonstrate that, by comparison with the $\psi \equiv 0$ data of Chapter 5, the presence of surfactant leads to a thickening of the tear film over the superior cornea during the early stages of flow, with a corresponding thinning over the inferior cornea. These results replicate *in vivo* observations (Benedetto *et al.*, 1984; Zhu *et al.*, 2007), and support the hypothesis that the lipid surfactant plays an important role in the formation of a stable tear film after a blink (see Chapter 1 for further details). Furthermore, the rapid migration of ψ from a non-uniform distribution to a near-steady state by a dimensional time of one second in Jones *et al.* (2006, Figure 9) is corroborated by the $\psi(\xi, 0.2)$ distributions of Figures 6.4 and 6.7, which distributions also show near-steady-state behaviour at a dimensional time of one second. The cessation of rapid movement of the lipid layer by this time is in agreement with the *in vivo* observations of

Berger & Corrsin (1974) and Owens & Phillips (2001), which report that lipid movement persists for roughly one second. After the rapid initial dynamics, slow movement of both the film thickness profile and the lipid distribution towards their respective steady states is shown to persist throughout the remainder of the blink cycle, as observed in Németh *et al.* (2002) and King-Smith *et al.* (2009). Moreover, the slow evolution of the lipid layer for (non-dimensional) $t \in [1, 2]$ shows a superiorly directed drift of surfactant that agrees with the majority of observations made by King-Smith *et al.* (2009). This directed large-time lipid movement is not observed in Jones *et al.* (2006), wherein the steady-state lipid distribution is reached after roughly one dimensional second, or in Aydemir *et al.* (2011, Figure 4, bottom right) and Zubkov *et al.* (2012, Figure 3, centre), both of which preclude solely-upward drift during the interblink period as their surfactant lies in reservoirs close to both eyelids after the opening phase of the blink.

These results demonstrate that both realistic ψ-induced redistribution of the tear film and realistic large-time drift of the surfactant layer are predicted by a model that eschews Dirichlet pinning of the menisci in favour of the Neumann boundary condition (2.76) for the film-thickness evolution equation. Notably, in the absence of pinning, the redistribution of the tear film occurs across the *whole* cornea, further alleviating the opportunity for the build-up of 'black-line' thinning (Miller *et al.*, 2002) that persists in the pinned models of Jones *et al.* (2006), Heryudono *et al.* (2007), Aydemir *et al.* (2011) and Zubkov *et al.* (2012). Through such results the use of boundary condition (2.76) opens up a new way to look at the tear film that is intended to augment and complement the existing studies through the so-called 'bi-behavioural' model hypothesized in §5.3. In this model, the tear-film contact lines may exhibit both pinning and slip, with pinned behaviour generating the meniscus-induced thinning evidenced in the existing literature, which thinning accelerates rupture of the tear film. Thus slip behaviour may be exhibited by healthy tear films, which do not experience rupture or dry-eye symptoms during normal interblink times. Such 'bi-behavioural' movement at the contact lines is supported by the *in vitro* observations of Leiske *et al.* (2011).

The initial superiorly directed drift of fluid is shown to be enhanced in simulations that use a non-uniform ψ_0, identifying that the two-stage deposition process of Brown & Dervichian (1969), Berger & Corrsin (1974) and Holly & Lemp (1977) generates a significant surge of fluid up the eye after the cessation of movement of the upper lid that agrees qualitatively with the observations of Berger & Corrsin (1974) and Owens & Phillips (2001). Comparatively, a uniform ψ_0 that emulates McDonald's (1968, 1969) 'pleated drape' behaviour generates a less-significant thickening of the tear film over the superior cornea, and also predicts an initial downward flux of lipid from near the upper lid that has not been observed *in vivo* (Berger & Corrsin, 1974; Owens & Phillips, 2001; King-Smith *et al.*, 2009). Importantly, these results illustrate that the presence of surfactant at the start of an interblink period, even in a uniform layer, acts to thicken the tear film by comparison with the $\psi \equiv 0$ case, as also reported in Aydemir *et al.* (2011).

For each ψ_0 tested, the surfactant-induced drift of bulk fluid during the initial phase of the flow increases the minimum film thickness for intermediate-to-large times, by comparison with clean films, as shown in Figure 6.8 ($t > 2.9 \times 10^{-2}$ when $\hat{\theta} = \pi/2$, and $t > 0.19$ when $\hat{\theta} = \pi/3$). This thickening is reduced over time as the surfactant migrates towards its steady-state distribution (2.91), and gravity acts to move the film towards its steady-state profile (2.90). However, noting that $t = 2$ corresponds to 10 dimensional seconds, the thickening is shown to persist throughout a typical human interblink period, and film profiles $h(\xi, 2)$ displayed in Figures 6.1 and 6.5 identify that the model does not predict rupture of the tear film to be an issue under normal conditions. Due to the persistence of the thickening of the tear film from lipid-induced advection, the present model predicts that for the 70% of patients who suffer both aqueous-deficient dry eye and Meibomian gland dysfunction (Bron, 2001), emphasis during treatment should be put on improving the quality of the lipid layer, in tandem with allowing slippage of the contact lines at the eyelid margins, to increase the longevity of the intact tear film by improving the level of superior thickening.

An analysis of the evolution of contact-line positions, velocities and stresses, respectively displayed in Figures 6.3, 6.9 and 6.10, shows the presence of surfactant to have a significant effect on the transient dynamics of the tear film during the period between the initial retraction of the menisci and the subsequent gravitational redistribution. A discussion of the evolution of these contact-line quantities is novel to the field of tear-film modelling, with dynamic changes to the contact-line positions and velocities being enabled in the present model through the new Neumann boundary condition (2.76), employed in favour of the Dirichlet pinning of the menisci used in all prior models[5]. The effect of ψ_0 on the initial contact-line stresses and velocities is demonstrated to be negligible, hence the initial dynamics of all simulations are dominated by the falling menisci. As the menisci fall, the rapid recession of the contact lines and adjacent fluid advects the lipid towards the centre of the eye, creating concentration gradients that subsequently act to advect the underlying tear film. Figures 6.9 and 6.10 show the surfactant to significantly alter the early evolution of the contact-line velocities and stresses, slowing the dynamics of the tear-film flow by comparison with the $\psi \equiv 0$ simulations, before the aforementioned advection of the bulk fluid. At later times, the contact-line quantities are shown to tend towards the $\psi \equiv 0$ datasets as the influence of the surfactant layer subsides and the coupled system moves towards its steady state. As such, the coupled model predicts the dissipation of contact-line stresses through slippage at the eyelid margins, which precludes the build-up of pressures that could harm the cellular structure of the eyelid.

A discussion of the conclusions drawn from the modelling of the tear film is given in the following chapter. Amendments are moreover suggested that will improve both the representation of physical processes that are important in the evolution of the tear-film flow, and the mathematical modelling techniques used in the derivation of future models.

[5]Evidence in Chapter 5 has shown such pinning to be implausible in the presence of evaporation, and, moreover, fixed boundary values have been shown to contradict with the non-zero contact-line velocities predicted within existing models (*cf.* §2.4.2, and discussions in Zubkov *et al.*, 2013).

Chapter 7

Conclusions

> *"It is good to have an end to journey toward; but it is the journey that matters, in the end."* – Ernest Hemingway (1899 - 1961)

On account of the individual detailed and cross-referencing summaries given at the ends of each of the preceding chapters, the main emphases of each chapter are reiterated here. A brief description of possible future work is also given.

7.1 Summary of findings

A pair of coupled evolution equations modelling the movement of the human tear film under the influence of its superficial lipid surfactant layer is derived in Chapter 2. To investigate the influence of the curved corneal substrate on the tear-film flow, the equations of motion are derived using a novel curvilinear coordinate system in which the curvature of the cornea is specified in terms of a parameter, δ, that quantifies the departure from the rectilinear coordinate system used in all prior studies (with the exception of Braun *et al.*, 2012). In this way, the neglect or inclusion of terms arising through the curvature

of the substrate can be investigated and calibrated. Despite the existence of similar thin-film approximations in the mathematical literature on the tear film (and, moreover, within studies of rimming and coating flows) a full derivation of the model is presented not only for completeness, but mainly in order that a correct *a priori* scaling of the governing equations is made before asymptotic approximations are invoked. All field variables and non-dimensional groupings of physical parameters are scaled in terms of a small parameter ϵ before asymptotic expansions of the field variables are made, to ensure that all variables in the equations are of order $\mathcal{O}(1)$. This assumption, made through the thin-film lubrication approximation, enables the pair of uniformly-valid, leading-order evolution equations for the film thickness and surfactant concentration to be derived, and furthermore provides an understanding of the limit of their validity. Specifically, as mentioned in §2.3, if any variables or derivatives in the evolution equations become larger than $\mathcal{O}(1)$, the assumptions employed in the derivation of the model are invalidated, and the ordering used in the derivation ceases to be asymptotic. As such, the evolution equations presented in Chapter 2 are claimed only to represent the motion of the human tear film in an "$\mathcal{O}(1)$ gradient" régime.

A discussion of the boundary conditions used in the modelling of the fourth-order evolution equation for the film thickness (2.71) leads to the relaxation of the Dirichlet pinning conditions, used in *all* previously published tear-film models, in favour of the development of boundary condition (2.76) — for the gradient of the film thickness, h_ξ — at the eyelids; a development that is novel to the field of tear-flow modelling. The use of pinned boundary conditions is motivated, in the existing literature, by the presence of the mucocutaneous junction: a point on the eyelid margin at which the wettability changes, the region anterior to the mucocutaneous junction being unwettable due to the presence of lipid. Dirichlet boundary conditions are eschewed in the present model as such a change in wettability is seen only to present a barrier to fluid flowing *anteriorly* along the eyelid, and hence it does not give rise to a physically justifiable reason for the film not to slip *posteriorly* i.e. towards the ocular surface, along the

pre-wetted eyelid margin. Furthermore, the pinning thickness in all prior models is at least one order of magnitude greater than the thickness of the central film profile, immediately invalidating the approximations used in the derivation of such models. This invalidation is demonstrated by the results of Zubkov *et al.* (2013), wherein fluid velocities in the meniscus of a pinned lubrication-approximation simulation predict contact-line movement, contradicting the enforced boundary condition. Nevertheless, a comparison of results from the lubrication-approximation model and simulations of the full Navier-Stokes equations (*ibid.*) in the meniscus region shows the computed film profiles of the lubrication model to be qualitatively accurate, despite pinning of the meniscus at a level that is nearly two orders of magnitude greater than the central film thickness. It is felt, however, that this similarity of results is born of the scenario being modelled, specifically: a thin film coupled to a large, *pinned* meniscus, thus there is very little movement the film can exhibit that could lead to a significant difference in results.

The development of boundary condition (2.76) adds a significant complexity to the processes required to simulate the tear-film model. However, it is felt that the condition yields a more physically-realistic flow, especially in cases where pinning of the menisci is in direct contradiction with evaporation of the tear film. This modelling contradiction is highlighted by the observation that the eyelids maintain a higher temperature than the cornea (Tomlinson *et al.*, 2011), and thus will act to enhance evaporation at the contact line. By allowing slip of the contact line, the use of boundary condition (2.76) has opened up a completely new area for tear-film modelling, through which newly reported agreements with *in vivo* observations are enabled. These novel results are intended to augment the existing results in the published literature, with the aim that a better understanding of tear-film dynamics may ultimately be obtained.

Motivated by the scant level of information on numerics provided in the existing literature on the tear film, the numerical methods employed to solve the tear-flow model are described in detail and subsequently tested in Chapters 3 and 4, respectively.

Chebyshev spectral methods are employed due to their high-order convergence properties in the approximation of smooth functions, such as those required under the assumptions of the lubrication approximation used in Chapter 2. In the absence of Dirichlet boundary conditions in the model, non-trivial modifications of existing Chebyshev-differentiation methods are developed to yield a procedure that enforces the Neumann boundary conditions with spectral accuracy. Furthermore, to improve the accuracy in the numerical approximation of the higher-order derivatives present in the evolution equations, novel third- and fourth-order Chebyshev differentiation matrices are explicitly derived in §3.1.2 and their performance is shown in §4.1.1 to be less accurate than approximations obtained through repeated action of the first-order differentiation matrix (3.15). This reduction in the accuracy of derivatives calculated with the explicit higher-order differentiation matrices is attributed to the combined effects of the finite-precision arithmetic inherent in computer simulations, and the increasing magnitude of "border" matrix entries as the order of differentiation increases. Thus, by comparison with the first-order matrix, the finite-precision representation of the entries in higher-order matrices has a greater absolute error, which adversely affects the accuracy of the numerical approximations. In all tests of the differentiation matrices, and of a newly modified version of the spectral integration routine of Trefethen (2000), the numerical approximations are shown to be accurate to within the tolerance of the round-off plateau for $N \gtrsim 40$ Chebyshev discretization points. Hence the Chebyshev spectral discretization employed allows a significant saving to be made in the computational resource required to simulate the coupled system, by comparison with the number of discretization points required in the finite-difference simulations of, for example, Braun & Fitt (2003). Importantly, unlike the descriptions given in much of the prior literature, the methods outlined in Chapter 3 have been made transparent in order that they may be implemented independently not only to reproduce the results presented within this thesis, but also to model other nonlinear evolution equations on a bounded spatial domain in the presence of (only) Neumann boundary conditions.

Motivated by the results of existing models that employ spectral methods to simulate steep, pinned menisci, §4.3 contains an investigation of the errors encountered in the spectral approximation of derivatives of steep-sided functions. The results presented in Figures 4.9 - 4.12 show that the magnitude of the error in the approximation of derivatives is largest at the ends of the computational domain, and, moreover, that these largest errors grow as the number, N, of spatial discretization points is increased. Hence these results identify that the regions of the flow that drive the underlying fluid dynamics in such steep-sided models are the very regions that *must* contain the greatest numerical errors. Significantly, the spatial distribution of discretization error is not discussed in the existing literature. Furthermore, it is important to note that the results of Figures 4.9 - 4.12 are obtained using a *spectrally-accurate* method, thus motivating the question of the magnitude of the errors associated with the (mere) second-order spatial finite-difference schemes used in prior tear-flow models. Importantly, these results illustrate that what is happening in vicinity of the steep-sided menisci in other models is clear from neither a numerical point of view — as described above — nor from a modelling point of view — through the violation of assumptions of the lubrication approximation used in the derivation of each model.

In Chapters 5 and 6 the validated numerical methods of Chapter 3 are employed in the integration of the coupled evolution equations describing tear-film flow. Simulations in the absence of the superficial lipid layer are presented in Chapter 5, and illustrate that the novel boundary condition (2.76) yields behaviour that is unseen in *all* prior models of the tear film. Without the pinning of the contact lines, the menisci defined in the initial conditions rapidly retract towards the corneal substrate in reaction to the stresses manifest at the contact line by the shape of the free surface. This relaxation of the menisci precludes the tear film from developing the meniscus-induced thinning observed within other models, and hence is unable to predict phenomena similar to the ‘black line’ observations made in ophthalmic studies (McDonald & Brubaker, 1971; Bron *et al.*, 2011). It is noted, however, that such thinning is possible only through the violation

of the lubrication approximation, as mentioned previously, by pinning the menisci at a level that is (at least) an order of magnitude thicker than the central film height. Through variation of the contact angle formed between the tear film and the eyelid, the magnitude of the large-time contact-line stresses is seen to increase with decreasing angle, suggesting that significant stresses may develop within models that pin the menisci, particularly in models that predict ever-steepening menisci. Somewhat remarkably, a discussion of the stresses at the contact line is also novel for the field of tear-flow modelling, despite the damage that large stresses could cause to the underlying ophthalmic tissues that house the tear film. Additionally, the development of large stresses suggests that pinning of the menisci may be an extreme case for the tear film, and that the stresses may be alleviated through de-pinning of the contact line.

Motivated by the behaviour of the contact line in simulations of the present model, §5.3 advances a so-called 'bi-behavioural' model for the tear film, in which both slip *and* pinning are permitted at the contact line. Such a model is supported by the *in vitro* results of Leiske *et al.* (2011), wherein a dynamic wetting experiment using a Meibum-coated droplet is shown to exhibit pinning and de-pinning of the contact line. As such, under the 'bi-behavioural' model, pinning of the contact line is suggested to cause dry-eye pathologies through meniscus-induced thinning (as demonstrated by other tear-film models) and stress-induced damage to the eyelid margin, the combination of which may form a viscious circle of damage to the eye. Accordingly, slip of the contact line is suggested to occur in healthy eyes, and through the hypothesis it is suggested that dry-eye diseases could be treated by encouraging contact-line slippage along the eyelid margin. Hence, rather than thickening the bulk film, the focus of dry-eye treatment is shifted to thinning the menisci, allowing the redistribution of fluid throughout the tear film.

The surfactant-free model also reveals that the novel curvilinear coordinate system, which incorporates corneal curvature, yields only marginal differences in the tear-film distribution when compared to a Cartesian model. Nevertheless, by tracking the behaviour

of the contact-line stresses, the presence of a curved substrate is, for the first time, illustrated to alter the behaviour of the fluid significantly. Thus corneal curvature is an important feature of the ocular system that should be included for accurate modelling of tear-film behaviour. Constant evaporation of bulk fluid from the tear film is observed to have only long-term thinning effects, which, in the absence of meniscus-induced thinning, do not predict rupture of the tear film during a normal human interblink period of approximately five to eight seconds (Berger & Corrsin, 1974).

Finally, the results from the full coupled system presented in Chapter 6 demonstrate that the presence of the lipid surfactant at the free surface of the tear film generates a redistribution of the underlying bulk fluid that increases the minimum thickness of the film, agreeing qualitatively with the results of Aydemir *et al.* (2011). Through modelling an initial lipid distribution that emulates the behaviour of a lipid layer that lags behind the rapidly-opening upper lid, a significant thickening of the tear film over the superior cornea is observed in the early stages of the interblink period, qualitatively replicating the *in vivo* results of Benedetto *et al.* (1984) and Zhu *et al.* (2007). These results support the two-stage deposition model of Brown & Dervichian (1969), Holly & Lemp (1977) and Bron *et al.* (2004), in which the creation of a stable tear film after a blink is dependent on surfactant-induced thickening of the superior tear film after the cessation of movement of the upper lid. The duration of early lipid layer movements is shown to agree with the dimensional time of approximately one second observed *in vivo* by Berger & Corrsin (1974) and Owens & Phillips (2001), and the evolution of the surfactant distribution towards a uniform steady state over the same time period is similar to that observed in the model of Jones *et al.* (2006). Furthermore, the present model predicts a large-time counter-gravitational drift of surfactant as it tends towards its steady-state distribution, which agrees with the *in vivo* observations of King-Smith *et al.* (2009) and, moreover, shows that movement of the tear film persists after the initial surfactant-induced redistribution, agreeing with the observations of Németh *et al.* (2002). Through its redistributive effects, the presence of surfactant is found to alter the behaviours of both the

velocity and the stress at each contact line during the early phases of the flow. After these early changes, the contact-line velocities and stresses are seen to converge towards the surfactant-free values (observed in Chapter 5) as the influence of the surfactant subsides.

7.2 Future work

The primary emphasis of the work contained this thesis, which emphasis motivated the meticulous derivation of Chapter 2, has been to ensure that the correct physical behaviours are represented in a model that adheres to the assumptions made in its derivation. Accordingly, this methodology has meant that there are a number modelling opportunities that may be further explored for the model as a draining flow during the interblink period.

Firstly, tests of pathological tear films can be carried out using the existing model to emulate dry-eye phenomena reported in the ophthalmic literature (see, for example, Holly & Lemp, 1977). Such tests should employ initial configurations of the coupled system that have a: (i) reduced aqueous component; (ii) reduced total lipid mass; (iii) poorly-spread or discontinuous lipid layer, or; (iv) combination of these maladies. Through such alterations to the initial conditions, the dynamics of tear films that are more prone to rupture can be studied and the combined film-thickening effects of contact-line slippage and surfactant heterogeneity tested to observe how they may relieve dry-eye symptoms.

Secondly, the boundary conditions for the film thickness evolution equation (2.71) may be amended in line with the newly postulated ‘bi-behavioural’ model. This amendment would add further complexity to the treatment of the boundary conditions by creating a stick-slip model (Huh & Scriven, 1971; Thompson & Robbins, 1990) in which the contact line is permitted to exhibit both behaviours. Within such a model, simulations would remain pinned until the contact-line stress attains a given threshold level, after which the tear film would evolve as shown in the present model. Re-pinning of the contact line would occur when the contact-line stress and/or velocity drops to a given

level, or when the advancing contact line reaches the mucocutaneous junction, forming the anterior-most limit of the contact-line position. In the absence of ophthalmic data for the contact-line stresses in tear flow, a range of threshold levels may have to be tested by the model. A further level of complexity can be added by modelling a dynamic contact angle between the tear film and the eyelid margin, in which the *in vitro* results of Leiske *et al.* (2011, Figure 4) may be used to inform the contact-angle behaviour, as this data shows that the contact angle of spreading Meibum-coated drops does not adhere to the theoretical predictions of the Cox-Voinov law (Voinov, 1976; Cox, 1986). Through such amendments, the model can be employed to generate theoretical hysteresis curves for the tear film, the validity of which may be tested through *in vivo* observation.

Thirdly, the model can be amended to solve the full Navier-Stokes equations on the computational domain, whilst retaining the novel slip (or stick-slip) boundary conditions at the contact line. Results from such a model could then be compared and contrasted with the pinned results of Zubkov *et al.* (2013). As noted in Chapter 2, the equations of motion studied in Chapters 5 and 6 are leading-order *approximations* to the governing equations of fluid motion and their associated boundary conditions: through the use of the thin-film lubrication approximation, the flow is effectively depth-averaged, with the result that subtle behaviour within the menisci is impossible to resolve[1]. By adapting the present model to solve the full Navier-Stokes equations, the restrictions of the lubrication approximation will be circumvented, thus allowing the use of taller menisci and/or smaller contact angles without invalidating assumptions inherent in the derivation of the model.

Finally, the modelling of environmental factors affecting the tear film may be improved. The evidence of Chapter 5 identifies that the curvature of the corneal substate has a non-trivial influence on the evolution of the tear film. Hence, the existing model would be improved by adding further detail to the shaping of the corneal bulge over

[1]This is highlighted in §2.4.2 by the contradiction between pinned boundary conditions and the predicted contact-line velocities in existing models, and also shown in Zubkov *et al.* (2013)

the iris and pupil, in addition to the curvature of the spherical orbit. By adding a position-dependent substrate curvature, the underlying bulk-fluid dynamics may be subtly altered. This amendment has an obvious extension to the modelling of the tear flow in the presence of a contact lens (*cf.* Trinh *et al.*, 2014, and references therein). Additionally, the influence of the lipid layer as a barrier to evaporation can be studied by updating the heuristic constitutive relationship for the evaporative mass flux (2.34). Furthermore, recent publications by Braun and co-authors (Winter *et al.*, 2010; Li & Braun, 2012) update the modelling of both the corneal wettability and the evaporative flux. Such amendments could also be incorporated into the present model to allow a comparison of results.

The options described above demonstrate that there is a rich and diverse number of areas into which the present model can be expanded as a simple draining flow. The further extension to three dimensions, or to simulate a full blink cycle, identify that exploring human tear-film dynamics is an area that is dense with exciting future modelling opportunities.

Appendix

A Alternative differentiation matrices

The alternative forms of the higher-order Chebyshev differentiation matrices are now presented. The trigonometric identities (3.14) are used to improve the round-off error in the floating-point calculation of the entries in equations (3.10) - (3.12).

The alternative form of the second-order Chebyshev differentiation matrix (3.10) is

$$D_{ij}^{(2)} = \begin{cases} \dfrac{N^4-1}{15}, & i=j=0 \text{ and } i=j=N, \\ \dfrac{x_j^2\,(N^2-1)-N^2-2}{3\sin^4(j\pi/N)}, & i=j,\ i=1(1)N-1, \\ \dfrac{2(-1)^j}{1+\delta_{jN}}\left(\dfrac{2N^2+1}{6\sin^2(j\pi/2N)}-\dfrac{1}{2\sin^4(j\pi/2N)}\right), & i\neq j,\ i=0, \\ \dfrac{2(-1)^{j+N}}{1+\delta_{j0}}\left(\dfrac{2N^2+1}{6\cos^2(j\pi/2N)}-\dfrac{1}{2\cos^4(j\pi/2N)}\right), & i\neq j,\ i=N, \\ \dfrac{(-1)^{i+j+1}}{1+\delta_{j0}+\delta_{jN}}\left(\dfrac{x_i}{2\sin^2(i\pi/N)\,\sin[(i+j)\pi/2N]\,\sin[(j-i)\pi/2N]}\right. & \\ \quad\left.+\dfrac{1}{2\sin^2[(i+j)\pi/2N]\,\sin^2[(j-i)\pi/2N]}\right), & i\neq j,\ i=1(1)N-1. \end{cases} \tag{A.1}$$

The alternative entries of the third-order differentiation matrix (3.11) are

$$D_{ij}^{(3)} = \begin{cases} \dfrac{2N^6 - 7N^4 - 7N^2 + 12}{210}, & i = j = 0, \\ -\dfrac{2N^6 - 7N^4 - 7N^2 + 12}{210}, & i = j = N, \\ \dfrac{x_j\left(2x_j^2\,(N^2-1) - 2N^2 - 13\right)}{4\sin^6(j\pi/N)}, & i = j,\ i = 1(1)N-1, \\ \dfrac{2(-1)^j}{1+\delta_{jN}}\left(\dfrac{N^4-1}{10\sin^2(j\pi/2N)} - \dfrac{2N^2+1}{4\sin^4(j\pi/2N)} + \dfrac{3}{4\sin^6(j\pi/2N)}\right), & i \neq j,\ i = 0, \\ \dfrac{2(-1)^{N+j+1}}{1+\delta_{j0}}\left(\dfrac{N^4-1}{10\cos^2(j\pi/2N)} - \dfrac{2N^2+1}{4\cos^4(j\pi/2N)} + \dfrac{3}{4\cos^6(j\pi/2N)}\right), & i \neq j,\ i = N, \\ \dfrac{(-1)^{i+j}}{1+\delta_{j0}+\delta_{jN}}\left(\dfrac{x_i^2\,(N^2-1) - N^2 - 2}{2\sin^4(i\pi/N)\,\sin[(i+j)\pi/2N]\,\sin[(j-i)\pi/2N]}\right. & \\ \quad + \dfrac{3\,x_i}{4\sin^2(i\pi/N)\,\sin^2[(i+j)\pi/2N]\,\sin^2[(j-i)\pi/2N]} & \\ \quad \left. + \dfrac{3}{4\sin^3[(i+j)\pi/2N]\,\sin^3[(j-i)\pi/2N]}\right), & i \neq j,\ i = 1(1)N-1, \end{cases} \tag{A.2}$$

and finally, the alternative fourth-order Chebyshev differentiation matrix (3.12) is

$$D_{ij}^{(4)} = \begin{cases} \dfrac{N^8 - 12N^6 + 21N^4 + 62N^2 - 72}{945}, & i = j = 0 \text{ and } i = j = N, \\ \dfrac{N^4\sin^4(j\pi/N) - 5N^2\,x_j^2\sin^2(j\pi/N) - \left(6x_j^4 + 83x_j^2 + 16\right)}{5\,\sin^8(j\pi/N)}, & \\ & i = j,\ i = 1(1)N-1, \\ \dfrac{4(-1)^j}{1+\delta_{jN}}\left(\dfrac{(N^4-5N^2+4)\,(2N^2+3)}{210\sin^2(j\pi/2N)} - \dfrac{N^4-1}{10\sin^4(j\pi/2N)}\right. & \\ \quad \left. + \dfrac{2N^2+1}{4\sin^6(j\pi/2N)} - \dfrac{3}{4\sin^8(j\pi/2N)}\right), & i \neq j,\ i = 0, \\ \quad \vdots & \end{cases}$$

$$
D_{ij}^{(4)} = \begin{cases}
\dfrac{4(-1)^{j+N}}{1+\delta_{j0}}\left(\dfrac{(N^4-5N^2+4)\,(2N^2+3)}{210\cos^2(j\pi/2N)} - \dfrac{N^4-1}{10\cos^4(j\pi/2N)}\right. \\
\qquad \left. + \dfrac{2N^2+1}{4\cos^6(j\pi/2N)} - \dfrac{3}{4\cos^8(j\pi/2N)}\right), \qquad i \neq j,\ i = N, \\
\dfrac{(-1)^{i+j+1}}{1+\delta_{j0}+\delta_{jN}}\left(\dfrac{-x_i\Big(2x_i^2\,(N^2-1) - 2N^2 - 13\Big)}{2\sin^6(i\pi/N)\,\sin[(i+j)\pi/2N]\,\sin[(j-i)\pi/2N]}\right. \\
\qquad + \dfrac{x_i^2\,(N^2-1) - N^2 - 2}{\sin^4(i\pi/N)\,\sin^2[(i+j)\pi/2N]\,\sin^2[(j-i)\pi/2N]} \\
\qquad + \dfrac{3\,x_i}{2\sin^2(i\pi/N)\,\sin^3[(i+j)\pi/2N]\,\sin^3[(j-i)\pi/2N]} \\
\qquad \left. + \dfrac{3}{2\sin^4[(i+j)\pi/2N]\,\sin^4[(j-i)\pi/2N]}\right), \\
\qquad\qquad\qquad\qquad\qquad\qquad i \neq j,\ i = 1(1)N-1.
\end{cases}
\tag{A.3}
$$

Bibliography

[1] Acheson, D.J. 1990, *Elementary Fluid Dynamics*, Clarendon Press, Oxford.

[2] Adam, N.K. 1941, *The Physics and Chemistry of Surfaces*, 3rd Edition, Oxford University Press: H. Milford, London.

[3] Adam, N.K. & Jessop, G. 1926, The structure of thin films. Part VIII.– expanded films, *Proc. R. Soc. Lond. A*, **112** (761): 362 – 375.

[4] Afsar-Siddiqui, A.B., Luckham, P.F. & Matar, O.K. 2003a, The spreading of surfactant solutions on thin liquid films, *Adv. Colloid Interface Sci.*, **106**: 183 – 236.

[5] Afsar-Siddiqui, A.B., Luckham, P.F. & Matar, O.K. 2003b, Unstable spreading of aqueous anionic surfactant solutions on liquid films. Part 1. Sparingly soluble surfactant, *Langmuir*, **19**: 696 – 702.

[6] Afsar-Siddiqui, A.B., Luckham, P.F. & Matar, O.K. 2003c, Unstable spreading of aqueous anionic surfactant solutions on liquid films. 2. Highly soluble surfactant, *Langmuir*, **19**: 703 – 708.

[7] Alty, T. 1931, The reflection of vapour molecules at a liquid surface, *Proc. R. Soc. Lond. A*, **131**: 554 – 564.

[8] Aris, R. 1962, *Vectors, Tensors, and the Basic Equations of Fluid Mechanics*, Prentice-Hall, International, London.

[9] Atkinson, K.E. 1989, *An Introduction to Numerical Analysis*, 2nd Edition, John Wiley & Sons, Inc., New York.

[10] Avtar, R. & Srivastava, R. 2006, Modelling the flow of aqueous humor in anterior chamber of the eye, *Appl. Math. Comput.*, **181**: 1336 – 1348.

[11] Aydemir, E., Breward, C.J.W. & Witelski, T.P. 2011, The effect of polar lipids on tear film dynamics, *Bull. Math. Biol.*, **73**: 1171 – 1201.

[12] Baudouin, C. 2001, The pathology of dry eye, *Surv. Ophthalmol.*, **45** (Suppl 2): S211 – S220.

[13] Benedetto, D.A., Clinch, T.E. & Laibson, P.R. 1984, *In vivo* observation of tear dynamics using fluorophotometry, *Arch. Ophthalmol.*, **102**: 410 – 412.

[14] Benilov, E.S. & O'Brien, S.B.G. 2005, Inertial instability of a liquid film inside a rotating horizontal cylinder, *Phys. Fluids*, **17**: 052106.

[15] Berger, R.E. 1973, Pre-corneal tear film mechanics and the contact lens, PhD Thesis, Johns Hopkins University.

[16] Berger, R.E. & Corrsin, S. 1974, A surface tension gradient mechanism for driving the pre-corneal tear film after a blink, *J. Biomechanics*, **7**: 225 – 238.

[17] Borgas, M.S. & Grotberg, J.B. 1988, Monolayer flow on a thin film, *J. Fluid Mech.*, **193**: 151 – 170.

[18] Boyd, J.P. 2001, *Chebyshev and Fourier Spectral Methods*, Revised 2nd Edition, Dover Publications Inc., Mineola, NY.

[19] Braun, R.J. 2012, Dynamics of the tear film, *Annu. Rev. Fluid Mech.*, **44**: 267 – 297.

[20] Braun, R.J. & Fitt, A.D. 2003, Modelling drainage of the precorneal tear film after a blink, *Math. Med. Biol.*, **20**: 1 – 28.

[21] Braun, R.J. & King-Smith, P.E. 2007, Model problems for the tear film in a blink cycle: single-equation models, *J. Fluid Mech.*, **586**: 465 – 490.

[22] Braun, R.J., Usha, R., McFadden, G.B., Driscoll, T.A., Cook, L.P. & King-Smith, P.E. 2012, Thin film dynamics on a prolate spheroid with application to the cornea, *J. Engng Math.*, **73** (1): 121 – 138.

[23] Brenan, K.E., Campbell, S.L. & Petzold, L.R. 1989, *Numerical solution of initial-value problems in differential-algebraic equations*, Volume 14, SIAM, Philadelphia.

[24] Bron, A.J., Tripathi, R.C. & Tripathi, B.J. 1997, *Wolff's Anatomy of the Eye and Orbit*, 8th Edition, Chapman & Hall Medical, London, UK.

[25] Bron, A.J. 2001, Diagnosis of dry eye, *Surv. Ophthalmol.*, **45** (Suppl 2): S221 – S226.

[26] Bron, A.J., Tiffany, J.M., Gouveia, S.M., Yokoi, N. & Voon L.W. 2004, Functional aspects of the tear film lipid layer, *Exp. Eye Res.*, **78**: 347 – 360.

[27] Bron, A.J., Yokoi, N., Gaffney, E.A. & Tiffany, J.M. 2011, A solute gradient in the tear meniscus. 1. A hypothesis to explain Marx's line, *Ocul. Surf.*, **9** (2): 70 – 91.

[28] Brown, S.I. & Dervichian, D.G. 1969, Hydrodynamics of blinking, *Arch. Ophthalmol.*, **82**: 541 – 547.

[29] Burdon, R.S. 1949, *Surface Tension and the Spreading of Liquids*, 2nd Edition, Cambridge University Press, Cambridge.

[30] Burelbach, J.P., Bankoff, S.G. & Davis, S.H. 1988, Nonlinear stability of evaporating/condensing liquid films, *J. Fluid Mech.*, **195**: 463 – 494.

[31] Canuto, C., Hussaini, M.Y., Quarteroni, A. & Zang, T.A. 2006, *Spectral Methods: Fundamentals in Single Domains*, Springer-Verlag, Berlin.

[32] COMSOL Multiphysics®, 2012a, *Users Guide Version 4.3*, COMSOL, Inc., USA.

[33] COMSOL Multiphysics®, 2012b, *Reference Guide Version 4.3a*, COMSOL, Inc., USA.

[34] Cox, R.G. 1986, The dynamics of the spreading of liquids on a surface. Part 1. Viscous flow, *J. Fluid Mech.*, **168**: 169 – 194.

[35] Craig, J.P. & Tomlinson, A. 1997, Importance of the lipid layer in human tear film stability and evaporation, *Optom. Vis. Sci.*, **74** (1): 8 – 13.

[36] Craster, R.V. & Matar, O.K. 2009, Dynamics and stability of thin liquid films, *Rev. Mod. Phys.*, **81**: 1131 – 1198.

[37] Delhaye, J.M. 1974, Jump conditions and entropy sources in two-phase systems. Local instant formulation, *Int. J. Multiphase Flow*, **1**: 395 – 409.

[38] Doane, M.G. 1980, Interaction of eyelids and tears in corneal wetting and the dynamics of the normal human eyeblink, *Am. J. Ophthalmol.*, **89** (4): 507 – 516.

[39] Edmonstone, B.D., Matar, O.K. & Craster R.V. 2004, Flow of surfactant-laden thin films down an inclined plane, *J. Engng Math.*, **50**: 141 – 156.

[40] Edmonstone, B.D., Matar, O.K. & Craster R.V. 2005, Surfactant-induced fingering phenomena in thin film flow down an inclined plane, *Physica D*, **209**: 62 – 79.

[41] Fitt, A.D. & Gonzalez, G. 2006, Fluid mechanics of the human eye: aqueous humour flow in the anterior chamber, *Bull. Math. Biol.*, **68**: 53 – 71.

[42] Fourier, J.B.J. 1822, *Théorie Analytique de la Chaleur*, F. Didot, Paris.

[43] Gaver, D.P., III, & Grotberg, J.B. 1990, The dynamics of a localized surfactant on a thin film, *J. Fluid Mech.*, **213**: 127 – 148.

[44] Gaver, D.P., III, & Grotberg, J.B. 1992, Droplet spreading on a thin viscous film, *J. Fluid Mech.*, **235**: 399 – 414.

[45] Gipson, I.K. 2004, Distribution of mucins at the ocular surface, *Exp. Eye Res.*, **78**: 379 – 388.

[46] Golding, T.R., Bruce, A.S. & Mainstone, J.C. 1997, Relationship between tear-meniscus parameters and tear-film breakup, *Cornea*, **16** (6): 649 – 661.

[47] Goto, E. & Tseng, S.C.G. 2003, Differentiation of lipid tear deficiency dry eye by kinetic analysis of tear interference images, *Arch. Ophthalmol.*, **121**: 173 – 180.

[48] Griffiths, R.W. 2000, The dynamics of lava flows, *Annu. Rev. Fluid Mech.*, **32**: 477 – 518.

[49] Groh, C.M. 2010, Asymptotic and numerical studies of nonlinear evolution equations of viscous thin-film flows, PhD Thesis, The University of Leeds.

[50] Halpern, D. & Grotberg, J.B. 1992, Fluid-elastic instabilities of liquid-lined flexible tubes, *J. Fluid Mech.*, **244**: 615 – 632.

[51] Heryudono, A., Braun, R.J., Driscoll, T.A., Maki, K.L., Cook, L.P. & King-Smith, P.E. 2007, Single-equation models for the tear film in a blink cycle: realistic lid motion, *Math. Med. Biol.*, **24** (4): 1193 – 1213.

[52] Higuera, F.J. 1987, The hydrodynamic stability of an evaporating liquid, *Phys. Fluids*, **30**: 679 – 686.

[53] Hinch, E.J. & Kelmanson, M.A. 2003, On the decay and drift of free-surface perturbations in viscous thin-film flow exterior to a rotating cylinder, *Proc. R. Soc. Lond. A*, **459**: 1193 – 1213.

[54] Hinch, E.J., Kelmanson, M.A. & Metcalfe, P.D. 2004, Shock-like free-surface perturbations in low-surface-tension, viscous, thin-film flow exterior to a rotating cylinder, *Proc. R. Soc. Lond. A*, **460**: 2975 – 2991.

[55] Hindmarsh, R.C.A. 2004, A numerical comparison of approximations to the Stokes equations used in ice sheet and glacier modeling, *J. Geophys. Res.*, **109**: F01012.

[56] Holly, F.J. 1973, Formation and rupture of the tear film, *Exp. Eye Res.*, **15**: 515 – 525.

[57] Holly, F.J. & Lemp, M.A. 1977, Tear physiology and dry eyes, *Surv. Ophthalmol.*, **22**: 69 – 87.

[58] Howell, P.D. 2003, Surface-tension-driven flow on a moving curved surface, *J. Engng Math.*, **45**: 283 – 308.

[59] Huh, C. & Scriven, L.E. 1971, Hydrodynamic model of steady movement of a solid/liquid/fluid contact line, *J. Colloid Interface Sci.*, **35**: 85 – 101.

[60] Huppert, H.E. 2006, Gravity currents: a personal perspective, *J. Fluid Mech.*, **554**: 299 – 322.

[61] Iserles, A. 1996, *A First Course in the Numerical Analysis of Differential Equations*, Cambridge University Press, Cambridge.

[62] Jensen, O.E. & Grotberg, J.B. 1992, Insoluble surfactant spreading on a thin viscous film: shock evolution and film rupture, *J. Fluid Mech.*, **240**: 259 – 288.

[63] Jensen, O.E. & Naire, S. 2006, The spreading and stability of a surfactant-laden drop on a prewetted substrate, *J. Fluid Mech.*, **554**: 5 – 24.

[64] Johnson, M.E. & Murphy, P.J. 2006, Temporal changes in the tear menisci following a blink, *Exp. Eye Res.*, **83**: 517 – 525.

[65] Jones, M.B., Please, C.P., McElwain, D.L.S, Fulford, G.R., Roberts, A.P. & Collins, M.J. 2005, Dynamics of tear film deposition and draining, *Math. Med. Biol.*, **22** (3): 265 – 288.

[66] Jones, M.B., McElwain, D.L.S, Fulford, G.R., Collins, M.J. & Roberts, A.P. 2006, The effect of the lipid layer on tear film behaviour, *Bull. Math. Biol.*, **68**: 1355 – 1381.

[67] Jones, M.B., Fulford, G.R., Please, C.P., McElwain, D.L.S. & Collins, M.J. 2008, Elastohydrodynamics of the Eyelid Wiper, *Bull. Math. Biol.*, **70**: 323 – 343.

[68] Joo, S.W., Davis, S.H. & Bankoff, S.G. 1991, Long-wave instabilities of heated falling films: two-dimensional theory of uniform layers, *J. fluid Mech.*, **230**: 117 – 146.

[69] Jossic, L., Lefevre, P., de Loubens, C., Magnin, A. & Corre, C. 2009, The fluid mechanics of shear-thinning tear substitutes, *J. Non-Newtonian Fluid Mech.*, **161**: 1 – 9.

[70] Kelmanson, M.A. 2009a, Pseudo-three-timescale approximation of exponentially modulated free-surface waves, *J. Fluid Mech.*, **625**: 435 – 443.

[71] Kelmanson, M.A. 2009b, On inertial effects in the Moffatt-Pukhnachov coating-flow problem, *J. Fluid Mech.*, **633**: 327 – 353.

[72] King, A.A., Cummings, L.J., Naire, S. & Jensen, O.E. 2007, Liquid film dynamics in horizontal and tilted tubes: Dry spots and sliding drops, *Phys. Fluids*, **19**: 042102.

[73] King-Smith, P.E., Fink, B.A., Fogt, N., Nichols, K.K., Hill, R.M. & Wilson, G.S. 2000, The thickness of the human precorneal tear film: evidence from reflection spectra, *Invest. Ophthalmol. Vis. Sci.*, **41** (11): 3348 – 3359.

[74] King-Smith, P.E., Fink, B.A., Hill, R.M., Koelling, K.W. & Tiffany, J.M. 2004, The thickness of the tear film, *Curr. Eye Res.*, **29**: 357 – 368.

[75] King-Smith, P.E., Nichols, J.J., Nichols, K.K., Fink, B.A. & Braun, R.J. 2008, Contributions of evaporation and other mechanisms to tear film thinning and break-up, *Optom. Vis. Sci.*, **85** (8): 623 – 630.

[76] King-Smith, P.E., Fink, B.A., Nichols, J.J., Nichols, K.K., Braun, R.J. & McFadden, G.B. 2009, The contribution of lipid layer movement to tear film thinning and breakup, *Invest. Ophthalmol. Vis. Sci.*, **50** (6): 2747 – 2756.

[77] Kundu, P.J. & Cohen, I.M. 2002, *Fluid Mechanics*, 2nd Edition Academic Press, San Diego CA 92101.

[78] Langmuir, I. 1934, Mechanical properties of monomolecular films, *J. Franklin Inst.*, **218** (2): 143 – 171.

[79] Leiske, D.L., Monteux, C., Senchyna, M., Ketelson, H.A. & Fuller, G.G. 2011, Influence of surface rheology on dynamic wetting of droplets coated with insoluble surfactants, *Soft Matter*, **7**: 7747 – 7753.

[80] Li, L. & Braun, R.J. 2012, A model for the human tear film with heating from within the eye, *Phys. Fluids*, **24**: 062103.

[81] Li, S. & Petzold, L.R. 1999, *Design of new* DASPK *for sensitivity analysis*, Technical report, University of California at Santa Barbara, Santa Barbara, CA.

[82] Liu, D.T.S., Di Pascuale, M.A., Sawai, J., Gao, Y.Y. & Tseng, S.C.G. 2005, Tear film dynamics in floppy eyelid syndrome, *Invest. Ophthalmol. Vis. Sci.*, **46** (4): 1188 – 1194.

[83] Maa, J.R. 1967, Evaporation coefficient of liquids, *Ind. Eng. Chem. Fundam.*, **6**: 504 – 518.

[84] Maki, K.L., Braun, R.J., Driscoll, T.A. & King-Smith, P.E. 2008, An overset grid method for the study of reflex tearing, *Math. Med. Biol.*, **25** (3): 187 – 214.

[85] Maki, K.L., Braun, R.J., Henshaw, W.D. & King-Smith, P.E. 2010a, Tear film dynamics on an eye-shaped domain I: pressure boundary conditions, *Math. Med. Biol.*, **27** (3): 227 – 254.

[86] Maki, K.L., Braun, R.J., Ucciferro, P., Henshaw, W.D. & King-Smith, P.E. 2010b, Tear film dynamics on an eye-shaped domain. Part 2. Flux boundary conditions, *J. Fluid Mech.*, **647**: 361 – 390.

[87] Mathers, W.D. 1993, Ocular evaporation in meibomian gland dysfunction and dry eye, *Ophthalmology*, **100**: 347 – 351.

[88] Mathers, W. 2004, Evaporation from the ocular surface, *Exp. Eye Res.*, **78**: 389 – 394.

[89] Maurice, D.M. 1973, The dynamics and drainage of tears, *Int. Ophthalmol. Clin.* **13** (1): 103 – 116.

[90] McDonald, J.E. 1968, Surface phenomena of tear films, *Trans. Am. Ophthalmol. Soc.*, **66**: 905 – 939.

[91] McDonald, J.E. 1969, Surface phenomena of the tear film, *Am. J. Ophthalmol.*, **67** (1): 56 – 64.

[92] McDonald, J.E. & Brubaker, S. 1971, Meniscus-induced thinning of tear films, *Am. J. Ophthalmol.*, **72**: 139 – 146.

[93] Miller, D. 1969, Measurement of the surface tension of tears, *Arch. Ophthalmol.*, **82**: 368 – 371.

[94] Miller, K.L., Polse, K.A. & Radke, C.J. 2002, Black-line formation and the "perched" human tear film, *Curr. Eye Res.*, **25** (3): 155 – 162.

[95] Mishima, S. & Maurice, D.M. 1961, The oily layer of the tear film and evaporation from the corneal surface, *Exp. Eye Res.*, **1**: 39 – 45.

[96] Moffatt, H.K. 1977, Behaviour of a viscous film on the outer surface of a rotating cylinder, *J. Méc.*, **187**: 651 – 673.

[97] Myers, T.G. 1998, Thin films with high surface tension, *SIAM Review*, **40** (3): 441 – 462.

[98] Myers, T.G., Charpin, J.P.F & Chapman, S.J. 2002, The flow and solidification of a thin fluid film on an arbitrary three-dimensional surface, *Phys. Fluids*, **14** (8): 2788 – 2803.

[99] Nagyová, B. & Tiffany, J.M. 1999, Components responsible for the surface tension of human tears, *Curr. Eye Res.*, **19**: 4 – 11.

[100] Navier, C.L.M.H. 1823, Mémoire sur les lois du mouvement des fluides, *Mem. Acad. Sci. Inst. France*, **6**: 389 – 440.

[101] Németh, J., Erdélyi, B., Csákány, B., Gáspár, P., Soumelidis, A., Kahlesz, F. & Lang, Z. 2002, High-speed videotopographic measurement of tear film build-up time, *Invest. Ophthalmol. Vis. Sci.*, **43** (6): 1783 – 1790.

[102] Nichols, B.A., Chiappino, M.L. & Dawson, C.R. 1985, Demonstration of the mucous layer of the tear film by electron microscopy, *Invest. Ophthalmol. Vis. Sci.*, **26**: 464 – 473.

[103] Noakes, C.J., King, J.R. & Riley, D.S. 2006, On the development of rational approximations incorporating inertial effects in coating and rimming flows: a multiple-scales approach, *Q. J. Mech. Appl. Math.*, **59** (2): 163 – 190.

[104] Noakes, C.J., King, J.R. & Riley, D.S. 2011, The effect of mass transfer on steady two-dimensional rimming flow, *J. Engng Math.*, **71**: 223 – 236.

[105] Norn, M.S. 1979, Semiquantitative interference study of fatty layer of precorneal film, *Acta Ophthalmol.*, **57**: 766 774.

[106] Oron, A., Davis, S.H. & Bankoff, S.G. 1997, Long-scale evolution of thin liquid films, *Rev. Mod. Phys.*, **69** (3): 931 – 980.

[107] Owens, H. & Phillips, J, 2001, Spreading of the Tears After a Blink: Velocity and Stabilization Time in Healthy Eyes, *Cornea*, **20** (5): 484 – 487.

[108] Palmer, H.J. 1976, The hydrodynamic stability of rapidly evaporating liquids at reduced pressure, *J. Fluid Mech.*, **75**: 487 – 511.

[109] Please, C.P., Fulford, G.R., McElwain, D.L.S, & Collins, M.J. 2011, Tear film thickness variations and the role of the tear meniscus, *Math. Med. Biol.*, submitted. Pre-print available from `http://eprints.maths.ox.ac.uk/1469/`.

[110] Prydal, J.I., Artal, P., Woon, H. & Campbell, F.W. 1992, Study of human precorneal tear film thickness and structure using laser interferometry, *Invest. Ophthalmol. Vis. Sci.*, **33** (6): 2006 – 2011.

[111] Pukhnachev, V.V. 1977, Motion of a liquid film on the surface of a rotating cylinder in a gravitational field, *J. Appl. Mech. Tech. Phys.*, **18**: 344 – 351.

[112] Repetto, R. 2006, An analytical model of the dynamics of the liquefied vitreous induced by saccadic eye movements, *Meccanica*, **41**: 101 – 117.

[113] Rolando, M. & Refojo, M.F. 1983, Tear evaporimeter for measuring water evaporation rate from the tear film under controlled conditions in humans, *Exp. Eye Res.*, **36**: 25 – 33.

[114] Rolando, M. & Zierhut, M. 2001, The ocular surface and tear film and their dysfunction in dry eye disease, *Surv. Ophthalmol.*, **45** (2): S203 – S210.

[115] Roy, R.V., Roberts, A.J. & Simpson, M.E. 2002, A lubrication model of coating flows over a curved substrate in space, *J. Fluid Mech.*, **454**: 235 – 261.

[116] Ruckenstein, E. & Jain, R.K. 1974, Spontaneous rupture of thin liquid films, *J. Chem. Soc., Faraday Trans. 2*, **70**: 132 – 147.

[117] Shampine, L.F. & Reichelt, M.W. 1997, The MATLAB ODE suite, *SIAM J. Sci. Comput.*, **18**: 1 22.

[118] Sharma, A. 1998, Acid-base interactions in the cornea-tear film system: surface chemistry of corneal wetting, cleaning, lubrication, hydration and defense, *J. Dispersion Sci. Technol.*, **19**: 1031 – 1068.

[119] Sharma, A., Khanna, R. & Reiter, G. 1999, A thin film analog of the corneal mucus layer of the tear film: an enigmatic long range non-classical DLVO interaction in the breakup of thin polymer films, *Coll. Surf. B*, **14**: 223 – 235.

[120] Shikhmurzaev, Y.D. 2008, *Capillary Flows With Forming Interfaces*, Chapman & Hall/CRC, Boca Raton FL.

[121] Singh, K.D., Logan, N.S. & Gilmartin, B. 2006, Three-dimensional modeling of the human eye based on magnetic resonance imaging, *Invest. Ophthalmol. Vis. Sci.*, **47** (6): 2272 – 2279.

[122] Slattery, J.C. 1972, *Momentum, Energy, and Mass Transport in Continua*, McGraw-Hill, Inc., USA.

[123] Smith, G.D. 1985, *Numerical Solution of Partial Differential Equations: Finite Difference Methods*, 3rd Edition, Oxford University Press, Oxford, UK.

[124] Snell, R.S. & Lemp, M.A. 1998, *Clinical Anatomy of the Eye*, 2nd Edition, Blackwell Science, Inc., Malden MA 02148.

[125] Snoeijer, J.H. & Andreotti. B 2013, Moving contact lines: scales, regimes, and dynamical transitions, *Annu. Rev. Fluid Mech.*, **45**: 269 – 292.

[126] Spiegel, M.R. 1959, *Schaum's Outline Series, Theory and Problems of Vector Analysis and an introduction to Tensor Analysis*, McGraw-Hill, Inc., USA.

[127] Stone, H.A. 1990, A simple derivation of the time-dependent convective-diffusion equation for surfactant transport along a deforming interface, *Phys. Fluids A*, **2** (1): 111 – 112.

[128] Struik, D.J. 1961, *Lectures on Classical Differential Geometry*, 2nd Edition, Addison-Wesley Publishing Company, Inc., Reading MA.

[129] Szczęsna, D.H., Jaroński, J. & Kasprzak, H.T. 2006, Interferometric measurements of dynamic changes of tear film, *J. Biomed. Opt.*, **11** (3): 034028.

[130] Thompson, P.A. & Robbins, M.O. 1990, Origin of stick-slip motion in boundary lubrication, *Science*, **250** (4982): 792 – 794.

[131] Tiffany, J.M., Winter, N. & Bliss G. 1989, Tear film stability and tear surface tension, *Curr. Eye Res.*, **8** (5): 507 – 515.

[132] Tomlinson, A. & Khanal, S. 2005, Assessment of tear film dynamics: quantification approach, *The Ocular Surface*, **3** (2): 81 – 95.

[133] Tomlinson, A., Bron, A.J., Korb, D.R., Amano, S., Paugh, J.R., Pearce, E.I., Yee, R., Yokoi, N., Arita, R. & Dogru, M. 2011, The international workshop on meibomian gland dysfunction: report of the diagnosis subcommittee, *Invest. Ophthalmol. Vis. Sci.*, **52** (4): 2006 – 2049.

[134] Trefethen, L.N. 2000, *Spectral Methods in* MATLAB, SIAM, Philadelphia.

[135] Trinh, P.H., Wilson, S.K. & Stone, H.A. 2014, A pinned or free-floating plate on a thin viscous film. Part 1: A rigid plate, *under consideration for publication in J. Fluid Mech.*.

[136] Voinov, O.V. 1976, Hydrodynamics of wetting, *Fluid Dynamics*, **11** (5): 714 – 721.

[137] Warner, M.R.E., Craster, R.V. & Matar, O.K. 2004a, Fingering phenomena associated with insoluble surfactant spreading on thin liquid films, *J. Fluid Mech.*, **510**: 169 – 200.

[138] Warner, M.R.E., Craster, R.V. & Matar, O.K. 2004b, Fingering phenomena created by a soluble surfactant deposition on a thin liquid film, *Phys. Fluids*, **16**: 2933 – 2951.

[139] Weideman, J.A.C. & Reddy, S.C. 2000, A MATLAB differentiation matrix suite, *ACM TOMS*, **26**: 467 – 519.

[140] Winter, K.N., Anderson, D.M. & Braun, R.J. 2010, A model for wetting and evaporation of a post-blink precorneal tear film, *Math. Med. Biol.*, **27**: 211 – 225.

[141] Wong, H., Fatt, I. & Radke, C.J. 1996, Deposition and thinning of the human tear film, *J. Colloid Interface Sci.*, **184**: 44 – 51.

[142] Wyllie, G. 1949, Evaporation and surface structure of liquids, *Proc. R. Soc. Lond. A*, **197**: 383 – 395.

[143] Young, T. 1805, An essay on the cohesion of fluids, *Philos. Trans. R. Soc. Lond.*, **95**: 65 – 87.

[144] Zhu, H. & Chauhan, A. 2005, A mathematical model for tear drainage through the canaliculi, *Curr. Eye Res.*, **30**: 621 – 630.

[145] Zhu, M., Collins, M.J. & Iskander, D.R. 2007, Dynamics of ocular surface topography, *Eye*, **21**: 624 – 632.

[146] Zubkov, V.S., Breward, C.J.W. & Gaffney, E.A. 2012, Coupling fluid and solute dynamics within the ocular surface tear film: a modelling study of black line osmolarity, *Bull. Math. Biol.* **74**: 2062 – 2093.

[147] Zubkov, V.S., Breward, C.J.W. & Gaffney, E.A. 2013, Meniscal tear film fluid dynamics near Marx's line, *Bull. Math. Biol.* **75**: 1524 – 1543.